

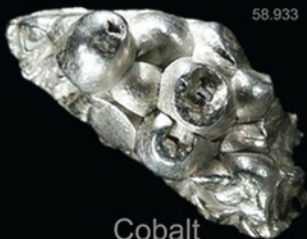






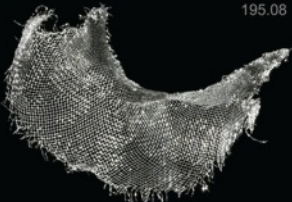

# Конденсированные среды и межфазные границы

РЕЦЕНЗИРУЕМЫЙ НАУЧНЫЙ ЖУРНАЛ

# Condensed Matter and Interphases

PEER-REVIEWED SCIENTIFIC JOURNAL

Том 26, № 1  
Vol. 26, No. 1  
2024

<p>Co 27 58.933</p>  <p>Cobalt</p>	<p>Ni 28 58.693</p>  <p>Nickel</p>	<p>Cu 29 63.546</p>  <p>Copper</p>
<p>Rh 45 102.91</p>  <p>Rhodium</p>	<p>Pd 46 106.42</p>  <p>Palladium</p>	<p>Ag 47 107.87</p>  <p>Silver</p>
<p>Ir 77 192.22</p>  <p>Iridium</p>	<p>Pt 78 195.08</p>  <p>Platinum</p>	<p>Au 79 196.97</p>  <p>Gold</p>



# Condensed Matter and Interphases

## Kondensirovannye sredy i mezhfaznye granitsy

Peer-reviewed scientific journal

Published since January 1999

Periodicity: Quarterly

Volume 26, No. 1, 2024

Full-text version is available in the Russian language on the website: <https://journals.vsu.ru/kcmf>

**Condensed Matter and Interphases** (Kondensirovannye Sredy i Mezhfaznye Granitsy) publishes articles in Russian and English dedicated to key issues of condensed matter and physicochemical processes at interfaces and in volumes.

**The mission of the journal** is to provide open access to the results of original research (theoretical and experimental) at the intersection of contemporary condensed matter physics and chemistry, material science and nanoindustry, solid state chemistry, inorganic chemistry, and physical chemistry, and to share scientific data in the **following sections**: atomic, electron, and cluster structure of solids, liquids, and interphase boundaries; phase equilibria and defect formation processes; structure and physical and chemical properties of interphases; laser thermochemistry and photostimulated processes on solid surfaces; physics and chemistry of surface, thin films and heterostructures; kinetics and mechanism of formation of film structures; electrophysical processes in interphase boundaries; chemistry of surface phenomena in sorbents; devices and new research methods.

**The journal accepts for publication**: reviews, original articles, short communications by leading Russian scientists, foreign researchers, lecturers, postgraduate and undergraduate students.

### FOUNDER AND PUBLISHER:

Voronezh State University

The journal is registered by the Russian Federal Service for Supervision of Communications, Information Technology and Mass Media, Certificate of Registration ПИ № ФС77-78771 date 20.07.2020

The journal is included in the List of peer reviewed scientific journals published by the Higher Attestation Commission in which major research results from the dissertations of Candidates of Sciences (PhD) and Doctor of Science (DSc) degrees are to be published. Scientific specialties of dissertations and their respective branches of science are as follows: 1.4.1. – Inorganic Chemistry (Chemical sciences); 1.4.4. – Physical Chemistry (Chemical sciences); 1.4.6. – Electrochemistry (Chemical sciences); 1.4.15. – Solid State Chemistry (Chemical sciences); 1.3.8. – Condensed Matter Physics (Physical sciences).

The journal is indexed and archived in: Russian Scientific Index Citations, Scopus, Chemical Abstract, EBSCO, DOAJ, CrossRef

Editorial Board and Publisher Office:  
1 Universitetskaya pl., Voronezh 394018  
Phone: +7 (432) 2208445  
<https://journals.vsu.ru/kcmf>  
E-mail: [kcmf@main.vsu.ru](mailto:kcmf@main.vsu.ru)

When reprinting the materials, a reference to the Condensed Matter and Interphases must be cited

The journal's materials are available under the Creative Commons "Attribution" 4.0 Global License



© Voronezh State University, 2024

### EDITOR-IN-CHIEF:

**Victor N. Semenov**, Dr. Sci. (Chem.), Full Professor, Voronezh State University, (Voronezh, Russian Federation)

### VICE EDITORS-IN-CHIEF:

**Evelina P. Domashevskaya**, Dr. Sci. (Phys.–Math.), Full Professor, Voronezh State University, (Voronezh, Russian Federation)

**Polina M. Volovitch**, Ph.D. (Chem.), Associate Professor, Institut de Recherche de Chimie (Paris, France)

### EDITORIAL BOARD:

**Nikolay N. Afonin**, Dr. Sci. (Chem.), Voronezh State Pedagogical University (Voronezh, Russian Federation)

**Vera I. Vasil'eva**, Dr. Sci. (Chem.), Full Professor, Voronezh State University, (Voronezh, Russian Federation)

**Aleksandr V. Vvedenskii**, Dr. Sci. (Chem.), Full Professor, Voronezh State University, (Voronezh, Russian Federation)

**Victor V. Gusarov**, Dr. Sci. (Chem.), Associate Member of the RAS, Ioffe Physical-Technical Institute RAS (St. Petersburg, Russian Federation)

**Vladimir E. Guterman**, Dr. Sci. (Chem.), Full Professor, Southern Federal University (Rostov-on-Don, Russian Federation)

**Boris M. Darinskii**, Dr. Sci. (Phys.–Math.), Full Professor, Voronezh State University, (Voronezh, Russian Federation)

**Vladimir P. Zlomanov**, Dr. Sci. (Chem.), Full Professor, Moscow State University, (Moscow, Russian Federation)

**Valentin M. Ievlev**, Dr. Sci. (Phys.–Math.), Full Member of the RAS, Moscow State University, (Moscow, Russian Federation)

**Aleksandr D. Izotov**, Dr. Sci. (Chem.), Associate Member of the RAS, Kurnakov Institute of General and Inorganic Chemistry RAS (Moscow, Russian Federation)

**Oleg A. Kozaderov**, Dr. Sci. (Chem.), Associate Professor, Voronezh State University, (Voronezh, Russian Federation)

**Andrey I. Marshakov**, Dr. Sci. (Chem.), Full Professor, Frumkin Institute of Physical Chemistry and Electrochemistry RAS (Moscow, Russian Federation)

**Irina Ya. Mittova**, Dr. Sci. (Chem.), Full Professor, Voronezh State University, (Voronezh, Russian Federation)

**Victor V. Nikonenko**, Dr. Sci. (Chem.), Full Professor, Kuban State University (Krasnodar, Russian Federation)

**Oleg V. Ovchinnikov**, Dr. Sci. (Phys.–Math.), Full Professor, Voronezh State University, (Voronezh, Russian Federation)

**Sergey N. Saltykov**, Dr. Sci. (Chem.), Associate Professor, Novolipetsk Steel (Lipetsk, Russian Federation)

**Vladimir F. Selemenov**, Dr. Sci. (Chem.), Full Professor, Voronezh State University, (Voronezh, Russian Federation)

**Vladimir A. Terekhov**, Dr. Sci. (Phys.–Math.), Full Professor, Voronezh State University, (Voronezh, Russian Federation)

**Evgeny A. Tutov**, Dr. Sci. (Chem.), Associate Professor, Voronezh State Technical University (Voronezh, Russian Federation)

**Pavel P. Fedorov**, Dr. Sci. (Chem.), Full Professor, Prokhorov General Physics Institute RAS (Moscow, Russian Federation)

**Vitaly A. Khonik**, Dr. Sci. (Phys.–Math.), Full Professor, Voronezh State Pedagogical University (Voronezh, Russian Federation)

**Andrey B. Yaroslavtsev**, Dr. Sci. (Chem.), Full Member of the RAS, Kurnakov Institute of General and Inorganic Chemistry RAS (Moscow, Russian Federation)

### INTERNATIONAL MEMBERS OF THE EDITORIAL BOARD:

**Mahammad Babanly**, Dr. Sci. (Chem.), Associate Member of the ANAS, Institute of Catalysis and Inorganic Chemistry ANAS (Baku, Azerbaijan)

**Tiziano Bellezze**, Dr. Sci. (Chem.), Marche Polytechnic University (Ancona, Italy)

**Mane Rahul Maruti**, Ph.D. (Chem.), Shivaji University (Kolhapur, India)

**Nguyen Anh Tien**, Ph.D. (Chem.), Associate Professor, University of Pedagogy (Ho Chi Minh City, Vietnam)

**Vladimir V. Pankov**, Dr. Sci. (Chem.), Full Professor, Belarusian State University (Minsk, Belarus)

**Fritz Scholz**, Dr. Sci., Professor, Institut für Biochemie Analytische Chemie und Umweltchemie (Greifswald, Germany)

**Mathias S. Wickleder**, Dr. Sci., Professor, University of Cologne (Köln, Germany)

**Vladimir Sivakov**, Dr. rer. nat., Leibniz Institute of Photonic Technology (Jena, Germany)

### EXECUTIVE SECRETARY:

**Vera A. Logacheva**, Cand. Sci. (Chem.), Voronezh State University, (Voronezh, Russian Federation)

## CONTENTS

**Review**

*Abramova E. N., Kozlov R. Yu., Syrov Yu. V., Khokholov A. I., Parkhomenko*

Modern scientific and practical approaches to the production of substrates from semiconductor compounds A<sup>3</sup>B<sup>5</sup>. Review

*Biryukov A. I., Kozaderov O. A., Batmanova*

Features of the corrosion of coatings based on zinc alloys: oxidation products and the selective dissolution of zinc. Review

*Shaposhnik V. A.*

Prospects of membrane catalysis in hydrogen energetics. Mini review

**Original articles**

*Grevtseva I. G., Smirnov M. S., Chirkov K. S., Latyshev A. N., Ovchinnikov O. V.*

Synthesis and luminescent properties of PbS/SiO<sub>2</sub> core-shell quantum dots

*Zartsyn I. D., Vvedenskii A. V., Bobrinskaya E. V., Kozaderov O. A.*

Isolation of partial coupled processes of anodic oxidation of OH<sup>-</sup> ion on gold using a combination of a graph-kinetic analysis method and linear voltammetry data

*Quynh Nhu Le Thi, Thi Quynh Trang Ly, Anh Tien Nguyen, Quoc Thiet Nguyen, De-Hao Tsai, and Tien Khoa Le*

Simple synthesis of floating Fe<sub>2</sub>O<sub>3</sub>/Luffa catalysts for the photo-Fenton degradation of methyl orange at near neutral pH

*Lenshin A. S., Frolova V. E., Ivkov S. A., Domashevskaya E. P.*

Microstructural and hydrophilic properties of polyethylene terephthalate glycol polymer samples with different 3D printing patterns

*Mamand D. M., Aziz D. M., Qadr H. M.*

An investigation of the electronic structure and optoelectronic properties of 4-((2-hydroxy-3-methoxybenzylidene)amino)-N-(thiazol-2-yl)benzene sulfonamide

3 *Myasoedova T. N., Nedoedkova O. V., Yalovega G. E.*  
Electrophysical properties of composite materials based on graphene oxide and polyaniline

25 *Parchinskiy P. B., Gazizulina A. S., Nusretov R. A.*  
Spontaneous photomagnetolectric effect in ferromagnetic GaMnAs epitaxial layers

37 *Petukhov I. V., Kichigin V. I.*  
Electrochemical activity of electroless Ni-P coatings in the hydrogen evolution reaction

45 *Popov P. A., Zentsova A. A., Voronov V. V., Novikov I. A., Chernova E. V., Fedorov P. P.*  
Study of the thermal conductivity of natural carbonates

*Syugaev A. V., Porsev V. E.*  
Electrochemical impedance of porous tantalum solids: modeling of frequency response

55 *Timushkov P. V., Burmistrov V. A., Ulyanov M. N., Semenov V. N.*  
Composition and structure of tungsten antimony acid

68 *Chuvenkova O. A., Boikov N. I., Ryabtsev S. V., Parinova E. V., Chumakov R. G., Lebedev A. M., Smirnov D., Makarova A., Titova S. S., Fateev K. A., Turishchev S. Yu.*

Electronic structure and composition of tin oxide thin epitaxial and magnetron layers according to synchrotron XANES studies

78 *Shatskaia M. G., Nazarovskaia D. A., Gonchar K. A., Lomovskaya Ya. V., Tsiniiaikin I. I., Shalygina O. A., Kudryavtsev A. A., Osminkina L. A.*

Photoluminescent porous silicon nanowires as contrast agents for bioimaging

In memory of Professor V. A. Shaposhnik

Guide for Authors – 2024

88

104

111

117

127

135

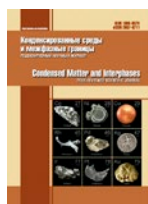
146

153

161

168

169



# Condensed Matter and Interphases

Kondensirovannye Sredy i Mezhfaznye Granitsy  
<https://journals.vsu.ru/kcmf/>

## Review

Review article

<https://doi.org/10.17308/kcmf.2024.26/11805>

## Modern scientific and practical approaches to the production of substrates from semiconductor compounds $A^3B^5$ . Review

E. N. Abramova<sup>1</sup>✉, R. Yu. Kozlov<sup>1</sup>, Yu. V. Syrov<sup>1</sup>, A. I. Khokholov<sup>1</sup>, Yu. N. Parkhomenko<sup>2</sup>

<sup>1</sup>AO «Giredmet» PAO «Rosatom»,  
2-1 Elektrodnyaya st., Moscow 111524, Russian Federation

<sup>2</sup>National University of Science and Technology MISIS  
4-1 Leninskiy prospekt, Moscow 119049, Russian Federation

### Abstract

Modern electronic and optical engineering uses  $A^3B^5$  single-crystal semiconductor materials (GaAs, GaSb, InAs, InSb, and InP) as substrates for epitaxial growth. These materials are obtained in the form of massive single-crystal ingots. Therefore, technologies for processing of these  $A^3B^5$  wafers are developed to produce the substrates for epitaxial growth. The miniaturization of modern systems and devices demands the high quality of the substrates surface. One of the main criteria is a low surface roughness ( $R_q$ ) (of about 0.5 nm). To meet this requirement, it is necessary to elaborate the existing methods of surface treatment.

The review analyses the current approaches to the treatment of the surface of semiconductor wafers of  $A^3B^5$  single-crystal materials. It considers the specifics of wafers machining followed by their polishing. The article also presents an analysis of the polishing methods. It reveals that at the moment the chemical-mechanical polishing of  $A^3B^5$  wafers is the most commonly used method. The review presents the main parameters of this process and systematizes the existing theoretical approaches. The analysis determined the key tendencies in the development of chemical-mechanical polishing of semiconductor  $A^3B^5$  wafers aimed at increasing the quality of wafers. The article also analyses the latest studies regarding the methods of chemical polishing as an alternative to chemical-mechanical polishing. The next section focuses on surface passivation methods used upon obtaining wafers with a low roughness. Passivation is performed to reduce the reactivity of the surface and stabilize surface states of wafers.

A classification of passivation methods is suggested based on the obtained chemical composition of the surface, when the passivation layers are created using oxidation, sulfidizing, or nitriding. Another classification is based on the method of creating passivating coatings and includes wet chemical methods and physico-chemical methods.

**Keywords:** Semiconductor plates,  $A^3B^5$  materials, Machining, Polishing, Chemical mechanical polishing, Surface passivation

**For citation:** Abramov E. N., Kozlov R. U., Syrov U. V., Khokholov A. I., Parkhomenko Yu. N. Modern scientific and practical approaches to the production of substrates from semiconductor compounds  $A^3B^5$ . Review. *Condensed Matter and Interphases*. 2024;26(1): 3–24. <https://doi.org/10.17308/kcmf.2024.26/11805>

**Для цитирования:** Абрамова Е. Н., Козлов Р. Ю., Сыров Ю. В., Хохлов А. И., Пархоменко Ю.Н. Современные научные и практические решения в технологии изготовления подложек полупроводниковых соединений  $A^3B^5$ . Обзор. *Конденсированные среды и межфазные границы*. 2024;26(1): 3–24. <https://doi.org/10.17308/kcmf.2024.26/11805>

✉ Elena N. Abramova, e-mail: [overmind11@rambler.ru](mailto:overmind11@rambler.ru)

© Abramov E. N., Kozlov R.U., Syrov U. V., Khokholov A. I., Parkhomenko Yu. N., 2024



The content is available under Creative Commons Attribution 4.0 License.



## 1. Introduction

The variety of binary compounds  $A^3B^5$  includes antimonides, arsenides, nitrides, and phosphides of indium, gallium, aluminum, and boron. Many of them are of special interest for the development of electrical engineering, microwave electronics, optoelectronics, photonics, and the production of sensors. At the moment, some of the  $A^3B^5$  compounds are obtained during the production of semiconductors as single-crystal ingots, which are then divided into wafers for further production of semiconductor devices. Another way is to obtain such compounds in the form of films on substrates by means of epitaxial growth methods. Direct band gap materials with high electron mobility, including GaAs, GaSb, InAs, InSb, InP, and GaN, are most commonly used as substrate materials. Gallium nitride is grown by both epitaxial growth methods on substrates made of other materials and an expensive ammonothermal method from a Na-Ga-N melt [1]. There are also techniques for the industrial production of GaAs, GaSb, InAs, InSb, and InP single crystals, which are then divided into wafers. However, dividing single-crystal ingots into wafers results in a highly defective surface. Therefore, it is important to consider these materials due to two factors. First, they are of great interest for instrument manufacturers. Second, the industrial production of massive single-crystal ingots uses GaAs, GaSb, InAs, InSb, and InP semiconductor compounds, and the techniques for obtaining high quality wafers for the precision epitaxial growth are being developed for these materials only.

The rapid development of various fields of optics and electronics requires the miniaturization of semiconductor devices and structures. This, in turn, requires a higher quality of wafers used to produce such devices. At the moment, epi-ready wafers are in high demand [2], as they are the most technologically advanced. According to [3], epi-ready single-crystal semiconductor wafers can be used (primarily in the epitaxy processes) with no further treatment. However, there is no universal definition of the term epi-ready. Besides the specific electrophysical characteristics and low defectiveness, another important criterion for the quality of semiconductor wafers is the planarity of the surface with a maximum roughness ( $R_a$ ) of 0.5 nm.

At the moment, single-crystal  $A^3B^5$  wafers are produced following a technological scheme, which generally includes five main stages:

1. a single crystal is cut into wafers;
2. the wafers are beveled;
3. the wafers are machined and chemically purified;
4. the surface is polished and washed;
5. the surface is passivated.

The purpose of this review was to systematize and analyze the existing scientific approaches and practical recommendations on machining and polishing of semiconductor wafers obtained from single crystal ingots of GaAs, GaSb, InAs, InSb, and InP.

## 2. Machining of semiconductor wafers

After a single crystal is cut into wafers, they need to be flattened. If semiconductor single crystals are cut using dicing blades, a rough non-planar layer is formed in the near-surface region of the wafers. This is mainly caused by the large diamond points with an average size of 28–40  $\mu\text{m}$  used for dicing [4]. Therefore, further machining is required to reduce the roughness of the surface and ensure its planarization, which results in significant losses of the expensive material. Diamond wire sawing of single crystals helps to reduce the thickness of rough layers due to a smaller size of diamond grains (less than 20  $\mu\text{m}$ ) as well as due to a small degree of thermodynamic tension in the region of contact between the saw and the ingot [4, 5]. This helps to avoid material losses, but does not solve the problem of surface planarization. Therefore, today the main purpose of the machining process is to ensure high surface planarity and low roughness.

During the machining process, abrasive grains penetrate into the material and remove its fragments. As a result, the thickness of the wafer becomes more uniform, while the wafer itself becomes thinner. At the same time, a damaged area is formed [6], including a rough layer, a crack layer, and a defective layer, containing residual cracks and tensions. The thickness of this area is proportional to the size of abrasive grains [7, 8], their number, and the hardness of the abrasive (usually about three times larger than the abrasive grain).

There are two basic methods of machining of semiconductor wafers: grinding and lapping [9, 10].

There are generally three material removal mechanisms:

- chipping the material microparticles with abrasive embedded into the plate;
- cutting of the material with an abrasive;
- chipping the material after the free (loose) abrasive are indented into the material and cracks and tensions are formed.

Lapping presents a combination of all three methods. The most preferable method of material removal is to chip the material at the intersections of cracks formed as a result of indentation of loose abrasive particles. This helps to remove the material evenly. Grinding involves the first two mechanisms with machining being the main part of the process. Grinding can also be performed by means of quasi-elastic material removal [12, 13], when the required tension is obtained in the surface layer [10, 12, 14]. This seems to be a promising approach to the processing of  $A^3B^5$ . However, grinding is rarely used by the manufacturers of  $A^3B^5$  semiconductors and therefore is beyond the scope of this review.

### 2.1. Lapping of semiconductor wafers

The purpose of lapping is to ensure that the roughness  $R_a$  of  $A^3B^5$  wafers is about 0.63–1.0  $\mu\text{m}$  and their total thickness variation ( $TTV$ ) is 4–6  $\mu\text{m}$ .

Double-sided lapping is usually characterized by a smaller total thickness variation of wafers than single-sided lapping due to a more homogeneous treatment of wafers. The lapping pressure induces the indentation of abrasive grains into the surface layers of the wafer at a depth of 5–10% of their size and cutting/chipping off fragments of those layers [15]. There should be a gap between the surface of the wafer and the surface of the abrasive so that the lapping suspension could distribute evenly. For this, an inert solvent with a required viscosity is used (water or organic solvents including oils).

Abrasive grains can be of various shapes: round, flattened, cylindrical, and polygonal amorphous. The shape of the grains affects the above described material removal mechanisms. Grains of various sizes (from 3 to 63  $\mu\text{m}$ ) can

be used for lapping. The most common are grains with a size of 5–20  $\mu\text{m}$  [16]. There are also various national standards used to classify abrasive powders: GOST 52381-2005 (Russia), FEPA (Europe, USA), ANSI – CAMI (USA), and JIS (Japan).

Coarse-grained powders (with grains of a large size) are usually used to remove larger asperities and make the thickness of the wafer more uniform. Then, fine powders with grains of a smaller size are used. We should note that wire cutting allows obtaining a high enough quality of wafers to perform one-stage lapping.

To ensure the effective planarization of a rough wafer, the abrasive used should be harder than the wafer material. Both hard and softer abrasive powders are studied as possible abrasives for the lapping of fragile  $A^3B^5$  materials. Thus, in [17] (100) oriented InSb wafers were flattened using a diamond suspension with a particle size of 1  $\mu\text{m}$ . In [18], an  $\text{Al}_2\text{O}_3$  abrasive with a particle size of 5  $\mu\text{m}$  was used for the lapping of GaAs. In [2], the lapping of GaAs and InSb was performed using aluminum oxide powders with grain sizes of 10–14  $\mu\text{m}$  and 5–7  $\mu\text{m}$  respectively. These lapping conditions allowed obtaining a flat surface without curling [17], while the strength of GaAs and InSb wafers slightly increased after cutting [2]. There are also a number of commercially available abrasive powders and suspensions containing, for instance,  $\text{Al}_2\text{O}_3$ ,  $\text{SiO}_2$ , and  $\text{ZrO}_2$ . However, it is not clear, if the composition of such powders presents a mixture of the said compounds, or there is an equal amount of all the three substances in each particle of the powder [19].

Another factor affecting the lapping process is the material of the lapping plate. Prior to the lapping of semiconductor wafers, it is necessary to flatten the lapping plates. As a result, the planarity of the lapping plates should be equal to the mean size of abrasive grains. The most common are lapping plates made of pig iron and glass of various makes, which are harder than the abrasives. Therefore, abrasive grains do not penetrate into the lapping plates. This allows them to roll about the surface of a semiconductor wafer, which destroys the abrasive grains.

Besides selecting the size of abrasive grains and the lapping plates, optimization of the lapping conditions involves determining the



lapping pressure, the concentration of the abrasive particles in the lapping suspension, the suspension supply rate, and the velocity of the grinding disk. Optimization of these parameters can result in  $R_a$  of about  $0.63 \div 1 \mu\text{m}$  and  $TTV$  of about  $2 \div 4 \mu\text{m}$ .

### 3. Polishing of semiconductor wafers

Semiconductor wafer polishing follows the machining stage. The main task is to remove the damaged layer and smooth out the surface while retaining the shape obtained during lapping. Polished wafers should have no mechanical defects (cracks, scratches) and residual abrasive particles on the surface [12].

There are the following main methods of polishing:

- mechanical polishing;
- chemical polishing (chemical-dynamic polishing, electrochemical polishing, dry etching);
- chemical-mechanical polishing (CMP) with or without an abrasive.

Since GaAs, GaSb, InAs, InSb, and InP are highly fragile and soft, mechanical polishing does not meet the requirements for the epitaxy quality of the surface [20].

#### 3.1. Chemical-mechanical polishing

##### 3.1.1. CMP parameters

Chemical-mechanical polishing is most commonly used for the industrial treatment of  $A^3B^5$  semiconductor materials. This type of polishing is based on a combined effect of the chemical and mechanical treatment of materials. The process is performed on a rotary polishing pad with or without an abrasive. There are also other configurations of polishing pads. Thus, [21] studies the functioning of a roll-type linear chemical mechanical polishing system.

Various CMP techniques have been developed for particular  $A^3B^5$  materials. In [22], the polishing of InP wafers involves the interaction with an oxidizing agent, NaClO. The formed oxide layer is mechanically removed by the polishing pad without an abrasive. The GaAs CMP method presented in [23] involves formation of oxide layers on the wafer surface when interacting with  $H_2O_2$  or NaClO. The oxides then interact with alkali producing hydroxides, which are mechanically removed by an abrasive.

On the whole, chemical mechanical polishing involves changing the chemical form of the processed material, primarily to oxides or hydroxides, followed by the mechanical removal of these compounds. The specific features of these processes depend on the conditions of CMP. Optimal polishing conditions are determined for every particular system.

Generally, the key parameters of the CMP process determining the quality of the surface are the following:

1. Parameters of mechanical treatment:
    - 1.1. the material and hardness of the polishing pad, the position of grooves, the geometry of grooves, and the surface morphology of the polishing pad;
    - 1.2. the polishing pressure (load, down force) applied to the wafer;
    - 1.3. the size and concentration of abrasive particles;
    - 1.4. the temperature;
    - 1.5. the relative velocity between the wafer to the polishing pad;
    - 1.6. the viscosity of the polishing slurry.
  2. Parameters of chemical treatment:
    - 2.1. the substances constituting the polishing slurry and their concentrations: an oxidizer, a complexant, a passivating agent, an abrasive, a dispersant ensuring stable distribution of the abrasive particles in the solution, and a solvent; stability of the components during storage, pH of the slurry;
    - 2.2. the slurry supply rate.
  3. Parameters of the polished material:
    - 3.1. the total thickness variation and geometric parameters of the wafer after lapping;
    - 3.2. the type, chemical composition, and specific features of the treated material, the crystallographic orientation of the wafer.
- The parameters listed above are interconnected and can affect each other. Therefore, it is reasonable to analyze the connections between them.
- a) The optimization of CMP modes usually starts with determining the required **polishing pressure on the wafer and the relative velocity between the wafer and the polishing pad**. They contribute greatly to the rate of material removal from the surface of the wafer. Publication [24] demonstrated that when polishing GaAs 4”

wafers at a pressure lower than 90 H, the material removal rate is not uniform. At a polishing pressure over 90 H, the material removal rate becomes even and the roughness of the surface decreases.

Publication [25] shows that when polishing InSb wafers using a slurry based on a colloidal solution of silicon dioxide (0.2 vol. % of SiO<sub>2</sub> colloidal solution with a particle size of 50 nm, the content of silicon dioxide in the initial colloidal solution – 31 wt.%), hydrogen peroxide, and citric or lactic acid at pH = 4 and the velocity of the polishing pad 60 r/min, the optimal polishing pressure is 80 g/cm<sup>2</sup>. This is accounted for by the optimal thickness of the polishing slurry between the wafer and the polishing pad as well as the correspondence between the chemical reaction rate and the material removal rate. When the pressure is reduced to 40 g/cm<sup>2</sup>, the surface becomes rougher. The authors believe that this can be caused by a thicker layer of the polishing slurry between wafer and polishing pad, which results in the inhomogeneity of the chemical processes on the wafer surface. When the pressure is over 100 g/cm<sup>2</sup>, the material is mainly removed mechanically, which also results in the deterioration of the wafer properties[25].

The wetting mode and thickness of the slurry between the wafer and the polishing pad are determined by the polishing pressure and its ratio with the relative velocity between wafer and pad and the viscosity of the polishing slurry ( $\eta \cdot V/P$ ).

b) **Viscosity** of the polishing slurry also affects the mass transfer of the reaction products removed from the surface and the movement of the abrasive particles. When the viscosity is too high, it hinders the movement of the abrasive particles in the polishing slurry and the removal of the CMP products from the surface of the wafer. Local accumulations of CMP products are also possible, which prevents the even flow of the polishing slurry.

When the viscosity is too low, the wafer is in direct contact with the polishing pad, which increases mechanical pressure on the material. This can result in uneven material removal and increased roughness.

The viscosity is determined by the chemical composition of the polishing slurry, its pH;

type, particle size, and the concentration of the abrasive [26]; as well as by the mechanical parameters of the CMP process. Publication [27] studies the dependence between the viscosity of the polishing slurry with colloidal particles of silicon dioxide and the shear rate calculated as a velocity of the wafer to the polishing pad (m/s) and the distance between them (m). The study demonstrates that a significant growth in the shear rate results in higher viscosity of a polishing slurry based on a colloidal solution of silicon dioxide, and the fact that polishing slurries can show non-Newtonian behavior. Additionally, the authors [27] note that at increased velocity between the wafer and the polishing pad, the slurry movement becomes turbulent.

c) Silicon dioxide is the most common commercial abrasive used for the CMP of A<sup>3</sup>B<sup>5</sup>. It is used in the form of colloidal solutions. To prevent the coagulation and sedimentation of particles, stabilization additives are used. However, the manufacturers keep the composition of such additives a secret. The function of the abrasive is to remove mechanically the material as well as to absorb the products of polishing and to take them away from the wafer surface. The existing studies [21, 28] provide different experimental results regarding the effect of the **size and concentration of abrasive particles** in the polishing slurry on the characteristics of CMP, including the material removal rate. The main requirements for abrasives are the following: they should be as hard as the polished material (or softer), inert to the components of the polishing slurry, and have a small particle size (tens and hundreds of nm, most commonly 10÷100 nm [29]). Publication [30] demonstrates that SiO<sub>2</sub> has a low reactivity with regard to GaAs. It also shows that CeO<sub>2</sub> abrasive particles tend to chemically interact with GaAs. It is still important to further investigate the effect of dispersants on the properties of abrasives [31–33].

Some researchers do not use abrasive particles when polishing A<sup>3</sup>B<sup>5</sup> materials [22, 34, 35]. This makes the polishing process different, because the oxidized forms of the material are removed by the polishing pad only.

d) Polyurethane **polishing pads** of various hardness are used for the CMP of semiconductor



materials both with and without abrasives. Article [36] shows that softer polishing pads ensure a smaller number of defects on A<sup>3</sup>B<sup>5</sup> wafers.

The surface morphology of the polishing pad should facilitate the removal of most asperities from the surface of the wafer. When modelling the CMP process in [37, 38] the authors tried to take into account the impact of polishing pad area being in contact with a wafer on the material removal rate. For this, the Greenwood-Williamson model was used (1):

$$A_T = (f_s / C) \cdot (R_p / \sigma_p)^{1/2} \cdot (P \cdot A_w / E_{pw}), \quad (1)$$

where  $A$  is the contact area between the polishing pad and the wafer,  $R_p$  is the curvature radius of the pad asperities,  $\sigma_p$  is the standard deviation of asperity heights of the polishing pad,  $P$  is the polishing pressure,  $A_w$  is the nominal surface area of the wafer,  $E_{pw}$  is the average Young's modulus of the wafer and the polishing pad (the elastic modulus of the polishing pad is usually three times smaller than that of the material [22]),  $f_s$  is the density of asperities of the polishing pad divided by grooves, and  $C$  is a constant equal  $0.3 \div 0.4$ .

This model was used to develop a methodology for assessing the polishing rate [52]. The contact area between the polishing pad and the wafer is not constant because of the glazing and mechanical wear of the polishing pad [37, 38]. To reduce the glazing effect, the surface of the polishing pad can be conditioned, for instance, with diamond tips [39, 40, 41, 42]. Therefore, the number of abrasive particles in the polishing pad may vary [43]. Additionally, larger number of pad asperities results in a higher chance of pad glazing [44].

e) The number of abrasive particles supplied to the polishing pad per unit of time depends on the **polishing slurry supply rate**. If the slurry supply rate is too fast, the abrasive particles can cover the whole surface of the polished wafer. This can reduce the rate of chemical reactions of the CMP due to preventing reagents access to the reaction region [21, 45].

If the slurry supply rate is too slow, the slurry can distribute unevenly over the polishing pad, which will result in inhomogeneous chemical interactions on the surface of the wafer and increased roughness.

Therefore, the slurry supply rate can affect the kinetics of the chemical interactions, the wetting of the surface, and the heat removal and reducing/maintaining the temperature in the reaction area.

f) **Temperature** is another important parameter of the CMP process. Publication [46] suggests using an IR sensor to control the temperature. Temperature affects the kinetics of the chemical processes, the viscosity of the polishing slurry (at higher temperatures the viscosity decreases), the zeta potential of abrasive particles, their hydrodynamic radius, the mechanism of material removal, and the pH of the polishing slurry. At higher temperatures, more oxygen from the air can dissolve in the polishing slurry, which can lead to the undesirable and uncontrollable oxidation of the polished material.

Taking into account the high reactivity of polished materials and chemical agents, the CMP of A<sup>3</sup>B<sup>5</sup> is performed at room temperature.

g) The chemical interaction between the polished material and the polishing slurry is the first stage of the CMP process. Generally, A<sup>3</sup> and B<sup>5</sup>, elements are oxidized, with the oxidized forms of each element having different compositions depending on the pH of the environment [47]. H<sub>2</sub>O<sub>2</sub> or NaClO are most commonly used as oxidizers. Along with an oxidizer, an abrasive, and an abrasive dispersant, polishing slurries can include a number of substances functioning as complexants, passivating agents, and solvents, as well as buffer solutions. The **composition of the slurry** determines its pH, the possible reactions, and the composition of the oxidized forms and complex compounds, which have various degrees of solubility and are more or less easily mechanically removed from the surface.

Various polishing slurries are used with particular materials (the examples of their compositions are given in Table 1, section 3.1.3). The existing literature on the problem does not provide any information about the exact composition of buffer solutions [48].

Article [49] demonstrates that the rate of chemical reactions between the polishing slurry and the polished material depends on the ratio of the slurry components and their concentrations.

h) Some studies focus on the effect of the polishing slurry pH on the rate of CMP for various A<sup>3</sup>B<sup>5</sup> materials. For instance, article [28] demonstrates that a strongly acidic or a highly alkaline environment increases the rate of GaAs removal, while a neutral pH leads to a lower material removal rate. The lowest roughness of GaAs was observed at pH = 10. Patent [25] demonstrates that polishing of InSb wafers in a solution with an alkaline pH results in the formation of scratches on the surface. When the pH decreases from 7 to 2, the roughness of the surface gradually increases together with an increase in the material removal rate. The patent suggests a method of polishing InP and InSb wafers at pH = 4÷6 with a polishing slurry containing a colloidal solution of silicon dioxide particles, hydrogen peroxide, and citric acid [25].

Therefore, polishing slurries of various chemical compositions are used for the CMP of specific A<sup>3</sup>B<sup>5</sup> materials.

i) The chemical composition of the polishing slurry, in turn, is chosen to the **characteristics of the polished material**, including its chemical composition and the crystallographic orientation of wafers. Elements of A<sup>3</sup>B<sup>5</sup> semiconductor compounds have different oxidation rates. The formed oxides, in turn, have different solubilities. Thus, gallium (Ga<sub>2</sub>O<sub>3</sub> [35]) and indium (In<sub>2</sub>O<sub>3</sub>) oxides are difficult to dissolve in neutral environments. Their hydroxides also have a low solubility at pH = 5÷9, for instance:  $\log C_{\text{Ga(OH)}_3} = -7.5$  at pH = 7.5;  $\log C_{\text{In(OH)}_3} = -9$  at pH = 7.0 [50]. Conversely, As and Sb oxides are easily dissolved in neutral environments [47].

As a result, atoms of different elements are removed at different rates during the polishing process, and the roughness increases [51]. Therefore, it is important to take into account the crystallographic orientation of the polished wafer. For instance, the surface of [111] oriented wafers can be comprised of atoms of the same type. Surfaces of [100] and [110] oriented wafers include atoms of III and V groups.

Therefore, multiple CMP parameters demonstrate complex interconnections, which makes the optimization of the polishing process a multifactor nonlinear problem. To solve this problem, various models of the process are

developed taking into account the key factors of CMP.

### 3.1.2. Models of the CMP process

Despite the fact that CMP is widely used, its basic mechanisms are still a matter of numerous discussions [54]. Models describing CMP are usually aimed at determining the dependence between the material removal rate and the polishing pressure or the relative velocity between the wafer and the polishing pad (the Preston model), expression 2:

$$MRR = K \cdot P \cdot V, \quad (2)$$

where *MRR* is the material removal rate, *K* is the Preston's coefficient, *P* is the polishing pressure, *V* is the relative velocity of the wafer and the polishing pad, which can be simply calculated as the distance between the centers of the wafer and the polishing pad multiplied by the relative velocity *r*/min [55].

However, the Preston's equation does not take into account experimentally observed nonlinear changes in the material removal rate at a higher pressure and relative velocity. To solve this problem, correction indices are used (*a*, *b*, expression (3)) to assess the actual effect of these parameters [55]:

$$MRR = K \cdot P^a \cdot V^b. \quad (3)$$

Authors [56] suggest a polynomial model of chemical mechanical planarization based on a transformed Preston's equation taking into account the dependence between the planarization rate and time.

These approaches help to take into account other CMP factors affecting the material removal rate. However, they do not detail these factors and the way they affect the process.

Publication [53] suggests a model for assessing the material removal rate by abrasive particles taking into account their number and geometry; the down pressure, relative velocity between the polishing pad and the wafer asperities; the overall pressure and the relative velocity of the wafer to the pad. However, the model does not take into account the chemical aspect of the CMP process.

Article [57] considers a model for erosion during CMP and focuses on the chemical part



of the process. According to the erosion model presented in [58], the surface of the wafer is polished due to erosion whose rate is calculated as follows:

$$v_n = f(\sigma_t(t), \sigma_n(t)), \quad (4)$$

where  $v_n$  is the erosion rate along the normal to the surface of the wafer,  $f$  is the empirical ratio of chemical and mechanical erosion, which depends on the mean down pressure on the wafer and the values of  $\sigma_n$ ,  $\sigma_t$  – normal and shear stresses at a particular point on the wafer's surface.

The material removal rate is then described by expression (5):

$$V_n = K(P) \cdot (\sigma_t + D \cdot \sigma_t^2), \quad (5)$$

where  $V_n$  is the material removal rate,  $K$  and  $D$  are constants determined by the properties of the material and the chemical processes.

Thus, the study presents an effort to take into account the chemical processes taking place during polishing. It also suggests that chemical reactions and diffusion rate impact the down pressure [57].

Article [59] presents a new theoretical approach to the description of the CMP process based on the material removal rate and taking into account both mechanical and chemical aspects (expression (6)):

$$MMR_{\text{thickness}} = C3(1 - \Phi[3 - C2 \cdot P_0^{1/3}]) \sqrt{P_0} \cdot V, \quad (6)$$

where  $C2$  is a parameter determined by the mean particle size of the abrasive, the particle size distribution, the hardness of the wafer and the polishing pad, the asperities of the polishing pad, and the Young's modulus of the polishing pad;  $C3$  is a parameter determined by the degree of dilution of the polishing slurry with water, the density and mass concentration of the slurry before dilution, the mean particle size of the abrasive, the particle size distribution, the density of the abrasive, the density of the asperities of the polishing pad, its roughness and the Young's modulus;  $\Phi$  is determined as  $(x_{\max} - x_{\text{avr}})/\sigma$  – the ratio of the difference between the maximum and mean values to the standard deviation,  $P_0$  is the down pressure;  $V$  is the relative velocity of the wafer to the polishing pad.

Publication [60] proposes another model for calculating the polishing rate (expression (7)):

$$MRR(x, y) = K \cdot P_{\text{avg}}^a(x, y) \cdot V_{\text{avg}}^a(x, y) \cdot \{\Omega(x, y)\}, \quad (7)$$

where  $MMR(x, y)$  is the material removal rate at a particular point of the wafer,  $P_{\text{avg}}$ ,  $V_{\text{avg}}$  are the mean pressure and relative velocity of the wafer to the pad, the exponent  $a$  is a constant determined as the contribution of the pressure and the relative velocity between the wafer and the pad, and  $\Omega$  is a spatial parameter showing the impact of pressure distribution along the wafer, the relative velocity, and the chemical processes.

Authors [42] consider various dependencies between the material removal rate and the down pressure for various interaction mechanisms between the polishing pad, the abrasive, and the polished surface. The study also tries to take into account chemical interaction between the active substance of the polishing slurry and the polished surface.

The proposed model takes into account the chemical aspect of polishing through the diffusion coefficient of the reagent in the polished material.

Article [52] suggests expressions for evaluating the material removal rate taking into account the properties of the material – the hardness of the initial material and the oxidized forms on the surface (the Brinell harness). The authors suggest various expressions for various depths of abrasive indentation in the surface layers.

Therefore, one of the main problems when modelling the CMP process is to detail the contribution of the chemical reaction and mechanical removal to the end result. The existing approaches to the problem can be classified as mechanical, chemical-mechanical, and chemical. The suggested models of the polishing process are mainly based on particular experimental conditions. This accounts for the limitations of such models and the need to adapt them to other conditions of polishing of semiconductor materials. At the same time, some authors point out the limitations of the suggested expressions for estimating the material removal rate [42, 52, 59].

### 3.1.3. Modes of CMP of $A^3B^5$

Table 1 provides examples of CMP conditions and compositions of polishing slurries used for

InSb, GaSb, GaAs, and InAs. The effectiveness of the polishing process is assessed based on the quality of the wafer. Generally, assessment of the quality of wafers is based on the following parameters: roughness (including  $R_a$ ,  $R_z$ ), the total thickness variation of the wafer; total indicator reading (*TIR*); the wafer's bow (*BOW*); and the wafer's warp (*WARP*). It is also important to monitor other defects on the wafer's surface, including scratches and residual particles (abrasive, dust, and material particles). The lower the values of these parameters are, the higher the quality of the wafer. Most studies assess the quality of polished wafers based on the roughness values, because the experiments are conducted on fragments, rather than on whole wafers.

Methods of roughness measurement include atomic force microscopy and contact and non-contact optical profilometry. Optical quality control systems usually make it possible to assess the whole wafer and determine the *TTV*, *TIR*, *WARP*, and *BOW*. Defects can be monitored by means of optical (including with a 3-*d* digital optical microscope [61]) and electron microscopy. Another common method is by scanning the surface with a laser beam. To assess the surface morphologies, crystalline quality and surface defects of single-crystal wafers after CMP, other methods are also used, including white light interferometry, laser interferometry, X-ray tomography, and high-resolution X-ray diffraction [62, 63]. The need to control the chemical composition of the polished surface is determined by the chemical properties of the elements of the III and V groups. For this, X-ray photoelectron spectroscopy (XPS), Auger electron spectroscopy [34, 64], and energy dispersive X-ray spectroscopy are used.

Chemical mechanical polishing of GaAs is also performed using polishing slurries based on  $\text{Br}_2/\text{MeOH}$ ;  $\text{NH}_3 \cdot \text{H}_2\text{O}$  and  $\text{H}_2\text{O}_2$ ;  $\text{H}_2\text{SO}_4$  and  $\text{H}_2\text{O}_2$ ;  $\text{H}_3\text{PO}_4$  and  $\text{H}_2\text{O}_2$  [23].

An analysis of the CMP modes presented in Table 1 demonstrated that the following characteristics are required for a high quality polishing of  $\text{A}^3\text{B}^5$  wafers.

1) Specific chemical mechanical polishing methods and polishing slurries are developed

for each  $\text{A}^3\text{B}^5$  material.  $\text{H}_2\text{O}_2$  and  $\text{NaOCl}$  are most commonly used as oxidizers. However, the use of  $\text{NaOCl}$  may result in the formation of chlorine gas, so other oxidizers are being studied, e.g.  $(\text{NH}_4)_2\text{Cr}_2\text{O}_7$ ,  $\text{NaIO}_3$ ,  $\text{NaIO}_4$ .

During the CMP of arsenides and phosphides, toxic gases  $\text{AsH}_3$  and  $\text{PH}_3$  [65–68] can be formed even in an oxidizing environment. At the same time, arsenic oxide ( $\text{As}_2\text{O}_3$ ) formed during CMP transforms into  $\text{HAsO}_2$ ,  $\text{H}_3\text{AsO}_4$ , and  $\text{AsO}_4^{3-}$  depending on the pH of the solution. When polishing In and Ga antimonides, the composition of the polishing slurry affects the oxidation of the III group elements, because antimony oxide ( $\text{Sb}_2\text{O}_3$ ) is stable practically within the whole pH range [64]. At the same time, a more homogeneous removal of material from the surface of the wafers is observed in solutions with pH below or close to 7 (the pH ranges from 4 to 7). In alkaline solutions (pH > 7), the material removal rate is significantly higher than in acidic solutions, while the surface quality decreases dramatically (the roughness increases, grooves begin to appear). Grooves can also be caused by abrasive particles in the polishing slurry. This can result from the softness of polished materials.

2) Taking into account the mentioned above, researchers are investigating the possibility of conducting polishing of the studied materials without abrasive particles or with relatively soft abrasive particles [69–72] of a nanometer size (not over a few dozen nm). The most common are polishing slurries based on  $\text{SiO}_2$ . The mechanism of the functioning of abrasive particles is still a matter of debate [73, 74]. In particular, there is no single opinion as to the participation of  $\text{SiO}_2$  in the chemical processes of CMP of  $\text{A}^3\text{B}^5$  [30, 66];

3) To remove the material more evenly and obtain surfaces of a better quality, the polishing process can also be divided into several consequent stages (from coarse to fine polishing). This is aimed at the decrease of the material removal rate during fine polishing. A decrease in the CMP rate is a general tendency for both single-stage and multistage polishing. For this, several techniques are used, including the following [75, 76]:

**Table 1.** Examples of the parameters of CMP of A<sup>3</sup>B<sup>5</sup> materials (where  $P$  – is the down pressure on the wafer,  $V_{\text{pad}}$  is the velocity of the polishing pad,  $V_{\text{wafer}}$  is the velocity of the wafer,  $V_{\text{supply}}$  is the polishing slurry supply rate,  $\tau$  is the duration of the process,  $T$  is temperature, and  $MMR$  is the material removal rate)

Material	CMP slurry composition	Polish conditions	Characterization
1	2	3	4
InSb [114]	1 step - Al <sub>2</sub> O <sub>3</sub> (3÷9 µm): H <sub>2</sub> O = 1:30; 2 step - H <sub>2</sub> O <sub>2</sub> : SiO <sub>2</sub> dispersion (25÷40 vol.%) = 1: 2÷4 (vol. ratio)	$P$ : 10÷15 g/cm <sup>2</sup> ; $V_{\text{pad}}$ : 60÷90 rpm; $V_{\text{droppng}}$ : 10÷20 drops/min; $\tau$ : ~ 20 h	Roughness < 0.1 µm
InSb <Te> (111), [87]	ZrO <sub>2</sub> (dispersion in acidic solution): 20% solution C <sub>4</sub> H <sub>6</sub> O <sub>6</sub> (tartaric acid) in H <sub>2</sub> O <sub>2</sub> (40%) = 5:1		
InSb (112) [115]	(NH <sub>4</sub> ) <sub>2</sub> Cr <sub>2</sub> O <sub>7</sub> (26 wt.%): HBr (42 wt.%): CH <sub>2</sub> (OH)CH <sub>2</sub> (OH) (ethylene glycol – EG) = 11: 49:40 (vol.%) dissolved in EG (0÷ 95 vol.%)	Pad: cambric tissue; $T=293$ K; $V_{\text{droppng}}$ : 2÷3 ml/min; $\tau$ : 2÷3 min	Roughness $R_a$ – 0.3 nm
InSb [34]	230 ml H <sub>2</sub> O <sub>2</sub> (30% solution), 75 ml EG, C <sub>4</sub> H <sub>6</sub> O <sub>6</sub> , NaCl (0.08 M for rough and 0.02 M for precise polish) in 1 l CMP slurry	$P$ : 5×10 <sup>-3</sup> H/m <sup>2</sup> ; $V_{\text{pad}}$ : 35 rpm	Roughness $R_a$ 0.3÷0.5 kÅ (30÷50 nm)
InSb (100) [25]	SiO <sub>2</sub> (dispersion of 50 nm particles), C <sub>6</sub> H <sub>8</sub> O <sub>7</sub> (C <sub>5</sub> H <sub>6</sub> O <sub>3</sub> ), H <sub>2</sub> O <sub>2</sub>	Pad: polyurethane and polyester; pH = 4÷6; $P$ : 0÷120 g/cm <sup>2</sup> ; $V_{\text{pa}}$ : 60 rpm; $V_{\text{droppng}}$ : 160 ml/min; $MMR$ : 0.2÷0.7 µm/min	Roughness $R(\text{max})$ – 3 nm
InSb [35]	NaOCl (10% solution) and C <sub>6</sub> H <sub>8</sub> O <sub>7</sub> (50% solution)	$P$ : 0.4; 0.7 psi; $V_{\text{pad}}$ : 50; 70 rpm; $V_{\text{wafer}}$ : 30 rpm; $\tau$ : 2÷3 min	Roughness 1.5 nm. There are apparent defects
GaSb (100), GaSb <Te> (100) [86]	1 step – Br <sub>2</sub> : C <sub>2</sub> H <sub>4</sub> (OH) <sub>2</sub> = 1:100; 2, 3 steps - anodic oxidation and chemical etching	Pad: Pocerfarm 404	Roughness – 0.3÷0.4 nm
GaSb (100) [64]	NaOCl (10% solution) и C <sub>6</sub> H <sub>7</sub> O <sub>8</sub> (10% solution)	Pad: polyurethane; pH=7; $P$ : 4 kP; $V_{\text{pad}}$ : 30 rpm; $MMR$ : 10 nm/min	Roughness – 0.5 nm
GaSb [62]	SiO <sub>2</sub> (35% dispersion of 50 nm particles) and C <sub>3</sub> Cl <sub>2</sub> N <sub>3</sub> NaO <sub>3</sub> (10% solution of sodium dichloroisocyanurate): H <sub>2</sub> O = 1:20 and 2 wt.% NaHCO <sub>3</sub>	Pad: polyurethane; pore size 42÷58 µm, pore density 325/mm <sup>2</sup> , velvet length 310 µm, compressibility 15%, Shore A Hardness 42; $\tau$ : 50 min; $MMR$ : 0.216 µm/min	Roughness – 0.13 nm



**Table 1 (continued)**

1	2	3	4
GaSb [116]	1 step – Al <sub>2</sub> O <sub>3</sub> 10÷30%; grinding aid 5÷10%; dispersant 1÷10%; H <sub>2</sub> O 2 step – NaClO 1÷10%; SiO <sub>2</sub> (up to 100 nm) 10÷30%; H <sub>3</sub> PO <sub>4</sub> 0.01÷0.2%; H <sub>2</sub> O 3 step – H <sub>2</sub> O <sub>2</sub> 0.1÷10 %; PH value regulator 0.01÷5%; H <sub>2</sub> O	1 – Pad: CeO <sub>2</sub> ; P: 100÷200 g/cm <sup>2</sup> ; V <sub>pad</sub> : 10÷40 rpm; V <sub>dropping</sub> : 10÷50 ml/min. 2 – Pad: polyurethane; pH=6; P: 80÷150 g/cm <sup>2</sup> , V <sub>pad</sub> : 60÷100 rpm; V <sub>dropping</sub> : 10÷30 ml/min 3 – Pad: synthetic leather; pH = 4	Roughness R <sub>a</sub> < 0.3 nm
GaSb (100) [117]	Commercial polishing agents “BGY- 903”, “FA/OF3210”, Dongguan company “3030”, Tianjin Xi Lika “2360” : H <sub>2</sub> O: clorox = (1÷10): (50÷100): (1÷10) (vol. ratio)	T = 15÷60 °C; P: 2÷25 psi; V <sub>dropping</sub> : 10÷150 ml/min; τ: 10÷60 min	Roughness R <sub>a</sub> – 0.1÷0.2 μm; WARP – 20 μm; TTV – 5 μm
InAs [118]	NH <sub>2</sub> SO <sub>2</sub> OH (sulphamic acid): C <sub>4</sub> H <sub>6</sub> O <sub>6</sub> : H <sub>2</sub> O <sub>2</sub> : H <sub>2</sub> O = 3:1:10:86 (%)	Pad: Synthetic buckskin; pH = 1÷2; P: 0.08÷0.12 Pa; V <sub>pad</sub> : 55÷65 rpm; V <sub>dropping</sub> : 10 ml/min	
InAs (001) [86]	(NH <sub>4</sub> ) <sub>2</sub> Cr <sub>2</sub> O <sub>7</sub> (26 wt.%): HBr (42 mas.%): CH <sub>2</sub> (OH)CH <sub>2</sub> (OH) = 11: 49:40 (vol.%) dissolved in EG (0÷ 95 vol.%)	Pad: cambric tissue; T = 293 K; V <sub>dropping</sub> : 2÷3 ml/min; τ: 2÷3 min	Roughness R <sub>a</sub> – 0.2 nm
InAs [64]	NaOCl (10% solution) and C <sub>6</sub> H <sub>7</sub> O <sub>8</sub> (50% solution)	Pad: polyurethane; pH=7; P: 4 kPa; V <sub>pad</sub> : 30 rpm; MMR: 10 nm/min	Roughness – 0.4 nm
GaAs [65]	Commercial SiO <sub>2</sub> (30 wt.% aq. dispersion 35 nm particles): H <sub>2</sub> O <sub>2</sub> (30 wt.% aq. solution) (or NaIO <sub>3</sub> , NaIO <sub>4</sub> ): H <sub>2</sub> O = 3: 1: 96 (wt.%). Additionally HNO <sub>3</sub> or KOH.	pH = 2÷3; P: 3.5 psi; V <sub>pad</sub> : 80 rpm; V <sub>wafer</sub> : 72 rpm; V <sub>dropping</sub> : 200 ml/min; τ: 1 min	Roughness – 0.7; 0.5 nm. (Increase from primary value of 0.2 nm)
GaAs [24]	NaCl, C <sub>6</sub> H <sub>5</sub> O <sub>3</sub> SNa (sodium benzenesulfonate), Na <sub>4</sub> P <sub>2</sub> O <sub>7</sub> , Na <sub>2</sub> CO <sub>3</sub> , SiO <sub>2</sub> dispersion	T=16°C; P: ≥ 90 H/81 cm <sup>2</sup> ; V <sub>pad</sub> : 40 rpm; V <sub>wafer</sub> : 30÷40 rpm; V <sub>dropping</sub> : 500 ml/min; τ: 10 min	Roughness R <sub>a</sub> ~ 15 nm; TTV < 5 μm
GaAs [64]	a) NaOCl: H <sub>2</sub> O= 1:10; b) NaOCl (10% aq. solution) and C <sub>6</sub> H <sub>7</sub> O <sub>8</sub> (10% aq. solution)	Pad: polyurethane; a) pH=11; b) pH=7; P: 4 kPa; V <sub>pad</sub> : 30 rpm; MMR: 10 nm/min	Roughness – a) 0.5 nm; b) 0.4 nm;

**Table 1 (end)**

1	2	3	4
n-GaAs (100) [82]	TiO <sub>2</sub> (anatase) (5÷10 nm): 7.4 wt.% in H <sub>2</sub> O <sub>2</sub> (15% aq. solution)	Pad: suede; P: 9.8 kPa; V <sub>pad</sub> : 80 rpm; V <sub>wafer</sub> : 60 rpm; V <sub>dropping</sub> : 30 ml/min; UV light: λ = 250 nm (380 nm)	Roughness R <sub>a</sub> – 0.4÷0.5 nm
GaAs (2 inch) [119]	H <sub>2</sub> O <sub>2</sub> 7.0÷70.0 vol.%; C <sub>4</sub> H <sub>6</sub> O <sub>6</sub> (30% solution) 7.0÷60.0; EG 5.0÷15.0; H <sub>2</sub> O	Pad: cambric; P: 4.3÷7.5 kPa; V <sub>pad</sub> : 20 rpm; V <sub>dropping</sub> : 15÷20 ml/min; MMR: 0.4÷1.2 μm/min	TIR – 2÷3 μm
GaAs (100 mm) [120]	1 step) dichloroisocyanuric acid (C <sub>3</sub> O <sub>3</sub> N <sub>3</sub> CL <sub>2</sub> NA) 23 wt.%; sodium triphosphosphate (Na <sub>5</sub> P <sub>3</sub> O <sub>10</sub> ) 20÷31 wt.%; Na <sub>2</sub> SO <sub>4</sub> 8 wt.%; Na <sub>2</sub> CO <sub>3</sub> 3 mas.%; H <sub>2</sub> O SiO <sub>2</sub> (50 wt.% dispersion). 2 step) dichloroisocyanuric acid 23 wt.%; sodium triphosphosphate 13÷19 wt.%; Na <sub>2</sub> SO <sub>4</sub> 8 mas.%; Na <sub>2</sub> CO <sub>3</sub> 3 wt.%; H <sub>2</sub> O SiO <sub>2</sub> (50 mas.% dispersion).	Pad: polyurethane; Two side polish: P: 50 g/cm <sup>2</sup> ; V <sub>pad</sub> : up – 7.7 rpm, bottom – 23.2 rpm; V <sub>dropping</sub> : 800 ml/min; τ: 1 step) 30 min, 2 step) 15 min; MMR: 1 step) 0.6÷1.2 μm/min; 2 step) 0.2÷0.4 μm/min	
InP [36]	Commercial SiO <sub>2</sub> (dispersion of 100 nm particles in acidic media)	Pad: shore hardness D13	Roughness – 0.4÷0.5 nm
InP (001) (4 inch) [22]	a) NaOCl: H <sub>2</sub> O = 1:20; b) C <sub>6</sub> H <sub>8</sub> O <sub>7</sub> : H <sub>2</sub> O = 1:4;	Pad: polyurethane; P: 4 kPa; V <sub>pad</sub> : 30 rpm; MMR: 5 nm/min. τ: 150÷210 min	Roughness < 1 nm
InP [121]	Commercial SiO <sub>2</sub> (30 wt.% aq. dispersion 35 nm particles): H <sub>2</sub> O <sub>2</sub> (wt.% aq. solution): C <sub>2</sub> H <sub>2</sub> O <sub>4</sub> (or C <sub>4</sub> H <sub>6</sub> O <sub>6</sub> , C <sub>6</sub> H <sub>8</sub> O <sub>7</sub> ) = 3: 1: 0.72 (wt.%) in H <sub>2</sub> O. HNO <sub>3</sub> or KOH added	a) pH = 6 (C <sub>2</sub> H <sub>2</sub> O <sub>4</sub> ); b) pH = 8 (C <sub>6</sub> H <sub>8</sub> O <sub>7</sub> ); P: 24.1 kPa; V <sub>pad</sub> : 72 rpm; V <sub>wafer</sub> : 80 rpm; V <sub>dropping</sub> : 200 ml/min	Roughness – a) 0.1 nm; b) 0.7 nm
InP <S> (100) (2 inch) [25]	SiO <sub>2</sub> (dispersion 50 nm particles), C <sub>6</sub> H <sub>8</sub> O <sub>7</sub> (C <sub>5</sub> H <sub>6</sub> O <sub>3</sub> ), H <sub>2</sub> O <sub>2</sub>	Pad: polyurethane and polyester; pH=4÷6; P: 0÷100 g/cm <sup>2</sup> ; V <sub>pad</sub> : 60 rpm; V <sub>dropping</sub> : 160 ml/min; MMR: 0.2÷0.7 μm/min	Roughness R(max) – 1.5 nm
InP<S> (100) (2 inch) [122,123]	a) NaOCl (50 vol.%) и C <sub>6</sub> H <sub>8</sub> O <sub>7</sub> ; b) NaOCl (50 vol.%), C <sub>6</sub> H <sub>8</sub> O <sub>7</sub> , SiO <sub>2</sub> (5 wt.% dispersion)	Pad: polyurethane and polyester; pH = 5÷6; P: 100 g/cm <sup>2</sup> ; V <sub>pad</sub> : 40 rpm; V <sub>dropping</sub> : 30 ml/min; MMR: a) 0.05 ml/min, b) 0.78 ml/min	Roughness – a) R <sub>a</sub> – 0.1 nm, R(max) – 0.8 nm; б) R <sub>a</sub> – 0.4 nm, R(max) – 3 nm

- reducing the down pressure on the polished wafer to optimal values;
- adapting the pH of the polishing slurry (as discussed earlier in the article);
- optimizing, including reducing the concentration of reagents in the polishing slurry [22, 34].

Today, the industrial processing of wafers obtained from single-crystal ingots of GaAs, GaSb, InAs, InSb, and InP involves CMP [77]. However, the theoretical basis of CMP has not been developed enough yet. This concerns primarily the chemical aspects: kinetics and thermodynamics of the material interaction with various oxidizers and the impact of the properties of the material (its crystallographic orientation, defects); the effect of the mechanical polishing on the chemical processes; the interaction of the oxidation products with complexants; and the effect of the presence of buffer solutions in the polishing slurry on the kinetics of the processes. Authors [65] note that pH is maintained by adding KOH, HNO<sub>3</sub>, and NaHCO<sub>3</sub>. It is assumed that they do not interact with the polished materials. However, most studies do not mention these additives.

Besides the conditions and polishing slurries used in traditional CMP, new approaches to the technology are also studied based on various semiconductor materials. For instance, publication [78] suggests using the chemical etching of silicon wafers followed by polishing with Double Disk Magnetic Abrasive Finishing. Magnetic field-assisted polishing is also studied in [79, 80]. CMP of GaAs was also performed with an abrasive ice disc [81], and a TiO<sub>2</sub> abrasive and an ultraviolet ray [82]. A new method of surface planarization of 4H-SiC is investigated in [83], where silicon is oxidized by means of plasma electrolytic processing followed by the removal of the oxide with an abrasive slurry. This method involves moving the polished wafer from the electrolytic cell to the polishing pad, which makes it difficult to upscale the technology. Article [84] suggests a way to modernize CMP of gallium nitride by putting gold nanoparticles onto the polishing pad. The authors assume that gold nanoparticles interact with the polished surface under UV light, which

results in the formation of charge carriers (holes) in the valence band of the polished material. This, in turn, facilitates the oxidation process. This approach allowed obtaining a roughness  $R_a$  of about 1.3 nm. However, the use of gold nanoparticles makes the process significantly more difficult and expensive.

Authors [85] propose modernizing the slurry supply system by the slurry ionization, when a cathode and anode are put into the slurry tank. The ionized slurry is atomized with oxygen or nitrogen gas using a spray slurry nozzle.

### **3.2. Chemical polishing of semiconductor wafers: new approaches**

Non-contact chemical polishing of semiconductor wafers is performed under hydrodynamic conditions in a rotary barrel polishing pad [17] or while stirring the solution close to the polished surface in order to ensure the homogeneity of chemical reaction with the etchant. Solutions based on etchants including HF, HCl, Br<sub>2</sub>, and NH<sub>3</sub>·H<sub>2</sub>O [86] and oxidizers, like HNO<sub>3</sub> and H<sub>2</sub>O<sub>2</sub> [87], are used for chemical polishing of A<sup>3</sup>B<sup>5</sup>. Publications [88, 89] report the effect of bromine on chemical etching of InSb, InAs, and GaAs wafers. The studies demonstrate that such solutions are the most suitable for etching of InAs. However, a drawback of bromine is its high reactivity and toxicity.

Publication [90] suggests a method which combines the electrogeneration of the etchant Br<sub>2</sub> and chemical etching of a GaAs wafer.

Article [86] studies the electrochemical anodizing of wafers in a mixture of C<sub>4</sub>H<sub>6</sub>O<sub>6</sub>/C<sub>2</sub>H<sub>4</sub>(OH)<sub>2</sub> at the voltage of 50÷100 V followed by the chemical removal of the resulting oxides with a HCl solution.

Authors [91] investigate a method based on polishing the SiC surface with a KOH melt. This method is also applicable to A<sup>3</sup>B<sup>5</sup> materials. A promising field of study seems a research of reagents to treat GaAs, GaSb, InAs, InSb, and InP materials with their melts.

Publication [92] suggests using hydride vapor-phase epitaxy for the planarization of (100) GaAs. However, the authors note that the method is rather expensive. The literature on the problem also suggests polishing GaSb by means of etching



of the surface in argon and reactive ion etching in  $\text{CCl}_2\text{F}_2$  or  $\text{CCl}_4$  plasma [86].

Therefore, the approaches to the chemical polishing include polishing with melts, as well as wet chemical, gas-phase, and electrochemical treatment. The most developed is wet chemical polishing. The main drawback of the wet and electrochemical polishing is that it is difficult to ensure homogeneous interaction of the etchant with the surface of the wafer.

New methods of chemical polishing of semiconductor wafers are indeed of a great scientific interest. Their application requires non-trivial engineering solutions as well as ensuring economic feasibility.

#### 4. Cleaning and passivation of the surface of $\text{A}^3\text{B}^5$ materials

The high reactivity of  $\text{A}^3\text{B}^5$  materials results in the formation of nonstoichiometric oxides of the elements of III and V groups on the surface of wafers in the air. The chemical composition and the thickness of oxide layers depend on the environment and change over time [93]. The presence of natural oxides results in the inhomogeneity of the properties of the material both on the surface and in the bulk. The most significant are the increased density of surface states and the appearance of new levels in the band gap in near-surface layers. All this affects the electronic, chemical, and optical properties of wafers [86,94]. The presence of oxides also affects the nucleation process during the initial stage of epitaxial growth on substrates and the density of defects in the epitaxial layers [93].

In this regard, various methods are developed for the cleaning [40] and passivation of the surface of  $\text{A}^3\text{B}^5$ . Passivation can either be a separate stage of processing of semiconductor substrates, or be combined with polishing without any significant gaps in the process. (Passivation techniques for semiconductor structures are out of scope of our review.) The purpose of the passivation of substrates is to significantly reduce the reactivity of the semiconductor surface and stabilize surface states of the wafer.

Wafer cleaning can involve washing in solutions of acids, for instance  $\text{HCl}$ ,  $\text{HNO}_3$ , and  $\text{HF}$  or bromine [95–97], as well as atomic hydrogen cleaning [98]. Thermal annealing can be used to

remove natural oxide layers from the surface of only some of the  $\text{A}^3\text{B}^5$  materials. For instance, for InSb material oxides of In are removed at a temperature of about 325 °C, while oxides of Sb are removed at a temperature close to the melting point of the material.

There are various classifications of passivation methods [99]. One such classification is based on the resulting chemical composition of the surface, when the passivation layers are created using oxidation, sulfidizing, nitriding, etc. [100].

There is also a classification based on the methods of passivation, which are generally divided into wet-chemical techniques and physico-chemical techniques.

At the moment, plasma and anodic oxidation methods are being developed for wafers from single-crystal materials. Thus, electrochemical oxidation of GaSb, InSb, and InAs is performed in electrolytes based on  $\text{KMnO}_4$ ,  $\text{KOH}$ ,  $\text{H}_2\text{O}_2$ , and  $\text{H}_3\text{AsO}_4$  [86]. However, a significant drawback of the electrochemical treatment is the inhomogeneity of the anodizing process in various regions of the wafer's surface [101]. Publication [88] focuses on chemical oxidation of (111) InSb wafers in  $\text{HBr}-\text{Br}_2$  solutions:  $\text{H}_2\text{O}$  and  $\text{H}_3\text{PO}_4-\text{H}_2\text{O}_2$ :  $\text{H}_2\text{O}$ . The study demonstrates that oxidation in phosphoric acid results in thicker and more loose layers enriched with In. At the same time, oxidation in  $\text{Br}_2$  based solutions results in thinner oxide layers on the surface.

Article [102] considers the methods of sulfidizing InAs surface in solutions of thiols, cystamine, thioacetamide,  $(\text{NH}_4)_2\text{S}_x$ , as well as amino acids and peptides. It is assumed that thiols formed by carbon chain and the SH- group tend to self-assemble and form a passivating monolayer on the  $\text{A}^3\text{B}^5$  surface, which prevents oxidation [95, 103].

Publications [93,84] suggest a method for sulfidizing the InSb surface in a sodium sulfide at a temperature of 45°C. According to [105], unlike most  $\text{A}^3\text{B}^5$  compounds, annealing of InSb wafers after treatment with sulfur-containing solutions results in the braking of the In-S and Sb-S bonds at temperatures of 310 and 400 °C respectively. Authors [106] propose a method for the passivation of InSb in a  $\text{Na}_2\text{S}$  based electrolyte. At the same time, in [107] anodic sulfidizing of InSb in a sulfuric acid based electrolyte resulted in

the enrichment of the surface with Sb. Generally, sulfidizing of the surface of  $A^3B^5$  wafers helps to significantly reduce the density of surface states and electroactive centers and prevent interaction with atmospheric oxygen by creating chemical bonds with sulfur [106,108]. However, when exposed to atmosphere for a long time,  $A^3B^5$  wafers with sulfidized surface can still be oxidized [109].

Publication [109] suggests a different approach to GaAs surface passivation – deposition of silicon nitride on a sulfidized GaAs surface by means of low-frequency plasma enhanced chemical deposition. This approach is based on the passivation method of finished semiconductor structures.

GaAs nitriding methods are also being developed in hydrazine solutions [96, 110] and in nitrogen plasma [111].

Therefore, effective passivation of single-crystal wafers of  $A^3B^5$  materials is an important technological and scientific problem [112,113]. The applicability and feasibility of the existing solutions depend on the application area of a particular material. Instrument engineering usually requires both the chemical purity of the substrate surface and high planarity. Removing passivating heteroatoms when preparing substrates for epitaxial growth can significantly undermine the surface planarity. This accounts for the need of further studies and development of new passivation methods.

## 5. Conclusions

In our study, we reviewed the current approaches to the machining, polishing, and passivation of the surface of GaAs, GaSb, InAs, InSb, and InP semiconductor wafers. Unique characteristics of these materials, including fragility, various degrees of reactivity of Ga, In, Sb, As, P and anisotropy of properties in different crystallographic directions, make it necessary to determine special polishing techniques and the compositions of polishing slurries. The review systematizes the existing approaches to wafer polishing: mechanical polishing, chemical-mechanical polishing, and chemical polishing.

Since mechanical polishing does not provide the required quality of GaAs, GaSb, InAs, InSb,

and InP wafers, it was not considered in the article.

The chemical-mechanical polishing of  $A^3B^5$  includes single-stage and multistage approaches with or without abrasives. CMP is the main method of GaAs, GaSb, InAs, InSb and InP surface treatment, since it has the highest productive capacity and ensures the required surface quality. However, the theoretical aspects of the chemical processes and the impact of the mechanical polishing are developed incompletely. The suggested models for chemical mechanical polishing are mainly based on specific experimental conditions (polished materials, compositions of the polishing slurries, and abrasives). This accounts for the limitations of such models and the need to adapt them to other conditions of polishing. Besides theoretical issues, the main practical problem of CMP of arsenides and phosphides is the formation of toxic gases  $AsH_3$  and  $PH_3$ . This problem is not observed for antimonides. This makes CMP the most practical and promising method for InSb and GaSb. CMP also appears to be the most used method of surface treatment of arsenides and phosphides. However, to optimize the technology for the treatment of these materials, it is necessary to reduce and prevent the formation of toxic gases during the process.

Chemical polishing includes polishing with melts, as well as wet chemical, gas-phase, electrochemical polishing. Wet-chemical polishing is performed in two ways: in a rotary barrel polishing pad or while stirring the solution close to the polished surface. It is the most developed theoretically and practically method. The main drawback of wet chemical and electrochemical polishing is that it is difficult to ensure homogeneous polishing of the whole surface of the wafer. A promising research area with regard to polishing of antimonides, arsenides, and phosphides of indium and gallium can be surface treatment with melts of etching agents.

The review also systematized the existing methods of surface passivation. The classification approaches are based on the following principles: the resulting chemical composition of the surface (oxidation, sulfidizing, nitriding) and the method

of creation of passivating coatings (wet-chemical methods and physico-chemical methods).

### Contribution of the authors

The authors contributed equally to this article.

### Conflict of interest

The authors declare that they have no known competing financial interests or personal relationships that could have influenced the work reported in this paper.

### References

1. Voronenkov V. V., Bochkareva N. I., Virko M. V., ... Shreter Yu. G. Gallium nitride substrates state of the art, problems and possibilities. *Nanoindustriya*. 2017;S(74): 478–483. Available at: <https://www.elibrary.ru/item.asp?id=29871698>
2. Kormilitsina S. S., Molodtsova E. V., Knyzev S. N., Kozlov R. Yu., Zavrzhin D. A., Zharikova E. V., Syrov Yu. V. Study of the influence of treatment on the strength of undoped indium antimonide single-crystal plates. *Izvestiya Vysshikh Uchebnykh Zavedenii. Materialy Elektronnoi Tekhniki = Materials of Electronics Engineering*. 2021;24(1): 48–56. (In Russ.). <https://doi.org/10.17073/1609-3577-2021-1-48-56>
3. Allwood D. A., Cox S., Mason N. J., Palmer R., Young R., Walke P. J. Monitoring epi-ready semiconductor wafers. *Thin Solid Films*. 2002;412(1-2): 76–83. [https://doi.org/10.1016/S0040-6090\(02\)00316-4](https://doi.org/10.1016/S0040-6090(02)00316-4)
4. Kiselev M. G., Drozdov A. V., Yamnaya D. A. *Technology of mechanical sawing of fragile non-metallic materials with forced vibrations of the workpiece*. Minsk: BNTU Publ.; 2017. Available at: [https://rep.bntu.by/bitstream/handle/data/37305/Tekhnologiya\\_mekhanicheskogo\\_raspilivaniya\\_hrupkih\\_nemetallicheskih\\_materialov.pdf?sequence=5&isAllowed=y&ysclid=1hkrigps56194871673](https://rep.bntu.by/bitstream/handle/data/37305/Tekhnologiya_mekhanicheskogo_raspilivaniya_hrupkih_nemetallicheskih_materialov.pdf?sequence=5&isAllowed=y&ysclid=1hkrigps56194871673)
5. Cetyrkina S. A., Zujkov I. F., Chumakova I. V., Chumakova A. V. Technology for cutting monocrystalline silicon rods. *Current problems of aviation and astronautics*. 2010;1(6): 25–26. (In Russ.). Available at: <https://elibrary.ru/item.asp?ysclid=lhkt9qaobe438551147&id=22634031>
6. Pei Z., Billingsley S., Miura S. Grinding induced subsurface cracks in silicon wafers. *International Journal of Machine Tools and Manufacture*. 1999;39(7): 1103–1116. [https://doi.org/10.1016/S0890-6955\(98\)00079-0](https://doi.org/10.1016/S0890-6955(98)00079-0)
7. Meng Q., Zhang X., Lu Y., Si J. Calculation and verification of thermal stress in InSb focal plane arrays detector. *Optical and Quantum Electronics*. 2017;49(402) <https://doi.org/10.1007/s11082-017-1243-9>
8. Zhang X., Meng Q., Zhang L., Lv Y. Modeling and deformation analyzing of InSb focal plane arrays detector under thermal shock. *Infrared Physics & Technology*. 2014;63: 28–34. <https://doi.org/10.1016/j.infrared.2013.12.004>
9. Ponomarev V. B., Loshkarev A. B. *Equipment for electronic materials plants. Methodology guideline. Lecture course*. Ekaterinburg: GOU-VPO UGTU-UPI Publ.; 2008. 87 p. (In Russ.). Available at: [file:///C:/Users/Lab351/Downloads/Ponomarev\\_Loshkarev.pdf](file:///C:/Users/Lab351/Downloads/Ponomarev_Loshkarev.pdf)
10. *Technology of integral electronics*. Ed.: A. P. Dostanko, L. I. Gurskogo. Minsk: Integralpoligraf Publ.; 2009. 571 p. (In Russ.)
11. *Lapping and finishing machine elements*. Eds.: S. G. Babaeva, P. G. Sadygova. M.: Mashinostroenie Publ.; 1976. 128 s. (In Russ.)
12. Marinescu I. D., Rowe W. B., Dimitrov B., Ohmori H. Loose abrasive processes. In book: *Tribology of Abrasive Machining Processes. Second Edition*. Oxford: William Andrew Publishing; 2013. 399–421. <https://doi.org/10.1016/b978-1-4377-3467-6.00013-6>
13. Teplova T. B. Quasi-plastic removal of the surface layer of hard brittle materials to obtain a nanometer surface relief. *Scientific Newsletter*. 2010;8: 73–88. (In Russ.) Available at: <https://www.elibrary.ru/item.asp?id=15278524>
14. Gorokhov V., Zakharevich E., Shavva M. Cutting in the quasiplastic mode. *Technology equipment and technologies. Photonics Russia*. 2015;49(1): 36–43. (In Russ., abstract in Eng.). Available at: <https://www.elibrary.ru/item.asp?id=23107041>
15. Doi T., Marinescu I. D., Kurokawa S. The current situation in ultra-precision technology – silicon single crystals as an example. In book: *Advances in CMP Polishing Technologies*. USA: William Andrew Publishing; 2012. 15–111 p. <https://doi.org/10.1016/b978-1-4377-7859-5.00003-x>
16. Deaconescu A., Deaconescu T. Experimental and statistical parametric optimisation of surface roughness and machining productivity by lapping. *Transactions of famena XXXIX-4*. 2015;39: 65–78. Available at: <https://hrcak.srce.hr/152134>
17. Mirofyanchenko E. V., Mirofyanchenko A. E., Popov V. S. The influence of back thinning technique of the InSb (100) FPA on its geometric characteristics and crystal structure. *Applied Physics (Prikladnaya Fizika)*. 2020;2: 46–52. (In Russ., abstract in Eng.). Available at: <https://www.elibrary.ru/item.asp?edn=rmmbya>
18. Prakash S. J., Tyagi R., Gupta A. Backside thinning of GaAs wafer by lapping using DOE approach. In: *India International Conference on Power Electronics: Materials of international conference IICPE2010, 2010, India: New Delhi*; 2011. p. 1–4. <https://doi.org/10.1109/IICPE.2011.5728072>



19. URL: <https://www.fujimico.com/catalog/Lapping/5>
20. Vizer L. N. *Technology of elements and structures of microelectronics*. Stavropol: North-Caucasus Federal University Publ.; 2017.
21. Lee H., Wang H., Park J., Jeong H. Experimental investigation of process parameters for roll-type linear chemical mechanical polishing (Roll-CMP) system. *Precision Engineering*. 2014;38: 928–934. <https://doi.org/10.1016/j.precisioneng.2014.06.003>
22. Brightup S. J., Goorsky M. S. Chemical-mechanical polishing for III-V wafer bonding applications: polishing, roughness, and an abrasive-free polishing model. *ECS Transactions*. 2010;33(4): 383–389. <https://doi.org/10.1149/1.3483528>
23. Deng Q., Kong T., Li G., Yuan J. Study on polishing technology of GaAs wafer. *Advanced Materials Research*. 2012;497: 200–204. <https://doi.org/10.4028/www.scientific.net/AMR.497.200>
24. Yi D., Li J., Cao J. Study on fundamental polishing characteristics in chemical mechanical polishing of gallium arsenide (GaAs) wafer. *Bulgarian Chemical Communications*. 2017;49(Special Issue-K1): 113–117. Режим доступа: [http://bcc.bas.bg/BCC\\_Volumes/Volume\\_49\\_Special\\_K\\_2017/BCC-49-SI-K1-2017.pdf#page=111](http://bcc.bas.bg/BCC_Volumes/Volume_49_Special_K_2017/BCC-49-SI-K1-2017.pdf#page=111)
25. 祐二森澤, 直紀高山, NIPPON EKUSHIIDO KK. *Polishing liquid for compound semiconductor and method for polishing compound semiconductor using the same*. Patent No. JP2585963B2, No. JP5341276A; Application 10.12.1993; Publ. 26.02.1997.
26. Lyu B. H., Dai W. T., Weng H. Z., Li M., Deng Q. F., Yuan J. L. Influence of components on the rheological property of shear thickening polishing slurry. *Advanced Materials Research*. 2016;1136: 461–465. <https://doi.org/10.4028/www.scientific.net/amr.1136.461>
27. Lortz W., Menzel F., Brandes R., Klaessig F., Knothe T., Shibasaki T. News from the M in CMP—Viscosity of CMP slurries, a constant? *MRS Proceedings*. 2003;767(17): 767. <https://doi.org/10.1557/PROC-767-F1.7>
28. Peddeti Sh., Ong P., L. Leunissen H. A., Babu S. V. Chemical mechanical polishing of Ge using colloidal silica particles and H<sub>2</sub>O<sub>2</sub>. *Electrochemical and Solid-State Letters*. 2011;14(7): 254–257. <https://doi.org/10.1149/1.3575166>
29. Zhao D., Lu X. Chemical mechanical polishing: Theory and experiment. *Friction*. 2013;1(12): 306–326. <https://doi.org/10.1007/s40544-013-0035-x>
30. Gao J., Zhou H., Du J., ... Qian L. Effect of counter-surface chemical activity on mechanochemical removal of GaAs surface. *Tribology International*. 2022;176: 107928. [doi.org/10.1016/j.triboint.2022.107928](https://doi.org/10.1016/j.triboint.2022.107928)
31. Cheng J., Huang S., Li Y., Wang T., Xie L., Lu X. RE (La, Nd and Yb) doped CeO<sub>2</sub> abrasive particles for chemical mechanical polishing of dielectric materials: Experimental and computational analysis. *Applied Surface Science*. 2020;506: 144668. <https://doi.org/10.1016/j.apsusc.2019.144668>
32. Seo J., Gowda A., Khajornrungruang P., Hamada S., Song T., Babu S. Trajectories, diffusion, and interactions of single ceria particles on a glass surface observed by evanescent wave microscopy. *Journal of Materials Research*. 2020;35: 321–331. <https://doi.org/10.1557/jmr.2020.6>
33. Gowda A., Seo J., Ranaweera C. K., Babu S. Cleaning solutions for removal of ~30 nm ceria particles from proline and citric acid containing slurries deposited on silicon dioxide and silicon nitride surfaces. *ECS Journal of Solid State Science and Technology*. 2020;9: 044013. <https://doi.org/10.1149/2162-8777/ab8ffa>
34. Kiseleva L. V., Lopukhin A. A., Mezin Yu. S., Savostin A. V., Vlasov P. V., Vyatkin O. S. Influence of conditions of the InSb monocrystals chemical processing on a surface composition and structure\*. *Applied Physics (Prikladnaya Fizika)*. 2015;5: 84–89. (In Russ., abstract in Eng.). Available at: <https://www.elibrary.ru/item.asp?id=24839899>
35. Linehan D.M. Chemical Mechanical Polishing of InSb. Master's thesis in nanoscience. Lund University: 2021. 39 p. URL: <https://lup.lub.lu.se/student-papers/search/publication/9069263>
36. Bhonsle R. K., Teugels L., Ibrahim S. A. U., ... Leunissen L. H. A. Inspection, characterization and classification of defects for improved CMP of III-V materials. *ECS Journal of Solid State Science and Technology*. 2015;4(11): 5073–5077. <https://doi.org/10.1149/2.0111511jss>
37. Lee H. Semi-empirical material removal model with modified real contact area for CMP. *International Journal of Precision Engineering and Manufacturing*. 2019;20: 1325–1332. <https://doi.org/10.1007/s12541-019-00161-6>
38. Chen C.-C., Li J.-C., Liao W.-C., Ciou Y.-J., Chen C.-C. Dynamic pad surface metrology monitoring by swingarm chromatic confocal system. *Applied Sciences*. 2021;11(1): 179. <https://doi.org/10.3390/app11010179>
39. Lee B. Modeling of chemical mechanical polishing for shallow trench isolation. PhD Dissertation. USA: MIT, 2002. 201 p. Available at: <https://core.ac.uk/download/pdf/4397042.pdf>
40. Terayama Y., Khajornrungruang P., Suzuki K., Kusatsu K., Hamada S., Wada Y., Hiyama H. Real time

- nanoscale cleaning phenomenon observation during PVA brush scrubbing by evanescent field. *ECS Trans.* 2019;92(2): 191–197. <https://doi.org/10.1149/09202.0191ecst>
41. Khanna A. J., Jawali P., Redfeld D., ... Bajaj R. Methodology for pad conditioning sweep optimization for advanced nodes. *Microelectronic Engineering.* 2019;216(15): 111101. <https://doi.org/10.1016/j.mee.2019.111101>
42. Goldstein R. V., Osipenko M. N. Chemical – mechanical polishing. Part 2. Model of local interactions. *Perm State Technical University Mechanics Bulletin.* 2011;3: 26–42. (In Russ., abstract in Eng.). Available at: <https://www.elibrary.ru/item.asp?id=16898671>
43. Khanna A. J., Gupta S., Kumar P., Chang F.-C., Singh R. K. Quantification of shear induced agglomeration in chemical mechanical polishing slurries under different chemical environments. *Microelectronic Engineering.* 2019;210: 1–7. <https://doi.org/10.1016/j.mee.2019.03.012>
44. Han R., Sampurno Y., Theng S., Sudargho F., Zhuang Y., Philipossian A. Application of the Stribeck+ curve in silicon dioxide chemical mechanical planarization. *ECS Journal of Solid State Science and Technology.* 2017;6: 161–164. <https://doi.org/10.1149/2.0241704jss>
45. Liao X., Sampurno Y., Zhuang Y., Philipossian A. Effect of slurry application/injection schemes on slurry availability during chemical mechanical planarization (CMP). *Electrochemical and Solid-State Letters.* 2012;15(4): H118–H122. <https://doi.org/10.1149/2.009205esl>
46. Lee J.-T., Lee E.-S., Won J.-K., Choi H.-Z. Wafer polishing process with signal analysis and monitoring for optimum condition of machining. *Advanced Materials Research.* 2010;126–128: 295–304. <https://doi.org/10.4028/www.scientific.net/AMR.126-128.295>
47. Pourbaix M. Atlas of electrochemical equilibria in aqueous solutions. USA: National Association of Corrosion Engineers, 2<sup>nd</sup> edition; 1974. 645 p.
48. Lo R., Lo S.-L. A pilot plant study using ceramic membrane microfiltration, carbon adsorption and reverse osmosis to treat CMP (chemical mechanical polishing) wastewater. *Water Supply.* 2004;4(1): 111–118. <https://doi.org/10.2166/ws.2004.0013>
49. Sioncke S., Brunco D. P., Meuris M., ... Heyns M. M. Etch rates of Ge, GaAs and InGaAs in acids, bases and peroxide based mixtures. *ECS Transactions.* 2008;16(10): 451–460. <https://doi.org/10.1149/1.2986802>
50. Frank-Rotsch Ch., Dropka N., Rotsch P. III Arsenide. In Book: *Single crystals of Electronic Materials: Growth and Properties.* UK: Woodhead Publishing, Elsevier; 2018. pp. 181–240. <https://doi.org/10.1016/B978-0-08-102096-8.00006-9>
51. Ong P., Teugel L. CMP processing of high mobility channel materials: alternatives to Si. In book: *Advances in Chemical Mechanical Planarization (CMP), 2<sup>nd</sup> Edition.* UK: Woodhead Publishing, Elsevier; 2022. pp. 125–142. <https://doi.org/10.1016/B978-0-12-821791-7.00020-4>
52. Qin K., Moudgil B., Park C. W. A chemical mechanical polishing model incorporating both the chemical and mechanical effects. *Thin Solid Films.* 2004;446(2): 277–286. <https://doi.org/10.1016/j.tsf.2003.09.060>
53. Lee H. S., Jeong H. D., Dornfeld D. A. Semi-empirical material removal rate distribution model for SiO<sub>2</sub> chemical mechanical polishing (CMP) processes. *Precision Engineering.* 2013;37: 483–490. <https://doi.org/10.1016/j.precisioneng.2012.12.006>
54. Seo J. A review on chemical and mechanical phenomena at the wafer interface during chemical mechanical planarization. *Journal of Materials Research.* 2021;36(1): 235–257. <https://doi.org/10.1557/s43578-020-00060-x>
55. Park B., Kim Y., Kim H., Jeong H., Dornfeld D. A. Effect of ceria abrasives on planarization efficiency in STI CMP Process. *ECS Transactions.* 2009;19(7): 51–59. <https://doi.org/10.1149/1.3123774>
56. Amirhanov A. V., Gladkih A. A., Makarchuk V. V., Pshennikov A. G., Shahnov V. A. Polynomial model of chemical-mechanical planarization in production of sub-micrometer VLSIC. *Herald of the Bauman Moscow State Technical University. Series Instrument Engineering.* 2012;2: 20–36. (In Russ., abstract in Eng.). Available at: <https://www.elibrary.ru/item.asp?id=17734975>
57. Goldstein R. V., Osipenko M. N. Chemical – mechanical polishing. Part 1. Main characteristics: review. *Perm State Technical University Mechanics Bulletin. Vestnik PGTU. Mekhanika.* 2011;3: 26–42. (In Russ., abstract in Eng.). Available at: <https://www.elibrary.ru/item.asp?id=16898670>
58. Runnels S. R. Feature-scale fluid-based erosion modeling for Chemical-Mechanical Polishing. *Journal of Electrochemical Society.* 1994;141(7): 1900–1904. <https://doi.org/10.1149/1.2055024>
59. Luo J., Dornfeld D. A. Material removal mechanism in chemical mechanical polishing: theory and modelling. *IEEE Transactions on Semiconductor Manufacturing.* 2001;14(2): 112–133. <https://doi.org/10.1109/66.920723>
60. Lee H., Lee D., Jeong H. Mechanical aspects of the chemical mechanical polishing process: a review. *International Journal of Precision Engineering and Manufacturing.* 2016;17(4): 525–536. <https://doi.org/10.1007/s12541-016-0066-0>

61. Papis Polakowska E., Leonhardt E., Kaniewski J. Characterization of (100) GaSb passivated surface using next generation 3D digital microscopy. *Acta Physica Polonica Series a*. 2014;125(4): 1052–1055. <https://doi.org/10.12693/APhysPolA.125.1052>
62. Yan B., Liang H., Liu Y., ... Huang L. Chemical mechanical polishing of GaSb wafers for significantly improved surface quality. *Frontiers in Materials*. 2021;8: 773131. <https://doi.org/10.3389/fmats.2021.773131>
63. Hayashi S., Joshi M. B., Goorsky M. S. Chemical mechanical polishing of exfoliated III-V layers. *ECS Transactions*. 2008;16(8): 295–302. <https://doi.org/10.1149/1.2982881>
64. Seo D., Na J., Lee S., Lim S. Behavior of GaSb (100) and InSb (100) surfaces in the presence of H<sub>2</sub>O<sub>2</sub> in acidic and basic cleaning solutions. *Applied Surface Science*. 2017;399: 523–534. <https://doi.org/10.1016/j.apsusc.2016.12.114>
65. Matovu J. B., Ong P., Leunissen L. H. A., Krishnan S., Babua S. V. Fundamental investigation of chemical mechanical polishing of GaAs in silica dispersions: material removal and arsenic trihydride formation pathways. *ECS Journal of Solid State Science and Technology*. 2013;2(11): 432–439. <https://doi.org/10.1149/2.008311jss>
66. Peddeti Sh., Ong P., Leunissen L. H. A., Babu S. V. Chemical mechanical polishing of InP. *ECS Journal of Solid State Science and Technology*. 2012;1(4): 184–189. <https://doi.org/10.1149/2.016204jss>
67. Suryadevara B. *Advances in chemical mechanical planarization (CMP)*. 2<sup>nd</sup> edition. The UK, Cambridge: Woodhead Publishing; 2021. 648 p.
68. Lee H., Dornfeld D. A., Jeong H. Mathematical model-based evaluation methodology for environmental burden of chemical mechanical planarization process. *International Journal of Precision Engineering and Manufacturing-Green Technology*. 2014;1(1): 11–15. <https://doi.org/10.1007/s40684-014-0002-7>
69. Andreev V. M., Kudryashov D. A., Mizerov M. N., Pushnyj B. V. *Method for semiconductor polish*. Patent No RU245754, H01L 21/302, B82B 3/00; No 2011106341/28; Appl. 18.02.2011; Publ. 27.07.2012, bull. No 21. Available at: [https://patents.s3.yandex.net/RU245754C1\\_20120727.pdf](https://patents.s3.yandex.net/RU245754C1_20120727.pdf)
70. Joshida M., Ashidzava T., Terasaki H., Kurata Ya., Macudzava D., Tanno K., Ootuki Yu., *Cerium oxide composite and wafer polish method*. Patent No RU2178599C2, H01L 21/304; No 99109040/28; Appl. 30.09.1997; Publ. 20.01.2002, bull. No 2. Available at: <https://pubchem.ncbi.nlm.nih.gov/patent/RU-2178599-C2>
71. Lee H., Jeong H. Analysis of removal mechanism on oxide CMP using mixed abrasive slurry. *International Journal of Precision Engineering and Manufacturing*. 2015;16(3): 603–607. <https://doi.org/10.1007/s12541-015-0081-6>
72. Lee H., Lee D., Kim M., Jeong H. Effect of mixing ratio of non-spherical particles in colloidal silica slurry on oxide CMP. *International Journal of Precision Engineering and Manufacturing*. 2017;18(10): 1333–1338. <https://doi.org/10.1007/s12541-017-0158-5>
73. Lee H. S., Jeong H. D. Chemical and mechanical balance in polishing of electronic materials for defect-free surfaces. *CIRP Annals*. 2009;58(1): 485–490. <https://doi.org/10.1016/j.cirp.2009.03.115>
74. Lee H. Tribology research trends in chemical mechanical polishing (CMP) process. *Tribology and Lubricants*. 2018;34(3): 115–122. <https://doi.org/10.9725/KTS.2018.34.3.115>
75. Suzuki N., Hashimoto Y., Yasuda H., Yamaki S., Mochizuki Y. Prediction of polishing pressure distribution in CMP process with airbag type wafer carrier. *CIRP Annals*. 2017;66(1): 329–332. <https://doi.org/10.1016/j.cirp.2017.04.088>
76. Park J.-Y., Han J.-H., Kim C. A study on the influence of the cross-sectional shape of the metal-inserted retainer ring and the pressure distribution from the multi-zone carrier head to increase the wafer yield. *Applied Sciences*. 2020;10(23): 8362. <https://doi.org/10.3390/app10238362>
77. Martinez B., Flint J. P., Dallas G., ... Furlong M. J. Standardizing large format 5" GaSb and InSb substrate production. *Proceedings Volume 10177, Infrared Technology and Applications XLIII*. 2017; 10177. <https://doi.org/10.1117/12.2263961>
78. Pandey Kh., Pandey P. M. Chemically assisted polishing of monocrystalline silicon wafer Si (100) by DDMAF. *Procedia Engineering*. 2017;184: 178–184. <https://doi.org/10.1016/j.proeng.2017.04.083>
79. Kum Ch. W., Sato T., Guo J., Liud K., Butler D. A novel media properties-based material removal rate model for magnetic field-assisted finishing. *International journal of mechanical sciences*. 2018;141: 189–197. <https://doi.org/10.1016/j.ijmecsci.2018.04.006>
80. Zhang J., Wang H., Kumar S., Jin M. Experimental and theoretical study of internal finishing by a novel magnetic driven polishing tool. *International Journal of Machine Tools and Manufacture*. 2020;153: 103552. <https://doi.org/10.1016/j.ijmachtools.2020.103552>
81. Lu W. Z., Zuo D. W., Sun Y. L., Zhao Y. F., Xu F., Chen R. F. Temperature field during CMP GaAs wafer using an AID. *Key Engineering Materials*. 2009;416: 28–33. <https://doi.org/10.4028/www.scientific.net/KEM.416.28>
82. Hong S. H., Isii H., Touge M., Watanabe J. Investigation of chemical mechanical polishing of



- GaAs wafer by the effect of a photocatalyst. *Key Engineering Materials*. 2005;291-292: 381–384. <https://doi.org/10.4028/www.scientific.net/KEM.291-292.381>
83. Ma G., Li S., Liu X., Yin X., Jia Z., Liu F. Combination of plasma electrolytic processing and mechanical polishing for single-crystal 4H-SiC. *Micromachines*. 2021;12: 606–618. <https://doi.org/10.3390/mi12060606>
84. Ou L., Dong Zh., Kang R., Shi K., Guo D. Photoelectrochemically combined mechanical polishing of n-type gallium nitride wafer by using metal nanoparticles as photocathodes. *The International Journal of Advanced Manufacturing Technology*. 2019;105: 4483–4489. <https://doi.org/10.1007/s00170-018-03279-5>
85. Jo H., Lee D. S., Jeong S. H., Lee H. S., Jeong H. D. Hybrid CMP slurry supply system using ionization and atomization. *Applied Sciences*. 2021;11: 2217–2233. <https://doi.org/10.3390/app11052217>
86. Papis Polakowska E. Surface treatments of GaSb and related materials for the processing of mid-infrared semiconductor devices. *Electron Technology – Internet Journal*. 2006;37/38(4): 1–34. Режим доступа: <https://yadda.icm.edu.pl/baztech/element/bwmeta1.element.baztech-article-BWA0-0014-0022>
87. Eminov Sh. O., Jalilova Kh. D., Mamedova E. A. Wet chemical etching of the (111)In and Sb planes of InSb substrates. *Inorganic Materials*. 2011;47(4): 340–344. <https://doi.org/10.1134/S0020168511040091>
88. Aureau D., Chaghi R., Gerard I., Sik H., Fleury J., Etcheberry A. Wet etching of InSb surfaces in aqueous solutions: Controlled oxide formation. *Applied Surface Science*. 2013;276: 182–189. <https://doi.org/10.1016/j.apsusc.2013.03.063>
89. Tomashik Z. F., Kussyak N. V., Tomashik V. N. Chemical etching of InAs, InSb, and GaAs in H<sub>2</sub>O<sub>2</sub>–HBr solutions. *Inorganic Materials*. 2002;38(5): 434–437. <https://doi.org/10.1023/A:1015402501421>
90. Han L., Xu H., Sartin M. M., ... Tian Zh.-Q. Pulse potential confined electrochemical polishing on gallium arsenide wafer. *Journal of The Electrochemical Society*. 2021;168: 043507. <https://doi.org/10.1149/1945-7111/abf96f>
91. Zhang Y., Chen H., Liu D., Deng H. High efficient polishing of sliced 4H-SiC (0001) by molten KOH etching. *Applied Surface Science*. 2020;525: 146532. <https://doi.org/10.1016/j.apsusc.2020.146532>
92. Braun A. K., Ptak A. J. Planarization of rough (100) GaAs substrates via growth by hydride vapor phase epitaxy. *IEEE 48th Photovoltaic Specialists Conference (PVSC): Conference Record, 2021*, Fort Lauderdale, FL, USA; 2021. pp. 1437–1439. <https://doi.org/10.1109/PVSC43889.2021.9518828>
93. Lvova T. V., Dunaevskii M. S., Lebedev M. V., Shakhmin A. L., Sedova I. V., Ivanov S. V. Chemical passivation of InSb (100) substrates in aqueous solutions of sodium sulfide. *Semiconductors*. 2013;47(5): 721–727. <https://doi.org/10.1134/s106378261305014x>
94. Kul'chickij N. A., Naumov A. V., Starcev V. V. Photonic is a new driver of gallium arsenide market. *Photonics Russia*. 2020;14(2): 138–149. <https://doi.org/10.22184/1993-7296.FRos.2020.14.2.138.149>
95. Holloway G. W., Haapamaki Ch. M., Kuyanov P., LaPierre R. R., Baugh J. Electrical characterization of chemical and dielectric passivation of InAs nanowires. *Semiconductor Science and Technology*. 2016;31(11): 114004. <https://doi.org/10.1088/0268-1242/31/11/114004>
96. Zou X., Li Ch., Su X., ... Yartsev A. Carrier recombination processes in GaAs wafer passivated by wet nitridation. *ACS Applied Materials and Interfaces*. 2020;12(25): 28360–29367. <https://doi.org/10.1021/acsami.0c04892>
97. Tereshchenko O. E., Chikichev S. I., Terexkhov A. S. Atomic structure and electronic properties of HCl–isopropanol treated and vacuum annealed GaAs 100 surface. *Applied Surface Science*. 1999;142: 75–80. [https://doi.org/10.1016/S0169-4332\(98\)00634-5](https://doi.org/10.1016/S0169-4332(98)00634-5)
98. Haworth L., Lu J., Westwood D. I., MacDonald J. E. Atomic hydrogen cleaning, nitriding and annealing InSb (100). *Applied Surface Science*. 2000;166: 253–258. [https://doi.org/10.1016/S0169-4332\(00\)00425-6](https://doi.org/10.1016/S0169-4332(00)00425-6)
99. Mittova I., Sladkopevtsev B., Dontsov A., Syrov Yu., Kovaleva A., Tarasova O. Thermal oxidation of a single-crystal GaAs surface treated in sulfur vapor. *Inorganic Materials*. 2021;57(7): 663–668. <https://doi.org/10.1134/s002016852107013x>
100. Syrov Y. V. Indium antimonide interaction with tellurium vapors\*. *Physical-chemical processes in condensed matter and interfaces: theses of VII Russian conference, 10–13 November 2015, Voronezh. Voronezh: Izdatel'sko-poligraficheskij centr "Nauchnaya kniga"; 2015. pp. 292–293. (In Russ.)*
101. Hasegawa H., Hartnagel H. L. Anodic oxidation of GaAs in mixed solutions of glycol and water. *Journal of The Electrochemical Society*. 1976;123(5): 713–723. <https://doi.org/10.1149/1.2132915>
102. Jewett S. A., Ivanisevic A. Wet-chemical passivation of InAs: toward surfaces with high stability and low toxicity. *Accounts of Chemical Research*. 2012;45(9): 1451–1459. <https://doi.org/10.1021/ar200282f>
103. Sun M. H., Joyce H. J., Gao Q., Tan H. H., Jagadish C., Ning C. Z. Removal of surface states and recovery of band-edge emission in InAs nanowires through surface passivation. *Nano Letters*. 2012;12(7): 3378–3384. <https://doi.org/10.1021/nl300015w>

104. Solov'ev V. A., Sedova I. V., Lvova T. V., ... Ivanov S. V. Effect of sulfur passivation of InSb (0 0 1) substrates on molecular-beam homoepitaxy. *Applied Surface Science*. 2015;356: 378–382. <https://doi.org/10.1016/j.apsusc.2015.07.200>
105. Zhernokletov D. M., Dong H., Brennan B., Kim J., Wallace R. M. Optimization of the ammonium sulfide (NH<sub>4</sub>)<sub>2</sub>S passivation process on InSb(111)A. *Journal of Vacuum Science & Technology B*. 2012;30(4): 04E103. <https://doi.org/10.1116/1.4719961>
106. Mirofyanchenko A. E., Mirofyanchenko E. V., Lavrentyev N. A., Popov V. S. Anodic passivation of InSb (100) by sodium sulfide solution with additional sulfidation pretreatment. *Applied Physics (Prikladnaya Fizika)*. 2020;3: 33–39. (In Russ., abstract in Eng.). Available at: <https://www.elibrary.ru/item.asp?id=43807692>
107. Künstler-Hourriez B., Ern e B., Lef evre F., ... Etcheberry A. Surface reactivity of InSb studied by cyclic voltammetry coupled to XPS. *Journal de Physique IV (Proceedings)*. 2006;132: 147–151. <https://doi.org/10.1051/jp4:2006132029>
108. Gong X. Y., Yamaguchi T., Kan H., ... Rinfret R. Sulphur passivation of InAs. *Applied Surface Science*. 1997;113/114: 388–392. [https://doi.org/10.1016/S0169-4332\(96\)00936-1](https://doi.org/10.1016/S0169-4332(96)00936-1)
109. Richard O., Blais S., Ar es R., Aimez V., Jaouad A. Mechanisms of GaAs surface passivation by a one-step dry process using low-frequency plasma enhanced chemical deposition of silicon nitride. *Microelectronic Engineering*. 2020;233: 111398. <https://doi.org/10.1016/j.mee.2020.111398>
110. Chellu A., Koivusalo E., Raappana M., ... Hakkarainen T. Nanotechnology paper GaAs surface passivation for InAs/GaAs quantum dot based nanophotonic devices. *Nanotechnology*. 2021;32(13): 130001. <https://doi.org/10.1088/1361-6528/abd0b4>
111. Mehdi H., R everet F., Robert-Goumet C... Pelissier B. Investigation of N<sub>2</sub> plasma GaAs surface passivation efficiency against air exposure: towards an enhanced diode. *Applied Surface Science*. 2022;579: 152191. <https://doi.org/10.1016/j.apsusc.2021.152191>
112. Syrov Y. V. Interaction of indium antimonide with saturated sulfur vapor. *Doklady Chemistry*. 2016;471(2): 365–367. <https://doi.org/10.1134/S0012500816120077>
113. Dobrovolskij D. S., Davygora A. P., Syrov Yu. V., Molodcova E. V. *Physical-chemical processes in condensed matter and interfaces: theses of VII Russian conference, 10–13 November 2015, Voronezh. Voronezh: Izdatel'sko-poligraficheskij centr "Nauchnaya kniga"; 2015. pp. 192–193. (In Russ.)*
114. 龚晓霞, 李德香, 张丽霞, 吴宇, 杨雪, 种苏然, 杨文运, 太云见, 黄晖. *Polishing method of indium antimonide single crystal wafer*. Patent CN110788739A, B24B 57/02, C09G 1/0; N  CN201911058927.XA; Application 31.10.2019; Publ. 14.02.2020.
115. Levchenko I., Tomashyk V., Stratiychuk I., Malanych G. Formation of the InAs-, InSb-, GaAs-, and GaSb-polished surface. *Applied Nanoscience*. 2018;8: 949–953. <https://doi.org/10.1007/s13204-018-0788-7>
116. 高飞, 李晖, 徐世海, 张颖武, 练小正, 张弛, 王磊, 徐永宽, 程红娟. *A kind of polishing method for gallium antimonide monocrystalline piece*. Patent No CN 106064326 B, B 24 B 1/0, B 24 B; No CN201610615129.2A; Application 01.08.2016; Publ. 03.06.2018. Available at: <https://patents.google.com/patent/CN106064326A/en>
117. 李超, 林泉, 郑安生, 龙彪, 马锦伟. *Double-surface polishing method for gallium antimonide wafer*. Patent No CN102554750A, H01L 21/304; No CN2010106226200A; Application 29.12.2009; Publ. 11.07.2012.
118. Kovalishina E. A. *Method of finish chemical-mechanical polish InAs*. Patent No RU2582904C1, H01L 21/304; No 2014153880/28; Appl. 29.12.2014; Publ. 27.04.2016, bul. No 12. (In Russ.). Available at: <https://patents.google.com/patent/RU2582904C1/en>
119. Kiseleva L. V., Boltar' K. O., Vlasov P. V., ... Savostin A. V. *Method for chemical-mechanical polish of gallium arsenide wafers*. Patent No RU2545295C1, C30B 33/00, H01L 21/304, H01L 21/306, C30B 29/42; No 2014103552/05; Appl. 03.02.2014; Publ. 27.03.2015, bul. No 9. (In Russ.). Available at: [https://yandex.ru/patents/doc/RU2545295C1\\_20150327](https://yandex.ru/patents/doc/RU2545295C1_20150327)
120. Nakayama M., Itami H., Yamazaki T., Itami H. *Mechano-chemical polishing method for GaAs wafer*. Patent No DE102008004441A1, H01L 21/302, C09G 1/04; No 2007-030735; Application 09.02.2007; Publ. 14.08.2008. Available at: <https://patents.google.com/patent/EP1763071A1/en>
121. Matovu J. B., Ong P., Leunissen L. H. A., Krishnan S., Babu S. V. Use of multifunctional carboxylic acids and hydrogen peroxide to improve surface quality and minimize phosphine evolution during chemical mechanical polishing of indium phosphide surfaces. *Industrial and Engineering Chemistry Research*. 2013;52: 10664–10672. <https://doi.org/10.1021/ie400689q>
122. Morisawa Y., Kikuma I., Takayama N., Takeuchi M. Mirror polishing of InP wafer surfaces with NaOCl-citric acid. *Applied Surface Science*. 1996;92: 147–150. [https://doi.org/10.1016/0169-4332\(95\)00219-7](https://doi.org/10.1016/0169-4332(95)00219-7)
123. Morisawa Y., Kikuma I., Takayama N., Takeuchi M. Effect of SiO<sub>2</sub> powder on mirror polishing of InP wafers. *Journal of Electronic Materials*. 1996;26(1): 34–36. <https://doi.org/10.1007/s11664-997-0130-8>

**Information about the authors**

*Elena N. Abramova*, Cand. Sci. (Chem.), Research Fellow, AO «Giredmet», PAO «Rosatom» (Moscow, Russian Federation).

<https://orcid.org/0009-0002-7724-804X>  
overmind11@rambler.ru

*Roman Yu. Kozlov*, 4<sup>th</sup> year PhD student NUST MISIS, Head of the Laboratory AO «Giredmet», PAO «Rosatom» (Moscow, Russian Federation).

rykozlov@rosatom.ru

*Anatoliy I. Khokhlov*, Cand. Sci. (Tech.), Research Fellow, AO «Giredmet», PAO «Rosatom» (Moscow, Russian Federation).

yaniki-220@mail.ru

*Yuriy V. Syrov*, Cand. Sci. (Phis.-Math.), Research Fellow, AO «Giredmet», PAO «Rosatom» (Moscow, Russian Federation).

<https://orcid.org/0000-0003-2226-5790>  
yvsyrov@yandex.ru

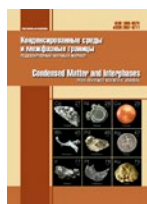
*Yuriy N. Parkhomenko*, Dr. Sci. (Phys.-Math.), Professor, Department of Materials Science of Semiconductors and Dielectrics, NUST MISIS (Moscow, Russian Federation).

<https://orcid.org/0000-0002-1970-9867>  
parkhomenko.in@misis.ru

*Received 07.04.2023; approved after reviewing 24.06.2023; accepted for publication 15.09.2023; published online 15.09.2023.*

*Translated by Yulia Dymant*





# Condensed Matter and Interphases

Kondensirovannye Sredy i Mezhfaznye Granitsy  
<https://journals.vsu.ru/kcmf/>

## Review

Review article

<https://doi.org/10.17308/kcmf.2024.26/11806>

## Features of the corrosion of coatings based on zinc alloys: oxidation products and the selective dissolution of zinc. Review

A. I. Biryukov<sup>1</sup>✉, O. A. Kozaderov<sup>2</sup>, T. V. Batmanova<sup>1</sup>

<sup>1</sup>Chelyabinsk State University,  
129 ul. Br. Kashirinykh, Chelyabinsk 454001, Russian Federation

<sup>2</sup>Voronezh State University,  
1 Universitetskaya pl., Voronezh 394018, Russian Federation

### Abstract

The literature review analyses and systematizes the results of corrosion studies of widely used anti-corrosion zinc coatings based on various binary systems Zn-Al, Zn-Mg, Zn-Fe, Zn-Ni, Zn-Co. The patterns of corrosion, the role of selective dissolution and corrosion products in increasing the corrosion resistance of coatings in neutral chloride-containing environments have been studied. The analysis shows that the corrosion rate depends on the chemical and phase composition of zinc coatings, which is due to differences in the corrosion behavior of the phase components of the alloys. Selective dissolution has an ambiguous effect on the corrosion resistance of coatings. On the one hand, the process of selective dissolution of zinc can be accompanied by the formation of corrosion cracks, which reduces the corrosion resistance of the coating. On the other hand, a rough surface enriched with an electropositive alloying component is formed. As a result, roughness stimulates the deposition of a denser and more compact layer of corrosion products, which reduces the access of oxygen and other electrolyte components to the coating's surface. Under certain conditions, a film of corrosion products can provide additional resistance to the corrosion process due to low electrical conductivity. With the uniform dissolution of coatings, both the co-precipitation of complex compounds of zinc and alloying metals and the doping of the product layer with oxides or hydroxides of alloying metals occur. This also results in increased compactness and reduced electrical conductivity, which increases the corrosion resistance of the coatings. The purpose of the article: an overview of the results of studies of corrosion of zinc coatings, physical and chemical features of the formation and composition of the layer of corrosion products, the influence of corrosion products and selective dissolution on the corrosion resistance of coatings.

A review of the results of studies relating to the corrosion of zinc coatings was carried out, taking into account the formation of a protective layer of corrosion products and the selective dissolution of zinc. The corrosion of zinc coatings is influenced by the structure and phase composition of the coatings, the selective dissolution of zinc, as well as the nature of the layer of corrosion products. The corrosion resistance of zinc coatings increases if a compact layer of corrosion products with low electrical conductivity is formed. The selective dissolution of zinc can have a positive effect on its protective ability due to the formation of a rough surface, which promotes the deposition of a denser layer of corrosion products. In the case of the uniform dissolution of zinc alloy coatings, alloying metals are able to integrate into the structure of zinc corrosion products, which makes the layer more compact and leads to a decrease in its electrical conductivity, significantly increasing the corrosion resistance of the coatings.

**Keywords:** Zinc coatings, Corrosion, Selective dissolution, Simoncolleite, Hydrozincite

**Funding:** The study received financial support from the Ministry of Science and Higher Education of the Russian Federation within the framework of the State Contract with the universities regarding scientific research in 2022–2024, project No. FZGU-2022-0003.

**For citation:** Biryukov A. I., Kozaderov O. A., Batmanova T. V. Features of corrosion of coatings based on zinc alloys: oxidation products and selective dissolution of zinc. Review. *Condensed Matter and Interphases*. 2024;26(1): 25–36. <https://doi.org/10.17308/kcmf.2024.26/11806>

✉ Alexander I. Biryukov, e-mail: [st4857@yandex.ru](mailto:st4857@yandex.ru)

© Biryukov A. I., Kozaderov O. A., Batmanova T. V., 2024



The content is available under Creative Commons Attribution 4.0 License.

**Для цитирования:** Бирюков А. И., Козадеров О. А., Батманова Т. В. Особенности коррозии покрытий на основе цинковых сплавов: продукты окисления и селективное растворение цинка. Обзор. *Конденсированные среды и межфазные границы*. 2024;26(1): 25–36. <https://doi.org/10.17308/kcmf.2024.26/11806>

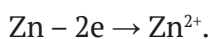
## 1. Introduction

Zinc and its alloys are widely used to protect structural materials and products from corrosion in various industries. Protective zinc coatings are produced by cathodic deposition, immersion in molten zinc, thermal diffusion methods and gas dynamic spraying using zinc powders, as well as their introduction into paint compositions. Regardless of the production method, the corrosion behavior of zinc coatings strongly depends on the composition, morphology and structure of the layer of corrosion products (CP), the physicochemical properties of which often determine the high corrosion resistance of zinc coatings. In addition to zinc oxide (ZnO) and zinc hydroxide (Zn(OH)<sub>2</sub>), depending on the chemical composition of the corrosive environment, the CP layer may include various basic zinc salts [1–4]. In addition, corrosion of zinc alloys can proceed through the mechanism of selective dissolution (SD) [5]. In this case, the accumulation of an alloying component on the surface of the alloy is possible, which has an additional effect on the physicochemical properties of the protective layer and the corrosion resistance of coatings. The degradation processes of zinc coatings play a special role in microelectronics, where they can be used as an intermediate layer, for example, at nickel-plating of aluminum contact pads. Considering that the possibility of the formation of zinc alloys with nickel and aluminum cannot be excluded, along with the formation of zinc oxidation products, it is necessary to take into account the probability of its selective dissolution.

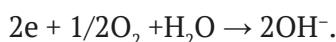
The study provides a review of the results of investigation of the patterns of formation of a protective layer of zinc corrosion products, which ensures the corrosion resistance of zinc-based coatings, taking into account the phenomenon of selective dissolution.

## 2. Corrosion of zinc

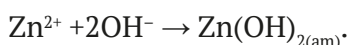
The process of the corrosive degradation of zinc includes its electrochemical oxidation at the anodic areas of the coating:



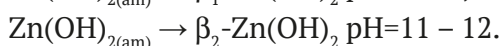
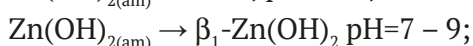
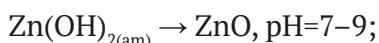
At the cathode sites in a neutral and alkaline aqueous environment, the reduction of oxygen dissolved in water occurs:



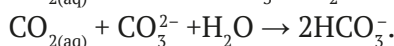
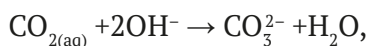
Accumulation of Zn<sup>2+</sup> and OH<sup>-</sup> ions in the surface layer of the solution leads to the rapid formation of zinc hydroxide precipitate:



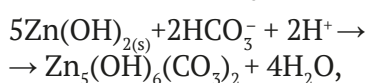
Being amorphous, it is capable of transformation into various products, the nature of which depends on the pH of the environment [6]:



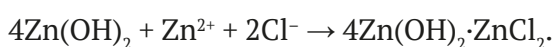
Subsequent transformations of Zn(OH)<sub>2</sub> mainly depend on the chemical composition of the medium, in particular, on the presence of Cl<sup>-</sup>, SO<sub>4</sub><sup>2-</sup> ions, and products of reactions of dissolved CO<sub>2</sub> with water:



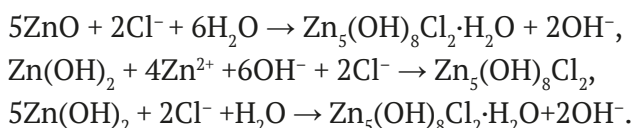
The latter, reacting with Zn(OH)<sub>2</sub> hydroxide, quickly (within several hours) form hydrozincite (HZ) or zinc hydroxycarbonate Zn<sub>5</sub>(OH)<sub>6</sub>(CO<sub>3</sub>)<sub>2</sub> (3Zn(OH)<sub>2</sub>·2Zn(CO<sub>3</sub>)<sub>2</sub>) [7, 8]:



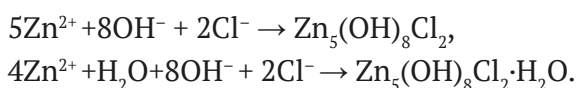
as well as zinc hydroxycarbonate monohydrate Zn<sub>4</sub>CO<sub>3</sub>(OH)<sub>6</sub>·H<sub>2</sub>O. In environments with a relatively high content of chloride ions, HZ transforms into simoncolleite (SC) or zinc hydroxychloride Zn<sub>5</sub>Cl<sub>2</sub>(OH)<sub>8</sub>·H<sub>2</sub>O (4Zn(OH)<sub>2</sub>·ZnCl<sub>2</sub>) within a few days. If the Cl<sup>-</sup> concentration in a solution is higher than 0.01 M and pH ≈ 7, and CO<sub>2</sub> is absent or its concentration is insignificant, then SC is formed directly from ZnO or Zn(OH)<sub>2</sub> [9–12]:



The formation of SC is also described by other chemical reactions, for example [9–12]:



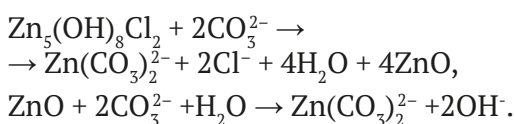
In addition, the formation of simoncolleite is also considered as chemical precipitation from an ion-saturated solution near the surface of a corroding metal [8, 13]:



The SC can transform into gordaite  $\text{NaZn}_4\text{Cl}_2(\text{OH})_6\text{SO}_4 \cdot 6\text{H}_2\text{O}$  with prolonged exposure for several years under the influence of  $\text{SO}_2$  and  $\text{SO}_4^{2-}$ .

Simoncolleite serves as a cathodic corrosion inhibitor of Zn, in the form of a dense protective layer, impeding both volumetric and intercrystalline diffusion of  $\text{O}_2$ . The corrosion of Zn is often local, which affects the homogeneity of the layer of products of the corrosion process. Thus, in chloride-containing media, the anodic areas are acidified, and the concentration of  $\text{Cl}^-$  ions increases near them, which contributes to the formation of predominantly simoncolleite [14, 15]. The cathode areas have a higher pH due to the reduction of dissolved  $\text{O}_2$ , as a result of which hydrozincite is formed on them [14, 15].

Simoncolleite is stable at relatively high  $\text{Cl}^-$  concentration in solution and in the absence of excess of  $\text{OH}^-$  and  $\text{CO}_3^{2-}$ . As the pH increases, it transforms into the less compact ZnO oxide. In the presence of  $\text{HCO}_3^-$  ions SC transforms into sodium-zinc carbonate  $\text{Na}_2\text{Zn}_3(\text{CO}_3)_4$  (at 0.5–1.0 M  $\text{HCO}_3^-$ ) or hydrozincite (at 0.05 M  $\text{HCO}_3^-$ ) [16]. With increasing  $\text{CO}_3^{2-}$  concentration zinc CP can transform into soluble carbonate complexes [16]:



All these factors contribute to a decrease in the degree of protection of zinc.

### 3. Corrosion of alloy coatings based on Zn-Al and Zn-Mg

Coatings with zinc alloys of the Zn-Al system of the “Galvalume” (GL) type (55 wt. % Al) and “Galfan” (GF) (5 wt. % Al + mischmetal additive) allow to provide corrosion resistance 2–4 times

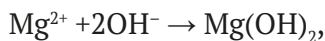
higher compared to zinc [17]. The microstructure of coatings obtained from Galfan and Galvalume alloys is different. In GF, the basis is the matrix of the  $\eta$ -phase is a solid solution of iron in zinc with a Fe concentration of 0.03 wt. %, and Al is present in the form of point inclusions ( $\beta$ -Al). In GL, the core consists of dendrites with a high Al content, and the interdendritic spaces are enriched with zinc [7, 18–22].

Differences in the microstructure of heterophase alloys of the Zn-Al system have a significant impact on their corrosion behavior. Thus, the process in the case of Galvalume alloys in a chloride environment starts on zinc-rich surface areas. Predominant dissolution of Zn from interdendritic regions occurs, while the phase enriched in Al has a more positive potential and accelerates corrosion of the coating, acting as a cathode [18]. At the same time, an increase in Al concentration in the alloy leads to the appearance of compounds such as  $\text{Al}_2\text{O}_3$ ,  $\text{AlOOH}$ , and  $\text{Al}(\text{OH})_3$  in the form of a thin film among CP. Local islands of mixed corrosion products of complex composition  $\text{Zn}_2\text{Al}(\text{OH})_6\text{Cl} \cdot \text{H}_2\text{O}$  and  $\text{Zn}_6\text{Al}_2\text{CO}_3(\text{OH})_{16} \cdot 4\text{H}_2\text{O}$  are formed predominantly on zinc-rich interdendritic regions [7, 22]. With a high  $\text{Cl}^-$  content aluminum hydroxy compounds transform into aluminum oxychloride  $\text{Al}_2(\text{OH})_5\text{Cl} \cdot 2\text{H}_2\text{O}$  [21]. Corrosion of Galfan-type alloys, characterized by a low aluminum content, is similar to the process involving metallic Zn. Indeed, the dissolution of the  $\eta$ -phase leads to the formation of CP characteristic of zinc, including  $\text{ZnO}$ ,  $\text{Zn}(\text{OH})_2$  and  $\text{Zn}_5(\text{OH})_8\text{Cl}_2 \cdot \text{H}_2\text{O}$ . When areas containing Al are dissolved,  $\text{Zn}_6\text{Al}_2\text{CO}_3(\text{OH})_{16} \cdot 4\text{H}_2\text{O}$  or  $\text{Zn}_2\text{Al}(\text{OH})_6\text{Cl} \cdot \text{H}_2\text{O}$  appear among the corrosion products, similarly with the GL type coatings [7, 22].

The inclusion of aluminum compounds in the composition of corrosion products contributes to the formation of a denser protective layer, which ultimately leads to an increase in the protective effect and an increase in the corrosion resistance of coatings based on alloys of the Zn-Al system. An additional effect is exerted by the selective dissolution of zinc from the heterophase surface, which leads to an increase in roughness and creates topologically favorable conditions for the deposition of CP, forming a protective layer [19, 20, 22].



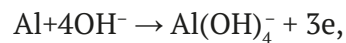
The microstructure of Zn,Al coatings changes with the introduction of magnesium and silicon. At a relatively low magnesium concentration, dendrites of an aluminum-based solid solution are formed, and in the interdendritic region, relatively rich in Zn, the formation of a dense intermetallic  $MgZn_2$  phase is observed. High Mg content and Si additive (0.4 wt. %) provide the formation of the  $Mg_2Si$  phase in the coating and also contribute to an increase in the thickness of the coating. During the corrosion of alloys,  $MgZn_2$  intermetallic compound acts as an anode and dissolves with the formation of  $Zn^{2+}$  and  $Mg^{2+}$  ions, and on the surface of the dendritic phase enriched in Al,  $O_2$  is reduced with release of  $OH^-$  ions. Magnesium ions can appear in the near-electrode layer as a result of selective dissolution, further increasing the corrosion resistance of the alloy [23]. Diffusion of  $Mg^{2+}$  ions into the near-cathode zone of the solution leads to the formation of a compact and dense precipitate of magnesium hydroxide [7]:



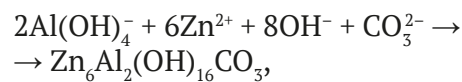
which contributes to the creation of a barrier for the diffusion of oxygen to the surface of the alloy [9, 23], suppressing the reaction of its reduction and slowing down the corrosion process. In addition to the formation of a protective deposit, the role of  $Mg^{2+}$  in increasing corrosion resistance is associated with neutralization of  $OH^-$  and  $CO_3^{2-}$  [9, 23]. The binding of  $OH^-$  into  $Mg(OH)_2$  hydroxide leads to buffering of the pH of the near-electrode layer, which creates favorable conditions for the precipitation of simoncolleite, since  $OH^-$  ions lead to alkaline destruction of SC. In turn,  $CO_3^{2-}$  binding into insoluble  $MgCO_3$  prevents the transition of SC into hydrozincite [24]. According to an alternative approach [25–27], the presence of  $Mg^{2+}$  does not affect the formation of SC, and the positive contribution of magnesium to the protective effect of CP is the formation of mixed oxides such as  $Zn_{(1-x)}Mg_xO$ . As a result, the amount of  $OH^-$  groups and a negative charge on the surface of the barrier layer increase [25, 26], therefore, the electron work function increases, the electrical resistivity of the layer increases, and the rate of charge transfer and corrosion in general, on the contrary, decreases. Regardless of the mechanism of action, magnesium compounds

increase the protective ability of the barrier layer of corrosion products, as a result the corrosion resistance of the coating increases.

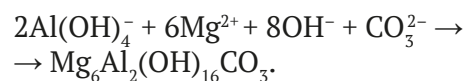
During the corrosion of zinc coatings with Al and Mg additives, the co-precipitation of double layered hydroxides, which additionally prevent the diffusion of  $O_2$  to the metal surface is also possible. The mechanism of their formation involves the dissolution of aluminum from dendrites without the formation of a protective layer:



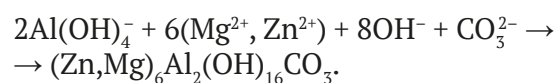
The presence of  $Zn^{2+}$  and  $Mg^{2+}$  ions in the medium determines the possibility of coprecipitation of hydroxide compounds of zinc, magnesium, and aluminum. According to [29, 30], the ZnAlMg coating corroded in salt spray, transforms into a stable, durable, aluminum-rich protective layer, identified as zinc aluminum carbonate hydroxide,  $Zn_6Al_2(OH)_{16}CO_3$ :



which protects the steel base from corrosion and is the main reason for the increased corrosion resistance of the ZnMgAl coating. The participation of magnesium in the coprecipitation of double layered hydroxides is possible [31]:



as well as the formation of even more complex compounds:



It was shown in [32] that the formation of double layered hydroxides has a positive effect on increasing the corrosion resistance of coatings. The authors of [31] noted that the formation of these compounds reduces the alkalization of the CP layer, which prevents the decomposition of already formed products. At the same time, the corrosion process only slows down, since with increasing exposure time in a corrosive environment, zinc CP were revealed in the protective layer.

The undissolved residual aluminum “skeleton” can further enhance the protective function of the CP barrier layer [33, 34].

In studies [35–38], the influence of small (0.05–0.1 mass. %) rare earth metal (REM) additives on the corrosion resistance of “hot” zinc coatings, based on Zn–Al alloys (5 wt. %) was studied. It has been shown [15, 35] that the modified coating of the composition Zn-4.9Al-0.1REM was characterized by a 2.5 times lower rate of chloride corrosion compared to zinc. The main reasons for the increase in corrosion resistance are believed to be the formation of a dense fine-grained structure of the coating [35], as well as inhibition of the transformation of simoncolleite  $Zn_5(OH)_8Cl_2 \cdot H_2O$  into hydrozincite  $Zn_5(OH)_6(CO_3)_2$  [39] and a decrease in the electrical conductivity and ion-exchange properties of the protective layer of zinc CP in the presence of rare-earth metals [40].

#### 4. Corrosion of alloy coatings based on Zn-Fe

Coatings from alloys of the Zn-Fe system are produced by electrodeposition, immersion in molten zinc, the additional heat treatment of “hot” coatings, and thermal diffusion saturation from zinc powders. Phase composition of Zn,Fe coatings may include the following phases:  $\eta$ -phase (0.03 wt. % Fe),  $\zeta$ -phase ( $FeZn_{13}$  5.0–6.0 wt. % Fe);  $\delta$ -phase ( $FeZn_{10}$  7.0–11.5 wt. % Fe);  $\Gamma_1$ -phase ( $Fe_5Zn_{21}$  17.0–19.5 wt. % Fe);  $\Gamma$ -phase ( $Fe_3Zn_{10}$  23.5–28.0 wt. % Fe) [41]. Moreover, in the case of “hot” coatings, the surface layers predominantly consist of zinc-rich  $\eta$ - and  $\zeta$ -phases, while annealed and thermal diffusion coatings are represented mainly by the  $\delta$ -phase  $FeZn_{10}$ .

The corrosion rate of Zn,Fe coatings depends nonlinearly on the Fe concentration. Galvanic materials Zn-Fe coatings with iron concentration from 10 to 25 wt. % are characterized by significant corrosion resistance. [42–45]. An increase in the Fe content above 20 wt. % leads to an acceleration of corrosion, and according to data [45–59], the lower rate of the process was observed at an iron concentration of 10 wt. %. It should be noted that this optimal iron concentration in most cases corresponds to Zn,Fe coatings that have undergone additional annealing. The observed effect can be associated with the features of the crystal structure and the corrosion behavior of the  $\delta$ -phase. In addition, it was assumed [47] that at a concentration of 10 wt. % Fe inhibits

the reduction reactions of  $O_2$  in a neutral NaCl solution due to the formation of a barrier layer based on  $Zn(OH)_2$ , uniformly distributed over the surface of the coating and, unlike semiconductor ZnO [48], characterized by extremely low electronic conductivity [47, 51].

Corrosion of Zn,Fe coatings is accompanied by selective dissolution of Zn and leads to the enrichment of the surface with iron and its morphological development, which has a positive effect on the growth and morphology of corrosion products [47, 54], forming a fairly dense layer with low values of porosity [57], ionic conductivity, and, consequently, the corrosion rate [55, 60]. Moreover, according to various authors, the composition of CP of Zn,Fe coatings and pure zinc is similar and includes ZnO,  $Zn(OH)_2$ , SC and HZ [55, 61–63]. With prolonged exposure in the CP layer, the appearance of iron compounds is observed, for example,  $FeOOH$  of various modifications [59, 63–66],  $Fe_2O_3$  [66, 67] or  $Fe_3O_4$  [68] depending on the conditions of the corrosion process. Some assumptions about the influence of iron on the composition or properties of the CP film were proposed by the authors [69–71] based on data obtained using the chemical coprecipitation of synthetic CP from two electrolyte systems:  $ZnCl_2$ - $FeCl_2$  and  $ZnCl_2$ - $FeCl_3$ . Thus, in a solution with the addition of  $Fe^{2+}$  as its concentration increases, the morphology of the precipitate changes: first, small scattered agglomerates are formed, then sheets, which become thinner and again transform into small aggregates. According to X-ray diffraction data, the sheets are SC, and the thin sheets are complex zinc-iron hydroxychloride:  $[Zn_{(1-x)}Fe(III)_x(OH)_2]^{x+}[Cl^-]_x \cdot nH_2O$  [72]. At a molar ratio of  $Fe/(Zn+Fe) = 0.6–0.8$ , the precipitate is X-ray amorphous. With a further increase in iron concentration, ferrite  $ZnFe_2O_4$  and then magnetite  $Fe_3O_4$  appear in the precipitate.

In solution with the addition of  $Fe^{3+}$  only small agglomerates of ZnO particles are formed, and SC precipitation does not occur. In this case, due to the proximity of ionic radii and the electronegativity of iron and zinc, a fairly stable compact layer based on trioctahedral hydroxides can be formed [69–72].

The addition of simoncolleite to solutions from which iron hydroxide  $\beta$ - $FeOOH$  was

precipitated inhibits the crystallization and growth of hydroxide particles [73]. At the same time, no incorporation of Zn into the structure of  $\beta$ -FeOOH was detected, but the compact amorphous precipitate of  $\beta$ -FeOOH particles was characterized by low adsorption capacity with respect to  $H_2O$  and  $CO_2$ . The effect is explained by the fact that zinc CP, when dissolved, increases the pH of solutions, enhancing the hydrolysis of  $Fe^{3+}$  with the formation of hydroxo complexes  $Fe(OH)_x^{(3-x)+}$ , which condense into amorphous iron oxides/hydroxides. The adsorption of  $Zn^{2+}$  ions on them inhibits the crystallization of  $\beta$ -FeOOH particles, as a result, the precipitate becomes amorphous and more compact [73], and the rate of the corrosion of Zn,Fe coating decreases.

### 5. Corrosion of Zn-Ni, Zn-Co coatings

Coatings based on alloys of the Zn-Ni and Zn-Co systems are obtained by electrodeposition from solutions of zinc salts with the addition of nickel or cobalt salts [74–76]. At a Ni concentration of less than 5 at. % Zn,Ni coatings consist predominantly  $\eta$ -phase, with increasing Ni concentration from 10 to 15 at. %, the presence of  $\delta$ -phase ( $Ni_5Zn_{22}$ ) and  $\gamma$ -phase ( $Ni_5Zn_{21}$ ) is possible and at Ni concentrations above 15 at. % the appearance of the  $\alpha$ -phase is possible [77]. In Zn,Co coatings, the presence of both solid solutions of cobalt in zinc and the  $\gamma$ -phase ( $Co_5Zn_{21}$ ) is possible.

Similar to alloys of the Zn-Fe system, the corrosion rate of Zn,Ni and Zn,Co coatings nonlinearly depends on the concentration of the alloying metal. Among Zn,Ni coatings, systems with a nickel concentration of 10–15 wt. % have the highest corrosion resistance [77–84]. In this case, the corrosion current of the alloy with a concentration of 15 wt. % is two times lower compared to the alloy with 22 wt. % [80, 85]. The effect is associated with the presence of a cubic  $\gamma$ -phase ( $Ni_5Zn_{21}$ ) [80, 85, 86], and with the fact that in this concentration range the alloy is homogeneous [83]. The highest corrosion resistance of Zn,Co coatings is observed in the cobalt concentration range of 10–20 wt. % ZnNi [87, 88], also corresponding to one  $\gamma$ -phase ( $Co_5Zn_{21}$ ) [87], characterized by high corrosion resistance [89].

Zn-Ni coatings are noticeably susceptible to the selective dissolution of zinc. As a result, the

surface is enriched with nickel, and the formation of a  $\beta$ - or  $\alpha$ -phase cannot be excluded [83, 90]. According to [91, 92] the initial corrosion rate of Zn,Ni coatings is higher than that of pure Zn coatings since Ni accumulation stimulates the cathodic reaction. The development of the corrosion process causes the formation of cracks that can reach the steel substrate [90–92], and also leads to a further increase in the relative content of Ni in the corrosion products and/or in the alloying coating layers. As the area of the substrate in contact with the electrolyte and the surface fraction of nickel increase due to the increase of cracks, the resistance of the coating to galvanic corrosion decreases. According to [93], Zn-Ni alloys containing 14 wt. % Ni and lower, show longer galvanic protection of the steel substrate compared to coatings where the Ni concentration is higher than 18 wt. %.

Selective dissolution can also have a positive effect on the corrosion resistance of Zn,Ni and Zn,Co coatings due to the formation of the composite [94–96], consisting of corrosion products and a metal phase enriched in Ni or Co [95] on the surface. As in the case of other zinc alloys, an increase in roughness during SD has a positive effect on the formation of a compact dense CP layer characterized by high resistance [97–99].

The relatively high corrosion resistance of Zn,Ni and Zn,Co coatings is also associated with the peculiarities of the formation of corrosion products. Thus, it is assumed [100, 101] that in the presence of Co, the dissolution of Zn is accelerated, and, consequently, the formation of simoncolleite, due to which the corrosion resistance increases. The nickel component, according to [102], slows down the crystallization of the layered structure of SC during the corrosion of Zn,Ni alloys. The substitution of zinc by nickel occurs in the SC structure, the size and thickness of crystallites decreases, and the layered structure is disrupted. As a result, complex precipitates that have a low adsorption capacity with respect to corrosive gases are formed [102]. Similarly, during the corrosion of Zn-Co coatings, among CP double hydroxide of zinc and cobalt  $Zn_2Co_3(OH)_{10} \cdot 2H_2O$  was found along with simoncolleite [103]. Over time, the proportion of SC in corrosion products decreases, and  $\alpha$ - $Co(OH)_2$ ,  $CoCl_2 \cdot H_2O$ , and ZnO appears. The formation of complex compounds



with zinc atoms substituted by Ni and Co, according to the authors, leads to increased compactness and improved barrier properties of corrosion products. Wherein the authors of [104] note that even at a concentration in the coating of less than 1 wt. %, Co prevents the conversion of  $\text{Zn}(\text{OH})_2$  into ZnO. For this reason, the CP of the Zn-Co system alloy includes a very small amount of ZnO compared to the corrosion products of pure Zn. A similar effect was observed when studying the corrosion products of Zn-Ni coatings [105]. Considering the fact that unlike loose semiconductor ZnO, zinc hydroxide is compact and has low electrical conductivity, this composition of the corrosion products of Zn,Co coatings contributes to effective corrosion inhibition [104].

## 6. Conclusions

The corrosion of coatings based on zinc alloys occurs via a complex mechanism, which includes a number of both electrochemical and chemical processes. The key factors that influence the corrosion resistance of coatings are the microstructure and phase composition of the coatings; selective dissolution of zinc; and the chemical nature and properties of corrosion products.

Coatings with surface layers heterogeneous in phase composition have lower corrosion resistance compared to homogeneous materials. The role of selective dissolution of zinc from alloys is not so clear. Selective dissolution of zinc from alloys can have both a positive effect on the durability of the coating and stimulate its further oxidation. The latter occurs due to the appearance of corrosion cracks, through which the electrolyte reaches the surface of the protected product. In this case, the galvanic protection of the product may decrease due to the accumulation of positive metal and the improvement of the electrode potential of the coating. At the same time, as a result of selective dissolution, the surface of the coating becomes rough, which provides a high density of active nucleation centers on which corrosion products crystallize, which have a protective effect on the coating.

The corrosion products of zinc coatings are predominantly zinc oxide ZnO and zinc hydroxide  $\text{Zn}(\text{OH})_2$ , as well as basic salts with a complex

layered structure. The protective effect of the barrier layer of corrosion products is determined by increased compactness, the formation of a denser film, and low electrical conductivity. In the first case, the film creates a mechanical barrier to the diffusion of aggressive components of the electrolyte and oxygen, in the second case it creates additional resistance, slowing down the transfer of electrons and reducing the rate of the corrosion process as a whole.

With prolonged corrosion of coatings, selective dissolution of zinc is replaced by joint oxidation of the alloy metals. The alloying metal oxidizes and accumulates in the layer of corrosion products in the form of various compounds. Its effect on the physicochemical characteristics of zinc corrosion products and the increase in corrosion resistance can be different. Metal ions are able to integrate into the structure of basic zinc salts, forming complex layered compounds. In addition, the doping of the film of zinc corrosion products with oxides and hydroxides of alloying metals may occur. An increase in the compactness of the film of zinc corrosion products and a decrease in its electrical conductivity occur, which leads to an increase in the corrosion resistance of the coating.

## Author contributions

Biryukov A. I. – idea, review concept, text writing, final conclusions. Kozaderov O. A. – text writing, scientific editing of the text, final conclusions. Batmanova T. V. – selection and systematization of material, conducting research.

## Conflict of interests

The authors declare that they have no known competing financial interests or personal relationships that could have influenced the work reported in this paper.

## References

1. Falk T., Svensson J. E., Johansson L. G. The influence of  $\text{CO}_2$  and NaCl on the atmospheric corrosion of zinc: a laboratory study. *Journal of the Electrochemical Society*. 1998;145(9): 2993. <https://doi.org/10.1149/1.1838753>
2. Qu Q, Yan C., Wan Y., Cao C. Effects of NaCl and  $\text{SO}_2$  on the initial atmospheric corrosion of zinc. *Corrosion Science*. 2002;44(12): 2789–2803. [https://doi.org/10.1016/s0010-938x\(02\)00076-8](https://doi.org/10.1016/s0010-938x(02)00076-8)

3. Qu Q, Li L., Bai W., Yan C., Cao C. Effects of NaCl and NH<sub>4</sub>Cl on the initial atmospheric corrosion of zinc. *Corrosion Science*. 2005;47(11): 2832–2840. <https://doi.org/10.1016/j.corsci.2004.11.010>
4. Thierry D., Persson D., Luckeneder G., Stellnberger K. H. Atmospheric corrosion of ZnAlMg coated steel during long term atmospheric weathering at different worldwide exposure sites. *Corrosion Science*. 2019;148: 338–354. <https://doi.org/10.1016/j.corsci.2018.12.033>
5. Kaiser H. De-alloying and dissolution induced cracking of the Zinc-iron  $\delta$  phase. *Materials and Corrosion*. 1996;47(1): 34–41. <https://doi.org/10.1002/maco.19960470106>
6. Gilbert P. T. The nature of zinc corrosion products. *Journal of The Electrochemical Society*. 1952;99(1): 16–21. <https://doi.org/10.1149/1.2779652>
7. Odnevall Wallinder I., Leygraf C. A critical review on corrosion and runoff from zinc and zinc-based alloys in atmospheric environments. *Corrosion*. 2017;73(9): 1060–1077. <https://doi.org/10.5006/2458>
8. Lindström R., Svensson J. E., Johansson L. G. The atmospheric corrosion of zinc in the presence of NaCl the influence of carbon dioxide and temperature. *Journal of the Electrochemical Society*. 2000;147(5): 1751–1757. <https://doi.org/10.1149/1.1393429>
9. Hosking N. C., Ström M. A., Shipway P. H., Rudd C. D.. Corrosion resistance of zinc–magnesium coated steel. *Corrosion Science*. 2007;49(9): 3669–3695. <https://doi.org/10.1016/j.corsci.2007.03.032>
10. Graedel T. E. Corrosion mechanisms for zinc exposed to the atmosphere. *Journal of the Electrochemical Society*. 1989;136(4): 193–203. <https://doi.org/10.1002/chin.198933345>
11. Mouanga M., Berçot P., Rauch J. Y. Comparison of corrosion behaviour of zinc in NaCl and in NaOH solutions. Part I: Corrosion layer characterization. *Corrosion Science*. 2010;52(12): 3984–3992. <https://doi.org/10.1016/j.corsci.2010.08.003>
12. Liu Y., Li H., Li Z. EIS investigation and structural characterization of different hot-dipped zinc-based coatings in 3.5% NaCl solution. *International Journal of Electrochemical Science*. 2013;8: 7753–7767. [https://doi.org/10.1016/s1452-3981\(23\)12843-4](https://doi.org/10.1016/s1452-3981(23)12843-4)
13. Salgueiro Azevedo M., Allély C., Ogle K., Volovitch P. Corrosion mechanisms of Zn (Mg, Al) coated steel in accelerated tests and natural exposure: 1. The role of electrolyte composition in the nature of corrosion products and relative corrosion rate. *Corrosion Science*. 2015;90: 472–481. <https://doi.org/10.1016/j.corsci.2014.05.014>
14. Zhu F., Persson D., Thierry D., Taxen C. Formation of corrosion products on open and confined zinc surfaces exposed to periodic wet/dry conditions. *Corrosion*. 2000;56(12): 1256–1265. <https://doi.org/10.5006/1.3280514>
15. Azmat N. S., Ralston K. D., Muddle B. C., Cole I. S. Corrosion of Zn under acidified marine droplets. *Corrosion Science*. 2011;53(4): 1604–1615. <https://doi.org/10.1016/j.corsci.2011.01.044>
16. Yoo J. D., Volovitch P., Abdel Aal A., Allely C., Ogle, K. The effect of an artificially synthesized simonkolleite layer on the corrosion of electrogalvanized steel. *Corrosion Science*. 2013;70: 1–10. <https://doi.org/10.1016/j.corsci.2012.10.024>
17. Kania H., Mendala J., Kozuba J., Saternus M. Development of bath chemical composition for batch hot-dip galvanizing – A review. *Materials*. 2020;13(18): 4168. <https://doi.org/10.3390/ma13184168>
18. Persson D., Thierry D., LeBozec N. Corrosion product formation on Zn55Al coated steel upon exposure in a marine atmosphere. *Corrosion Science*. 2011;53(2): 720–726. <https://doi.org/10.1016/j.corsci.2010.11.004>
19. Vu T. N., Volovitch P., Ogle K. The effect of pH on the selective dissolution of Zn and Al from Zn–Al coatings on steel. *Corrosion Science*. 2013;67: 42–49. <https://doi.org/10.1016/j.corsci.2012.09.042>
20. Vu A. Q., Vuillemin B., Oltra R., Allély C. Cut-edge corrosion of a Zn–55Al-coated steel: a comparison between sulphate and chloride solutions. *Corrosion Science*. 2011;53(9): 3016–3025. <https://doi.org/10.1016/j.corsci.2011.05.048>
21. Zhang X., Odnevall Wallinder I., Leygraf C. Atmospheric corrosion of Zn–Al coatings in a simulated automotive environment. *Surface Engineering*. 2018;34(9): 641–648. <https://doi.org/10.1080/02670844.2017.1305658>
22. Zhang X., Odnevall Wallinder I., Leygraf C. Atmospheric corrosion of Zn–Al coatings in a simulated automotive environment. *Surface Engineering*. 2018;34(9): 641–648. <https://doi.org/10.1080/02670844.2017.1305658>
23. Prosek T., Nazarov A., Bexell U., Thierry D., Serak J. Corrosion mechanism of model zinc–magnesium alloys in atmospheric conditions. *Corrosion Science*. 2008;50(8): 2216–2231. <https://doi.org/10.1016/j.corsci.2008.06.008>
24. Volovitch P., Allely C., Ogle K. Understanding corrosion via corrosion product characterization: I. Case study of the role of Mg alloying in Zn–Mg coating on steel. *Corrosion Science*. 2009;51(6): 1251–1262. <https://doi.org/10.1016/j.corsci.2009.03.005>
25. Yao C., Chen W., Zhu T., Tay S. L., Gao W. A study on corrosion behaviour of magnetron sputtered Zn–Mg coating deposited onto electro-galvanized steel. *Surface and Coatings Technology*. 2014;249: 90–96. <https://doi.org/10.1016/j.surfcoat.2014.03.055>
26. Diler E., Rioual S., Lescop B., Thierry D., Rouvellou B. Chemistry of corrosion products of Zn and MgZn pure phases under atmospheric conditions.

- Corrosion Science*. 2012;65: 178–186. <https://doi.org/10.1016/j.corsci.2012.08.014>
27. Diler E., Lescop B., Rioual S., Nguyen Vien G., Thierry D., Rouvello B. Initial formation of corrosion products on pure zinc and MgZn<sub>2</sub> examined by XPS. *Corrosion Science*. 2014;79: 83–88. <https://doi.org/10.1016/j.corsci.2013.10.029>
28. Ishikawa T., Murai M., Kandori K., Nakayama T. Structure and composition of artificially synthesized rusts of Zn–Fe and Zn–Ti alloys. *Corrosion Science*. 2006;48: 3172–3185. <https://doi.org/10.1016/j.corsci.2005.11.015>
29. Duchoslav J., Truglas T., Groß H., ... Stifter D. Structure and chemistry of surface oxides on ZnMgAl corrosion protection coatings with varying alloy composition. *Surface and Coatings Technology*. 2019;368: 51–58. <https://doi.org/10.1016/j.surfcoat.2019.04.006>
30. Schürz S., Luckeneder G. H., Fleischanderl M., Mack P., Gsaller H., Kneissl A. C., Mori G. Chemistry of corrosion products on Zn–Al–Mg alloy coated steel. *Corrosion Science*. 2010;52(10): 3271–3279. <https://doi.org/10.1016/j.corsci.2010.05.044>
31. Duchoslav J., Steinberger R., Arndt M., ... Stifter D. Evolution of the surface chemistry of hot dip galvanized Zn–Mg–Al and Zn coatings on steel during short term exposure to sodium chloride containing environments. *Corrosion Science*. 2015;91: 311–320. <https://doi.org/10.1016/j.corsci.2014.11.033>
32. LeBozec N., Thierry D., Persson D., Riener C. K., Luckeneder G. Influence of microstructure of zinc-aluminium-magnesium alloy coated steel on the corrosion behavior in outdoor marine atmosphere. *Surface and Coatings Technology*. 2019;374: 897–909. <https://doi.org/10.1016/j.surfcoat.2019.06.052>
33. Salgueiro Azevedo M., Allély C., Ogle K., Volovitch P. Corrosion mechanisms of Zn (Mg, Al) coated steel: 2. The effect of Mg and Al alloying on the formation and properties of corrosion products in different electrolytes. *Corrosion Science*. 2015;90: 482–490. <https://doi.org/10.1016/j.corsci.2014.07.042>
34. Salgueiro Azevedo M., Allély C., Ogle K., Volovitch P. Corrosion mechanisms of Zn (Mg, Al) coated steel: the effect of HCO<sub>3</sub><sup>-</sup> and NH<sub>4</sub><sup>+</sup> ions on the intrinsic reactivity of the coating. *Electrochimica Acta*. 2015;153: 159–169. <https://doi.org/10.1016/j.electacta.2014.09.140>
35. Amadeh A., Pahlevani B., Heshmati-Manesh S. Effects of rare earth metal addition on surface morphology and corrosion resistance of hot-dipped zinc coatings. *Corrosion Science*. 2002;44(10): 2321–2331. [https://doi.org/10.1016/S0010-938X\(02\)00043-4](https://doi.org/10.1016/S0010-938X(02)00043-4)
36. Manna M., Naidu G., Rani N., Bandyopadhyay N. Characterisation of coating on rebar surface using hot-dip Zn and Zn-4.9 Al-0.1 misch metal bath. *Surface and Coatings Technology*. 2008;202(8): 1510–1516. <https://doi.org/10.1016/j.surfcoat.2007.07.001>
37. Li S., Gao B., Yin S. ... Zhu X. The effects of RE and Si on the microstructure and corrosion resistance of Zn–6Al–3Mg hot dip coating. *Applied Surface Science*. 2015;357: 2004–2012. <https://doi.org/10.1016/j.apsusc.2015.09.172>
38. Fan H., Xu W., Wei L., Zhang Z., Liu Y., Li Q. Relationship between La and Ce additions on microstructure and corrosion resistance of hot-dip galvanized steel. *Journal of Iron and Steel Research International*. 2020;27: 1108–1116. <https://doi.org/10.1007/s42243-020-00482-1>
39. Hölzl G., Luckeneder G., Duchaczek H., Kleber C., Hassel A. W. Evolution and interaction of corrosive species during the initial NaCl particle induced corrosion on zinc coated skin-passed steel. *Corrosion Science*. 2017;127: 222–229. <https://doi.org/10.1016/j.corsci.2017.08.001>
40. Rosalbino F., Angelini E., Macciò D., Saccone A., Delfino S. Application of EIS to assess the effect of rare earths small addition on the corrosion behaviour of Zn–5% Al (Galfan) alloy in neutral aerated sodium chloride solution. *Electrochimica Acta*. 2009;54(4): 1204–1209. <https://doi.org/10.1016/j.electacta.2008.08.063>
41. Marder A. R. The metallurgy of zinc-coated steel. *Progress in Materials Science*. 2000;45(3): 191–271. [https://doi.org/10.1016/S0079-6425\(98\)00006-1](https://doi.org/10.1016/S0079-6425(98)00006-1)
42. Fukuzuka T., Kajiwara K., Miki K. The properties of zinc-iron alloy electroplated steel Sheets. *Tetsu-to-Hagané*. 1980;66(7): 807–813. [https://doi.org/10.2355/tetsutohagane1955.66.7\\_807](https://doi.org/10.2355/tetsutohagane1955.66.7_807)
43. Watanabe T., Ohmura M., Honma T., Adaniya T. Iron-Zinc Alloy electroplated steel for automotive body pPanels. *SAE Technical Paper*. 1982;820424. <https://doi.org/10.4271/820424>
44. Suzuki I., Enjuji M. The development of the corrosion resistance of an Fe-Zn alloy coating on the basis of the behaviour of the corrosion product. *Corrosion Science*. 1986;26(5): 349–355. [https://doi.org/10.1016/0010-938X\(86\)90010-7](https://doi.org/10.1016/0010-938X(86)90010-7)
45. Chang J. C., Wei H. H. Electrochemical and Mössbauer studies of the corrosion behavior of electrodeposited Fe Zn alloys on steel. *Corrosion Science*. 1990;30(8-9): 831–837. [https://doi.org/10.1016/0010-938X\(90\)90006-Q](https://doi.org/10.1016/0010-938X(90)90006-Q)
46. Drewien C. A., Benschoter A. O., Marder A. R. Metallographic preparation technique for electrodeposited iron zinc alloy coatings on steel. *Materials Characterization*. 1991;26(1): 45–51. [https://doi.org/10.1016/1044-5803\(91\)90007-Q](https://doi.org/10.1016/1044-5803(91)90007-Q)
47. Sagiya M., Hiraya A., Watanabe T. Electrochemical behavior of electrodeposited zinc-iron alloys in 5% NaCl solution. *Tetsu-to-Hagané*.



- 1991;77(2): 244–250. [https://doi.org/10.2355/tetsutohagane1955.77.2\\_244](https://doi.org/10.2355/tetsutohagane1955.77.2_244)
48. Sagiya M., Hiraya A. Analysis of initial oxide films formed on zinc and zinc-iron alloy coatings. *Zairyo-to-Kankyo*. 1993;42(11): 721–727. <https://doi.org/10.3323/jcorr1991.42.721>
49. Sagiya M., Hiraya A. Corrosion behavior of Zn and Zn-Fe alloy electroplated steel sheets in atmospheric exposure test. *Zairyo-to-Kankyo*. 1996;45(7): 432–438. <https://doi.org/10.3323/jcorr1991.45.432>
50. Sagiya M., Hiraya A. Corrosion behavior of Zn and Zn-Fe alloy electroplated steel sheets in modified volvo test. *Zairyo-to-Kankyo*. 1996;45(8): 473–479. <https://doi.org/10.3323/jcorr1991.45.473>
51. Sagiya M., Hiraya A., Watanabe T. Electrochemical behavior of electrodeposited zinc-iron alloys in alkaline solutions. *Tetsu-to-Hagane*. 1991;77(2): 251–257. [https://doi.org/10.2355/tetsutohagane1955.77.2\\_251](https://doi.org/10.2355/tetsutohagane1955.77.2_251)
52. Miyoshi Y., Yoshida K., Azami T., Kanamaru T., Kado S. On the corrosion behavior of painted galvanized steel sheet. *Tetsu-to-Hagane*. 1980;66(7): 858–867. [https://doi.org/10.2355/tetsutohagane1955.66.7\\_858](https://doi.org/10.2355/tetsutohagane1955.66.7_858)
53. Bandyopadhyay N., Jha G., Singh A. K., Rout T. K., Rani N. Corrosion behaviour of galvanized steel sheet. *Surface and Coatings Technology*. 2006;200(14–15): 4312–4319. <https://doi.org/10.1016/j.surfcoat.2005.02.153>
54. Almeida E., Morcillo M. Lap-joint corrosion of automotive coated materials in chloride media. Part 2 – Galvanized steel. *Surface and Coatings Technology*. 2000;124(2–3): 180–189. [https://doi.org/10.1016/S0257-8972\(99\)00624-6](https://doi.org/10.1016/S0257-8972(99)00624-6)
55. Ooij W. J., Sabata A. Under-vehicle corrosion testing of primed zinc and zinc alloy-coated steels. *Corrosion*. 1990;46(2): 162–171. <https://doi.org/10.5006/1.3585083>
56. Lee H. H., Hiam D. Corrosion resistance of galvanized steel. *Corrosion*. 1989;45(10): 852–856. <https://doi.org/10.5006/1.3584993>
57. Dobias D., Pokorny P., Pernicova R. Evaluation of resistance of intermetallic Fe-Zn coating in the model environment as concrete pore solution. *Procedia Engineering*. 2017;172: 226–231. <https://doi.org/10.1016/j.proeng.2017.02.053>
58. Barranco V., Feliu Jr. S., Feliu S. EIS study of the corrosion behaviour of zinc-based coatings on steel in quiescent 3% NaCl solution. Part 1: directly exposed coatings. *Corrosion Science*. 2004;46(9): 2203–2220. <https://doi.org/10.1016/j.corsci.2003.09.032>
59. Pritzel dos Santos A., Manhabosco S. M., Rodrigues J. S., Dick L. F. P. Comparative study of the corrosion behavior of galvanized, galvanized and Zn55Al coated interstitial free steels. *Surface and Coatings Technology*. 2015;279: 150–160. <https://doi.org/10.1016/j.surfcoat.2015.08.046>
60. Rout T. K., Bandyopadhyay N., Venugopalan T., Bhattacharjee D. Mechanistic interpretation of electrochemical behaviour of galvanizing coating in saline environment. *Corrosion Science*. 2005;47(11): 2841–2854. <https://doi.org/10.1016/j.corsci.2004.11.005>
61. Hamlaoui Y., Pedraza F., Tifouti L. Corrosion monitoring of galvanized coatings through electrochemical impedance spectroscopy. *Corrosion Science*. 2008;50(6): 1558–1566. <https://doi.org/10.1016/j.corsci.2008.02.010>
62. Thierry D., LeBozec N. Corrosion products formed on confined hot-dip galvanized steel in accelerated cyclic corrosion tests. *Corrosion*. 2009;65(11): 718–725. <https://doi.org/10.5006/1.3319098>
63. Sato Y., Azumi K. Transition of the corrosion protection mechanism of iron partially covered with zinc coating. *Journal of The Electrochemical Society*. 2015;162(10): 509–514. <https://doi.org/10.1149/2.0241510jes>
64. El-Mahdy G. A., Nishikata A., Tsuru T. Electrochemical corrosion monitoring of galvanized steel under cyclic wet-dry conditions. *Corrosion Science*. 2000;42(1): 183–194. [https://doi.org/10.1016/S0010-938X\(99\)00057-8](https://doi.org/10.1016/S0010-938X(99)00057-8)
65. Autengruber R., Luckeneder G., Hassel A. W. Corrosion of press-hardened galvanized steel. *Corrosion Science*. 2012;63: 12–19. <https://doi.org/10.1016/j.corsci.2012.04.048>
66. Winiarski J., Tylus W., Lutz A., De Graeve I., Szczygieł B. The study on the corrosion mechanism of protective ternary ZnFeMo alloy coatings deposited on carbon steel in 0.5 mol/dm<sup>3</sup> NaCl solution. *Corrosion Science*. 2018;138: 130–141. <https://doi.org/10.1016/j.corsci.2018.04.011>
67. Almeida E., Morcillo M. Lap-joint corrosion of automotive coated materials in chloride media. Part 3 – Electrogalvanized steel/galvanized interface. *Surface and Coatings Technology*. 2000;124(1): 44–52. [https://doi.org/10.1016/S0257-8972\(99\)00625-8](https://doi.org/10.1016/S0257-8972(99)00625-8)
68. Padilla V., Alfantazi A. Corrosion performance of galvanized steel in Na<sub>2</sub>SO<sub>4</sub> and NaCl solutions at subfreezing temperatures. *Corrosion*. 2013;69(2): 174–185. <https://doi.org/10.5006/0645>
69. Ishikawa T., Matsumoto K., Yasukawa A., Kandori K., Nakayama T., Tsubota T. Influence of metal ions on the formation of artificial zinc rusts. *Corrosion Science*. 2004;46(2): 329–342. [https://doi.org/10.1016/S0010-938X\(03\)00155-0](https://doi.org/10.1016/S0010-938X(03)00155-0)
70. Ishikawa T., Murai M., Kandori K., Nakayama T. Structure and composition of artificially synthesized rusts of Zn-Fe and Zn-Ti alloys. *Corrosion Science*. 2006;48(10): 3172–3185. <https://doi.org/10.1016/j.corsci.2005.11.015>

71. Tanaka H., Fujioka A., Futouy A., Kandori K., Ishikawa T. Synthesis and characterization of layered zinc hydroxychlorides. *Journal of Solid State Chemistry*. 2007;180(7): 2061–2066. <https://doi.org/10.1016/j.jssc.2007.05.001>
72. Morimoto K., Tamura K., Anraku S., Sato T., Suzuki M., Yamada H. Synthesis of Zn–Fe layered double hydroxides via an oxidation process and structural analysis of products. *Journal of Solid State Chemistry*. 2015;228: 221–225. <https://doi.org/10.1016/j.jssc.2015.04.045>
73. Tanaka H., Wakatsuki J., Kandori K., Ishikawa T., Nakayama T. Role of zinc compounds on the formation, morphology, and adsorption characteristics of  $\beta$ -FeOOH rusts. *Corrosion Science*. 2010;52(9): 2973–2978. <https://doi.org/10.1016/j.corsci.2010.05.010>
74. Rashwan S. M., Mohamed A. E., Abdel-Wahaab S. M., Kamel M. M. Electrodeposition and characterization of thin layers of Zn–Co alloys obtained from glycinate baths. *Journal of Applied Electrochemistry*. 2003;33: 1035–1042. <https://doi.org/10.1023/A:1026280109296>
75. Bahrololoom M. E., Gabe D. R., Wilcox G. D. Microstructure, morphology and corrosion resistance of electrodeposited zinc-cobalt compositionally modulated alloy multilayer coatings. *Transactions of the IMF*. 2004;82(1-2): 51–58. <https://doi.org/10.1080/00202967.2004.11871554>
76. Carpenter E. O. S., Farr J. P. G. Characterization of zinc-cobalt electrodeposits. *Transactions of the IMF*. 1998;76(4): 135–143. <https://doi.org/10.1080/00202967.1998.11871213>
77. Tian W., Xie F. Q., Wu X. Q., Yang Z. Z. Study on corrosion resistance of electroplating zinc–nickel alloy coatings. *Surface and Interface Analysis*. 2009;41(3): 251–254. <https://doi.org/10.1002/sia.3017>
78. Siitari D. W., Sagiya M., Hara T. Corrosion of Ni–Zn electrodeposited alloy. *Transactions of the Iron and Steel Institute of Japan*. 1983;23(11): 959–966. <https://doi.org/10.2355/isijinternational1966.23.959>
79. Shastry C. R., Townsend H. E. Mechanisms of cosmetic corrosion in painted zinc and zinc-alloy-coated sheet steels. *Corrosion*. 1989;45(2): 103–119. <https://doi.org/10.5006/1.3577827>
80. Giridhar J., Van Ooij W. J. Study of Zn–Ni and Zn–Co alloy coatings electrodeposited on steel strips II: Corrosion, dezincification and sulfidation of the alloy coatings. *Surface and Coatings Technology*. 1992;53(1): 35–47. [https://doi.org/10.1016/0257-8972\(92\)90101-F](https://doi.org/10.1016/0257-8972(92)90101-F)
81. Baldwin K. R., Robinson M. J., Smith C. J. E. The corrosion resistance of electrodeposited zinc-nickel alloy coatings. *Corrosion Science*. 1993;35(5-8): 1267–1272. [https://doi.org/10.1016/0010-938X\(93\)90347-J](https://doi.org/10.1016/0010-938X(93)90347-J)
82. Ramanauskas R., Muleshkova L., Maldonado L., Dobrovolskis P. Characterization of the corrosion behaviour of Zn and Zn alloy electrodeposits: Atmospheric and accelerated tests. *Corrosion Science*. 1998;40(2-3): 401–410. [https://doi.org/10.1016/S0010-938X\(97\)00144-3](https://doi.org/10.1016/S0010-938X(97)00144-3)
83. Gavrilina M., Millet J. P., Mazille H., Marchandise D., Cuntz J. M. Corrosion behaviour of zinc–nickel coatings, electrodeposited on steel. *Surface and Coatings Technology*. 2000;123(2-3): 164–172. [https://doi.org/10.1016/S0257-8972\(99\)00455-7](https://doi.org/10.1016/S0257-8972(99)00455-7)
84. Byk T. V., Gaevskaya T. V., Tsybul'skaya L. S. Effect of electrodeposition conditions on the composition, microstructure, and corrosion resistance of Zn–Ni alloy coatings. *Surface and Coatings Technology*. 2008;202(24): 5817–5823. <https://doi.org/10.1016/j.surfcoat.2008.05.058>
85. Beltowska-Lehman E., Ozga P., Swiatek Z., Lupi C. Influence of structural factor on corrosion rate of functional Zn–Ni coatings. *Crystal Engineering*. 2002;5(3-4): 335–345. [https://doi.org/10.1016/S1463-0184\(02\)00045-X](https://doi.org/10.1016/S1463-0184(02)00045-X)
86. Fratesi R., Roventi G. Corrosion resistance of Zn–Ni alloy coatings in industrial production. *Surface and Coatings Technology*. 1996;82(1-2): 158–164. [https://doi.org/10.1016/0257-8972\(95\)02668-1](https://doi.org/10.1016/0257-8972(95)02668-1)
87. Hino M., Hiramatsu K., Nishida N., Hiramatsu M., Kawasaki H. Effect of Co content on corrosion resistance of electroplated Zn–Co alloys from sulfate solutions. *Journal of The Surface Finishing Society of Japan*. 1992;43(9): 873–877. <https://doi.org/10.4139/sfj.43.873>
88. De Lima-Neto P., Correia A. N., Colares R. P., Araujo W. S. Corrosion study of electrodeposited Zn and Zn–Co coatings in chloride medium. *Journal of the Brazilian Chemical Society*. 2007;18: 1164–1175. <https://doi.org/10.1590/S0103-50532007000600010>
89. Lichušina S., Chodosovskaja A., Sudavicius A., ... Juzeliunas E. Cobalt-rich Zn–Co alloys: electrochemical deposition, structure and corrosion resistance. *Chemija*. 2008;19(1): 25–31.
90. Stein M., Owens S. P., Pickering H. W., Weil K. G. Dealloying studies with electrodeposited zinc-nickel alloy films. *Electrochimica Acta*. 1998;43(1-2): 223–226. [https://doi.org/10.1016/S0013-4686\(97\)00228-4](https://doi.org/10.1016/S0013-4686(97)00228-4)
91. Hagi, H., Inokuchi K., Hayashi Y., Higashi K. Corrosion process of Zn–Co, Zn–Fe and Zn–Ni alloy electroplatings. *Tetsu-to-Hagane*. 1987;73(14): 1730–1737. [https://doi.org/10.2355/tetsutohagane1955.73.14\\_1730](https://doi.org/10.2355/tetsutohagane1955.73.14_1730)
92. Felloni L., Fratesi R., Quadri E., Roventi G. Electrodeposition of zinc-nickel alloys from chloride solution. *Journal of Applied Electrochemistry*. 1987;17: 574–582. <https://doi.org/10.1007/BF01084132>
93. Baldwin K. R., Robinson M. J., Smith C. J. E. Galvanic corrosion behaviour of electrodeposited Zn–Ni coatings coupled with steel. *British Corrosion Journal*. 1994;29(4): 299–304. <https://doi.org/10.1179/000705994798267557>

94. Fedrizzi L., Ciaghi L., Bonora P. L., Fratesi R., Roventi G. Corrosion behaviour of electrogalvanized steel in sodium chloride and ammonium sulphate solutions; a study by EIS. *Journal of applied electrochemistry*. 1992;22(3): 247–254. <https://doi.org/10.1007/BF01030185>
95. Hosny A. Y., El-Rafei M. E., Ramadan T. A., El-Gafari B. A., Morsy S. M. Corrosion resistance of zinc coatings produced from a sulfate bath. *Metal Finishing*. 1995;93(11): 55–59. [https://doi.org/10.1016/S0026-0576\(05\)80050-9](https://doi.org/10.1016/S0026-0576(05)80050-9)
96. Short N. R., Abibsi A., Dennis J. K. Corrosion resistance of electroplated zinc alloy coatings. *Transactions of the IMF*. 1989;67(1): 73–77. <https://doi.org/10.1080/00202967.1989.11870845>
97. Kawafuku J., Katoh J., Toyama M., Ikeda K., Nishimoto H., Satoh, H. Properties of zinc alloy coated steel sheets obtained by continuous vapor deposition pilot-line. *SAE Technical Paper*. 1991;912272. <https://doi.org/10.4271/912272>
98. Mosavat S. H., Shariat M. H., Bahrololoom M. E. Study of corrosion performance of electrodeposited nanocrystalline Zn–Ni alloy coatings. *Corrosion Science*. 2012;59: 81–87. <https://doi.org/10.1016/j.corsci.2012.02.012>
99. Kwon M., Jo D., Cho S. H., ... Park J. M. Characterization of the influence of Ni content on the corrosion resistance of electrodeposited Zn–Ni alloy coatings. *Surface and Coatings Technology*. 2016;288: 163–170. <https://doi.org/10.1016/j.surfcoat.2016.01.027>
100. Boshkov N., Petrov K., Vitkova S., Nemska S., Raichevsky G. Composition of the corrosion products of galvanic alloys Zn–Co and their influence on the protective ability. *Surface and Coatings Technology*. 2002;157(2-3): 171–178. [https://doi.org/10.1016/S0257-8972\(02\)00161-5](https://doi.org/10.1016/S0257-8972(02)00161-5)
101. Karahan I. H., Çetinkara H. A. Study of effect of boric acid on Zn–Co alloy electrodeposition from acid baths and on composition, morphology and structure of deposit. *Transactions of the IMF*. 2011;89(2): 99–103. <https://doi.org/10.1179/174591911X12968393517774>
102. Tanaka H., Moriwaki N., Ishikawa T., Nakayama T. Simulating study of atmospheric corrosion of Zn–Ni alloy coating on steels in marine zone: Structure and properties of artificially synthesized Ni (II)-doped zinc hydroxychloride rust particles. *Advanced Powder Technology*. 2015;26(2): 612–617. <https://doi.org/10.1016/j.apt.2015.01.010>
103. Ortiz Z. I., Díaz-Arista P., Meas Y., Ortega-Borges R., Trejo G. Characterization of the corrosion products of electrodeposited Zn, Zn–Co and Zn–Mn alloys coatings. *Corrosion Science*. 2009;51(11): 2703–2715. <https://doi.org/10.1016/j.corsci.2009.07.002>
104. Zhang-mi T., Zhe-long Y., Mao-zhong A., Wen-liang L., Jing-shuang Z. Research on the structure and the corrosion resistance of Zn–Co alloy coating. *Transactions of the IMF*. 1999;77(6): 246–247. <https://doi.org/10.1080/00202967.1999.11871293>
105. Ivaskevicius E., Selskis A., Sudavicius A., Ramanauskas R. Dealloying of electrodeposited zinc nickel alloy coatings. *Chemija*. 2001;12: 204–209.

#### Information about the authors

Alexander I. Biryukov, Cand. Sci. (Chem.), Assistant Professor, Department of Analytical and Physical Chemistry, Chelyabinsk State University (Chelyabinsk, Russian Federation).

<https://orcid.org/0000-0002-4020-8450>

[BiryukovAI.csu@yandex.ru](mailto:BiryukovAI.csu@yandex.ru)

Oleg A. Kozaderov, Dr. Sci. (Chem.), Senior Researcher, Laboratory of organic additives for the processes of chemical and electrochemical deposition of metals and alloys used in the electronics industry, Voronezh State University (Voronezh, Russian Federation).

<https://orcid.org/0000-0002-0249-9517>

[ok@chem.vsu.ru](mailto:ok@chem.vsu.ru)

Tanyana V. Batmanova, Senior Lecturer of Department of Analytical and Physical Chemistry (Chelyabinsk, Russian Federation).

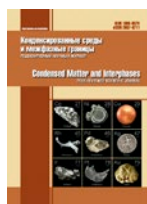
<https://orcid.org/0000-0001-8049-0940>

[batmanovatt@gmail.ru](mailto:batmanovatt@gmail.ru)

Received 30.03.2023; approved after reviewing 17.04.2023; accepted for publication 15.05.2023; published online 25.03.2024.

Translated by Valentina Mittova





## Review

Review article

<https://doi.org/10.17308/kcmf.2024.26/11807>

## Prospects of membrane catalysis in hydrogen energetics. Mini review

V. A. Shaposhnik✉

Voronezh State University,  
1 Universitetskaya pl., Voronezh 394018, Russian Federation

### Abstract

Hydrogen energetics is undoubtedly highly relevant today as it not only allows solving the issue of energy production from a renewable water source but can also prevent the formation of greenhouse gases. They say that any new idea is a well forgotten old one. The paper is dedicated to an excellent but still unimplemented work of Sainte-Claire Deville who managed to obtain hydrogen from water vapor using membrane technology. He used a clay pipe as a membrane which selectively permeated hydrogen. This process occurred with heating up to 950 °C. Sainte-Claire Deville managed to obtain only a mixture of hydrogen and oxygen in a ratio of 4:1 and then to clean the product from oxygen using chemical reactions.

Modern membrane catalysts based on palladium or its alloys are selectively permeable only for hydrogen. This means that the membrane catalysis method with palladium membranes could allow to realize of thermal water disassociation more effectively and solve the issues of hydrogen energetics using only renewable raw materials.

The history of hydrogen discovery and methods of its production was also studied in this review. Different methods of energy production were analyzed, including mineral resources, wind turbines, solar panels, hydroenergetics, electrolysis, and nuclear power, and a forecast was presented based on them. The review should be considered as an invitation to further discussions regarding this highly relevant and important topic.

**Keywords:** Energy, Hydrogen, Ecology, Economy, Sustainable development, Membranes, Palladium, Catalysis, Water vapor

**For citation:** Shaposhnik V. A. Prospects of membrane catalysis in hydrogen energetics. Mini-review. *Condensed Matter and Interphases*. 2024;26(1): 37–44. <https://doi.org/10.17308/kcmf.2024.26/11807>

**Для цитирования:** Шапошник В. А. Перспективы мембранного катализа в водородной энергетике. Мини-обзор. *Конденсированные среды и межфазные границы*. 2024;26(1): 37–44. <https://doi.org/10.17308/kcmf.2024.26/11807>

✉ Vladimir A. Shaposhnik, e-mail: [v.a.shaposhnik@gmail.com](mailto:v.a.shaposhnik@gmail.com)

© Shaposhnik V. A., 2024



## 1. Introduction

### 1.1. Early history of hydrogen energetics

There is no future yet. The present is the future that continually drifts into the past. Therefore, only the past is real, and prediction is also an action related to the past.

The discovery of hydrogen by Henry Cavendish in 1766 [1] was the preface to the history of hydrogen energetics, although Cavendish himself believed that he had discovered phlogiston, a combustible gas that his contemporaries had been looking for. To obtain hydrogen, Cavendish used the reaction of sulfuric or hydrochloric acid with zinc, iron, or tin. He discovered that hydrogen burns in the air. This method is now used in schools and for first-year chemistry students but it is not used for industrial production due to the high cost of reagents. The history of hydrogen energetics began in 1880. When Anthony Carlisle, professor of medicine from London, learned about the structure of the voltaic cell, he cancelled his lectures, postponed the surgeries, and produced the element using 17 silver half crowns and 17 zinc plates. Then he put the wires soldered to the outermost plates into water and observed the outgassing. William Nicholson helped him establish that one electrode released hydrogen and the other one released oxygen. The volume of the released hydrogen was twice more than the volume of the released oxygen. Having satisfied his curiosity, Carlisle returned to his previous work while Nicholson and Cruikshank continued the study of the electrolysis of solutions of salts and published their results [2].



Fig. 1. Sainte-Claire Deville (1818-1881)

Henri Sainte-Claire Deville suggested a new approach to the issue of hydrogen energetics (Fig. 1) [3–6]. Deville's array is presented in Fig. 2. Its main component is a pipe made from annealed non-glazed kaolin. Kaolin is an aluminosilicate  $\text{Al}_2\text{O}_3 \cdot 2\text{SiO}_2 \cdot 2\text{H}_2\text{O}$  with a porous structure and it has the properties of a weak cation exchanger. A kaolin pipe was placed in the middle of the furnace, and water vapor was supplied to the pipe through valve  $\delta$  from a flask or a retort. The kaolin pipe was inserted into a wider glazed porcelain pipe that was gas-impermeable. The edges of the pipe were sealed with clay paste. The pipes were placed in the furnace that was stoked with small pieces of coke. It was established that a

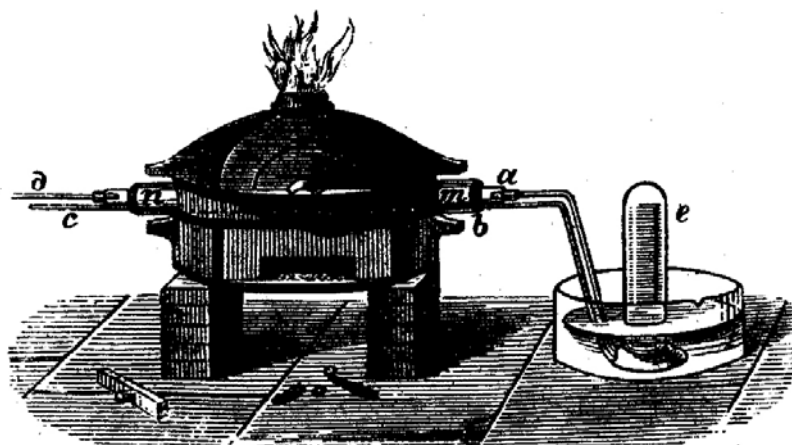


Fig. 2. Sainte-Claire Deville's array for the production of hydrogen

temperature of 950 °C is enough for the thermal disassociation of water molecules.

Sainte-Claire Deville was familiar with the works of Thomas Graham who studied membrane processes and founded colloid chemistry [7]. Graham showed that the flows of hydrogen through glass membranes or animal membranes are 4 times more than the flows of oxygen. The result obtained by Deville upon the diffusion through a kaolin membrane was similar to the result obtained by Graham upon the diffusion of hydrogen and oxygen through other kinds of membranes. Thus the space between the kaolin and porcelain pipes was enriched with hydrogen but still contained oxygen. To prevent the mixture of hydrogen and oxygen from burning, Sainte-Claire Deville passed carbon dioxide through pipe *c* between the pipes through the ring-like space. The rest of the oxygen reacted with hydrogen with the formation of water. Carbon dioxide that was released from pipe *b* was neutralized by alkali. As a result, at the outlet of the space between the pipes, Deville obtained pure hydrogen. A clay membrane is not highly selective in relation to hydrogen. Today there are membranes that permeate hydrogen selectively, which can significantly improve Sainte-Claire Deville's method. It should be noted that if there is no selective membrane upon thermal disassociation, even at the pressure of 0.1 at. 40 % the disassociation can be achieved only at 3000 °C.

### **1.2. Analysis of modern methods of hydrogen production**

In past centuries, technologies were evaluated only from an economical perspective. Due to the challenge thrown down to us by nature, it is now necessary to assess technologies not only from an economical, but also from an environmental perspective. Above all, we are talking about the deviation of the changes in the Earth's surface temperature from a cyclic dependence [8] towards an exponential increase over time [9]. It is considered to be global warming. It is caused by the increased concentration of greenhouse gases. Up until a certain concentration, greenhouse gases are necessary to keep warmth in the atmosphere but their excess results in global warming, the signs of which are already apparent. Up until

a certain concentration, greenhouse gases are necessary to keep warmth in the atmosphere but their excess results in global warming, the signs of which are already apparent. As a result, the generation of greenhouse gases and primarily carbon dioxide should be taken into account when evaluating new and existing technologies.

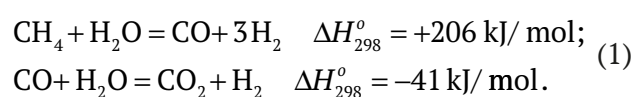
The words economics and ecology have the same root. It is a Greek word οἶκος which means home. In this case, it is the Earth, our home. However, despite the tendency towards globalization, economics is mostly of local nature, as countries are protected from one another by their borders, while the environmental situation is fundamentally global, as convection tends to equalize the gradients of temperatures and concentrations. Therefore, environmental issues are worldwide and cannot be nation-specific.

Let us discuss the issues of hydrogen energetics from this point of view. Industrial progress begins with science. Scientific ideas are implemented when a fertile field is provided for them. Some issues relating to implementation require additional research. This is how a close connection between science and production is formed. An example of this is Justus von Liebig's discovery of the irreversible extraction of minerals from soil for human nutrition [10]. He suggested using mineral fertilizers containing nitrogen, potassium, and phosphorus to preserve soil fertility. Potassium and phosphorus can be introduced into the soil as natural compounds while hydrogen is required in order to produce ammonia for nitrogen-containing fertilizers. BASF was the first to solve the issue of the production of ammonia for fertilizers. The researchers who worked on this project were awarded with a Nobel Prize (F. Haber and C. Bosch) [11]. A. Mittasch discovered an effective and cheap catalyst to synthesize ammonia from nitrogen and hydrogen. Large-tonnage production of ammonia was first organized in 1920 at a Leuna enterprise, not far from Merseburg. Nitrogen and hydrogen are required for the synthesis of ammonia. And while nitrogen is the main component of atmospheric air, hydrogen can be obtained through chemical technology methods. Thus the issue of large-scale production of hydrogen was encountered.

Today, hydrogen for the synthesis of ammonia is obtained through the reaction of methane



with water vapor [13]. The reactor's tube is a membrane catalyst. Pd, Pt, Ru, Rh, and Ir [14] are the most efficient materials for the tube, although an Ni catalyst, which is significantly cheaper, is more often used in practice. Fe and Co, which are more reactive, are not used due to their oxidation during the reaction. A typical catalyst consists of relatively large particles of nickel deposited on  $\text{Al}_2\text{O}_3$ . The process is conducted at high temperatures (up to 1000 °C), but when using membranes made of palladium and silver alloys, temperature must be reduced to 500 °C. The reaction results in a mixture of  $\text{H}_2$ , CO, and  $\text{CO}_2$ . The reaction proceeds as follows:



The method for the production of hydrogen for the synthesis of ammonia through the reaction of methane and water vapor is different from Sainte-Claire Deville's method that used only water vapor as a reagent. The use of the mixture of methane and water vapor is economically efficient. The profitability of methane for the production of hydrogen led to the idea of excluding water vapor from the reagents, but this method requires a non-renewable energy source that will become exhausted over the course of this century. Apart from that, an increased content of methane leads to the deposits in the form of curved graphite layers on the surface of the carbon catalyst [14]. The formation of threads from them is similar to the synthesis of carbon nanotubes. As a result, the reactor becomes blocked and the catalyst is destroyed. The introduction of water vapor into a reaction phase prevents the deposit of carbon on the surface of the catalyst. As a result of the experiments with various ratios of water vapor and methane, it was established that an increase in the proportion of water vapor leads to an increase in the proportion of methane that is converted over the course of the reaction [13]. Sulphur that is present in natural gas not only poisons the catalyst, but also hinders the use of hydrogen in the fuel cell [14]. Reactions (1) show that apart from hydrogen, carbon dioxide, a greenhouse gas, is also produced, while carbon oxide, a poisonous gas, is an intermediate product. As methane, the main component of natural gas, is a non-renewable energy source,

the improvement of methods and technologies of hydrogen production becomes a relevant task.

The method for the production of hydrogen by electrolysis from water or water solutions of salts has been known for a long time [2] and is still used today [15–20]. Electricity is required for electrolysis. Today, 37 % of electricity is generated by coal burning. The production of electricity by heat power plants seems to be environmentally friendly, but it gives the wrong impression, if we look at it from a consumer's perspective. To produce 1 kW of one hour of electricity by coal burning, 0.5 mol-Eq of sulfuric and nitric acids are released in the atmosphere, which leads to acid rain that destroys forests, damages architectural monuments, and increases metal corrosion. Apart from that, 1 kg of carbon dioxide (greenhouse gas), 14 g of slag, as well as radioactive isotopes are also released in the atmosphere [17–19]. The transition to the production of electricity from natural gas has considerably improved the environmental situation. Of all power plants, 24 % work on natural gas, although we should not forget that natural gas is a non-renewable energy source, and its exhaust product is carbon dioxide, a greenhouse gas [20].

The use of energy from the flow of rivers has been used for a long time, and now its proportion in the total production of electricity is 16 %. Although water-power is a renewable source of energy, there are a number of obstacles that prevent this method from being utilized more. Dams must be built in order to construct water power plants, which leads to changes in natural conditions. Water above the dams floods land that can be used for agriculture. And it also floods picturesque natural and historical places. Silt accumulates above the dams, while below the dams the concentration of nutritional substances in water decreases. Dams stand in the way of migration and the spawning of fish. Due to this, the USA is not planning to build new dams. Moreover, one dam in Maine has already been demolished, and they are going to demolish two more in Columbia [8]. Because of this, the future of hydroenergetics does not look optimistic.

Today, nuclear power stations produce 10 % of electricity. In some countries (USA, Russia, France, Japan, and others) nuclear power stations are considered to be the most promising source of

energy. Nuclear power stations produce electricity constantly, 24 hours a day, and since many enterprises do not operate at night, during this time nuclear power stations can be used for the production of hydrogen by electrolysis. Modern thermal-neutron and slow-neutron reactors operate on enriched uranium-235, the proportion of which is only 0.7% natural uranium. Fast-neutron reactors can operate on uranium-238 the content of which is 99.3 %, which allows using stocks as reactor fuel. In Russia, an energy unit with a fast-neutron reactor has been operating at the Belyarsk Nuclear Power Station for 30 years. Although this technology cannot be considered a completely renewable source of energy, still it can be said that it considerably expands the possibilities of obtaining a long-term energy source as compared to natural gas and oil. However, a number of countries (Germany, Italy, Spain, Belgium, Switzerland, and Austria) have decided against using nuclear power stations. It was due to the disquiet caused by the Chernobyl and Fukushima accidents. It is also possible that the leaders of these countries consider them to be dangerous in case of wars when nuclear power stations can easily cause a disaster. Today, the future of nuclear power stations cannot be definitely evaluated.

Wind power is a free, environmentally friendly, and renewable source of energy. Sailing boats and mills have been using wind power for a long time. At present, worldwide wind energetics is limited to 5 % of all power production, but European researchers and engineers are improving wind engines and are planning to have this figure increase up to 20 % by 2030. However, there are some issues related to the use of wind power. First of all, among them are the intermittent nature of the process and the transfer of energy over long distances. There are also some difficulties associated with the installation of wind generators, and wind turbines may freeze in winter. These issues do not prevent wind energetics from developing, but it is obvious that it will not be able to become the dominant source of energy.

Another relevant issue is how to increase the efficiency of solar energy. Currently, it claims only a tiny portion of the worldwide production of electricity (3 %). There have been both successes

and failures in this area. J. Carter, a former president of the USA, was keen on the idea of solar energy and had a solar heat collector installed on the roof of the White House, but there was a leak in the collector and it was then placed in the Jimmy Carter Library and Museum. Not all regions are effective for the use of solar energy, so, as part of a new project, photocells were placed in the Sahara Desert and the energy was later transferred to Europe.

As a result of the analysis, we can conclude that the production of hydrogen through the membrane catalysis of water vapor and the use of nuclear power stations for the electrolysis of water or water solutions of salts with the further use of fuel cells to create power stations are promising for energetics [20].

## 2. Membrane catalysis for hydrogen production

The term sustainable development was suggested in 1983 when UN assembled the World Commission on Environment and Development. The concept of sustainable development has become a paradigm and it should be understood as development that meets today's requirements without affecting the ability of future generations to satisfy their own needs. From this point of view, the present intensive use of hydrocarbon fuel and coal deprives future generations of energy sources. Thus, the method of membrane catalysis that uses water vapor as a reagent seems to be the most promising as it involves a renewable energy source and it is already free from harmful emissions into the soil and atmosphere.

The implementation of the method of membrane catalysis does not require any fundamentally new devices. The units that are used for hydrogen production from ammonia synthesis can be used for the industrial implementation of this method. To start using the new technology, one just has to stop using methane in the reforming processes and use materials with nanodispersed palladium on the surface as membranes. Palladium will act as a catalyst in this process.

The electronic structure of palladium in increasing energy is  $1s^2 2s^2 2p^6 3s^2 3p^6 4s^2 3d^{10} 4p^6 4d^{10}$ . As a result, the palladium membrane selectively permeates only hydrogen, which can

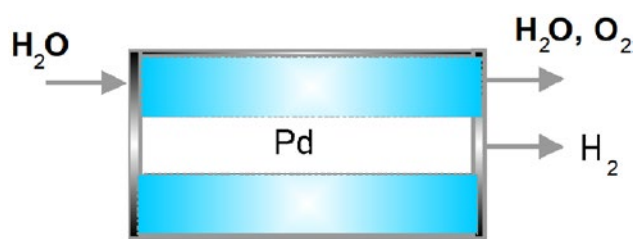


**Fig. 3.** Reactor for obtaining hydrogen from water vapor

be used as a source of energy or be converted into electrical energy using a fuel cell.

The exceptional selectivity of the palladium membrane can be explained from the perspective of the electrostatic interaction of its surface with water molecules. Fig. 4 shows an interaction model based on the example of a palladium atom and a water molecule. On the left is the initial state in which the water molecule is on the surface of the palladium. The water molecule has a constant electric dipole moment  $\mu = 1.84 (\pm 0.02) \cdot 10^{-18}$  el. un., see [19]. When determining the value of the dipole moment, the direction from the negative pole of the dipole to the positive one is conditionally introduced. The values of quadrupole and octupole moments of water also provide useful information on the redistribution of charge in a molecule. Each atom is also a dipole with a positively charged core and negatively charged mobile electron shell. Cores and electrons oscillate, and as a result, potential energy is conditioned by the electrostatic interaction between dipoles. It should be noted that the surface of any atom, and especially palladium due to its specific electron structure, is negatively charged, which is highly important for understanding the mechanism of any catalytic

process. As the water molecule is strongly polar, its hydrogen atoms are oriented towards the negatively charged surface of palladium. The conducted quantum chemical calculations show the result of the interaction [21] where the water molecule was broken by Coulomb forces and the hydrogen atoms were inside the palladium membrane, while the oxygen atom remained on the membrane's surface. The hydrogen atoms that passed through the palladium membrane due to the chemical potential are recombined into molecules on the opposite side of the membrane. Membrane catalysis is different from surface catalysis because reagents are adsorbed on the surface and after the reaction its products are detached from it. For example, a strong triple bond in the nitrogen molecule breaks on the catalyst surface during of the synthesis of ammonia, and then the nitrogen atoms react with hydrogen atoms and detach from the surface when ammonia molecules are obtained. The adsorption of reagent molecules on the catalyst surface is also a part of the membrane catalysis, but after that, one of the products diffuses through the membrane. This contributes to a more complete separation of products and reagents. This is the advantage of membrane catalysis.

The presented option for hydrogen production by membrane catalysis for its further use as a fuel or a component of a fuel cell is just one example of the global processes occurring in the universe. First of all, we use the energy of the sun directly or indirectly. At high temperatures, hydrogen atoms are ionized and turned into cores (protons) on the sun and other stars. The source of energy of stars is a chain of reactions, the main of which is the

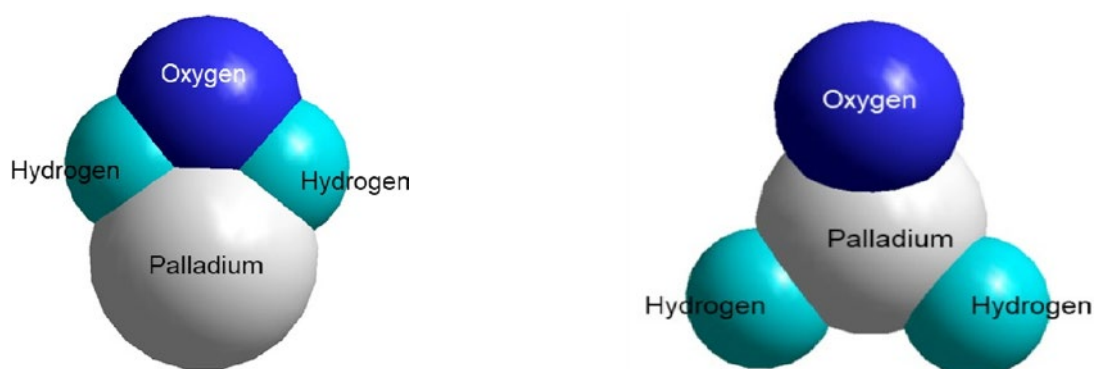
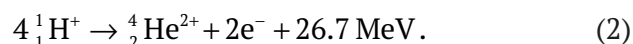


**Fig. 4.** Interaction model of water molecules and palladium atom. On the left: before the beginning of the catalytic reaction, on the right: during the reaction

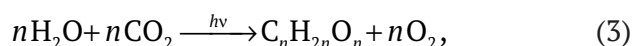


reaction between the hydrogen cores the result of which is helium:

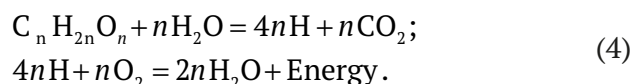


The sun is comprised of 75 % hydrogen and 24% helium. The interstellar medium is comprised of 90 % hydrogen and 10 % helium, which corresponds to the elemental composition of young stars. The lifetime of our planet is approximately 5 billion years and we are now in the middle of its life.

On average, only about 0.3% of all solar energy that reaches the surface of the Earth is captured in the course of photosynthesis. Chemists have set themselves the goal of synthesizing supermolecules that would allow the absorption of solar energy to be considerably increased, but no prominent results have been achieved so far [22]. According to A. Szent-Gyorgyi, a Nobel Prize laureate, the process of photosynthesis is primarily a reaction that uses solar energy for the disassociation of water:



while the obtained hydrocarbons, in his opinion, are similar to a hydrogen supply, which is mainly used to generate energy through its burning [23]:



He believed that living organisms contain only one type of fuel, hydrogen.

Photosynthesis produces a great amount of biomass that can be used as a renewable source of energy. In Brazil, ethanol produced from biomass amounts to 30–60 % of car fuel. Up to now, people have been extracting hydrocarbons that were obtained from the products of photosynthesis in the depths of the Earth millions of years ago. However, it is possible to transform the products of photosynthesis into a source of energy, right here and right now. Bioenergetics also has some issues. Today, ethanol is more expensive than gasoline, but it is not the only thing that prevents us from increasing the use of biomass. The main problem is that more space is needed for the production of biomass, and this comes into conflict with the need for more space for food crops due to the exponential growth of the population. The use of

algae seems to be promising for this purpose as they can provide three times more biomass per unit of space than palm plantations and six times more than corn plantations.

### 3. Conclusions

The analysis of the methods of energy production allowed determining the most promising methods for future hydrogen energetics. The first of them is energy from nuclear power plants that can be used for the production of electrolytic hydrogen. The second one is the use of ethanol obtained from biomass by photosynthesis. The third and the most promising one is the production of hydrogen by membrane catalysis through thermal disassociation of water vapor. A metal with palladium deposited on its surface that selectively permeates hydrogen can be used as a membrane. Hydrogen can be used as a fuel without any harmful emissions. However, hydrogen can also be used in a fuel cell in order to produce electricity. This is how we see the future of power plants. In some cases, the nuclear power plant energy can be used for the heating of a membrane reactor.

### Conflict of interests

The author declares that they have no known competing financial interests or personal relationships that could have influenced the work reported in this paper.

### References

1. Cavendish H. Three papers, containing experiments on factitious air. *Proceedings of the Royal Society of London, Philosophical Transactions of the Royal Society*. 1766; 56: 141–184. / Three papers, containing experiments on factitious air. *The Scientific Papers of the Honourable Henry Cavendish*. 77–101. <https://doi.org/10.1017/cbo9780511722424.005>
2. Nicholson W., Carlisle A. V. Letter from Henry Moyes M. D. to Maxwell Garthshore M. D. containing an account of some interesting experiments in galvanic electricity. *The Philosophical Magazine*. 1800; 7(28), 347–350. <https://doi.org/10.1080/14786440008562594>
3. Saint-Claire Deville H. Sur la phenomenes de dissociation. *Arch. Sci. Phys. Natur*. 1859;6: 266–275.
4. Sainte-Claire Deville H. Recherches sur la decomposition. *Arch. Sci. Phys. Natur*. 1860;9: 51–68.
5. Sainte-Claire Deville H. De la dissociation ou decomposition spontanee des corps sous l'influence de la chaleur. *Compt. Rend*. 1867;45: 857–861.

6. Sainte-Claire Deville H. *Lecons sur la dissociation professees devant la Societe Chimique de Paris en 1864 et 1865*. Paris; 1866. p. 255–278.
7. Graham T. LVIII. On the law of the diffusion of gases. In: *The London, Edinburgh, and Dublin Philosophical Magazine and Journal of Science*. 1833;2(11): 351–358. <https://doi.org/10.1080/14786443308648056>
8. Girard J. *Principles of environmental chemistry*. Boston: Iones & Batrtlett Publishers; 2005. 677 p.
9. Yergin D. *The Quest. Energy, security, and the remarking of the modern world*. N.Y., London, Toronto, Sydney: Penguin Books; 2002. 832 p.
10. Liebig J. *Die organische Chemie in ihrer Anwendung auf Agricultur und Physiologie*. Braunschweig, F. Vieweg; 1840. <https://doi.org/10.5962/bhl.title.42117>
11. Strube W. *Der historische Weg der Chemie Band 2*. Leipzig, VEB Deutscher Verlag fuer Grundstoffindustrie; 1976.
12. Kesore K., Ringer N., Gebert S., Rice D. Iron catalyst stands the test of time. *Nitrogen+Syngas*. 2009;300.
13. Delft van Y. V., Correia L. A., Overbeek J. P., ... Jansen D. *Hydrogen membrane reactor for industrial hydrogen*. Available at: [https://www.researchgate.net/publication/265665851\\_Hydrogen\\_membrane\\_reactor\\_for\\_industrial\\_hydrogen\\_production\\_and\\_power\\_generation](https://www.researchgate.net/publication/265665851_Hydrogen_membrane_reactor_for_industrial_hydrogen_production_and_power_generation)
14. Chorkendorf I., Niemantsverdriet J. W. *Concept of modern catalysis and kinetics*. Weinheim, Wiley-VCH Verlag GmbH & Co. KGaA; 2007. 457 p.
15. Schmidt O., Gamphir A., Staffell I., Hawkes A., Nelson J., Few S. Future cost and performance of water electrolysis: An aspect elicitation study. *International Journal of Hydrogen Energy*. 2017; 42(52), 30470–30492. <https://doi.org/10.1016/j.ijhydene.2017.10.045>
16. Shiva Kumar S., Himabindu V. Hydrogen production by PEM water electrolysis - A review. *Material Science for Energy Technologies*. 2019;2(3): 442–454. <https://doi.org/10.1016/j.mset.2019.03.002>
17. Shaposhnik V. A., Mazo A. A., Frölich P. Ecological aspects of the extreme purification of water. *Russian Chemical Reviews*. 1991;60(11): 1284–1292. <https://doi.org/10.1070/rc1991v060n11abeh001146>
18. Stiles D. A., Wells P. H. The production of ultrapure hydrogen. *Platinum Metals Rev*. 1972; 16(4); 124-128. Available at: <https://technology.matthey.com/documents/496120/626258/pmr-v16-i4-124-128.pdf/493ff7f4-d447-2b5b-52e2-800a3fa501bb?version=1.0&t=1656009920233>
19. Eisenberg D., Kauzmann W. *The structure and properties of water*. Oxford New York, University Press; 1969. 300 p. / Eisenberg D., Kauzmann W. *The structure and properties of water*. 2005. <https://doi.org/10.1093/acprof:oso/9780198570264.001.0001>
20. Maggio G., Nicita A., Squadrito G. How the hydrogen production from RES could change energy and fuel markets: A Review of recent literature. *International Journal of Hydrogen Energy*. 2019;44: 11371–11384. <https://doi.org/10.1016/j.ijhydene.2019.03.121>
21. Shaposhnik V. A. Ab initio calculation of catalytical atomization reaction of water molecules on the surface of palladium membrane. *Proceedings of the International Conference “Ion transport in organic and inorganic membranes”*. Sochi; 2015. p. 265-266.
22. Lehn J.-M. *Supramolecular chemistry. Concepts and perspectives*. VCH: Weinheim, N.Y., Basel, Tokyo; 1995. 271 p.
23. Szent-Györgyi A. *Oxidation, energy transfer and vitamin*. Available at: <https://www.nobelprize.org/prizes/medicine/1937/szent-gyorgyi/lecture/>

### Information about author

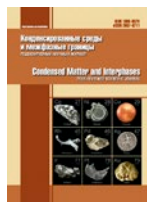
Vladimir A. Shaposhnik, Dr. Sci. (Chem.), Full Professor, Department of Analytical Chemistry, Voronezh State University (Voronezh, Russian Federation).

[v.a.shaposhnik@gmail.com](mailto:v.a.shaposhnik@gmail.com)

<https://orcid.org/0000-0002-9555-4633>

Received 16.06.2023; approved after reviewing 15.09.2023; accepted for publication 16.10.2023; published online 25.03.2024.

Translated by Marina Strepetova



## Original articles

Research article

<https://doi.org/10.17308/kcmf.2024.26/11808>

## Synthesis and luminescent properties of PbS/SiO<sub>2</sub> core-shell quantum dots

I. G. Grevtseva✉, M. S. Smirnov, K. S. Chirkov, A. N. Latyshev, O. V. Ovchinnikov

Voronezh State University,  
1 Universitetskaya pl., Voronezh 394018, Russian Federation

### Abstract

The research focuses on the development of techniques for creating core-shell structures, based on colloidal PbS quantum dots (PbS QDs) and establishing the influence of the dielectric SiO<sub>2</sub> shell on the luminescent properties of PbS QDs. The objects of the study were PbS QDs with an average size of 3.0±0.5 nm, passivated with thioglycolic acid (TGA) and PbS/SiO<sub>2</sub> QDs, based on them with an average size of 6.0±0.5 nm. When we passivated the PbS QD interfaces with thioglycolic acid molecules, there were two luminescence peaks at 1100 and at 1260 nm. It was found that increasing the temperature of the colloidal mixture to 60 °C provides an increase in the intensity of the long-wave peak. An analysis of the luminescence excitation spectra of both bands and the Stokes shift showed that the band at 1100 nm is associated with the radiative annihilation of an exciton, while the band at 1260 nm is due to recombination at trap levels. The formation of PbS/SiO<sub>2</sub> QDs suppresses trap state luminescence, indicating the localization of luminescence centers predominantly at QD interfaces. The exciton luminescence at 1100 nm becomes more intensive.

**Keywords:** Lead sulfide quantum dots, Core-shell structures, SiO<sub>2</sub> shell, Luminescence spectra, Excitation spectra

**Funding:** The study was funded by the Russian Science Foundation, research project No. 22-72-00098.

**Acknowledgements:** The results of transmission electron microscopy using a Libra 120 microscope were obtained with the help of the equipment of the Centre for Collective Use of Voronezh State University.

**For citation:** Grevtseva I. G., Smirnov M. S., Chirkov K. S., Latyshev A. N., Ovchinnikov O. V. Synthesis and luminescent properties of PbS/SiO<sub>2</sub> core-shell quantum dots. *Condensed Matter and Interphases*. 2024;26(1): 45–54. <https://doi.org/10.17308/kcmf.2024.26/11808>

**Для цитирования:** Гревцева И. Г., Смирнов М. С., Чирков К. С., Латышев А. Н., Овчинников О. В. Синтез и спектрально-люминесцентные свойства квантовых точек ядро/оболочка PbS/SiO<sub>2</sub>. *Конденсированные среды и межфазные границы*. 2024;26(1): 45–54. <https://doi.org/10.17308/kcmf.2024.26/11808>

✉ Irina G. Grevtseva, e-mail: [grevtseva\\_ig@inbox.ru](mailto:grevtseva_ig@inbox.ru)

© Grevtseva I. G., Smirnov M. S., Chirkov K. S., Latyshev A. N., Ovchinnikov O. V., 2024





## 1. Introduction

Scientific and practical interest in semiconductor colloidal quantum dots (QDs) is determined by a wide range of their potential applications. They are based on photoprocesses that provide size-dependent absorption and luminescent properties [1–16]. So, controlling the luminescent properties of colloidal QDs is a topical task of modern nanophotonics. There are studies demonstrating that it is possible to control the luminescent properties of QDs due to both the quantum-size effect and structural and impurity defects in the volume and at the interfaces of QDs [16–25]. Semiconductor colloidal PbS QDs are of significant interest in this field, since they exhibit luminescent properties in the visible and near-IR ranges [12–16, 26–30], which is due to the energy of the band gap of the PbS bulk crystal, which is 0.41 eV [26]. Accordingly, it is relevant to control the spectral composition and quantum yield of emission for PbS QDs due to the wide range of their potential applications. These include optoelectronic device technologies (detectors, emitters, nonlinear media for intensity and phase control, sensor systems, etc.), photocatalytic systems, as well as biomedical applications (luminescent markers), etc. [1–16].

Colloidal synthesis techniques involve QDs surface passivation with organic ligands. The chemical properties of the organic ligand, its concentration, and mechanism of interaction with the QD surface determine the presence/absence of surface states in QDs [17–25]. Despite the fact that numerous colloidal synthesis techniques have been proposed for PbS QDs, which provide highly dispersed QDs, there is still the problem of controlling the luminescent properties [24–30]. The available literature data concerning the size dependence of spectral-luminescent properties, value of the Stokes shift, and luminescence mechanism for PbS QDs are contradictory and ambiguous [24, 25, 29–34]. When the energy structure of exciton states changes due to the variations in the size of PbS QDs or their surface environment, new luminescence bands are often formed in the luminescence spectra due to optical transitions of charge carriers on the trap states [14, 16, 24, 25]. According to the atomistic calculations of the energy structure of QDs using

the density functional theory (DFT) [24, 35], the emitting trap states are formed at the synthesis stage of colloidal PbS QDs. They are caused by the presence of reduced or “undercharged” Pb atoms on the surface of QDs. In this case, the emitting trap states in PbS QDs are removed by changing the ligand, pH or polarity of the medium, which also leads to the loss of exciton luminescence intensity [24]. For most colloidal QD compositions, optical transitions involving trap states in QDs are controlled by forming a shell of wide-band gap semiconductors on the surface of QDs (core-shell structures) [17, 36–38]. The formation of core-shell structures, based on PbS QDs, in particular PbS/SiO<sub>2</sub> QDs, has been little studied [27, 39–41]. Whereas the formation of the SiO<sub>2</sub> shells on the QD interfaces contributes not only to the “curing” of the structural and impurity defects of QDs, involved in the formation of luminescent properties, but also allows controlling the monodispersity of QDs in the ensemble, increasing the colloidal QDs stability, and decreasing cytotoxicity [17, 27, 36–41]. Thus, controlling the luminescent properties of PbS QDs, including through the formation of core-shell structures on their basis, is an urgent task. Resolving this problem will provide an opportunity to create materials and devices for modern nanophotonics applications, based on PbS QDs.

The aim of the study was to form a SiO<sub>2</sub> shell on the interfaces of PbS QDs and to determine its influence on the luminescent properties of PbS QDs.

## 2. Experimental

### 2.1. Methods for the synthesis of colloidal PbS QDs and PbS/SiO<sub>2</sub> QDs

Samples of colloidal PbS QDs were obtained by aqueous synthesis, using thioglycolic acid (TGA) molecules as an organic passivator of the QD interface. The process was based on the methodology for the synthesis of colloidal QDs, previously implemented for silver and cadmium sulfide QDs [14–21]. This synthesis procedure consisted of mixing aqueous solutions of TGA and Pb(NO<sub>3</sub>)<sub>2</sub> with a molar ratio of 2:1, respectively, followed by adjusting the pH to 10. Next, an aqueous Na<sub>2</sub>S solution was added to the reaction mixture with a molar ratio of 0.2:1 to Pb(NO<sub>3</sub>)<sub>2</sub>.

At this stage of the synthesis, a sample was taken (PbS QD#1 sample). Then, the colloidal mixture was kept at 60 °C for 1 hour (PbS QD#2 sample); for 2 hours (PbS QD#3 sample).

PbS/SiO<sub>2</sub> core-shell QD structures were also formed by an aqueous synthesis technique. It is based on the use of (3-mercaptopropyl)trimethoxysilane (MPTMS) silica ligand as a coupling agent and sodium metasilicate (Na<sub>2</sub>SiO<sub>3</sub>) as a SiO<sub>2</sub> main layer precursor [17, 36, 38]. The concentration of the added MPTMS solution was calculated, based on the concentration and average size of PbS QDs in the ensemble. It was ~ 0.2 mM for all PbS QD samples. Next, an aqueous solution of Na<sub>2</sub>SiO<sub>3</sub> (0.5 mM) was added to the colloidal mixture and kept at room temperature for 24 h (samples PbS/SiO<sub>2</sub> QD#1, PbS/SiO<sub>2</sub> QD#2, and PbS/SiO<sub>2</sub> QD#3).

To avoid oxidation of PbS QDs, nitrogen purging was carried out during the synthesis stage. Afterwards, the obtained samples of PbS and PbS/SiO<sub>2</sub> QDs were stored at 5 °C.

## 2.2. Experimental techniques

The sizes of PbS QDs and core-shell structures of PbS/SiO<sub>2</sub> QDs, based on them were determined by transmission electron spectroscopy (TEM) using a Libra 120 microscope (CarlZeiss, Germany) and a digital analysis of TEM images and X-ray diffraction.

Photoluminescence spectra of PbS and PbS/SiO<sub>2</sub> QD samples in the near infrared range were recorded using a PDF 10C/M image sensor (ThorlabsInc., USA) with a built-in amplifier and a diffraction monochromator with a 600 mm<sup>-1</sup> grating. A NDB7675 semiconductor laser diode (Nichia, Japan) with the wavelength of 462 nm was used as a source of luminescence excitation. The luminescence spectra were corrected for the spectral characteristics of the devices which was measured using a reference incandescent lamp with a known color temperature.

To record the luminescence excitation spectra of PbS and PbS/SiO<sub>2</sub> QD samples, we used another diffraction monochromator with a 1200 mm<sup>-1</sup> grating and 400 W incandescent lamp. It provided the excitation range from 500 to 1300 nm. The intensity of the excitation radiation in the sample region was controlled by an optical power meter Thorlabs PM100A with Thermal Power Sensor

Head S401C, sensitive in the range of 0.19–20 μm. The excitation radiation power was in the range of 100–400 mW.

The quantum yield of luminescence for PbS and PbS/SiO<sub>2</sub> QDs was determined by the relative method using the equation:

$$QY = QY_r \frac{I}{I_r} \frac{D_r}{D} \frac{n^2}{n_r^2}, \quad (1)$$

where  $QY_r$  is the quantum yield of the reference luminescence,  $I$  and  $I_r$  are the integral intensities in the luminescence band of the QD sample and reference,  $D$  and  $D_r$  are the optical densities at the excitation wavelength for the QD sample and reference (in the experiments,  $D$  and  $D_r \sim 0.1$ ),  $n$  and  $n_r$  are the refractive indices of the solutions of the studied QD sample and reference, respectively. Distilled water ( $n = 1.33$  at a wavelength of 650 nm at 293 K [42]) served as a solvent for PbS and PbS/SiO<sub>2</sub> QDs. A DMSO solution of indocyanine green (ICG) dye with  $QY_k = 12\%$  in the region of 800 nm [43] ( $n_r = 1.47$  at a wavelength of 650 nm at 293 K according to [44]) was used as a reference for the quantum yield of luminescence of PbS and PbS/SiO<sub>2</sub> QDs in the near IR range.

## 3. Results and discussion

### 3.1. Structural data of the obtained PbS and PbS/SiO<sub>2</sub> QD samples

TEM images of all synthesized samples of PbS QDs showed that our synthesis procedure resulted in the formation of individual QDs with close average sizes in the range of 3.0±0.5 nm and dispersion within 25% (Fig. 1). X-ray diffraction data of all obtained samples of colloidal PbS QDs showed broadened reflections, which is due to the quantum size effect (Fig. 1). The observed peaks are correlated with the diffraction of atomic planes (111), (200), (220), (311), (222), (400), (311), and (420), indicating the formation of PbS nanocrystals in a cubic crystal lattice ( $Fm\bar{3}m$ ) [45].

The formation of PbS/SiO<sub>2</sub> QDs leads to an increase in the average size of PbS QDs to 5.5–6.0 nm (Fig. 1), which is probably due to the presence of a SiO<sub>2</sub> layer with a thickness of about 1.3–1.5 nm on the surface of QDs. In some cases, agglomerates of PbS/SiO<sub>2</sub> QDs were formed (Fig. 1).

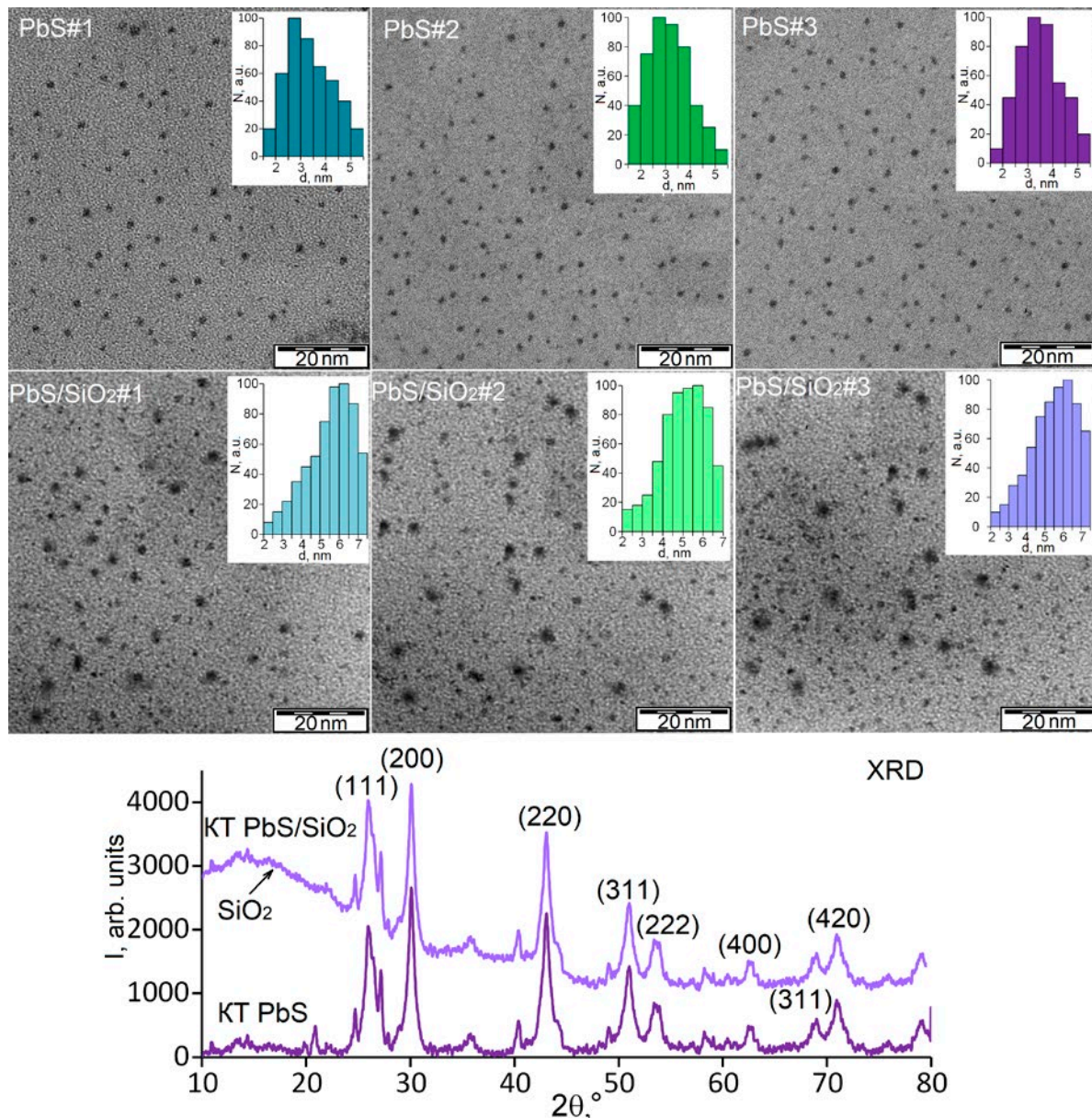


**Fig. 1.** TEM images and size distribution histograms of ensembles of PbS QDs and PbS/SiO<sub>2</sub> QDs. Diffractograms of PbS QDs and PbS/SiO<sub>2</sub> QDs

Also, during the formation of PbS/SiO<sub>2</sub> QDs, the diffraction pattern showed an additional diffuse band in the  $2\theta$  angle range from 15 to 40°. These changes in the diffraction were interpreted as the contribution of amorphous SiO<sub>2</sub> phase [46]. They were observed during the formation of the SiO<sub>2</sub> shell on the surface of QDs of other compositions [47, 48].

### 3.2. Spectral-luminescent properties of PbS QDs

UV-Vis absorption spectra of all PbS QD samples do not have an exciton structure, and

noticeable absorption begins in the wavelength range below 1000 nm (1.24 eV). Thus, the absorption edge of PbS QDs appears to be shifted toward shorter wavelengths compared to the absorption edge of PbS (3025 nm or 0.41 eV) [26]. It is a manifestation of quantum confinement effect. The structureless absorption edge characteristic of the studied samples may be due to a high concentration of defects [49, 50], as well as to a noticeable size dispersion of PbS QDs [51].



The luminescent properties of all obtained PbS QD samples turned out to be fundamentally different (Fig. 2).

The luminescence spectrum of the initial PbS QD#1 sample had a single band with a peak around 1100 nm (Fig. 2, curve 1). The luminescence band was not elementary, there was a specific feature in the long-wave part of the spectrum in the range of 1200–1280 nm. Keeping the samples of colloidal PbS QDs at 60 °C (PbS QD#2) for 1 hour resulted in the appearance of the second band in the luminescence spectrum in the region of 1260 nm (Fig. 2, curve 2). Subsequent of PbS QD samples at 60 °C for 2 hours (PbS QD#3) resulted in almost complete disappearance of the luminescence band at 1100 nm. In the luminescence spectrum, only one band at 1280 nm remained (Fig. 2, curve 3). The full width at half maximum (FWHM) of the luminescence band of PbS QDs for all studied samples was about 0.20–0.25 eV. Since the optical absorption spectra for all PbS QD samples do not have an exciton structure, we considered the luminescence excitation spectra (Fig. 2) to establish the luminescence mechanisms. As opposed to the absorption spectra that are determined by the absorption of each nanocrystal in the sample, only the QDs emitting at the recording wavelengths participate in the formation of the excitation spectra. This allowed achieving selectivity by the wavelength in the luminescence excitation spectra through a change in the recording wavelength [15, 16].

In the luminescence excitation spectra of all PbS QD samples, there is a specific feature with a peak at 980 nm in the short-wave band (1100 nm) (Fig. 2, curves 1', 2', and 3'). The position and shape of this peak suggest that it is associated with a probable exciton transition in the optical absorption spectrum. In this case, the Stokes shift of the luminescence peak at 1100 nm relative to the exciton absorption peak was 0.125 eV. On the contrary, no exciton structure was found in the excitation spectrum of the long-wave luminescence band with a peak at 1280 nm (Fig. 2, curves 1'', 2'', and 3''). The excitation band edge was located in the region of 980 nm, while the Stokes shift value increased up to 0.33 eV. The obtained data are

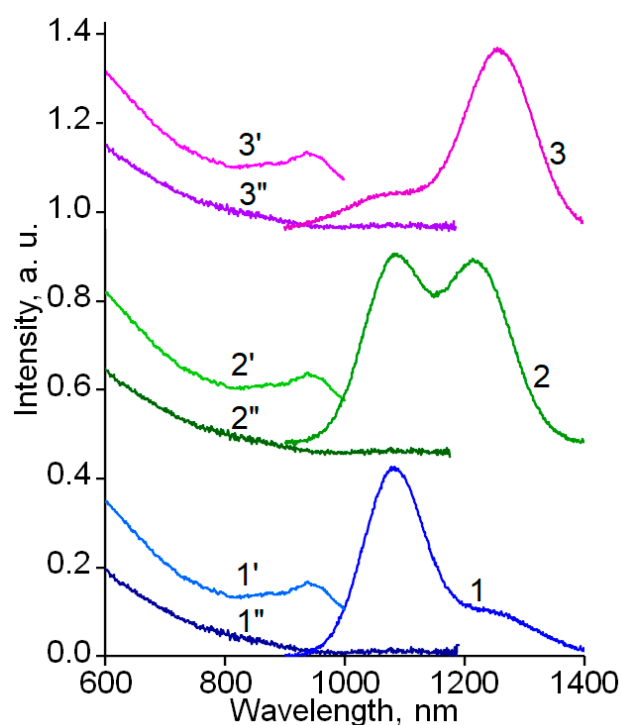


**Fig. 2.** Luminescence spectra of PbS QD#1 (1), PbS QD#2 (2), and PbS QD#3 (3). Luminescence excitation spectra in the region of 1100 nm (PbS QD#1 (1'), PbS QD#2 (2'), PbS QD#3 (3')) and 1260 nm (PbS QD#1 (1''), PbS QD#2 (2''), PbS QD#3 (3''))

in agreement with the data, obtained by the authors earlier [15, 16]. In study [16], based on experimental data on the temperature dependence of luminescence properties and luminescence excitation spectra of PbS QDs, a scheme defining IR luminescence was proposed. According to this scheme, the luminescence band at 1100 nm is due to the radiative annihilation of an exciton, and the long-wavelength band at 1260 nm is due to the recombination of free charge carriers on structural and impurity defects.

Thus, within the framework of a unified approach to the synthesis of PbS QDs, we obtained QD samples of close size but with different luminescent properties. According to the experimental data, the luminescence of PbS QD#1 is mainly due to exciton luminescence, PbS QD#2 is characterized by the simultaneous presence of both exciton and trap state luminescence bands in the spectrum, and the luminescence of PbS QD#3 is mainly due to trap state luminescence.

### 3.3. Spectral-luminescent properties of PbS/SiO<sub>2</sub> QDs

The main manifestations of core-shell PbS QDs formation were observed in the luminescence properties (Fig. 3).

The formation of PbS/SiO<sub>2</sub> QD#1 resulted in a shift of the exciton luminescence band from 1100 to 1080 nm, while the FWHM of the luminescence band decreased from 0.20 to 0.12 eV, and the quantum yield of luminescence increased from 2.5 to 4.5% (Fig. 3a, curves 1, 2). In the case of PbS QD#2 sample, upon the formation of the SiO<sub>2</sub> shell, the long-wave luminescence band in the region of 1260 nm, which was due to trap state luminescence, disappeared. At the same time, the luminescence band in the region of 1100 nm shifted to 1030 nm (Fig. 3b, curves 1, 2), its FWHM decreased from 0.25 to 0.13 eV, and the quantum yield increased from 1 to 3%. In the case of PbS QD#3, the formation of the shell resulted in the appearance of an intense luminescence band in the region of 1080 nm, while the band at 1260 nm shifted to a shorter wavelength of 1210 nm (Fig. 3c, curves 1, 2). The FWHM of both luminescence peaks was estimated to be within the range of 0.1–0.2 eV. No exciton structure was found in the luminescence excitation spectrum with a peak at 1210 nm. The excitation band edge

is located in the region of 950 nm, and the value of the Stokes shift is 0.3 eV (Fig. 3c, curves 2, 3), which is similar to the data for the original samples of PbS QD#3 and indicates the trap state nature of luminescence in the region of 1210 nm. The shift of the trap state luminescence peak to the shorter wavelength can probably be explained by the influence of the SiO<sub>2</sub> shell on the energy states of the structural and impurity defects of PbS QD#3. The quantum yield of PbS QD#3 remained unchanged upon the formation of the SiO<sub>2</sub> shell and amounted to 1.5 %.

For all PbS/SiO<sub>2</sub> QD samples, we recorded excitation spectra of the short-wavelength luminescence band (1030–1100 nm) due to exciton luminescence. They demonstrated a shift in the peak of the ground exciton transition to 900 nm compared to the peak in the region of 980 nm for PbS QDs (Fig. 3a, b, c, curves 4, 5). For PbS QD#1, the Stokes shift increased from 0.13 to 0.22 eV, for PbS QD#2 – from 0.13 to 0.17 eV, and for PbS QD#3 – from 0.13 to 0.22 eV. The observed regularities probably result from the change in the size distribution of PbS QDs in the ensemble during the formation of the SiO<sub>2</sub> shell [15]. Estimates of the average size of PbS QDs in the framework of the hyperbolic zone model [52] showed that the shift of the ground

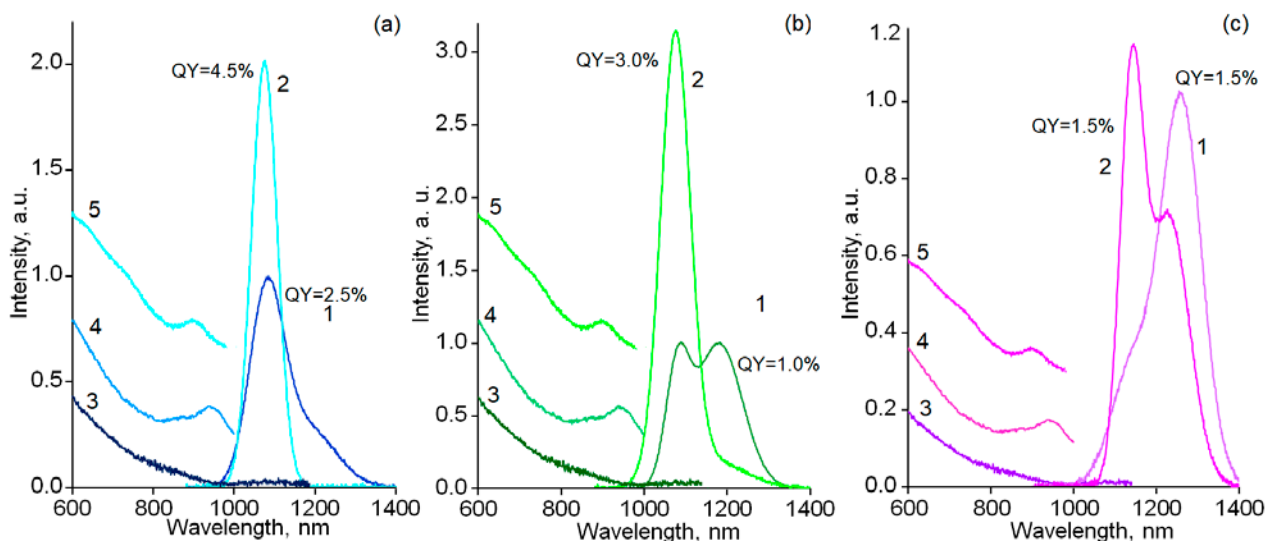


**Fig. 3.** Luminescence spectra of PbS QD#1 (1) and PbS/SiO<sub>2</sub> QD#1 (2) – a; PbS QD#2 (1) and PbS/SiO<sub>2</sub> QD#2 (2) – b; PbS QD#3 (1) и PbS/SiO<sub>2</sub> QD#3 (2) – c. Luminescence excitation spectra in the region of 1260 nm for PbS/SiO<sub>2</sub> QD#1 (3) – a; PbS/SiO<sub>2</sub> QD#2 (3) – b; PbS/SiO<sub>2</sub> QD#3 (3) – c. Luminescence excitation spectra in the region of 1100 nm for PbS QD#1 (4) – a; PbS QD#2 (4) – b; PbS QD#3 (4) – c. Luminescence excitation spectra in the region of 1080 nm for PbS/SiO<sub>2</sub> QD#1 (5) – a; PbS/SiO<sub>2</sub> QD#2 (5) – b; PbS/SiO<sub>2</sub> QD#3 (5) – c

exciton transition peak in the excitation spectra from 980 to 900 nm (0.1 eV) is due to a decrease in the diameter of PbS QDs within 0.4 nm. It is not possible to compare the obtained theoretical estimates of the QDs size change during the formation of core-shell structures with the TEM experimental data, since the TEM image of PbS/SiO<sub>2</sub> QDs is complicated by the presence of a contrast phase associated with the formation of the SiO<sub>2</sub> layer on the QD surface. The increase in the Stokes shift value as a result of the formation of the core-shell structure can also indicate an increase in the energy of the Coulomb and exchange interaction between the electron and hole in the exciton due to the enhancement of the quantum confinement of charge carriers [15].

Thus, the complete disappearance of the long-wavelength luminescence band at 1260 nm for PbS/SiO<sub>2</sub> QD#1 and PbS/SiO<sub>2</sub> QD#2, and its partial disappearance for PbS/SiO<sub>2</sub> QD#3 indicates the suppression of trap state luminescence in PbS QDs as a result of the formation of the SiO<sub>2</sub> shell. This suggests the interface nature of the luminescence centers.

#### 4. Conclusions

The study presented the principles of controlling the IR luminescence of colloidal PbS QDs. The technique of colloidal synthesis of PbS QDs, passivated with thioglycolic acid molecules that we used in this work makes it possible to obtain PbS QDs with an average size of 3.0±0.5 nm, predominantly with luminescence in the region of 1100 nm. Keeping colloidal solutions of PbS QDs at 60 °C has no significant effect on the average size of QDs in the ensemble, but leads to the appearance of a long-wavelength luminescence band at 1260 nm. Analysis of the luminescence excitation spectra of both bands and the Stokes shift showed that the band at 1100 nm is associated with the radiative annihilation of an exciton, while the band at 1260 nm is due to recombination at trap state levels. Thus, radiative recombination centers are formed at the interfaces of PbS QDs under the effect of temperature.

The formation of a SiO<sub>2</sub> shell on the interfaces of PbS QDs with the exciton luminescence at 1100 nm leads to the shift of the luminescence band towards the short-wave region by 20 nm and

a twofold increase in the luminescence quantum yield. The shift of luminescence to shorter waves is presumably associated with a decrease in the average size of PbS QDs in the ensemble upon the formation of core-shell structures. In the case of PbS QDs characterized by trap-state luminescence at 1260 nm, the formation of the SiO<sub>2</sub> shell results in partial or complete quenching of trap-state luminescence with a simultaneous increase in the quantum yield of exciton luminescence in the range of 1030-1100 nm. Thus, PbS/SiO<sub>2</sub> QDs ensure the suppression of trap state luminescence in PbS QDs, which in turn indicates the interface nature of the luminescence centers.

#### Contribution of the authors

Grevtseva I. G. – Conceptualization, Methodology, Investigation, Original Draft Preparation & Editing. Smirnov M. S. – Research Concept, Researching, Original Draft Preparation, Review & Editing. Chirkov K. S. – Investigation, Software. Latyshev A. N. – Result Discussion, Review & Editing. Ovchinnikov O. V. – Conceptualization, Methodology, Writing the Text, Final Conclusions.

#### Conflict of interests

The authors declare that they have no known competing financial interests or personal relationships that could have influenced the work reported in this paper.

#### References

1. Hafiz S. B., Scimeca M., Sahu A., Ko D.-K. Colloidal quantum dots for thermal infrared sensing and imaging. *Nano Convergence*. 2019;6(7). <https://doi.org/10.1186/s40580-019-0178-1>
2. Sergeev A. A., Pavlov D. V., Kuchmizhak A. A., ... Rogach A. L. Tailoring spontaneous infrared emission of HgTe quantum dots with laser-printed plasmonic arrays. *Light: Science and Applications*. 2020;9(16). <https://doi.org/10.1038/s41377-020-0247-6>
3. Reineck P., Gibson B. C. Near-infrared fluorescent nanomaterials for bioimaging and sensing. *Advanced Optical Materials*. 2017;5: 1600446. <https://doi.org/10.1002/adom.201600446>
4. Gu Yi.-P., Cui R., Zhang Z.-L., Xie Z.-X., Pang D.-W. Ultrasmall near-infrared Ag<sub>2</sub>Se quantum dots with tunable fluorescence for in vivo imaging. *Journal of the American Chemical Society*. 2012;134(1): 79–82. <https://doi.org/10.1021/ja2089553>
5. Xu S., Cui J., Wang L. Recent developments of low-toxicity NIR II quantum dots for sensing and



- bioimaging. *TrAC Trends in Analytical Chemistry*. 2016;80: 149–155. <https://doi.org/10.1016/j.trac.2015.07.017>
6. Zaini M. S., Liew J. Y. Ch., Ahmad S. A. A., Mohamad A. R., Kamarudin M. A. Quantum confinement effect and photoenhancement of photoluminescence of PbS and PbS/MnS quantum dots. *Applied Sciences*. 2020;10(18): 6282. <https://doi.org/10.3390/app10186282>
7. Tan L., Wan A., Zhao T., Huang R., Li H. Aqueous synthesis of multidentate-polymer-capping Ag<sub>2</sub>Se quantum dots with bright photoluminescence tunable in a second near-infrared biological window. *ACS Applied Materials and Interfaces*. 2014;6(9): 6217–6222. <https://doi.org/10.1021/am5015088>
8. Keuleyan S., Lhuillier E., Guyot-Sionnest P. Synthesis of colloidal HgTe quantum dots for narrow Mid-IR emission and detection. *Journal of the American Chemical Society*. 2011;133(41): 16422–16424. <https://doi.org/10.1021/ja2079509>
9. Yu Y., Zhang K., Sun S. One-pot aqueous synthesis of near infrared emitting PbS quantum dots. *Applied Surface Science*. 2012;258(18): 7181–7187. <https://doi.org/10.1016/j.apsusc.2012.04.031>
10. Qian H., Dong C., Peng J., Qiu X., Xu Y., Ren J. High-quality and water-soluble near-infrared photoluminescent CdHgTe/CdS quantum dots prepared by adjusting size and composition. *The Journal of Physical Chemistry C*. 2007;111(45): 16852–16857. <https://doi.org/10.1021/jp074961c>
11. Capoen B., Martucci A., Turrell S., Bouazaoui M. Effects of the sol-gel solution host on the chemical and optical properties of PbS quantum dots. *Journal of Molecular Structure*. 2003;651-653: 467–473. [https://doi.org/10.1016/S0022-2860\(02\)00667-1](https://doi.org/10.1016/S0022-2860(02)00667-1)
12. Yin Q., Zhang W., Zhou Y., Wang R., Zhao Z., Liu C. High efficiency luminescence from PbS quantum dots embedded glasses for near-infrared light emitting diodes. *Journal of Luminescence*. 2022;250: 119065. <https://doi.org/10.1016/j.jlumin.2022.119065>
13. Srivastava R. R., Mishra H., Singh V. K., Vikram K., Srivastava R. K., Srivastava S. K., Srivastava A. pH dependent luminescence switching of tin disulfide quantum dots. *Journal of Luminescence*. 2019;213: 401–408. <https://doi.org/10.1016/j.jlumin.2019.05.024>
14. Zvyagin A. I., Chevychelova T. A., Chirkov K. S., Smirnov M. S., Ovchinnikov O. V. Size dependence of nonlinear optical properties of PbS QDs, passivated with thioglycolic acid. *Optik*. 2023;272: 170276. <https://doi.org/10.1016/j.ijleo.2022.170276>
15. Grevtseva I., Chevychelova T., Ovchinnikov O., ... Chirkov K. Size effect features and mechanism of luminescence of colloidal PbS quantum dots, passivated with thioglycolic acid. *Optical and Quantum Electronics*. 2023;55(5): 433. <https://doi.org/10.1007/s11082-023-04658-3>
16. Grevtseva I. G., Ovchinnikov O. V., Smirnov M. S., Chirkov K. S. Trap state and exciton luminescence of colloidal PbS quantum dots coated with thioglycolic acid molecules. *Condensed Matter and Interphases*. 25(2), 182–189. <https://doi.org/10.17308/kcmf.2023.25/11099>
17. Grevtseva I. G., Ovchinnikov O. V., Smirnov M. S., ... Vozgorkova. Photostability of luminescence of Ag<sub>2</sub>S quantum dots and Ag<sub>2</sub>S/SiO<sub>2</sub> core/shell structure. *Optics and Spectroscopy*. 2022;130(12): 1634–1644. <https://doi.org/10.21883/os.2022.12.54100.4106-22>
18. Smirnov M. S., Ovchinnikov O. V., Grevtseva I. G., Zvyagin A. I., Perepelitsa A. S., Ganeev R. A. Photoinduced degradation of the optical properties of colloidal Ag<sub>2</sub>S and CdS quantum dots passivated by thioglycolic acid. *Optics and Spectroscopy*. 2018;124(5): 681–686. <https://doi.org/10.1134/S0030400X18050211>
19. Ovchinnikov O. V., Grevtseva I. G., Smirnov M. S., ... Matsukovich A. S. Effect of thioglycolic acid molecules on luminescence properties of Ag<sub>2</sub>S quantum dots. *Optical and Quantum Electronics*. 2020;52(4): 198. <https://doi.org/10.1007/s11082-020-02314-8>
20. Ovchinnikov O. V., Grevtseva I. G., Smirnov M. S., Kondratenko T. S. Reverse photodegradation of infrared luminescence of colloidal Ag<sub>2</sub>S quantum dots. *Journal of Luminescence*. 2019;207: 626–632. <https://doi.org/10.1016/j.jlumin.2018.12.019>
21. Kondratenko T., Ovchinnikov O., Grevtseva I., ... Tatianina E. Thioglycolic acid FTIR spectra on Ag<sub>2</sub>S quantum dots interfaces. *Materials*. 2020;13(4): 909. <https://doi.org/10.3390/ma13040909>
22. Kloepfer J. A., Bradforth S. E., Nadeau J. L. Photophysical properties of biologically compatible CdSe quantum dot structures. *The Journal of Physical Chemistry B*. 2005;109(20): 9996–10003. <https://doi.org/10.1021/jp044581g>
23. Krivenkov V. A., Samokhvalov P. S., Linkov P. A., ... Nabiev I. Surface ligands affect photoinduced modulation of the quantum dots optical performance. *SPIE Proceedings*. 2014;9126: 91263. <https://doi.org/10.1117/12.2057828>
24. Hwang G. W., Kim D., Cordero J. M., ... Bawendi M. G. Identifying and eliminating emissive sub-bandgap states in thin films of PbS nanocrystals. *Advanced Materials*. 2015;27: 4481–4486. <https://doi.org/10.1002/adma.201501156>
25. Nelson C. A., Zhu X.-Y. Reversible surface electronic traps in PbS quantum dot solids induced by an order disorder phase transition in capping molecules. *Journal of the American Chemical Society*. 2012;134(18): 7592–7595. <https://doi.org/10.1021/ja3004649>

26. Scanlon W. W. Recent advances in the optical and electronic properties of PbS, PbSe, PbTe and their alloys. *Journal of Physics and Chemistry of Solids*. 1959;8: 423–428. [https://doi.org/10.1016/0022-3697\(59\)90379-8](https://doi.org/10.1016/0022-3697(59)90379-8)
27. Wang D., Qian J., Cai F., He S., Han S., Mu Y. 'Green'-synthesized near-infrared PbS quantum dots with silica-PEG dual-layer coating: ultrastable and biocompatible optical probes for in vivo animal imaging. *Nanotechnology*. 2012;23: 245701. <https://doi.org/10.1088/0957-4484/23/24/245701>
28. Zhang J., Jiang X. Confinement-dependent below-gap state in PbS quantum dot films probed by continuous-wave photoinduced absorption. *The Journal of Physical Chemistry B*. 2008;112:32: 9557–9560. <https://doi.org/10.1021/jp8047295>
29. Ushakova E. V., Litvin A. P., Parfenov P. S., ... Baranov A. V. Anomalous size-dependent decay of low-energy luminescence from PbS quantum dots in colloidal solution. *ACS Nano*. 2012;6(10): 8913–8921. <https://doi.org/10.1021/nn3029106>
30. Voznyy O., Levina L., Fan F., ... Sargent E. H. Origins of Stokes shift in PbS nanocrystals. *Nano Letters*. 2017;17(12): 7191–7195. <https://doi.org/10.1021/acs.nanolett.7b01843>
31. Lewis J. E., Jiang X. J. Unconventional gap state of trapped exciton in lead sulfide quantum dots. *Nanotechnology*. 2010;21: 455402. <https://doi.org/10.1088/0957-4484/21/45/455402>
32. Gaponenko M. S., Tolstik N. A., Lutich A. A., Onushchenko A. A., Yumashev K. V. Temperature-dependent photoluminescence Stokes shift in PbS quantum dots. *Physica E: Low-dimensional Systems and Nanostructures*. 2013;53: 63–65. <https://doi.org/10.1016/j.physe.2013.04.018>
33. Nakashima S., Hoshino A., Cai J., Mukai K. Thiol-stabilized PbS quantum dots with stable luminescence in the infrared spectral range. *Journal of Crystal Growth*. 2013;378: 542–545. <http://dx.doi.org/10.1016/j.jcrysgro.2012.11.024>
34. Moreels I., Lambert K., Smeets D., ... Hens Z. Size-dependent optical properties of colloidal PbS quantum dots. *ACS Nano*. 2009;3(10): 3023–3030. <https://doi.org/10.1021/nn900863a>
35. Giansante C., Infante I. Surface traps in colloidal quantum dots: A combined experimental and theoretical perspective. *The Journal of Physical Chemistry Letters*. 2017;8(20): 5209–5215 <https://doi.org/10.1021/acs.jpcclett.7b02193>
36. Ovchinnikov O. V., Perepelitsa A. S., Smirnov M. S., Aslanov S. V. Control the shallow trap states concentration during the formation of luminescent Ag<sub>2</sub>S and Ag<sub>2</sub>S/SiO<sub>2</sub> core/shell quantum dots. *Journal of Luminescence*. 2022;243: 118616. <https://doi.org/10.1016/j.jlumin.2021.118616>
37. Vasudevan D., Gaddam R. R., Trinchi A., Cole I. Core-shell quantum dots: Properties and applications. *Journal of Alloys and Compounds*. 2015;636(5): 395–404. <https://doi.org/10.1016/j.jallcom.2015.02.102>
38. Perepelitsa A. S., Ovchinnikov O. V., Smirnov M. S., ... Khokhlov V. Y. Structural and optical properties of Ag<sub>2</sub>S/SiO<sub>2</sub> core/shell quantum dots. *Journal of Luminescence*. 2021;231: 117805. <https://doi.org/10.1016/j.jlumin.2020.117805>
39. Mukai K., Okumura I., Nishizaki Y., Yamashita S., Niwa K. Silica coating of PbS quantum dots and their position control using a nanohole on Si substrate. *Japanese Journal of Applied Physics*. 2018;57: 04FH01. <https://doi.org/10.7567/JJAP.57.04FH01>
40. Capoen B., Martucci A., Turrell S., Bouazaoui M. Effects of the sol-gel solution host on the chemical and optical properties of PbS quantum dots. *Journal of Molecular Structure*. 2023;651–653: 467–473. [https://doi.org/10.1016/S0022-2860\(02\)00667-1](https://doi.org/10.1016/S0022-2860(02)00667-1)
41. Dhlamini M. S., Terblans J. J., Ntwaeaborwa O. M., Joubert H. D., Swart H. C. Preparations and luminescent properties of PbS nanoparticle phosphors incorporated in a SiO<sub>2</sub> matrix. *Physica Status Solidi C*. 2008;5(2): 598–601. <https://doi.org/10.1002/pssc.200776808>
42. Kedenburg S., Vieweg M., Gissibl T., Giessen H. Linear refractive index and absorption measurements of nonlinear optical liquids in the visible and near-infrared spectral region. *Optical Materials Express*. 2012;2(11): 1588–1611. <https://doi.org/10.1364/ome.2.001588>
43. van Leeuwen F. W. B., Cornelissen B., Caobelli F., ... de Jong M. Generation of fluorescently labeled tracers – which features influence the translational potential? *EJNMMI Radiopharmacy and Chemistry*. 2017;2(15). <https://doi.org/10.1186/s41181-017-0034-8>
44. Kozma I. Z., Krok P., Riedle E. Direct measurement of the group-velocity mismatch and derivation of the refractive-index dispersion for a variety of solvents in the ultraviolet. *Journal of the Optical Society of America B*. 2005;22(7): 1479–1485. <https://doi.org/10.1364/JOSAB.22.001479>
45. Sadovnikov S. I., Kozhevnikova N. S., Rempel A. A., Pushin V. G. Microstructure of nanocrystalline PbS powders and films. *Inorganic Materials*. 2012;48(1): 21–27. <https://doi.org/10.1134/S002016851201013X>
46. Music S., Filipovic-Vincekovic N., Sekovanic L. Precipitation of amorphous SiO<sub>2</sub> particles and their properties. *Brazilian Journal of Chemical Engineering*. 2011;28(1): 89–94. <https://doi.org/10.1590/S0104-66322011000100011>
47. Zhong Q., Cao M., Hu H., ... Zhang Q., One-pot synthesis of highly stable CsPbBr<sub>3</sub>@SiO<sub>2</sub> core-shell nanoparticles. *ACS Nano*. 2018;12(8): 8579–8587. <https://doi.org/10.1021/acs.nano.8b04209>

48. Li B., Fan H., Zhao Q., Wang C. Synthesis, characterization and cytotoxicity of novel multifunctional Fe<sub>3</sub>O<sub>4</sub>@SiO<sub>2</sub>@GdVO<sub>4</sub>:Dy<sup>3+</sup> core-shell nanocomposite as a drug carrier. *Materials*. 2016;9(3): 149. <https://doi.org/10.3390/ma9030149>

49. Gilmore R. H., Liu Y., Shcherbakov-Wu W., ... Tisdale W. A. Epitaxial dimers and auger-assisted detrapping in PbS quantum dot solids. *Matter*. 2019;1(1): 250–265. <https://doi.org/10.1016/j.matt.2019.05.015>

50. Sadovnikov S. I., Rempel A. A. Nonstoichiometric distribution of sulfur atoms in lead sulfide structure. *Doklady Physical Chemistry*. 2009;428(1): 167–171. <https://doi.org/10.1134/S0012501609090024>

51. Ovchinnikov O. V., Smirnov M. S., Korolev N. V., Golovinski P. A., Vitukhnovsky A. G. The size dependence recombination luminescence of hydrophilic colloidal CdS quantum dots in gelatin. *Journal of Luminescence*. 2016;179: 413–419. <https://doi.org/10.1016/j.jlumin.2016.07.016>

52. Wang Y., Suna A., Mahler W., Kasowski R. PbS in polymers. From molecules to bulk solids. *The Journal of Chemical Physics*. 1987;87: 7315–7322. <https://doi.org/10.1063/1.453325>

## Информация об авторах

*Irina G. Grevtseva*, Cand. Sci. (Phys.–Math.), Associate Professor, Department of Optics and Spectroscopy, Voronezh State University (Voronezh, Russian Federation).

<https://orcid.org/0000-0002-1964-1233>  
grevtseva\_ig@inbox.ru

*Mikhail S. Smirnov*, Dr. Sci. (Phys.–Math.), Professor, Department of Optics and Spectroscopy, Voronezh State University (Voronezh, Russian Federation).

<https://orcid.org/0000-0001-8765-0986>  
smirnov\_m\_s@mail.ru

*Kirill S. Chirkov*, post-graduate student, Department of Optics and Spectroscopy, Voronezh State University (Voronezh, Russian Federation).

<https://orcid.org/0000-0003-0387-0733>  
kirill200598@mail.ru

*Anatoly N. Latyshev*, Dr. Sci. (Phys.–Math.), Professor, Department of Optics and Spectroscopy, Voronezh State University (Voronezh, Russian Federation).

<https://orcid.org/0000-0002-7271-0795>  
latyshev@phys.vsu.ru

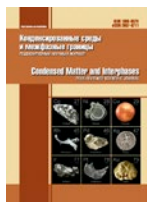
*Oleg V. Ovchinnikov*, Dr. Sci. (Phys.–Math.), Full Professor, Dean of the Faculty of Physics, Head of the Department of Optics and Spectroscopy, Voronezh State University (Voronezh, Russian Federation).

<https://orcid.org/0000-0001-6032-9295>  
ovchinnikov\_o\_v@rambler.ru

*Received 22.03.2023; approved after reviewing 23.05.2023; accepted for publication 15.06.2023; published online 25.03.2024.*

*Translated by Anastasiia Ananeva*





## Original articles

Research article

<https://doi.org/10.17308/kcmf.2024.26/11809>

## Isolation of partial coupled processes of anodic oxidation of OH<sup>-</sup> ion on gold using a combination of a graph-kinetic analysis method and linear voltammetry data

I. D. Zartsyn, A. V. Vvedenskii, E. V. Bobrinskaya , O. A. Kozaderov

Voronezh State University,  
1 Universitetskaya pl., Voronezh 394018, Russian Federation

**Abstract**

The presence of several interconnected electrochemical processes occurring on the surface of an electrode, strictly speaking, does not allow the use of the principle of independent reactions. Often, partial reactions of a complex multi-stage electrochemical process are coupled both through common intermediates and through the competitive adsorption of electroactive species. The presence of conjugation leads either to a change in the potential at which the corresponding electrochemical process becomes possible or to a change in the rate of partial processes. The latter is called kinetic coupling. This does not allow the simple calculation of the rate of each partial reaction as the difference between the current density of the target and background processes. The method of kinetic diagrams can be used to establish the kinetic patterns of such processes. This study shows that this method is applicable not only for the analysis of coupled electrochemical processes of various types, but can also be used in obtaining partial currents of the stages of a separate complex electrode reaction occurring in a background solution. As an example, options for the kinetic modelling of the total voltammogram of the anodic process on an Au electrode in an aqueous alkaline medium in the mode of linear potential change are considered.

The stationary degrees of covering of the gold surface with various surface-active forms of oxygen are calculated depending on the electrode potential. It was established that the change in concentration of OH<sup>-</sup> ions mainly affects the region of their adsorption potentials. A detailed analysis of stationary partial anodic processes in the Au|OH<sup>-</sup>, H<sub>2</sub>O system was carried out and the shape of the general stationary voltammogram was determined by calculation. The latter is in qualitative agreement with the experimental polarization dependence.


It was shown that the type of calculated polarization dependence is determined by the degree of reversibility of individual stages and the rate of their occurrence. The performed analysis is necessary not only for the detailed scheme of the background anodic reaction on gold in an alkaline solution, but also for the subsequent kinetic description of the electrooxidation process of organic substances on a gold electrode.

**Keywords:** Electrode processes, Conjugation, Graphic-kinetic analysis, Adsorption, Voltammetry

**Funding:** The study received financial support from the Ministry of Science and Higher Education of the Russian Federation within the framework of State Contract with universities regarding scientific research in 2022–2024, project No. FZGU-2022-0003.

**For citation:** Zartsyn I. D., Vvedenskii A. V., Bobrinskaya E. V., Kozaderov O. A. Isolation of partial coupled processes of anodic oxidation of OH<sup>-</sup> ion on gold using a combination of a graph-kinetic analysis method and linear voltammetry data. *Condensed Matter and Interphases*. 2024;26(1): 55–67. <https://doi.org/10.17308/kcmf.2024.26/11809>

**Для цитирования:** Зарцын И. Д., Введенский А. В., Бобринская Е. В., Козадеков О. А. Выделение парциальных сопряженных процессов анодного окисления OH-аниона на золоте сочетанием метода графо-кинетического анализа и данных линейной вольтамперометрии. *Конденсированные среды и межфазные границы*. 2024;26(1): 55–67. <https://doi.org/10.17308/kcmf.2024.26/11809>

 Elena V. Bobrinskaya, e-mail: [elena173.68@mail.ru](mailto:elena173.68@mail.ru)

© Zartsyn I. D., Vvedenskii A. V., Bobrinskaya E. V., Kozaderov O. A., 2024



The content is available under Creative Commons Attribution 4.0 License.

## 1. Introduction

When several multi-stage reactions simultaneously occur on the electrode surface, in the same potential region and at comparable rates, then the partial reactions are not independent. Usually they are interconnected (coupled) not only via common intermediates, but also due to the competition of different electroactive particles for adsorption centres.

The presence of conjugation provides the possibility of transferring the free energy of the electrode system between partial reactions, due to which some of them acquire the ability to take place at potentials more negative than the corresponding equilibrium potentials - thermodynamic coupling [1]. More often, however, only the rate of each of the partial processes changes accordingly, there is kinetic coupling [2,3].

The problem of coupled reactions is primarily associated with the problem of finding real partial rates, and therefore with establishing kinetics. Indeed, in the simplest case, only two interconnected processes occur on the electrode, target (1) and background (2), both in a non-diffusion mode. If  $i_1$  and  $i_2$  are the partial rates of each process, i.e., rates obtained taking into account coupling effects, then  $i = i_1 + i_2$ . Here  $i$  is the current measured in the external polarization circuit; the nature of its change over time is not important for subsequent consideration.

Often  $i_2^{\text{background}}$  is used as  $i_2$ , this is the current determined in the same potential region, but in the background electrolyte instead of the working one, containing an electrochemically active reagent. However, due to coupling  $i_2 \neq i_2^{\text{background}}$ , and therefore the  $i$  values often are determined with a noticeable error.

A typical example is the processes of anodic oxidation of organic substances on metal electrodes, which are also capable of anodic oxidation during polarization. Often, the areas of adsorption potential and electrochemical activity of organic substances and the metal substrate overlap, which predetermines the potential for the mutual influence of partial electrode processes [4–7]. In this situation, the graph-kinetic analysis method [8–11], where a multi-stage chemical process is represented as a set of interconnected cycles (graphs), is very useful. Due to the absence

of any significant internal limitations, the method is also applicable to electrochemical reactions occurring simultaneously on the electrode.

Such an analysis plays a special role in the study of complex electrochemical processes on metals and alloys in the presence of surfactants of various nature. Knowledge of the conjugation features of partial electrode processes in such systems makes it possible not only to theoretically describe the processes involving electrolyte solution components, but also to reasonably formulate technological principles for the production of electrochemical transformation products (including anodic oxidation of organic additives and cathodic deposition of metals and alloys) with specified properties and composition.

It is possible to obtain true partial currents by calculation by sequentially considering alternative kinetic situations that differ in the nature of the intermediates, the assumption about the nature of the limiting stage, or taking into account the presence of several stages with comparable rates and the sum of partial currents will provide the total  $i, E$ -dependence. This dependence is compared with an experimental voltammogram (VAG), allowing not only to estimate the complex of equilibrium and kinetic characteristics of individual stages, but also to draw a conclusion about the putative reaction scheme. It should be remembered that the graphic-kinetic analysis can also be used when interpreting the results of studies of individual electrode reactions.

Such reactions, usually, are complex and include the stages of adsorption, charge transfer, heterogeneous chemical transformations of intermediates, etc. In accordance with the assumed kinetic scheme of the general electrode process, its elementary stages successively replace each other as the potential changes.

On the other hand, an individual multi-stage electrode reaction can be interpreted only formally, as a set of “parallel” ongoing elementary processes, each of which corresponds to a separate stage, but is implemented over the entire range of potentials. The fact that in a certain range of potential values ( $E$ ) the rates of elementary processes, conventionally considered as partial, are practically equal to zero, is not important

for this approach. It is much more important that it becomes possible to identify the partial currents of individual stages, summarize them, and compare the result with experiment, which usually underlies the refinement of the general reaction scheme and the identification of the kinetic features of a complex reaction.

Finally, it should be noted, that graph-kinetic analysis initially assumes a stationary course of a complex reaction, which is usually characteristic of homogeneous chemical processes. However, heterogeneous electrode reactions, in particular reactions studied by linear voltammetry, when the potential changes at a rate of  $v = \frac{dE}{dt}$ , are usually non-stationary.

The subject of this study is the electrode process occurring over a wide range of anodic potentials on a polycrystalline Au electrode in a deaerated aqueous alkaline solution. The main objectives of the study were:

- by calculation, using the method of graphic-kinetic modelling, determine the stationary covering degrees of the gold surface with the starting substance, intermediates and products of the anodic oxidation reaction of OH ions in an alkaline medium;
- calculate stationary partials, as well as the total anode current of this process;
- compare calculated and experimental values of a number of basic kinetic parameters of the anodic overall reaction in the Au|OH<sup>-</sup>,H<sub>2</sub>O system;
- evaluate the correctness of the procedure for comparing the full calculated with the

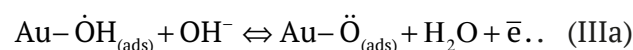
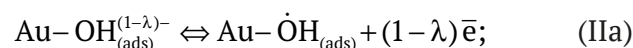
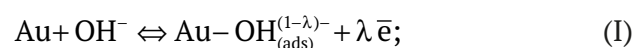
experimental voltammogram taken at a finite rate of potential change  $v = \frac{dE}{dt}$ .

## 2. Calculation procedure

### 2.1. Selection of reaction scheme

According to data [7], on the anodic branch of the cyclic  $i, E$ -dependence obtained in the Au|OH<sup>-</sup>,H<sub>2</sub>O system four main current maxima can be distinguished – A1, A2, A3, and A4 (Fig. 1.). Since the regularities of cathodic processes are not considered in this study, the region of cathodic currents is not presented; potentials are given relative to SHE.

At higher  $v$  the amplitude of all current peaks increases, the potentials of the A1 and A2 maxima do not change, and the A3-A4 maxima shift to the region of more positive values. This finding, like other data [12–20], indicates a multi-stage anodic process in the Au|OH<sup>-</sup>,H<sub>2</sub>O system. The latter proceeds via the chemisorption stage of the hydroxide anion, most likely with partial charge transfer, and is accompanied by the sequential formation of mono- and biradical forms of adsorbed atomic oxygen. A possible reaction scheme in the simplified form is:



Here  $\lambda$  - degree of partial charge transfer from an adsorbed particle with a charge  $z = 1$  per metal; eventually  $z_{\text{ads}} = 1 - \lambda$  [21]. It is assumed

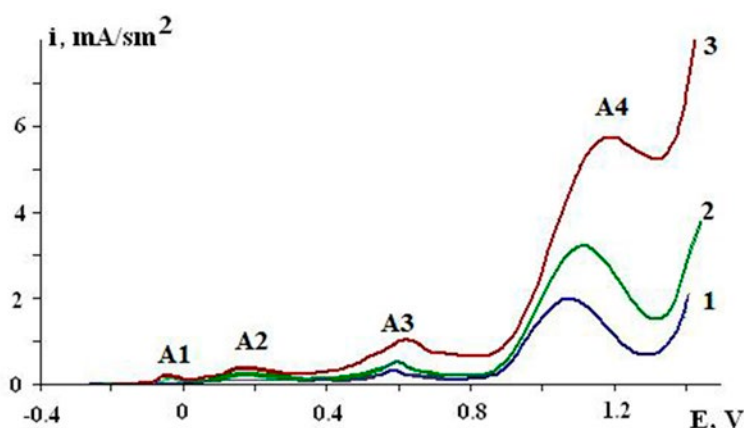
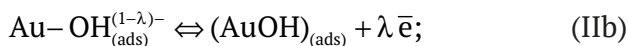


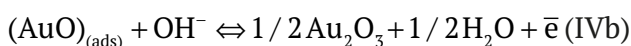
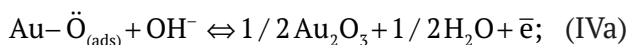
**Fig. 1.** Anode voltammograms experimentally obtained on a smooth gold electrode in 0.1 M NaOH solution at  $v = 0.04$  (1); 0.1 (2) и 0.6 (3) V/sec [7]



[22–24] that the radical ion state is stabilized due to the overlap of 6s- and  $sp^3$ - AO for Au and OH<sup>-</sup>, respectively. As an alternative, the appearance of 2D Au(I) and Au(II) compounds on the surface is possible in such processes as:



The formation of phase Au(III) oxide at sufficiently high potentials is the result of a series of sequential electrochemical, chemical, and crystallization stages. In overall form, the corresponding reaction can be represented as a process involving  $\text{Au-}\ddot{\text{O}}_{(\text{ads})}$  or  $(\text{AuO})_{\text{ads}}$ :



The formation of metastable phases, Au(OH) or  $\gamma$ -AuOOH, with subsequent dehydration, cannot be excluded; these issues are considered in more detail in [30].

The choice between alternative routes for anodic formation of  $\text{Au}_2\text{O}_3$  via (IIa), (IIIa), and (IVa), or (IIb), (IIIb), and (IVb) stages, must be based on information about the physical nature of the intermediates, which is usually missing. Thus, the question about the nature of the electron density redistribution in the  $\text{Au}|\text{OH}^-, \text{H}_2\text{O}$  system remains open: its “flow” from the oxygen of the hydroxide ion to the metal, stages (IIa) and (IIIa), or back from the metal to oxygen, stages (IIb) and (IIIb). The results of quantum chemical modelling [23], however, are in favour of the first scenario. Therefore, this scenario was used later on, during the stage of constructing graphs for the intermediates of heterogeneous processes of OH<sup>-</sup> oxidation in the aquatic environment  $\dot{\text{O}}\text{H}$  and  $\ddot{\text{O}}$ .

The potential range of anodic release of molecular oxygen, which further complicates oxide formation on gold in an alkaline medium, was not considered in the study.

## 2.2. Initial kinetic ratios

Let us assume that the surface of gold initially contains only one type of active adsorption centres. The number of these centres is  $G$ , expressed in mol/cm<sup>2</sup>, it is not only constant, but also significantly less than the number of metal atoms. The latter allows ignoring, albeit to a first

approximation, the effects of lateral interactions between adsorbate particles, and therefore to use the Langmuir isotherm model in the analysis.

Let  $G_i$  and  $G_j$  be the number of active surface centres, expressed in mol/cm<sup>2</sup> occupied by particles of  $i$ -th and  $j$ -th types, and  $G$  is the total surface concentration of such centres, respectively. The change in the state of the active site during  $i \rightarrow j$  process may be associated not only with the oxidation/reduction of particles, but also with their adsorption/desorption. Each of these processes is interpreted as a kinetically reversible first-order reaction, the rate of which is:

$$v_{ij} = k_{ij}\Gamma_i - k_{ji}\Gamma_j = \Gamma(k_{ij}\Theta_i - k_{ji}\Theta_j). \quad (1)$$

Here  $k_{ij}$  and  $k_{ji}$  are the formal rate constants, s<sup>-1</sup>,  $\Theta_i$  and  $\Theta_j$  are the proportion of surface adsorption centres occupied by reagents and products, respectively. We believe that there are no diffusion limitations for all types of particles; features of the structure of the electrical double layer and their influence on  $k_{ij}$  and  $k_{ji}$ , are not explicitly taken into account.

The current covering of adsorption centres is assumed to be stationary. In this approximation

$$\sum_i k_{ij}\Theta_i = \sum_j k_{ji}\Theta_j, \quad (2)$$

actually representing the so-called stationary kinetic adsorption isotherm, and

$$\sum_i \Theta_i + \sum_j \Theta_j = 1. \quad (3)$$

Since in this case  $k_{ij} = k_{ij}^0 c_i^v$ ,  $k_{ji} = k_{ji}^0 c_j^v$ , then the concentration constant of adsorption equilibrium  $K_{ij} = k_{ij} / k_{ji} = K_{ij}^0 (c_i^v / c_j^v)$ .  $K_{ij}^0 = k_{ij}^0 / k_{ji}^0$  is the standard equilibrium constant, and  $c^v$  is the volumetric molar concentration, expressed in mol/cm<sup>3</sup>.

Taking into account the possibility of partial charge transfer, the rate constants of adsorption stages involving singly charged anions are:

$$k_{ij} = k_{ij}^0 (E^0) c_i^v \exp[\lambda \beta F (E - E^0) / RT]; \quad (4a)$$

$$k_{ji} = k_{ji}^0 (E^0) c_j^v \exp[-\lambda \alpha F (E - E^0) / RT], \quad (4b)$$

whereas for electrochemical stages:

$$k_{ij} = k_{ij}^0 (E^0) c_i^v \exp[(1 - \lambda) \beta F (E - E^0) / RT]; \quad (5a)$$

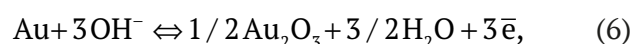
$$k_{ji} = k_{ji}^0 (E^0) c_j^v \exp[-(1 - \lambda) \alpha F (E - E^0) / RT]. \quad (5b)$$

Here  $E$  and  $E^0$  are the current and standard electrode potentials for a given reaction;  $a$  and  $b$  cathode and anodic charge transfer coefficients, respectively; everywhere further  $a = b = 0.5$ . If the adsorption of a charged particle is not accompanied by a redistribution of electron density, and therefore  $\lambda = 0$ , then the influence of  $E$  on the rate constants of adsorption processes in equations (4a) and (4b) disappears, and formulas (5a) and (5b) take their usual form. It is obvious that in the general case the values of  $K_{ij}$ ,  $K_{ji}$  also depend on the potential, although to varying degrees.

### 3. Analysis of kinetic diagrams

#### 3.3. Stationary reaction mode

According to the analysis technique proposed in [8–11] and detailed for electrode reactions in [2, 3], a kinetic diagram of the anodic process on the Au electrode in a background alkaline electrolyte was constructed (Fig. 2). The active centre of the gold surface, initially occupied by a water molecule was taken as the initial state (1); the vertices of the graph (2), (3), (4), and (5) correspond to the sequential formation  $\text{Au}-\text{OH}_{\text{ads}}^-$ ,  $\text{Au}-\dot{\text{O}}_{\text{ads}}$ ,  $\text{Au}-\ddot{\text{O}}_{\text{ads}}$ . Each of these processes, previously presented as (I), (IIa), (IIIa), and (IVa), has a corresponding graph edge. The covering of the surface with a certain adsorbate is, respectively,  $\Theta_1$ ,  $\Theta_2$ ,  $\Theta_3$ ,  $\Theta_4$ , and  $\Theta_5$ ; traversing the loop counterclockwise is considered positive. Kinetically reversible overall reaction:



representing the sum of stages (I), (IIa), (IIIa), and (IVa), proceeds at the rate:

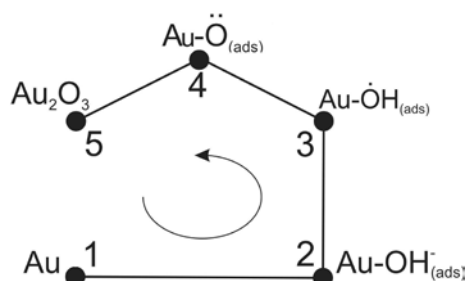


Fig. 2. Kinetic diagram of adsorption and electrochemical processes occurring on an Au electrode in an alkaline medium in the region of potentials preceding the anodic release of molecular oxygen

$$i_{15} = 3F(k_{15}\Theta_1 - k_{51}\Theta_5). \quad (7)$$

A detailed mathematical justification for the method of graph-kinetic analysis is described in detail in [34] and is not given within the framework of this study.

During the first stage, stationary degrees of surface covering with adsorbate particles were determined:

$$\Theta_1 = \frac{1}{1 + K_{12} + K_{12}K_{23} + K_{12}K_{23}K_{34} + K_{12}K_{23}K_{34}K_{45}}; \quad (8)$$

$$\Theta_2 = \frac{1}{1 + K_{21} + K_{23} + K_{23}K_{34} + K_{23}K_{34}K_{45}}; \quad (9)$$

$$\Theta_3 = \frac{1}{1 + K_{21}K_{32} + K_{32} + K_{34} + K_{34}K_{45}}; \quad (10)$$

$$\Theta_4 = \frac{1}{1 + K_{21}K_{32}K_{43} + K_{32}K_{43} + K_{43} + K_{45}}; \quad (11)$$

$$\Theta_5 = \frac{1}{1 + K_{21}K_{32}K_{43}K_{54} + K_{32}K_{43}K_{54} + K_{43}K_{54}}. \quad (12)$$

It is important that the meaning of the denominator in equations (8)–(12) is the same: each of them contains the concentration equilibrium constants of the transition processes from a given  $i$ -th state into all other states. The equilibrium constant values required for the calculation were determined by a brute-force search method.

It was found that the surface coverage of each of the adsorbed forms of oxygen, as expected, significantly depends on the electrode potential (Fig. 3a). It is very important that different potential regions can correspond to the presence of either one or the coexistence of several adsorbed forms. Thus, up to the values of  $E \leq 0.3$  V the surface is covered only with adsorbed OH<sup>-</sup> ions. With a further increase in the potential the surface coverage with the second adsorbed form also becomes non-zero, namely,  $\dot{\text{O}}$ , and at  $E \approx 0.7$  V, the degree of covering with this particle reaches unity. The subsequent increase in  $E$  leads to the appearance of biradicals  $\ddot{\text{O}}$  on the gold surface, the covering with which is very small and, moreover, noticeably decreases with increasing electrode

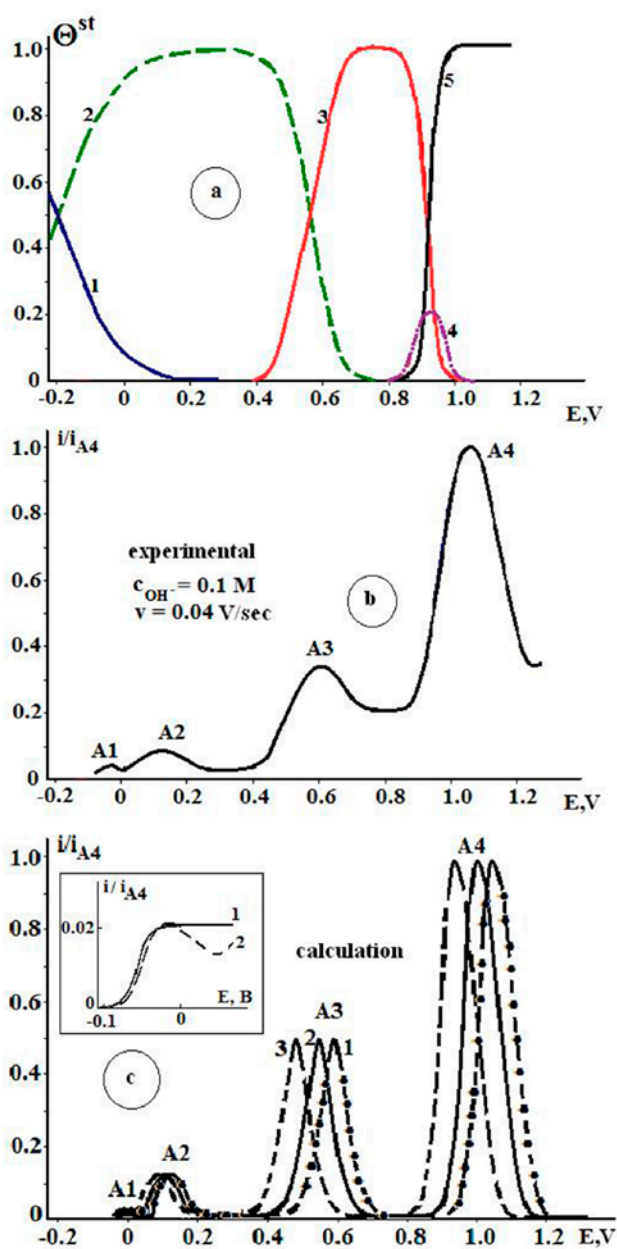


**Fig. 3.** a) The dependence of the stationary degrees of covering of the gold surface with various adsorbed forms and oxygen compounds at  $\text{SN}^- = 0.1 \text{ M}$ : (1) – the initial surface, (2) –  $\text{OH}^-$ , (3) –  $\text{OH}^\cdot$ , (4) –  $\ddot{\text{O}}$ , (5) –  $\text{Au}_2\text{O}_3$ ; b) Experimental voltammogram, obtained in the  $\text{Au}|\text{OH}^-, \text{H}_2\text{O}$  [7] system and normalized to the maximum current A4; c) Calculated voltammograms normalized to the maximum current A4, with an alkali concentration equal to (1) – 0.1; (2) – 0.5 and (3) – 0.7 M. Inset: Area of the potential of maximum A1 without taking into account partial charge transfer during adsorption of hydroxide ion (1), as well as taking into account this process (2)

potential and the accumulation of  $\text{Au}_2\text{O}_3$  occurs. An increase in the concentration of an alkaline solution from 0.1 M to 1.0 M manifests only as a slight expansion of the range of adsorption potentials of hydroxyl ions (not reflected in Fig. 3a), but practically does not affect the degree of surface covering with other adsorbed forms of oxygen.

The comparison of the potential regions of the maxima observed on the anodic branch of the experimental voltammogram, normalized to the current in the A4 maximum (Fig. 3b) with the corresponding regions of existence of various adsorbed forms of oxygen indicates that:

- A1 and A2 maxima characterize the process of adsorption of  $\text{H}_2\text{O}$  and  $\text{OH}^-$  ions respectively;
- in the region of A3 maximum, adsorbed  $\text{OH}^-$  ions and monoradicals  $\text{OH}^\cdot$  are present on the Au surface, and the anodic maximum corresponds to an almost equal covering of the electrode with each particle;
- potential region A4 corresponds to the coexistence of three adsorbed particles at once, and the maximum corresponds to the almost complete covering of the surface with gold oxide.

At the second stage of the analysis of the stationary anodic process in the  $\text{Au}|\text{OH}^-, \text{H}_2\text{O}$  system, the rate  $v_i$  of each partial reaction and, accordingly, the corresponding partial current, were determined using the expression:

$$i_i = z_i F \Gamma v_i = z_i F \Gamma v \frac{d\Theta^{st}}{dE}, \quad (13)$$

Here it is taken into account that  $dE = v dt$ , and for a heterogeneous reaction of the first order  $v_i = d\Theta_i/dt$ . we assumed that as the potential changes, the covering of the surface with each particle of  $i$ -th grade stabilizes very quickly, i.e., the rate of potential scanning is significantly less than the speed of achieving stationary covering with adsorbate.

Expressions for partial currents were obtained by differentiating relations (8)–(12) with respect to potential, and then expressions for partial currents were found, using (4a)÷(5b). Their summation provides the desired  $i, E$ -dependence, which is quite cumbersome. For example, just one expression for  $d\Theta_2^{st} / dE$ , is this:



$$\frac{d\Theta_2^{st}}{dE} = \frac{F}{RT} \left[ \frac{K_{21}^0 c_{OH^-}^{-1} \lambda \exp\left(-\frac{\lambda FE}{RT}\right) - K_{23}^0 \exp\left(\frac{FE}{RT}\right) - 2K_{23}^0 K_{34}^0 c_{OH^-} \exp\left(\frac{2FE}{RT}\right) - 3K_{23}^0 K_{34}^0 K_{45}^0 c_{OH^-}^2 \exp\left(\frac{3FE}{RT}\right)}{\left(1 + K_{21}^0 c_{OH^-}^{-1} \exp\left(-\frac{\lambda FE}{RT}\right) + K_{23}^0 \exp\left(\frac{FE}{RT}\right) + K_{23}^0 K_{34}^0 c_{OH^-} \exp\left(\frac{2FE}{RT}\right) + K_{23}^0 K_{34}^0 K_{45}^0 c_{OH^-}^2 \exp\left(\frac{3FE}{RT}\right)\right)^2} \right] \quad (14)$$

Nevertheless, it has been established that the full calculated VAG also contains four characteristic current maxima. Unfortunately, direct comparison of calculated and experimental  $i, E$ -dependencies is impossible, since the  $G_i$  value used in the calculations a priori unknown. Therefore, the calculated VAG were subjected to comparative analysis, which, like the experimental ones, were normalized to the current at the A4 maximum; the corresponding data are presented in Fig. 3c.

It is important that the maximum A1 in the calculated voltammogram can still be obtained, but only under the assumption of partial charge transfer in process (I), i.e., assuming  $\lambda \neq 0$ . Otherwise, in this region of potentials at  $(i/i_0), E$  the dependence a horizontal plateau appears (inset to Fig. 3c), which contradicts the experimental data.

At the same time, the number and position of current maxima in the calculated and experimental voltammograms coincide. Moreover, the nature of the influence of the concentration of the alkaline solution on the position of the anodic current maxima turned out to be similar for the calculated and experimentally obtained  $i, E$ -dependencies (Table 1).

Thus, the position of A1 and A2 peaks do not change with increasing  $c_{OH^-}$  (Fig. 3c, Table 1), the potentials of A3 and A4 peaks somewhat reduce, and the value of the parameter  $dE_a^m/d \lg c_{OH^-}$ , obtained from the calculated VAG, practically coincide with

the experimental value. Some differences in the shape of the experimental and calculated VAG during the transition from A3 to A4 peak are due to the fact that the calculated voltammogram was obtained under the assumption of an equilibrium distribution of adsorbed particles, which is hardly true under real conditions.

Based on the condition of matching the position of each of the calculated and experimental anodic maxima, the values of the standard equilibrium constants of individual stages were determined and presented in Table 2.

During the third stage of comparing the calculated and experimental data, the concentration of surface adsorption centres was already specified. Moreover, the  $\Gamma$  value was chosen in such a way that the amplitudes of the experimental and calculated VAG at the corresponding potential scanning rate coincided.

It has been established that the nature of the change in the amplitude of the anodic maxima on the experimental and calculated VAG with increasing  $v$ , up to  $v = 1.0$  V/s, is almost the same. Thus, the amplitudes of all anodic maxima change linearly with increasing potential scanning speed (Fig. 4), and the slopes of the corresponding experimental  $\lg i, \lg v$ , the dependences not only practically coincide for the A1-A3 maxima, but are also close to unity (Table 3).

However, for the A4 maximum the pattern is more complicated: the experimental value of

**Table 1.** Values of the slopes of the dependence of the potential of the maxima on the concentration of OH<sup>-</sup> ions: experimental (numerator) and calculated (denominator) value ( $v = 0.04$  V/sec)

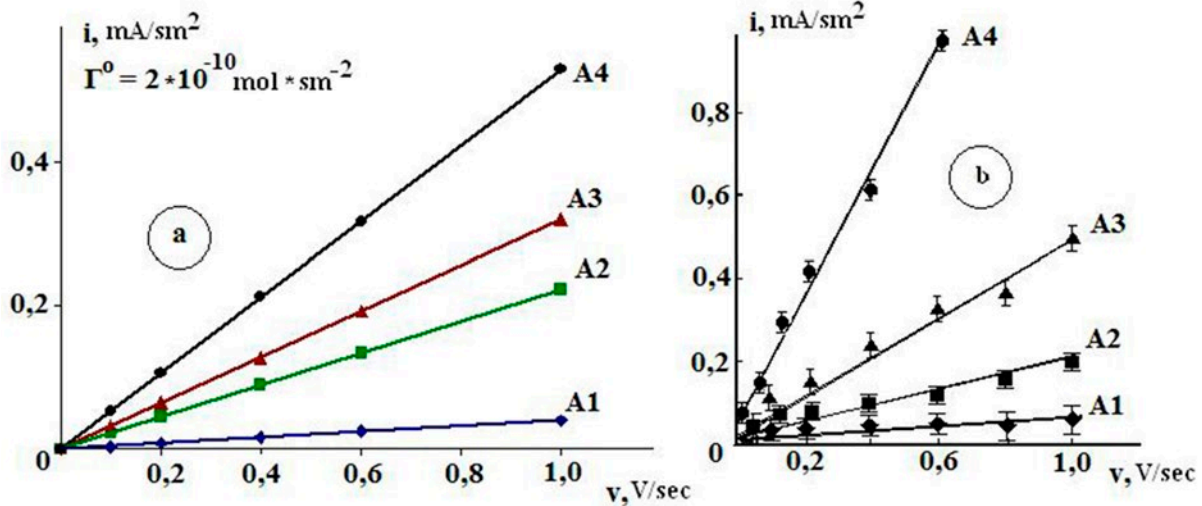
Parameter	A1	A2	A3	A4
Maximum				
$\frac{dE_a^m}{d \lg c_{OH^-}}, B$	$\frac{0}{0}$	$\frac{0}{0}$	$\frac{-0.043 \pm 0.004}{-0.045}$	$\frac{-0.062 \pm 0.005}{-0.075}$

**Table 2.** Concentration equilibrium constants of partial reactions occurring in the Au|OH<sup>-</sup>, H<sub>2</sub>O system and presented in Fig. 2

Constant	Edge of the graph			
	(1↔2)	(2↔3)	(3↔4)	(4↔5)
$K_{ij}^0$	$1.5 \cdot 10^4$	$8.0 \cdot 10^{-11}$	$2.5 \cdot 10^{-13}$	$7.0 \cdot 10^{-13}$

**Table 3.** Values of the slope of the current in the maximum – scanning speed dependence of the in 0.1 M NaOH solution: experimental (numerator) and calculated (denominator)

Parameter \ Maximum	A1	A2	A3	A4
$\frac{d \lg i_a^m}{d \lg v}$	$\frac{0,87 \pm 0,08}{1.00}$	$\frac{0,83 \pm 0,08}{1.00}$	$\frac{0,85 \pm 0,08}{1.00}$	$\frac{0,62 \pm 0,06}{1.00}$


**Fig. 4.** Dependences of the current in the maximum of the voltammogram on the scanning speed of the potential: calculated (a) and experimental (b) [7] data

the parameter  $\frac{d \lg i_a^m}{d \lg v}$  rather closer to 0.5, while

the calculated value, as for the others, is equal to unity. In our opinion, this discrepancy is due to the fact that the calculation takes into account the presence of only adsorbed Au<sub>2</sub>O<sub>3</sub> oxide, whereas under the experimental conditions in the region of A4 maximum, a phase layer of Au(III) oxide is also most likely present on the surface [7; 12; 15; 31–32].

### 3.2. Unsteady reaction mode

Previously, it was experimentally established [7] that the potentials of the first two maxima, namely A1 and A2, are practically invariant to changes in the potential scanning rate up to  $v > 8$  V/s, while the potentials of A3 and A4 peaks significantly improve with increasing  $v$  [7]. Naturally, the assumption used above about the stationarity of processes, primarily adsorption, occurring in the Au|OH<sup>-</sup>, H<sub>2</sub>O system excludes the possibility of considering the influence of  $v$  to the position of current maximums. Therefore, a complete equation for a nonstationary anodic voltammogram, including the potential regions of all current maxima should be obtained.

However, solving this general problem is extremely difficult. Therefore, at first we will assume that heterogeneous adsorption processes occurring at the potentials of A1 and A2 peaks are quasi-stationary, while only processes in the region of potentials of A3 and A4 peaks are non-stationary.

A detailed procedure for taking into account nonstationarity effects using the graph method is presented in [33]. The kinetic diagram of a non-stationary process, taking into account the assumptions made, has a form similar to the stationary diagram (Fig. 2), but with additional branches (Fig. 5). Here  $l$  is a complex

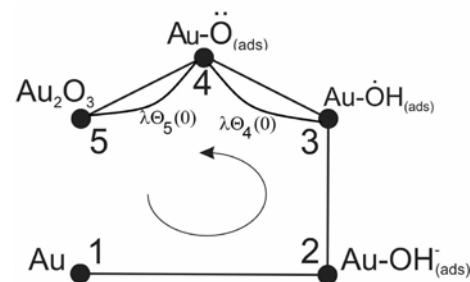

**Fig. 5.** Kinetic diagram of adsorption and electrochemical processes occurring on an Au electrode in an alkaline medium, taking into account the unsteadiness of processes in the potential range A3–A4

image of time. In this case, the rate constant of any non-stationary stage  $k_{ij}^*$  would be:  $k_{ij}^* = k_{ij} + \lambda\Theta_j(0)$ , and for the solution the Laplace–Carson transformation should be used [4, 34–35] under the assumption of a non-zero initial concentration of intermediate particles.

For further facilitation of the procedure of graphic-kinetic analysis, we will limit ourselves to considering only part of the general diagram presented in Fig. 2, assuming that adsorbed OH<sup>-</sup> ions are initially present on the Au surface. Obviously, that in this case the region of their adsorption potentials falls out of consideration. Nevertheless, even within the framework of this simplification the situation remains very complicated, since the overall transformation process Au–OH<sub>ads</sub><sup>-</sup> in Au<sub>2</sub>O<sub>3(ads)</sub> is a multi-stage process. Which of these elementary stages, or their combination, is slow and therefore determining the rate is not known a priori. Possible options are presented in Table 1. In addition to the anodic transformations of OH<sup>-</sup> on gold with one limiting stage, situations with several rate-determining reactions are also considered here.

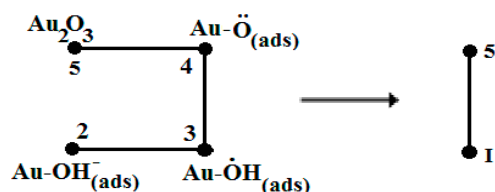
As an example, in this study we will limit ourselves to considering two kinetic scenarios from Table 4 – (a) and (b); both with a single rate-limiting stage.

**Table 4.** Alternative kinetic scenarios corresponding to the gross process of anodic transformation in the Au/OH<sup>-</sup>, H<sub>2</sub>O system

Process scenario	Transformation scheme
(a)	(2) → (3) = (4) = (5)
(b)	(2) = (3) → (4) = (5)
(c)	(2) = (3) = (4) → (5)
(d)	(2) → (3) = (4) → (5)
(e)	(2) = (3) → (4) → (5)
(f)	(2) → (3) → (4) = (5)
(g)	(2) → (3) → (4) → (5)

#### Kinetic scenario (a)

We will use the graph technique and combine the elementary states (2), (3), and (4) into a formally initial state (I), which does not have a clear physical interpretation:



Now, to obtain the final equation of the voltammogram, it is enough to solve the differential equation of the following form:

$$\frac{d\Theta_I}{dt} = -k_{I5}\Theta_I + k_{5I}\Theta_5, \quad (15)$$

taking into account that  $\Theta_I + \Theta_5 = 1$ . Final expressions for  $\Theta_I$  and  $\Theta_4$  have the form of:

$$\begin{aligned} \Theta_I(t) &= \Theta_I(0)\exp(-t(k_{I5} + k_{5I})) + \\ &+ \frac{k_{5I}}{k_{I5} + k_{5I}}(1 - \exp(-t(k_{I5} + k_{5I}))); \\ \Theta_5(t) &= 1 - \Theta_I(t). \end{aligned} \quad (16)$$

Taking into account that between the rate constants  $k_{23}$ ,  $k_{34}$ ,  $k_{32}$ ,  $k_{43}$ , and  $k_{15}$ , as well as between degrees of surface covering  $\Theta_2$ ,  $\Theta_3$ ,  $\Theta_4$  there is a relationship, we obtain expressions for the corresponding partial degrees of covering:

$$\begin{aligned} \Theta_2(t) &= \Theta_I(t)(1 + K_{23} + K_{23}K_{34})^{-1} = \Theta_I(t)\beta_2; \\ \Theta_3(t) &= \Theta_I(t)(1 + K_{32} + K_{34})^{-1} = \Theta_I(t)\beta_3; \\ \Theta_4(t) &= \Theta_I(t)(1 + K_{43} + K_{43}K_{32})^{-1} = \Theta_I(t)\beta_4. \end{aligned} \quad (17)$$

It should be noted that the coefficients  $\beta_i$ , appearing in (17), clearly do not depend on time. Nevertheless, such a dependence is still implicitly present, since in the potentiodynamic polarization regime  $\beta_i$  depends on  $E$ , and the potential varies linearly with time.

Let us differentiate expressions (17), i.e., find  $\frac{d\Theta_i}{dt} = \frac{d(\Theta_i\beta_i)}{dt} = \beta_i \frac{d\Theta_i}{dt} + \Theta_i \frac{d\beta_i}{dt}$ , where  $i = 2, 3, 4$ .

Since  $\frac{d\beta_i}{dt} = \left(\frac{\partial\beta_i}{\partial E}\right)\left(\frac{\partial E}{\partial t}\right)$ , for current densities, we

obtain expressions for the rates of partial anodic processes, and by summing them we would obtain a complete voltammogram (Fig. 6). Quite notably, that the use of this rather simplified, scheme allows us to obtain the  $i, E$ -dependence in which the rate of the anodic process between the second and third maxima no longer decreases to zero, as was previously (Fig. 3c), however, between the A3 and A4 maxima, the anodic current density in this case is zero, which contradicts the experiment. The position of the A2 maximum, as calculations show, does not depend on the potential scanning speed and alkali concentration, but the potentials of the A3 and A4 peaks with an increasing



$c_{\text{OH}^-}$  shift to the more negative values (Fig. 6b), whereas with increasing  $v$ , the potentials noticeably improve.

#### Kinetic scenario (b)

Let us assume that an equilibrium distribution is established between states 1 and 2, as well as 3 and 4, while there is no equilibrium between states 2 and 3. Let us again combine the elementary states and the process diagram as follows:

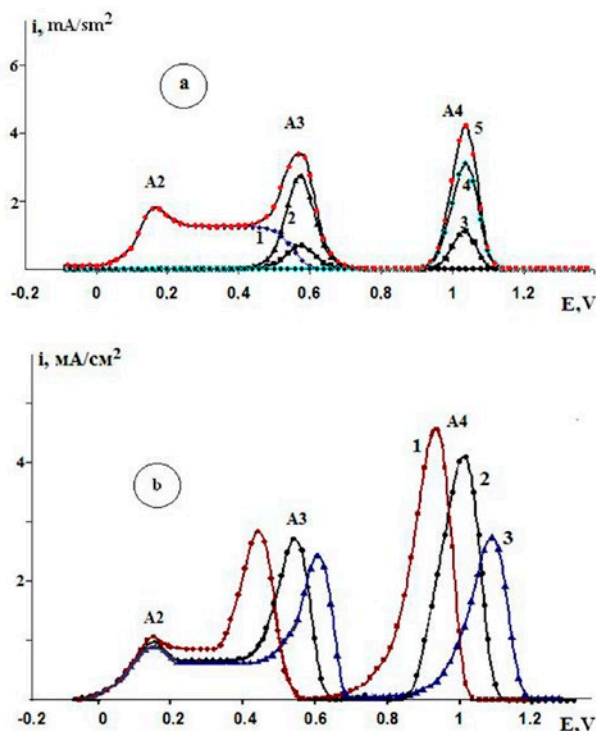
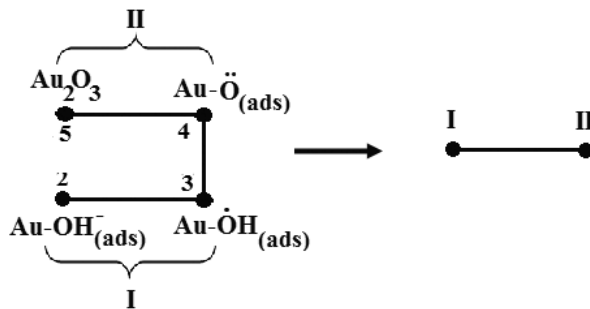


**Fig. 6.** (a) - Calculated velocities of partial anode processes  $i_1$  (1),  $i_2$  (2)  $i_3$  (3)  $i_4$  (4) and a voltammogram (5) obtained under the assumption that  $c_{\text{OH}^-} = 0.1 \text{ M}$  and scanning rate of potential 0.6 V/sec; (b) - calculated voltammograms obtained in the Au|OH<sup>-</sup>, H<sub>2</sub>O system at an alkali concentration 1.0 (1); 0.1 (2) 0.01 M (3) and  $v = 0.6 \text{ V}/\text{sec}$

Solving equations similar to (15) and carrying out the corresponding transformations, we again obtain the calculated  $i, E$ -dependencies (Fig. 7).

It appeared that such a process scheme already allows to obtain a non-zero current between the A3 and A4 maxima, but only when  $v \geq 0.60 \text{ V}/\text{s}$ , although the current density values in this potential region are still much lower than those experimentally observed. The influence of  $v$  on the position of the A3 and A4 peaks is reflected correctly by the calculation. However, when  $v \leq 0.4 \text{ V}/\text{s}$ , the A3 maximum practically disappears, and this, in principle, contradicts the experimental results [7].

#### 4. Conclusions

The method of kinetic diagrams allows performing a fairly detailed analysis of stationary partial anodic processes in the Au|OH<sup>-</sup>, H<sub>2</sub>O

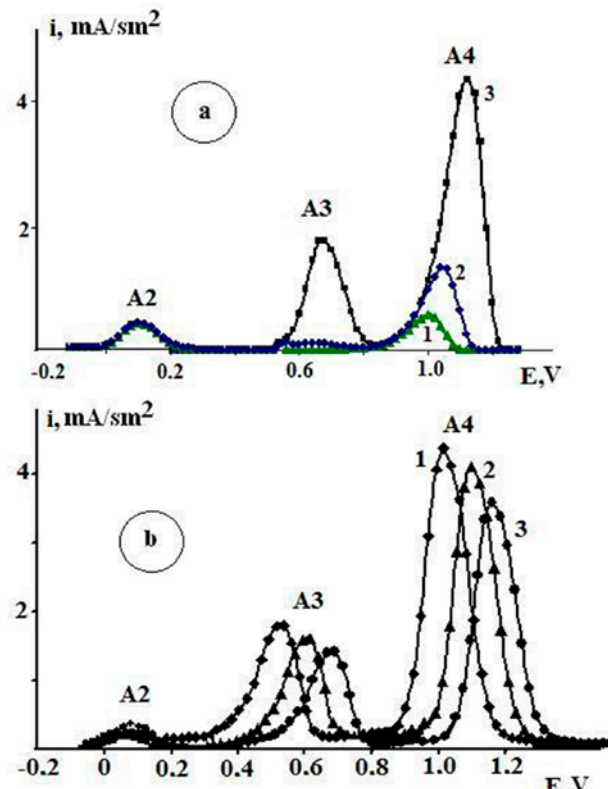


**Fig. 7.** a) Calculated voltammograms obtained according to the kinetic scenario scheme (b) at a potential scanning rate equal to 0.04 (1); 0.10 (2) and 0.60 (3)  $\text{V}/\text{sec}$  and an alkali concentration of 0.1 M; b) Calculated voltammograms obtained according to the kinetic scenario scheme (c) at a potential scanning speed equal to 0.60  $\text{V}/\text{sec}$  and an alkali concentration of 1.0 (1); 0.1 (2) and 0.01 M (3)

system and also to identify the shape of the general stationary voltammogram by calculation methods. The latter is qualitatively consistent with the experimental one, which is also characterized by the presence of four main current peaks.

Within the framework of the basic assumption of the implementation of the Langmuir adsorption model, we calculated the stationary degrees of covering of the gold surface with various surface-active forms of oxygen as a function of the electrode potential. It was found that the change in the concentration of OH<sup>-</sup> ions mainly affects the region of their adsorption potentials.

The formal equilibrium constants of individual electrode stages were calculated using the enumeration method. Their values correlate by the order of magnitude with the tabulated data [36], which indicates the correctness of our results.

Taking into account the non-stationary nature of processes occurring predominantly in the region of the A3 and A4 potentials' maxima on the voltammogram, in the general case requires consideration of seven different kinetic situations. For two of them, associated with the delayed formation of Au<sub>2</sub>O<sub>3(ads)</sub>, as well as with the heterogeneous transformation of the monoradical  $\dot{\text{O}}\text{H}_{\text{ads}}$  to diradical  $\ddot{\text{O}}_{\text{ads}}$ , a qualitative agreement between the calculated and experimental data was found. It is mainly related to the nature of the influence of the scanning rate of the potential and the volume concentration of OH<sup>-</sup> ions on the position and amplitude of the A3 and A4 peaks present on the anodic voltammogram of gold in an alkaline medium. However, it was not possible to establish complete correspondence between the shapes of the calculated and experimental voltammograms over the entire range of anodic potentials. This was probably due to the implementation of the mixed kinetics regime of the anodic oxidation of OH<sup>-</sup> ions on Au, the consideration of which goes beyond the goals and objectives of this work.

### Contribution of the authors

The authors contributed equally to this article.

### Conflict of interests

The authors declare that they have no known competing financial interests or personal

relationships that could have influenced the work reported in this paper.

### References

1. Zartcyn I. D., Shugurov A. E., Marshakov I. K. Thermodynamic coupling of anode and cathodic reactions in case of metal dissolution in the electrolytes. *Tambov University Reports. Series Natural and Technical Sciences*. 1997;2: 23–26. (In Russ., abstract in Eng.). Available at: <https://www.elibrary.ru/item.asp?id=16398081>
2. Zartcyn I. D., Shugurov A. E., Marshakov I. K. The anomalous dissolution of iron as a result of the chemical conjugation between iron ionization and hydrogen evolution. *Protection of Metals*. 2001;37(2): 138–143. <https://doi.org/10.1023/a:1010369904266>
3. Zartcyn I. D., Shugurov A. E., Marshakov I. K. Kinetics of chemically conjugate reactions of metal dissolution in the presence of oxidant. *Protection of Metals*. 2000;36(2): 140–145. <https://doi.org/10.1007/bf02758337>
4. Zhen C.-H., Sun S.-G., Fan C.-J., Chen S.-P., Mao B.-W., Fan Y.-J. In situ FTIRS and EQCM studies of glycine adsorption and oxidation on Au (111) electrode in alkaline solutions. *Electrochimica Acta*. 2004;49(8): 1249–1255. <https://doi.org/10.1016/j.electacta.2003.09.048>
5. Chun-Hua Z., Chun-Jie F., Yan-Juan G., Sheng-Pei C., Shi-Gang S. Adsorption and oxidation of glycine on Au film electrodes in alkaline solutions. *Acta Physico-Chimica Sinica*. 2003;19: 60–64. <https://doi.org/10.3866/pku.whxb20030114>
6. Beltowska-Brzezinka M., Łuczak T., Holze R. Electrocatalytic oxidation of mono- and polyhydric alcohols on gold and platinum. *Journal of Applied Electrochemistry*. 1997;27(9): 999–1011. <https://doi.org/10.1023/A:1018422206817>
7. Kraschenko T. G., Bobrinskaya E. V., Vvedenskii A. V., Kuleshova N. E. Kinetics of electrochemical oxidation of anion glycine on gold. *Condensed Matter and Interphases*. 2014;16 (1): 42–49. (In Russ., abstract in Eng.). Available at: <https://www.elibrary.ru/item.asp?id=21490889>
8. Goldshtein B. N., Volkenshtein M. V. Investigation of nonstationary complex monomolecular reactions by the graph method\*. *Doklady of the USSR Academy of Sciences*. 1968;78: 386–388. (In Russ.)
9. Goldshtein B. N., Magarshak D. B., Volkenshtein M. V. Analysis of monosubstrate enzyme reactions by graph method\*. *Doklady of the USSR Academy of Sciences*. 1970;191: 1172–1174. (In Russ.)
10. Goldshtein B. N., Shevelev E. A., Volkenshtein M. V. Stability analysis of enzyme systems with feedbacks by the graph method\*. *Doklady of the USSR Academy of Sciences*. 1983;273: 486–488. (In Russ.)

11. Goldshtein B. N., Volkenshtein M. V. Simple kinetic models explaining critical phenomena in enzymatic reactions with enzyme and substrate isomerization\*. *Doklady of the USSR Academy of Sciences*. 1988;22: 1381–1392. (In Russ.)
12. Štrbac S., Hamelin A., Adžić R. R. Electrochemical indication of surface reconstruction of (100), (311) and (111) gold faces in alkaline solutions. *Journal of Electroanalytical Chemistry*. 1993;362: 47–53. [https://doi.org/10.1016/0022-0728\(93\)80005-3](https://doi.org/10.1016/0022-0728(93)80005-3)
13. Chang S. C., Ho Y., Weaver M. J. Applications of real-time FTIR spectroscopy to the elucidation of complex electroorganic pathways: electrooxidation of ethylene glycol on gold, platinum, and nickel in alkaline solution. *Journal of the American Chemical Society*. 1991;113(25): 9506–9513. <https://doi.org/10.1021/ja00025a014>
14. Beltramo G. L., Shubina T. E., Koper M. T. M. Oxidation of formic acid and carbon monoxide on gold electrodes studied by surface-enhanced Raman spectroscopy and DFT. *ChemPhysChem*. 2005;6: 2597–2606. <https://doi.org/10.1002/cphc.200500198>
15. Martins M. E., Córdova O. R., Arvia A. J. The potentiodynamic electroformation and electroreduction of the O-containing layer on gold in alkaline solutions. *Electrochimica Acta*. 1981;26: 1547–1554. [https://doi.org/10.1016/0013-4686\(81\)85127-4](https://doi.org/10.1016/0013-4686(81)85127-4)
16. Bruckenstein S., Shay M. An in situ weighing study of the mechanism for the formation of the adsorbed oxygen monolayer at gold electrode *Journal of Electroanalytical Chemistry and Interfacial Electrochemistry*. 1985;188: 131–136. [https://doi.org/10.1016/s0022-0728\(85\)80057-7](https://doi.org/10.1016/s0022-0728(85)80057-7)
17. Burke L. D., Cunnane V. J., Lee B. H. Unusual postmonolayer oxide behavior of gold electrodes in base. *Journal of The Electrochemical Society*. 1992;139: 399–406. <https://doi.org/10.1149/1.2069230>
18. Vitus C. M., Davenport A. J. In situ scanning tunneling microscopy studies of the formation and reduction of a gold oxide monolayer on Au(111). *Journal of The Electrochemical Society*. 1994;141(5): 1291–1298. <https://doi.org/10.1149/1.2054912>
19. Goldshtein B. N., Zalkind Ts. I., Veselovskii V. I. Electrochemical adsorption of oxygen on a gold electrode in solutions of chloric and sulfuric acids\*. *Soviet Electrochemistry*. 1973;9 (5): 699–702. (In Russ.)
20. Chen A., Lipkowski J. Electrochemical and spectroscopic studies of hydroxide adsorption at the Au(111) electrode. *The Journal of Physical Chemistry B*. 1999;103: 682–691. <https://doi.org/10.1021/jp9836372>
21. Vetter K. J. *Elektrochemische Kinetik*. Springer Berlin, Heidelberg; 1961. <https://doi.org/10.1007/978-3-642-86547-3>
22. Tremiliosi-Filho G., Gonzalez E. R., Motheo A. J., Belgsir E. M., Léger J.-M., Lamy C. *Journal of Electroanalytical Chemistry*. 1998;444: 31–39. [https://doi.org/10.1016/S0022-0728\(97\)00536-6](https://doi.org/10.1016/S0022-0728(97)00536-6)
23. Nechaev I. V., Vvedenskii A. V. Quantum chemical modeling of hydroxide ion adsorption on group IB metals from aqueous solutions. *Protection of Metals and Physical Chemistry of Surfaces*. 2009;45(4): 391–397. <https://doi.org/10.1134/s2070205109040029>
24. Patritio E. M., Olivera P. P., Sellers H. The nature of chemisorbed hydroxyl radicals. *Surface Science*. 1994;306: 447–458. [https://doi.org/10.1016/0039-6028\(94\)90085-x](https://doi.org/10.1016/0039-6028(94)90085-x)
25. Alonso C., Gonzalez-Velasco J. Study of the electrooxidation of 1,3-propanediol on a gold electrode in basic medium. *Journal of Applied Electrochemistry*. 1988;18: 538–545. <https://doi.org/10.1007/bf01022248>
26. Safronov A. U., Kristensen P. A. IR spectroscopic characteristics of the surface of the gold electrode in solutions with different pH\*. *Soviet Electrochemistry*. 1990;26(7): 869–873. (In Russ.)
27. Kirk D. W., Foulkes F. R., Graydon W. F. The electrochemical formation of Au(I) hydroxide on gold in aqueous potassium hydroxide. *Journal of The Electrochemical Society*. 1980;127(10): 1069–1076. <https://doi.org/10.1149/1.2129819>
28. Icenhower D. E., Urbach H. B., Harrison J. H. Use of the potential-step method to measure surface oxides. *Journal of The Electrochemical Society*. 1970;117(12): 1500–1506. <https://doi.org/10.1149/1.2407359>
29. Štrbac S., Adžić R. R. The influence of OH- chemisorption on the catalytic properties of gold single crystal surfaces for oxygen reduction in alkaline solutions. *Journal of Electroanalytical Chemistry*. 1996;403: 169–181. [https://doi.org/10.1016/0022-0728\(95\)04389-6](https://doi.org/10.1016/0022-0728(95)04389-6)
30. Burke L. D. Scope for new applications for gold arising from the electrocatalytic behaviour of its metastable surface states. *Gold Bulletin*. 2004;37(1-2): 125–135. <https://doi.org/10.1007/bf03215520>
31. Dobberpuhl D. A., Johnson D. C. Pulsed electrochemical detection at ring of a ring-disk electrode applied to a study of amine adsorption at gold electrodes. *Analytical Chemistry*. 1995;67: 1254–1258. <https://doi.org/10.1021/ac00103a017>
32. Xiao Sun S.-G., Yao J.-L., Wu Q.-H., Tian Z.-Q. Surface-enhanced Raman spectroscopic studies of dissociative adsorption of amino acids on platinum and gold electrodes in alkaline solutions. *Langmuir*. 2002;18: 6274–6279. <https://doi.org/10.1021/la025817f>
33. Hill T. L. Studies in irreversible thermodynamic IV. Diagrammatic representation of steady state fluxes for unimolecular systems. *Journal of Theoretical Biology*. 1966;10: 442–459. [https://doi.org/10.1016/0022-5193\(66\)90137-8](https://doi.org/10.1016/0022-5193(66)90137-8)



34. Goldshtein B. N. *Kinetic graphs in enzymology*. Moscow: Nauka Publ.; 1989. 164 p. (In Russ.)

35. Volkenshtein M. V., Goldshtein B. N., Stefanov V. E. Investigation of nonstationary enzyme reactions. *Doklady of the USSR Academy of Sciences*. 1967;1: 52–58. (In Russ.)

36. Suhotin A. M. *Handbook of electrochemistry\**. Moscow: Khimiya Publ.; 1981. 487 p. (In Russ.)

\* *Translated by author of the article*

### Информация об авторах

*Ilya D. Zartsyn*, Dr. Sci. (Chem.), Professor of the Department of Physical Chemistry of the Voronezh State University (Voronezh, Russian Federation).  
zar-vrn@mail.ru

*Alexander V. Vvedenskii*, Dr. Sci. (Chem.), Full Professor of the Department of Physical Chemistry of the Voronezh State University (Voronezh, Russian Federation).

<https://orcid.org/0000-003-2210-5543>  
alvved@chem.vsu.ru

*Elena V. Bobrinskaya*, Cand. Sci. (Chem.), Associate Professor of the Department of Physical Chemistry of the Voronezh State University (Voronezh, Russian Federation).

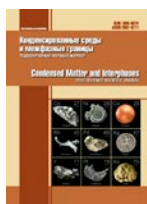
<https://orcid.org/0000-0001-7123-4224>  
elena173.68@mail.ru

*Oleg A. Kozaderov*, Dr. Sci. (Chem.), Docent, Head of the Department of Physical Chemistry, Voronezh State University (Voronezh, Russian Federation).

<https://orcid.org/0000-0002-0249-9517>  
ok@chem.vsu.ru

*Received 28.03.2023; approved after reviewing 08.04.2023; accepted for publication 15.06.2023; published online 25.03.2023.*

*Translated by Translated by Valentina Mittova*



# Condensed Matter and Interphases

Kondensirovannye Sredy i Mezhfaznye Granitsy  
<https://journals.vsu.ru/kcmf/>

## Original articles

Research article

<https://doi.org/10.17308/kcmf.2024.26/11813>

## Simple synthesis of floating Fe<sub>2</sub>O<sub>3</sub>/Luffa catalysts for the photo-Fenton degradation of methyl orange at near neutral pH

Quynh Nhu Le Thi<sup>1,2</sup>, Thi Quynh Trang Ly<sup>1,2</sup>, Anh Tien Nguyen<sup>3</sup>, Quoc Thiet Nguyen<sup>4</sup>, De-Hao Tsai<sup>5</sup>, and Tien Khoa Le<sup>1,2</sup>✉

<sup>1</sup>Faculty of Chemistry, University of Science, Ho Chi Minh city, Vietnam

<sup>2</sup>Faculty of Chemistry, University of Science, Vietnam National University, Ho Chi Minh City, Vietnam

<sup>3</sup>Ho Chi Minh City University of Education, Ho Chi Minh City, Vietnam

<sup>4</sup>Institute of Applied Materials Science, Vietnam Academy of Science and Technology, 1B TL29 District 12, Ho Chi Minh City, Vietnam

<sup>5</sup>Department of Chemical Engineering, National Tsing Hua University, Hsinchu, Taiwan, ROC

### Abstract

Although widely used in the textile industry, methyl orange is considered one of the most toxic dyes, which have negative impacts on the aquatic environment and needs to be removed from water bodies. Hence, the present paper reports the synthesis of new floating photo-Fenton catalysts based on the immobilization of Fe<sub>2</sub>O<sub>3</sub> nanoparticles on the surface of Luffa sponges for the oxalate-induced-degradation of methyl orange. The floating catalytic sponges were prepared through a simple precipitation method followed by a reflux heating process and then characterized by field emission scanning electron microscopy, X-ray diffraction, atomic absorption spectrometry, and nitrogen adsorption-desorption experiments. According to the experimental results, methyl orange was effectively degraded over our floating catalytic sponges under light illumination at near neutral pH. The catalytic activity was also found to be enhanced with the increase in crystallinity of Fe<sub>2</sub>O<sub>3</sub> nanoparticles, which can be achieved by the reflux heating. Besides, owing to the floating feature, these sponges are easily separated from the solution, thereby not forming a secondary source of pollution for water.

**Keywords:** Photo-Fenton catalyst; Floating material; Fe<sub>2</sub>O<sub>3</sub>; Luffa; Crystallinity

**Funding:** The research is funded by University of Science, VNU-HCM under grant number U2022-11.

**For citation:** Le T. Q. N., Ly T. Q. T., Nguyen A. T., Nguyen Q. Th., Tsai D.-H., Le T. Kh. Simple synthesis of floating Fe<sub>2</sub>O<sub>3</sub>/Luffa catalysts for the photo-Fenton degradation of methyl orange at near neutral pH. *Condensed Matter and Interphases*. 2024;26(1): 68–77. <https://doi.org/10.17308/kcmf.2024.26/11813>

**Для цитирования:** Ле Т. К. Н., Ли Т. К. Ч., Нгуен А. Т., Нгуен К. Т., Цай Д.-Х., Ле Т. К. Простой синтез плавающих фотокатализаторов Fe<sub>2</sub>O<sub>3</sub>/Luffa по типу Фентона для деградации метилоранжа при значении pH, близком к нейтральному. *Конденсированные среды и межфазные границы*. 2024;26(1): 68–77. <https://doi.org/10.17308/kcmf.2024.26/11813>

✉ Tien Khoa Le, e-mail: [ltkhoa@hcmus.edu.vn](mailto:ltkhoa@hcmus.edu.vn)

© Le T. Q. N., Ly T. Q. T., Nguyen A. T., Nguyen Q. Th., Tsai D.-H., Le T. Kh., 2024



The content is available under Creative Commons Attribution 4.0 License.

## 1. Introduction

Due to the dyeing efficiency without mordant and the affordable prices of azo dyes, they have been extensively used and become the most important class of synthetic dyes in the textile industry [1]. Among different azo dyes, methyl orange is an anionic, water-soluble sulfonated azo dye which is able to give the vibrant orange color to numerous materials, such as cotton, paper, nylon, and leather [2]. Nevertheless, like other azo dyes, methyl orange was reported to be toxic, potentially carcinogenic, and thereby harmful to the natural environment [3, 4]. In addition, since methyl orange contains azo groups (-N=N-) as well as aromatic groups, this organic dye is highly resistant and hardly remediated by conventional physical or biological methods [5]. Hence, the removal of methyl orange from effluents should require the advanced oxidation process using photocatalysts [6] or photo-Fenton catalysts [7] in order to degrade methyl orange molecules to smaller fractions which can be possibly eliminated by further biological treatments [2]. In fact, this azo dye was reported to be decomposed under visible light by a heterogeneous catalytic system based on  $\text{Fe}_2\text{O}_3/\text{TiO}_2$  nanoparticles which follow both photocatalytic and photo-Fenton mechanisms [8]. Likewise,  $\alpha\text{-Fe}_2\text{O}_3$  with different morphologies (croissant-like structures, urchin-like structures, and textured microspheres) were successfully prepared via hydrothermal method and applied as photo-Fenton catalyst for the degradation of methyl orange under UV-C light in the presence of  $\text{H}_2\text{O}_2$  [9]. However, most of these catalysts were used in the form of fine powders, when dispersed in effluents, they are difficult to be separated from the water body and easily become a source of secondary pollution.

In view of practical applications, the immobilization of catalytic  $\text{Fe}_2\text{O}_3$  on a recoverable substrate could be of great benefit. It was reported that  $\text{Fe}_2\text{O}_3$  particles can be deposited on various fiber substrates such as cellulose [10], fiberglass [11], carbon fiber cloth [12], etc. Recently, Luffa sponges, derived from the fruit of *Luffa cylindrica*, have attracted much attention in serving as a low-cost and eco-friendly substrate/support for inorganic catalysts [13, 14]. This natural net-like material provides fibrous strand morphologies with high porosity and high adsorption capacity

[15]. Moreover, Luffa sponges have low density, which allow them to float on the water surface. Hence, the combination between photo-Fenton catalysts and Luffa sponges is expected to facilitate the light absorption of catalysts as well as the separation of catalysts from the effluents after the treatment.

However, to the best of our knowledge, the application of  $\alpha\text{-Fe}_2\text{O}_3$  nanoparticles deposited on Luffa sponges as floating photo-Fenton catalysts for the degradation of methyl orange still remains unexplored. Furthermore, the synthesis of  $\alpha\text{-Fe}_2\text{O}_3$ /Luffa sponges is also a challenge. Generally, the immobilization of  $\alpha\text{-Fe}_2\text{O}_3$  on a substrate could be started by the precipitation of  $\text{Fe}^{3+}$  ions in the form of  $\text{Fe}(\text{OH})_3$  on the substrate surface, followed by the annealing at high temperatures to transform  $\text{Fe}(\text{OH})_3$  to  $\alpha\text{-Fe}_2\text{O}_3$ . But this annealing step can destroy the floating  $\alpha\text{-Fe}_2\text{O}_3$ /Luffa catalyst since the Luffa fibers are not able to withstand temperatures above 200 °C. Therefore, in this work, we proposed to synthesize new floating  $\alpha\text{-Fe}_2\text{O}_3$ /Luffa sponge catalysts by a reflux heating process at about 100 °C instead of annealing at high temperatures. These recoverable photo-Fenton catalysts were used to degrade methyl orange under both UVA light and visible light in the presence of oxalic acid as a radical-producing source.

## 2. Experimental

### 2.1. Materials and reagents

In this work,  $\text{H}_2\text{C}_2\text{O}_4 \cdot 2\text{H}_2\text{O}$  (> 98%), NaOH ( $\geq 97\%$ ) and methyl orange (indicator grade) were purchased from Xilong Scientific Co., Ltd. (China).  $\text{Fe}(\text{NO}_3)_3 \cdot 9\text{H}_2\text{O}$  ( $\geq 98.5\%$ ) was obtained from Shanghai Zhanyun Chemical Co., Ltd (China). All these chemical reagents were used as received, without purification. The dried Luffa fruits were purchased from VINHANDS Co. (Ho Chi Minh city, Vietnam) and subsequently cut into rectangular sponges with dimensions of 20×30 mm and thickness of 5 mm. They were washed with deionized water several times and treated with NaOH solution ( $0.1 \text{ mol} \cdot \text{L}^{-1}$ ) at 80 °C for 2 hours in order to remove lignin, natural oils, waxes and other impurities. This step is also necessary to support the interactions between catalyst particles and Luffa fibers. Then, the sponges were rinsed with deionized water to remove the



left over NaOH from their surface, dried at 100 °C to obtain the pretreated Luffa sponges for the immobilization of Fe<sub>2</sub>O<sub>3</sub> nanoparticles.

## 2.2. Synthesis of floating catalysts

The immobilization of Fe<sub>2</sub>O<sub>3</sub> nanoparticles on Luffa sponges consists of two simple steps: precipitation and reflux heating process. In the first step, the pretreated Luffa sponges were impregnated in 200 mL of Fe(NO<sub>3</sub>)<sub>3</sub> solution (0.5 mol·L<sup>-1</sup>) for 1 hour. Afterwards, NaOH solution (1.5 mol·L<sup>-1</sup>) was dropwise added to the above mixture up to pH 11 under regular stirring to produce a brown Fe(OH)<sub>3</sub> precipitate. In the next step, all the mixture was heated at reflux (~ 100 °C) for 2 hours to form Fe<sub>2</sub>O<sub>3</sub> nanoparticles on the surface of Luffa fibers. The mixture was cooled to room temperature, then the Fe<sub>2</sub>O<sub>3</sub>-coated Luffa sponges were washed with deionized water until the pH of washing water reached 7. Finally, the sponges were dried at 150 °C for 1 hour and named as Fe<sub>2</sub>O<sub>3</sub>/Luffa-2. For the comparison, the uncoated Luffa sponges and the Fe<sub>2</sub>O<sub>3</sub>-coated Luffa sponges without reflux heating were also prepared and named as Luffa and Fe<sub>2</sub>O<sub>3</sub>/Luffa-0, respectively.

## 2.3. Material characterization

Powder X ray diffraction (XRD) was used to study the crystal structure and the phase composition of all Fe<sub>2</sub>O<sub>3</sub>/Luffa catalysts. These samples were dried in vacuum at 100 °C for 3 hours, ground to fine powder, and then analyzed by using a SIEMENS D5000 diffractometer (Bruker, Billerica, MA, USA) equipped with Cu K $\alpha$  radiation ( $\lambda = 1.5406 \text{ \AA}$ ). The applied current and the operating voltage were set at 40 mA and 45 kV, respectively. The morphology and the microstructure of our samples were observed by field emission scanning electron microscopy (FESEM) taken on a SU8000 microscope (Hitachi, Tokyo, Japan) at the accelerating voltage of 10 kV. The content of Fe species on the surface of Luffa fibers was determined by atomic absorption spectrometry (AAS) using an AA-6300 spectrometer (Shimadzu, Japan). Moreover, the Brunauer–Emmett–Teller surface area ( $S_{\text{BET}}$ ) of Luffa sponges before and after depositing Fe<sub>2</sub>O<sub>3</sub> nanoparticles were measured via nitrogen adsorption-desorption isotherms recorded on a Nova 1000e analyzer (Quantachrome, Boynton Beach, FL, USA) at 77 K.

## 2.4. Photo-Fenton catalytic tests

The photo-Fenton catalytic degradation of methyl orange (MO) over our floating Fe<sub>2</sub>O<sub>3</sub>/Luffa-X samples were carried out under both ultraviolet A light and visible light in the presence of oxalic acid as a radical-producing source. All the experiments were performed at room temperature controlled by a water circulation system. For each catalytic test, 8 pieces of Fe<sub>2</sub>O<sub>3</sub>/Luffa sponges were dispersed in a static glass reactor containing 250 mL aqueous solution of MO (10<sup>-5</sup> mol·L<sup>-1</sup>) and oxalic acid (10<sup>-3</sup> mol·L<sup>-1</sup>). The initial pH of this solution was adjusted at 6 using dilute solution of H<sub>2</sub>SO<sub>4</sub> or NaOH. Before irradiation, the reaction solution was magnetically stirred in the dark for 1 hour to stabilize the adsorption of MO molecules on catalyst surface. Subsequently, an ultraviolet A (UVA) light lamp (9W Radium 78, 33.0 W·m<sup>-2</sup>) or a visible light lamp (9W Osram Dulux S, 12.5 W·m<sup>-2</sup>) was used to effectuate the photo-Fenton catalytic process. These lamps were set up at the height of 10 cm above the solution surface. During irradiation, 5 mL of dye solution was withdrawn from the reactor at certain intervals and its MO concentration was determined by Helios Omega UV–VIS spectrophotometer (Thermo Fisher Scientific, USA) at 464 nm (the maximum absorbance wavelength of methyl orange [16]).

## 3. Results and discussion

### 3.1. Characterization of floating catalysts

Fig. 1 shows the numerical photographs of Luffa sponges, Fe<sub>2</sub>O<sub>3</sub>/Luffa-0, and Fe<sub>2</sub>O<sub>3</sub>/Luffa-2 samples. It was observed that the uncoated sponges display a characteristic yellow color of dried Luffa fruits whereas Fe<sub>2</sub>O<sub>3</sub>/Luffa-0 sample presents a brown color, indicating the presence of Fe(III)-containing species on the Luffa fibers. Interestingly, when Fe<sub>2</sub>O<sub>3</sub>/Luffa sponges were heated at reflux for 2 hours, the brown color gradually turns into reddish brown. This color change suggests that there has been an evolution in crystal structure, morphology or quantity of Fe(III)-containing species on Luffa surface.

The morphology of Luffa and Fe<sub>2</sub>O<sub>3</sub>/Luffa sponges was examined by FESEM micrographs. As seen in Fig. 2a, the uncoated Luffa sponges possess a fibrous strand texture with high surface roughness. Such morphology is expected

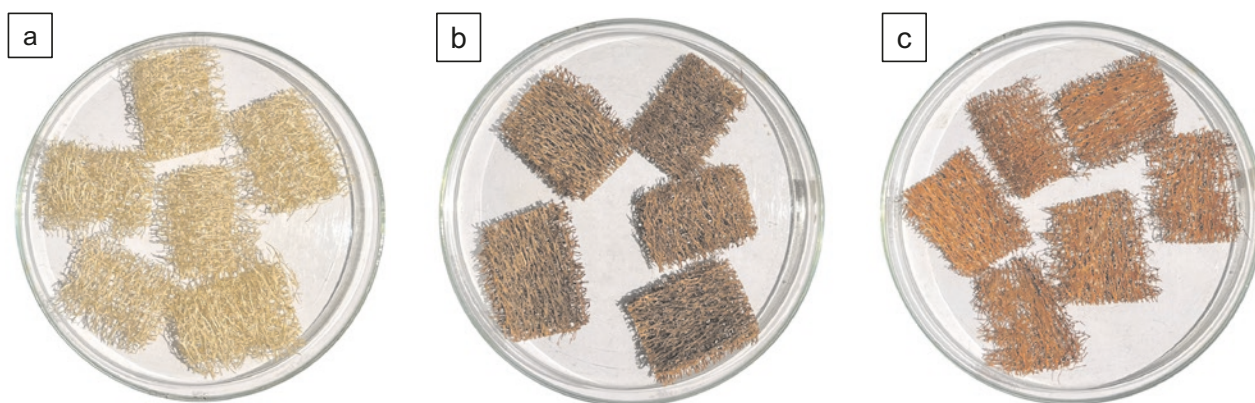


**Fig. 1.** Numerical photographs of Luffa (a),  $\text{Fe}_2\text{O}_3/\text{Luffa-0}$  (b), and  $\text{Fe}_2\text{O}_3/\text{Luffa-2}$  (c) sponges

to increase the surface accessibility towards Fe(III)-containing nanoparticles. In fact, the  $\text{Fe}_2\text{O}_3/\text{Luffa-0}$  sample shows aggregates attached to the surface of Luffa fibers with the aggregate size of about 100 nm (Fig. 2b). These aggregates are composed of tiny particles joined together by sides, which are possibly assigned to  $\text{Fe}_2\text{O}_3$  nanoparticles with low crystallinity degree. Moreover, in addition to the aggregates emerging on Luffa surface, a considerable quantity of nanoparticles seems to be mixed up underneath the Luffa fibers. Only when the  $\text{Fe}_2\text{O}_3/\text{Luffa}$  sponges were heated at reflux for 2 hours, the  $\text{Fe}_2\text{O}_3$  nanoparticles were clearly seen with the polyhedral shape and the particle size ranging from 50 nm to 100 nm (Fig. 2c). These grown nanoparticles are still in agglomerated status but their grain boundaries can be easily observed, suggesting a good degree of crystallization for  $\text{Fe}_2\text{O}_3$  nanoparticles in this sample.

The crystal structure and the phase composition of Luffa sponges and  $\text{Fe}_2\text{O}_3/\text{Luffa}$  samples were characterized through their XRD

patterns (Fig. 3). The XRD pattern of Luffa sponges shows a characteristic behavior of cellulose I crystals with four diffraction peaks at  $15.0^\circ$ ,  $16.5^\circ$ ,  $22.8^\circ$ , and  $34.5^\circ$ , corresponding to (10), (110), (002), and (023) planes (space group  $P-2$ , JCPDS No. 03-0226). For  $\text{Fe}_2\text{O}_3/\text{Luffa-0}$  sample, two additional weak peaks were observed at  $33.1^\circ$  and  $35.6^\circ$ , which can be attributed to the (104) and (110) planes of  $\text{Fe}_2\text{O}_3$  hematite phase [17] (space group  $R-3c$ , JCPDS No. 86-0550). However, the intensity of these diffraction peaks is very low and the signal-to-noise ratio is also low, indicating the low crystallinity of  $\text{Fe}_2\text{O}_3$  component. Conversely, the diffraction peaks of hematite phase and cellulose I phase in the XRD pattern of  $\text{Fe}_2\text{O}_3/\text{Luffa-2}$  sample were clearly enhanced in intensity. This result confirms the fact that heating at reflux can be a simple method to improve the crystallinity of both  $\text{Fe}_2\text{O}_3$  nanoparticles and cellulose fibers, which is in good agreement of FESEM study.

Since the changes in the morphology and the crystal structure of our catalytic samples can

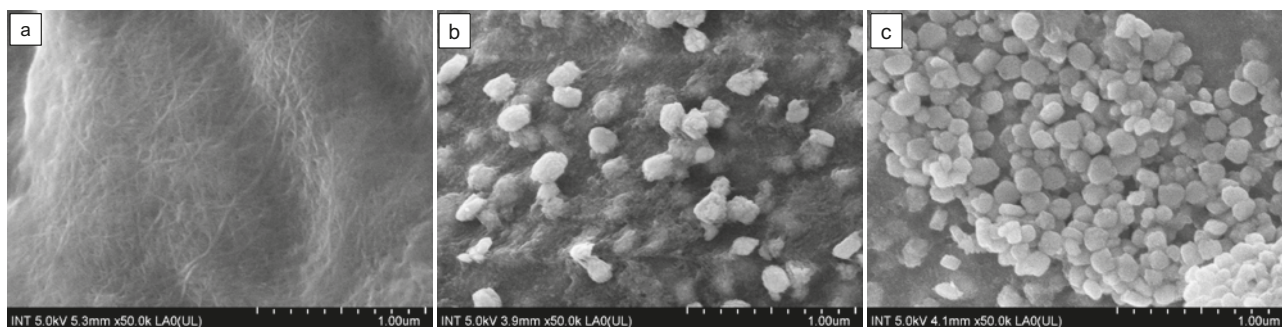


**Fig. 2.** FESEM micrographs of Luffa (a),  $\text{Fe}_2\text{O}_3/\text{Luffa-0}$  (b), and  $\text{Fe}_2\text{O}_3/\text{Luffa-2}$  (c) sponges

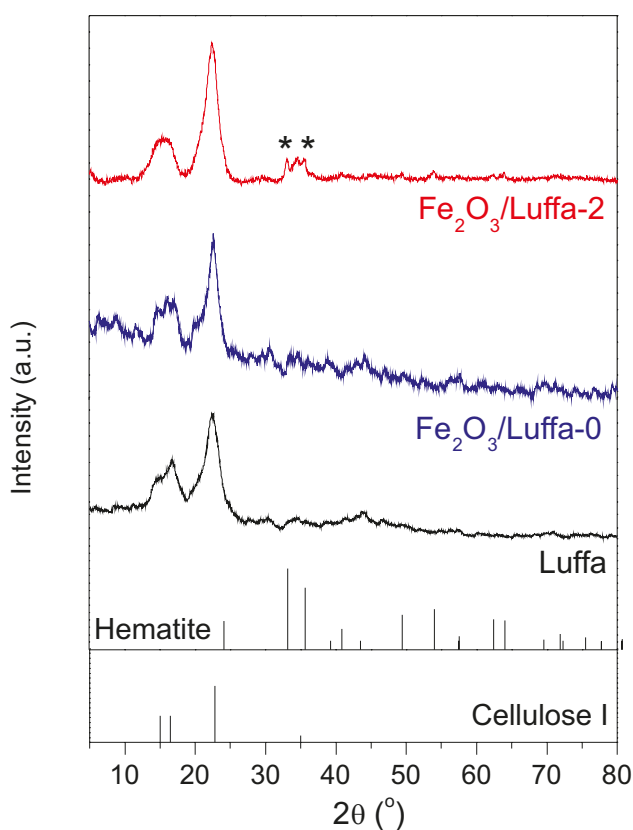


**Fig. 3.** XRD patterns of Luffa,  $\text{Fe}_2\text{O}_3$ /Luffa-0, and  $\text{Fe}_2\text{O}_3$ /Luffa-2 samples

affect their specific surface area, the nitrogen adsorption-desorption isotherm experiments were carried out. From these isotherms, the BET specific surface areas were calculated and shown in Table 1. Surprisingly, although the uncoated sponges show high surface roughness, their specific surface area is very restricted ( $0.554 \text{ m}^2\cdot\text{g}^{-1}$ ). On the contrary, when  $\text{Fe}_2\text{O}_3$  nanoparticles were immobilized on Luffa fibers, the specific surface was greatly enhanced. In fact, the  $\text{Fe}_2\text{O}_3$ /Luffa-0 sample displays the highest specific surface area ( $3.241 \text{ m}^2\cdot\text{g}^{-1}$ ), which can be explained by the presence of numerous tiny particles on Luffa fibers. For  $\text{Fe}_2\text{O}_3$ /Luffa-2 sample, the specific surface area decreases, corresponding to the growth of  $\text{Fe}_2\text{O}_3$  nanoparticles.

**Table 1.** Specific surface area and surface Fe content of Luffa,  $\text{Fe}_2\text{O}_3$ /Luffa-0, and  $\text{Fe}_2\text{O}_3$ /Luffa-2 samples

Sample	$S_{\text{BET}} (\text{m}^2\cdot\text{g}^{-1})$	Fe-content ( $\text{mg}\cdot\text{g}^{-1}$ )
Luffa	0.554	
$\text{Fe}_2\text{O}_3$ /Luffa-0	3.241	58.2
$\text{Fe}_2\text{O}_3$ /Luffa-2	1.820	36.3

Table 1 also reveals the Fe-contents, determined by AAS analysis, in  $\text{Fe}_2\text{O}_3$ /Luffa-0 and  $\text{Fe}_2\text{O}_3$ /Luffa-2 samples, proving the successful immobilization of Fe-containing species on the Luffa surface. Without heating at reflux, the content of Fe species on Luffa fibers ( $58.2 \text{ mg}\cdot\text{g}^{-1}$ ) is higher than that of  $\text{Fe}_2\text{O}_3$ /Luffa-2 sample ( $36.3 \text{ mg}\cdot\text{g}^{-1}$ ). This evolution supports the hypothesis that the reflux heating can help to grow  $\text{Fe}_2\text{O}_3$  nanoparticles on Luffa fibers, but when the particles grow large enough, the van der Waals interactions between them and the fibers gradually weaken, making an amount of  $\text{Fe}_2\text{O}_3$  particles possible to be removed from the fibers during the washing process.

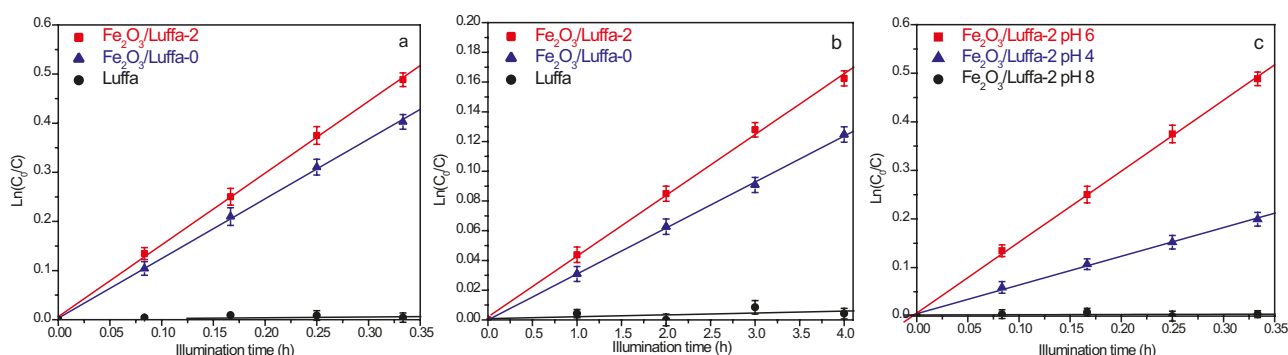
### 3.2. Catalytic activity

Prior to illumination, the MO adsorption on the surface of our floating sponges was evaluated in the dark. At pH 6, all samples exhibited low MO adsorption percentages, and the difference in MO adsorption capacity between our samples is not significant (Table 2). Fig. 4a and 4b depicts time-dependent plots of MO degradation over our floating catalysts under UVA light and visible light, respectively. It was found that the MO concentration nearly remains unchanged during several hours of UVA-visible light exposure in the presence of oxalic acid and the uncoated Luffa sample, indicating that the direct self-photolysis of MO and the photo-Fenton catalytic activity of Luffa are negligible. Likewise, in the absence of oxalic acid, both  $\text{Fe}_2\text{O}_3$ /Luffa-0 and  $\text{Fe}_2\text{O}_3$ /Luffa-2 samples did not exhibit any activity for MO degradation under UVA light or under visible light. Only when using acid oxalic as a radical-producing source, these samples showed promising UVA-light-induced and visible-light-induced catalytic performance. The photo-Fenton degradation of MO was found to fit well with the pseudo-first-order kinetic model, which allows to evaluate the catalytic activity of our samples by their apparent rate constants (Table 2). Accordingly, the rate constants of MO degradation over  $\text{Fe}_2\text{O}_3$ /Luffa-2 catalyst were always higher than those over  $\text{Fe}_2\text{O}_3$ /Luffa-0 catalyst under both UVA and visible light illumination, pointing out that the reflux heating is an important factor for the improvement of our floating photo-Fenton catalysts.



**Table 2.** Comparison of MO adsorption percentage and rate constants of MO degradation over floating catalysts under visible light and UVA light in the presence of oxalic acid

	Sample				
	Luffa pH 6 9.5	Fe <sub>2</sub> O <sub>3</sub> /Luffa-0 pH 6 11.6	pH 4 14.5	Fe <sub>2</sub> O <sub>3</sub> /Luffa-2 pH 6 10.8	pH 8 3.9
MO adsorption percentage (%)					
Rate constant of MO degradation $k$ (h <sup>-1</sup> ) under UVA light	No activity	1.174	0.591	1.461	No activity
Rate constant of MO degradation $k$ (h <sup>-1</sup> ) under visible light	No activity	0.031		0.041	

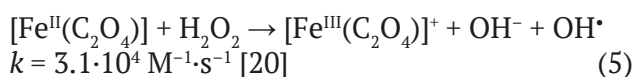
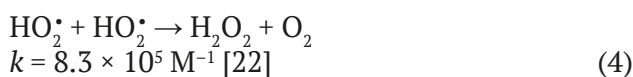
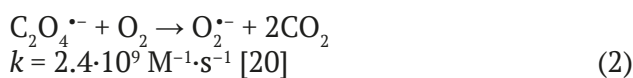
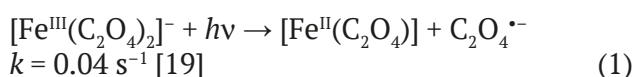
**Fig. 4.**  $\ln(C_0/C)$  versus time plot of oxalate-induced-MO degradation on floating catalysts under UVA light at pH 6 (a); under visible light at pH 6 (b); and under UVA light at different pH values (c).  $C$  is the MO concentration (mol·L<sup>-1</sup>) at time  $t$  and  $C_0$  is the initial MO concentration (mol·L<sup>-1</sup>).

The influences of initial solution pH values on the MO adsorption and the photo-Fenton catalytic discoloration of MO over Fe<sub>2</sub>O<sub>3</sub>/Luffa-2 catalyst with oxalic acid were also investigated (Fig. 4c and Table 2). Accordingly, the MO adsorption on this catalyst tended to decrease with increasing pH of solution. In contrast, under UVA light illumination, the rate constant of MO degradation significantly increased from pH 4 ( $k = 0.591$  h<sup>-1</sup>) to pH 6 ( $k = 1.461$  h<sup>-1</sup>). However, at pH 8, no MO degradation was observed. These results indicate that our floating photo-Fenton catalysts can effectively operate at near neutral pH, but their performance is reduced at lower pH values or suppressed at basic medium.

### 3.3. Discussion

As shown in the experimental results of catalytic tests, the photo-Fenton catalytic degradation of MO only effectively occurs over floating Luffa sponges when these sponges were coated with Fe<sub>2</sub>O<sub>3</sub> nanoparticles and exposed to light illumination in the presence of oxalic acid. This is most likely explained by the ability

of surface Fe(III)-species to form ferrioxalate complexes with oxalate ions, which can be excited by light to initiate a series of reactions as follows [18]:



Due to their high oxidizing capacity [23], the generated hydroxyl radicals are able to stimulate a fruitful degradation process for MO molecules. In fact, in order to justify the ability of our catalytic sponges to generate hydroxyl radicals, the scavenger tests were carried out by using tert-butyl alcohol as an agent to scavenge hydroxyl

radicals [24]. As shown in Table 3, when the molar concentration of tert-butyl alcohol gradually increased, the rate constant of MO degradation over Fe<sub>2</sub>O<sub>3</sub>/Luffa-2 catalyst was greatly reduced, proving that hydroxyl radicals play a vital role in the photo-Fenton catalytic performance of our floating catalysts.

Base on the above mechanism and the results of scavenger tests, the surface Fe(III)-species can be considered as the active centers for photo-Fenton processes in the presence of oxalic acid. It is also expected that the more the Fe<sub>2</sub>O<sub>3</sub> nanoparticles are immobilized on the surface of Luffa fibers, the more the possibility of ferrioxalate complexation increases, which enhances the photo-Fenton catalytic activity. However, in this work, our Fe<sub>2</sub>O<sub>3</sub>/Luffa-2 catalyst always showed better performances than Fe<sub>2</sub>O<sub>3</sub>/Luffa-0 catalyst under both UVA light and visible light despite the fact that the Fe-content on the surface of Fe<sub>2</sub>O<sub>3</sub>/Luffa-2, determined by AAS technique, is inferior to that of Fe<sub>2</sub>O<sub>3</sub>/Luffa-0. Even, the floating catalyst prepared with reflux heating also showed a lower specific surface area than Fe<sub>2</sub>O<sub>3</sub>/Luffa-0 sample. These results indicate that there must be other factors besides Fe-content and specific surface area affecting the catalytic performances of our floating samples.

According to XRD and FESEM studies, the reflux heating used in the catalyst synthesis can improve the crystallinity of Fe<sub>2</sub>O<sub>3</sub> nanoparticles on Luffa fibers, thereby reducing the bulk defects in the hematite lattice. This factor may be the main reason for the enhancement of photo-Fenton catalytic performance of Fe<sub>2</sub>O<sub>3</sub>/Luffa-2 sample. In the literature, although Fe<sub>2</sub>O<sub>3</sub> was considered as a potential photocatalyst with a narrow bandgap (~2.2 eV), its photocatalytic activity was usually reported to be very low for practical applications due to its high electron-hole recombination and poor conductivity [25, 26]. Our work also proved that MO was not degraded by the photocatalytic activity of Fe<sub>2</sub>O<sub>3</sub>/Luffa sponges without oxalic acid as a radical-producing source.

Nevertheless, we believe that the photocatalytic features of α-Fe<sub>2</sub>O<sub>3</sub> nanoparticles still contribute to their photo-Fenton catalytic performances. It was noticed that the transformation from [Fe<sup>III</sup>(C<sub>2</sub>O<sub>4</sub>)<sub>2</sub>]<sup>-</sup> to [Fe<sup>II</sup>(C<sub>2</sub>O<sub>4</sub>)] (Eq. 1) is the slowest step in the oxalate-induced photo-Fenton catalysis whereas the consumption of [Fe<sup>II</sup>(C<sub>2</sub>O<sub>4</sub>)] (Eq. 5) is fairly fast, which potentially unbalances the whole process and then reduces the photo-Fenton activity. Fortunately, owing to the photocatalytic activity, Fe<sub>2</sub>O<sub>3</sub> nanoparticles can be excited under light illumination to produce electron-hole pairs. For Fe<sub>2</sub>O<sub>3</sub>/Luffa-2 sample, since the Fe<sub>2</sub>O<sub>3</sub> nanoparticles were well grown with high degree of crystallization, these photogenerated electrons are easily transferred to the oxide surface and react with [Fe<sup>III</sup>(C<sub>2</sub>O<sub>4</sub>)<sub>2</sub>]<sup>-</sup> to promote the regeneration of Fe(II)-species, which significantly enhances the catalytic performances. In contrast, without reflux heating, the Fe<sub>2</sub>O<sub>3</sub> particles in Fe<sub>2</sub>O<sub>3</sub>/Luffa-0 sample are not grown enough to have a stable structure for the transfer of photogenerated electrons.

Furthermore, pH of reaction solution is also another important factor that needs to be taken into consideration for our photo-Fenton catalytic system. When the pH increases, the charge of our catalyst surface became less positive, more negative, which prevents the adsorption of anionic dyes such as MO molecules. As a result, the probability of hydroxyl radicals approaching MO molecules could be reduced. Moreover, based on the above-mentioned mechanism, especially on the Eq. 5, it is expected that the presence of OH<sup>-</sup> ions at basic pH values will hinder the generation of hydroxyl radicals. This explains why our floating catalysts are almost inactive at pH 8. Interestingly, the experimental results indicated that the Fe<sub>2</sub>O<sub>3</sub>/Luffa-2 catalyst work best at near neutral pH (pH 6) instead of more acidic pH values (pH 4) although the MO adsorption capacity of the catalyst at pH 6 is lower than that at pH 4. This can be attributed to the weak acidity of oxalic acid. At acidic media, oxalic acid difficultly dissociates to

**Table 3.** Comparison of rate constants of MO degradation over Fe<sub>2</sub>O<sub>3</sub>/Luffa-2 catalyst under UVA light with tert-butyl alcohol at different molar concentrations

Scavenger tests				
[tert-butyl alcohol] (mol·L <sup>-1</sup> )	0	5·10 <sup>-4</sup>	10 <sup>-3</sup>	1.5·10 <sup>-3</sup>
Rate constant of MO degradation <i>k</i> (h <sup>-1</sup> )	1.461	0.574	0.442	0.350

form oxalate ions, which inhibits the formation of ferrioxalate complexes on the surface of our floating catalysts. Consequently, their photo-Fenton catalytic performance was declined.

### 3.4. Reuse tests

The reusability of our  $\text{Fe}_2\text{O}_3/\text{Luffa}$ -2 catalyst was evaluated through three repeated cycles. Since these sponges float on water surface (Fig. 5a), after each cycle, they were easily separated from the solution, washed with distilled water and reused directly for the next run. As shown in Fig. 5b, the rate constant of MO degradation considerably decreases from  $1.461 \text{ h}^{-1}$  to  $0.890 \text{ h}^{-1}$  at the second run and slightly decreases to  $0.804 \text{ h}^{-1}$  at the third run. This decline of photo-Fenton catalytic activity may be explained by the partial passivation of the catalyst surface due to the absorption of decomposition products. Nevertheless, our floating catalysts still exhibits promising performances for MO degradation after two-time reuses as well as facile recoverability, which minimizes negative impacts of  $\text{Fe}_2\text{O}_3$  nanoparticles on the environment.

### 4. Conclusions

In this work, by using the simple precipitation-reflux heating method, we successfully prepared floating  $\text{Fe}_2\text{O}_3/\text{Luffa}$  sponges as effective oxalate-induced-photo-Fenton catalysts for the degradation of methyl orange under both UVA light and visible light. The reflux heating process

in synthesis procedure was proved to increase the crystallinity of  $\text{Fe}_2\text{O}_3$  nanoparticles on Luffa fibers, resulting in the enhanced catalytic performance. These catalysts sponges were also found to work best at near neutral pH, making them well suited for practical wastewater treatments. Moreover, since the catalytic sponges float on water surface, they are easily separated from the effluent and potentially reused for the next runs.

### Contribution of the authors

The authors contributed equally to this article.

### Conflict of interests

The authors declare that they have no known competing financial interests or personal relationships that could have influenced the work reported in this paper.

### References

1. Shah M. Effective treatment systems for azo dye degradation: a joint venture between physico-chemical & microbiological process. *Journal of Environmental Bioremediation & Biodegradation*. 2014;2: 231–242. <https://doi.org/10.12691/ijebb-2-5-4>
2. Fan J., Guo Y., Wang J., Fan M. Rapid decolorization of azo dye methyl orange in aqueous solution by nanoscale zerovalent iron particles. *Journal of Hazardous Materials*. 2009;166: 904–910. <https://doi.org/10.1016/j.jhazmat.2008.11.091>
3. Haque M. M., Haque M. A., Mosharaf M. K., Marcus P. K. Decolorization, degradation and detoxification of carcinogenic sulfonated azo dye methyl orange by newly developed biofilm consortia. *Saudi*

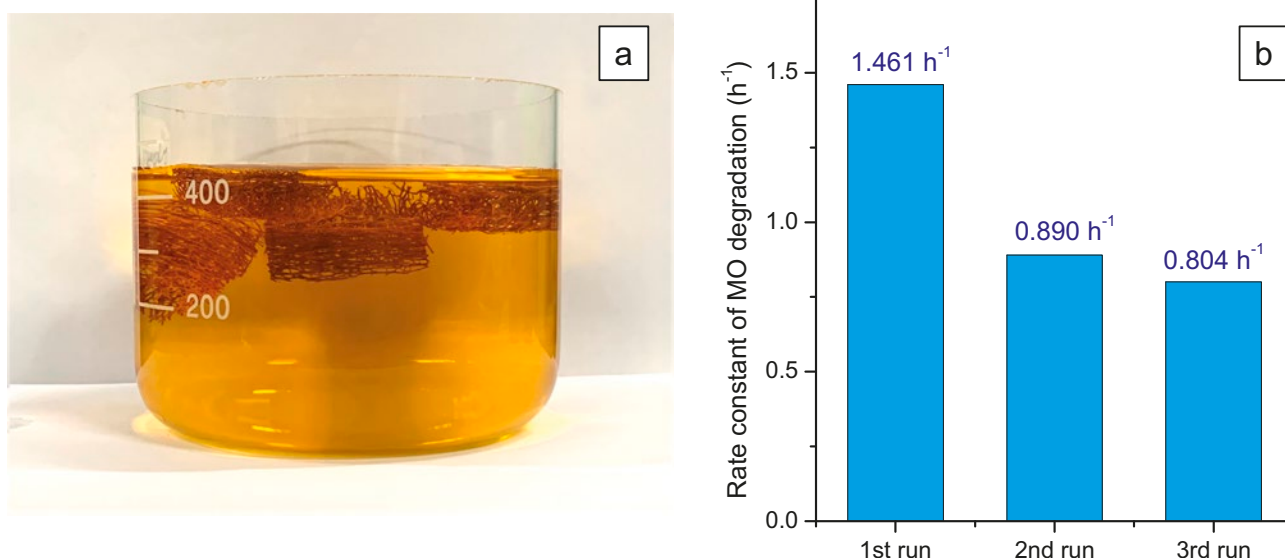


**Fig. 5.** Numerical photograph of  $\text{Fe}_2\text{O}_3/\text{Luffa}$  sponges floating on the surface of MO solution (a) and degradation of MO on  $\text{Fe}_2\text{O}_3/\text{Luffa}$ -2 catalyst in three consecutive experiments (b)



- Journal of Biological Sciences*. 2021;28: 793–804. <http://doi.org/10.1016/j.sjbs.2020.11.012>
4. Kant R. Textile dyeing industry an environmental hazard. *Natural Sciences*. 2012;4: 22–26. <http://doi.org/10.4236/ns.2012.41004>
  5. Akansha K., Chakraborty D., Sachan S. G. Decolorization and degradation of methyl orange by *Bacillus stratosphericus* SCA1007. *Biocatalysis and Agricultural Biotechnology*. 2019;18: 101044. <https://doi.org/10.1016/j.bcab.2019.101044>
  6. Stepanova K. V., Yakovleva N. M., Kokatev A. N., Pettersson, H. The structure and properties of nanoporous anodic oxide films on titanium aluminate. *Condensed Matter and Interphases*. 2019;21(1): 135–145. <https://doi.org/10.17308/kcmf.2019.21/724>
  7. Xu Z. Zhang M., Wu J., Liang J., Zhou L., Lü B. Visible light-degradation of azo dye methyl orange using TiO<sub>2</sub>/β-FeOOH as a heterogeneous photo-Fenton-like catalyst. *Water Science & Technology*. 2013;68(10): 2178–2185. <https://doi.org/10.2166/wst.2013.475>
  8. Hassan M. E., Chen Y., Liu G., Zhu D., Cai J. Heterogeneous photo-Fenton degradation of methyl orange by Fe<sub>2</sub>O<sub>3</sub>/TiO<sub>2</sub> nanoparticles under visible light. *Journal of Water Process Engineering*. 2016;12: 52–57. <https://doi.org/10.1016/j.jwpe.2016.05.014>
  9. Domacena A. M. G., Aquino C. L. E., Balela M. D. L. Photo-Fenton degradation of methyl orange using hematite (α-Fe<sub>2</sub>O<sub>3</sub>) of various morphologies. *Materials Today: Proceedings*. 2020;22: 248–254. <https://doi.org/10.1016/j.matpr.2019.08.095>
  10. Shaabani A., Nosrati H., Seyyedhamzeh M. Cellulose@Fe<sub>2</sub>O<sub>3</sub> nanoparticle composites: magnetically recyclable nanocatalyst for the synthesis of 3-aminoimidazo[1,2-a]pyridines. *Research on Chemical Intermediates*. 2013;41: 3719–3727. <https://doi.org/10.1007/s11164-013-1484-6>
  11. Mikenin P., Zazhigalov S., Elyshev A., Lopatin S., Larina T., Cherepanova S., Pisarev D., Baranov D., Zagoruiko A. Iron oxide catalyst at the modified glass fiber support for selective oxidation of H<sub>2</sub>S. *Catalysis Communications*. 2016;87: 36–40. <https://doi.org/10.1016/j.catcom.2016.08.038>
  12. Bian L., Liu Y., Zhu G., Yan C., Zhang J., Yuan A. Ag@CoFe<sub>2</sub>O<sub>4</sub>/Fe<sub>2</sub>O<sub>3</sub> nanorod arrays on carbon fiber cloth as SERS substrate and photo-Fenton catalyst for detection and degradation of R6G. *Ceramics International*. 2018;44(7): 7580–7587. <https://doi.org/10.1016/j.ceramint.2018.01.172>
  13. Mohamad E. R., Haidar Z., Lakiss L., Toufaily J., Frederic T. S. Immobilization of TiO<sub>2</sub> nanoparticles on natural *Luffa cylindrica* fibers for photocatalytic applications. *RSC Advances*. 2013;3: 3438–3445. <https://doi.org/10.1039/C2RA22438K>
  14. Feng L., Zhang P., Li J., Han X., Tang S. Facile preparation, characterization, and formaldehyde elimination performance of MnO<sub>x</sub>/natural loofah composites. *Environmental Progress and Sustainable Energy*. 2020;39(6): e13437. <https://doi.org/10.1002/ep.13437>
  15. Annunciado T. R., Sydenstricker T. H. D., Amico S. C. Experimental investigation of various vegetable fibers as sorbent materials for oil spills. *Marine Pollution Bulletin*. 2005;50: 1340–1346. <https://doi.org/10.1016/j.marpolbul.2005.04.043>
  16. Wu M. C., Lin M. P., Chen S. W., Lee P. H., Lic J. H., Su W. F. Surface-enhanced Raman scattering substrate based on a Ag coated monolayer array of SiO<sub>2</sub> spheres for organic dye detection. *RSC Advances*. 2014;4: 10043. <https://doi.org/10.1039/c3ra45255g>
  17. Mittova I. Y., Sladkopevtsev B. V., Mittova V. O., Nguyen A. T., Kopeychenko E. I., Khoroshikh N. V., Varnachkina I. A. Formation of nanoscale films of the (Y<sub>2</sub>O<sub>3</sub>-Fe<sub>2</sub>O<sub>3</sub>) on the monocrystal InP. *Condensed Matter and Interphases*. 2019;21(3): 406–418. <https://doi.org/10.17308/kcmf.2019.21/1156>
  18. Huang Y. H., Huang Y. J., Tsai H. C., Chen H. T. Degradation of phenol using low concentration of ferric ions by the photo-Fenton process. *Journal of the Taiwan Institute of Chemical Engineers*. 2010;41: 699–704. <https://doi.org/10.1016/j.jtice.2010.01.012>
  19. Dueterberg C. K., Cooper W. J., Waite T. D. Fenton-mediated oxidation in the presence and absence of oxygen. *Environmental Science & Technology*. 2005;39: 5052–5058. <https://doi.org/10.1021/es048378a>
  20. Mulazzani Q. G., D'Angelantonio M., Venturi M., Hoffman M. Z., Rodgers M. A. J. Interaction of formate and oxalate ions with radiation-generated radicals in aqueous solution. Methylviologen as a mechanistic probe. *Journal of Physical Chemistry*. 1986;90: 5347–5352. <https://doi.org/10.1021/j100412a090>
  21. Walling C. Fenton's reagent revisited. *Accounts of Chemical Research*. 1975;8: 125–131. <https://doi.org/10.1021/ar50088a003>
  22. Sedlak D. L., Hoigné J. The role of copper and oxalate in the redox cycling of iron in atmospheric waters. *Atmospheric Environment*. 1993;27: 2173–2185. [https://doi.org/10.1016/0960-1686\(93\)90047-3](https://doi.org/10.1016/0960-1686(93)90047-3)
  23. Wang X., Zhang L. Kinetic study of hydroxyl radical formation in a continuous hydroxyl generation system. *RSC Advances*. 2018;8: 40632. <https://doi.org/10.1039/C8RA08511K>
  24. Biswas A., Saha S., Jana N. R. ZnSnO<sub>3</sub> nanoparticle-based piezocatalysts for ultrasound-assisted degradation of organic pollutants. *ACS Applied Nano Materials*. 2019;2: 1120–1128. <https://doi.org/10.1021/acsanm.9b00107>
  25. Kormann C., Bahnemann D. W., Hoffmann M. R. Environmental photochemistry: Is iron oxide (hematite) an active photocatalyst? A comparative study: α-Fe<sub>2</sub>O<sub>3</sub>, ZnO, TiO<sub>2</sub>. *Journal of Photochemistry and Photobiology*

*logy A: Chemistry*. 1989;48: 161–169. [https://doi.org/10.1016/1010-6030\(89\)87099-6](https://doi.org/10.1016/1010-6030(89)87099-6)

26. Mishra M., Chun D. M.  $\alpha\text{-Fe}_2\text{O}_3$  as a photocatalytic material: A review. *Applied Catalysis A: General*. 2015;498: 126–141. <https://doi.org/10.1016/j.apcata.2015.03.023>

### Information about the authors

*Quynh Nhu Le Thi*, 4<sup>th</sup> year student, Faculty of Chemistry, University of Science, Vietnam National University (Ho Chi Minh City, Vietnam).

[ltqnhu2608@gmail.com](mailto:ltqnhu2608@gmail.com)

*Thi Quynh Trang Ly*, 3<sup>rd</sup> year student, Faculty of Chemistry, University of Science, Vietnam National University (Ho Chi Minh City, Vietnam).

[lythiquynhtrang02@gmail.com](mailto:lythiquynhtrang02@gmail.com)

*Anh Tien Nguyen*, PhD in Chemistry, Chief of Inorganic Chemistry Department, Ho Chi Minh City University of Education Vietnam (Ho Chi Minh City, Vietnam).

[tienna@hcmue.edu.vn](mailto:tienna@hcmue.edu.vn)

*Quoc Thiet Nguyen*, PhD in Chemistry, Institute of Applied Materials Science, Vietnam Academy of Science and Technology (Ho Chi Minh City, Vietnam).

[ngqthiet@yahoo.com](mailto:ngqthiet@yahoo.com)

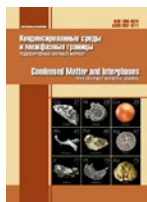
*De-Hao Tsai*, PhD in Chemistry, Professor of Department of Chemical Engineering, National Tsing Hua University (Hsinchu, Taiwan, ROC).

[dhtsai@mx.nthu.edu.tw](mailto:dhtsai@mx.nthu.edu.tw)

*Tien Khoa Le*, PhD in Chemistry, Chief of Inorganic Chemistry Department, University of Science, Vietnam National University (Ho Chi Minh City, Vietnam).

[ltkhoa@hcmus.edu.vn](mailto:ltkhoa@hcmus.edu.vn)

*Received 16.05.2023; approved after reviewing 29.05.2023; accepted for publication 15.06.2023; published online 25.03.2024.*



## Original articles

Research article

<https://doi.org/10.17308/kcmf.2024.26/11810>

## Microstructural and hydrophilic properties of polyethylene terephthalate glycol polymer samples with different 3D printing patterns

A. S. Lenshin, V. E. Frolova✉, S. A. Ivkov, E. P. Domashevskaya

Voronezh State University,  
1 Universitetskaya pl., Voronezh 394018, Russian Federation

### Abstract

The aim of the work is to study the influence of the 3-D printing process with the Hercules Original printer by sequentially applying polymer layers using the FDM (Fused Deposition Modeling) method on the microstructural and hydrophilic properties of polyethylene terephthalate glycol (PETG) samples with different printing patterns. X-ray phase analysis revealed the presence of a greater ordering of amorphous PETG polymer chains in printed samples, which occurs during thermal and mechanical impact on the initial filamentous sample during 3D printing. This manifests itself in the increase of relative intensity for the main diffraction peak of the amorphous PETG polymer by an order of magnitude for all of the samples with five different print patterns. At the same time, IR spectroscopy data revealed the preservation of all intrastructural chemical bonds of the polymer both in the original thread and in printed samples. Close contact angles of about  $\theta \approx 50^\circ$  for all printed samples, which is much smaller than the right angle  $\theta = 90^\circ$ , show that the surfaces of all five printed PETG samples with different patterns are hydrophilic.

**Keywords:** Polyethylene terephthalate-glycol PETG, Model drawings 3D printing, X-ray amorphous phase, Ordering of polymer chains, IR spectra, Intrastructural chemical bonds of the polymer, Hydrophilic surface

**Funding:** The research was carried out with the support of the Ministry of Education and Science of the Russian Federation partly within the framework of the state task for universities in the field of scientific activity, project No. FZGU-2023-006, and Agreement No. 075-15-2021-1351 in parts of the XRD research.

**For citation:** Lenshin A. S., Frolova V. E., Ivkov S. A., Domashevskaya E. P. Microstructural and hydrophilic properties of polyethylene terephthalate glycol polymer samples with various 3D printing patterns. *Condensed Matter and Interphases*. 2024;26(1): 78–87. <https://doi.org/10.17308/kcmf.2024.26/11810>

**Для цитирования:** Леньшин А. С., Фролова В. Е., Ивков С. А., Домашевская Э. П. Микроструктурные и гидрофильные свойства образцов полимера полиэтилентерефталат-гликоля с различными рисунками 3D-печати. *Конденсированные среды и межфазные границы*. 2024;26(1): 78–87. <https://doi.org/10.17308/kcmf.2024.26/11810>

✉ Vera E. Frolova, e-mail: [ternovaya@phys.vsu.ru](mailto:ternovaya@phys.vsu.ru)

© Lenshin A. S., Frolova V. E., Ivkov S. A., Domashevskaya E. P., 2024



The content is available under Creative Commons Attribution 4.0 License.



## 1. Introduction

One of the most important tasks of semiconductor microelectronics has always been the creation of high-quality packages for integrated circuits. At present, the manufacture of high-quality and relatively inexpensive packages for integrated circuits from polymers seems to be especially relevant.

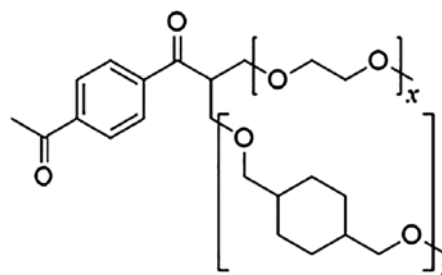
One of these polymers is polyethylene terephthalate glycol PETG (PETG), a high-strength, wear-resistant material with a fairly high melting point (230–240 °C), resistance to most chemicals and ultraviolet radiation. Along with the ease of printing, it has received the widest application in additive manufacturing in the form of threads (filaments) or granules. [1–5]. Glycol-modified PETG polyethylene terephthalate has become a popular material for additive manufacturing and is used, in particular, for printing employing the technology of layer-by-layer imposition of polymer layers by the FDM method (Fused Deposition Modeling) [1]. PETG is an amorphous thermoplastic copolyester [2]. The amorphous nature of PETG is due to the glycol modification of semi-crystalline polyethylene terephthalate (PET). The mechanical characteristics of PETG are similar to those ones of PET [6]. However, PETG is generally regarded as the best polymer for 3D printing. [7]. It is very suitable for extrusion, blow molding, injection molding as well as thermoforming [8]. At the same time, it has excellent chemical resistance, good tensile strength and flexibility [7]. Due to the amorphous structure and relatively strong interlayer bonding, products printed from PETG exhibit a lower anisotropy of mechanical properties compared to other materials manufactured using the FDM technology [8].

In addition, due to its good biocompatibility, it is a suitable material for 3D printing in bone tissue engineering [9].

The dielectric properties of this material make it possible to its widely use in electrical engineering and electronics in the production of cases and elements of electronic devices [10].

PETG is an ideal material for fabricating objects that are subjected to constant loads, systematic shocks or vibrations. PETG is a thermoplastic and is a polycondensation product of ethylene glycol with terephthalic acid (or its dimethyl ester)

with the chemical formula  $(C_{10}H_8O_4)_n$ . Structural formula of PETG is shown below [2]:



PETG is a solid, colorless, transparent substance in the amorphous state and white, opaque in the crystalline state. It turns into a transparent state when heated to the glass transition temperature (85 °C) and remains in this state when it is abruptly cooled and quickly passes through the “crystallization zone”. One of the important parameters of PETG is the intrinsic viscosity, which is determined by the length of the polymer molecule. As the intrinsic viscosity increases, the rate of crystallization decreases. PETG can be dyed, metallized, and printed.

The aim of this work is to study the effect of 3D printing of polyethylene terephthalate glycol (PETG) samples with different model patterns on their microstructural properties and surface wettability.

## 2. Experimental

*Objects and methods of research.* The samples for the study were made from a polyethylene terephthalate glycol PETG filament with a diameter of 1.75 mm employing Hercules Original 3D printer by layer-by-layer superposition of FDM polymer layers (Fused Deposition Modeling) [1]. Extruder temperature – 260 °C, power – 500 W. 5 cylindrical specimens with a diameter of 20 mm and a thickness of 5 mm were printed. The printed samples differed in 3D printing patterns (five model types).

Figure 1 shows the studied types of model drawings.

Along with the printed samples, the original filamentous PETG sample (Filament) was studied. Therefore, in the next section of the article, the results of the study of microstructural properties for six samples will be presented.

*X-ray phase analysis (XRD)* of all the above PETG samples was carried out with DRON-4.07

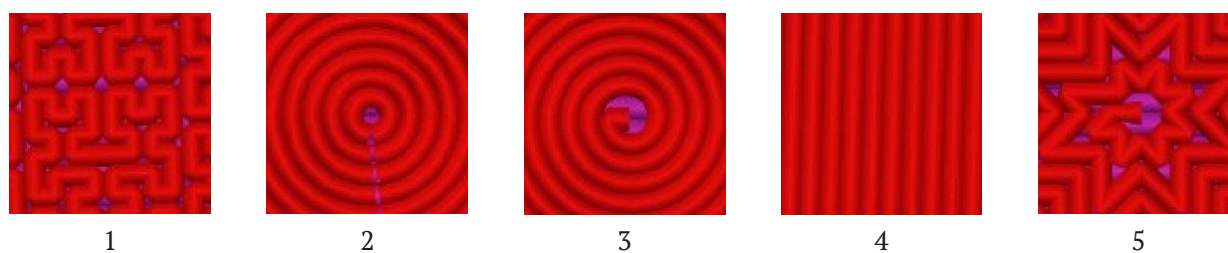


**Fig. 1.** Five types of 3-D printing patterns on polyethylene terephthalate glycol (PETG) polymer samples: 1\_Hilbert, 2\_Concentric, 3\_Archimedean, 4\_Rectilinear, 5\_Octagram

diffractometer with  $\text{CuK}\alpha$  - radiation in the step-by-step scanning mode applying sample rotation, with copper radiation  $\text{CuK}\alpha$   $\lambda = 1.54 \text{ \AA}$  at high voltage and filament current of the X-ray tube anode  $U = 29 \text{ kV}$  and  $I = 25 \text{ mA}$ .

The measurements of small-angle X-ray diffraction of the samples were carried out at the Central Collective Use Center of the NO VSU on an ARLX'TRA diffractometer in parallel beam geometry and the  $\theta$ - $\theta$  mode in the angle range  $2\theta = 1$ – $10^\circ$  using  $\text{CuK}\alpha_1$  radiation with the use of a monochromator.

*IR spectroscopy* is a universal method for obtaining information about the molecular structure of substances and allows to determine the nature of atomic groups, the nature of chemical bonds and their changes under the influence of external conditions. Any molecule has its own individual spectrum of vibrations; therefore, by comparing the modes of the obtained experimental spectrum with the known literature data, it is possible to identify the substance under study. Studies of the molecular structure of PETG samples were carried out on five 3D printed samples with different model

patterns (Fig. 1) and the original filament by measuring IR transmission spectra using the ATR (attenuated total internal reflection) method on a Bruker Vertex 70 IR-Fourier spectrometer of the Center for Collective Use of the Voronezh State University.

*The wettability studies* of the surface of flat printed samples with various 3D printed model patterns (Fig. 1) were carried out with a setup for measuring contact angles (Fig. 2), which we made with 3D printer. The setup is a stand with a sample holder on which a flat sample is placed. A drop-meter is installed on top, with the help of which drops are created on the surface of the sample to measure the contact angle of wetting. Opposite the stand with the test sample, a webcam is installed, which displays the image of the drop on the screen, and using the Pic-pic graphics editor, the wetting angle of the sample  $\theta$  is measured. A drop of liquid on the surface of a solid, depending on the nature of the solid, the liquid and the environment in which it is located, can spread completely or partially and take the form shown in Fig. 3. The angle  $\theta$  between the tangent to the surface of the drop and the surface



**Fig. 2.** Installation for measuring contact angles



**Fig. 3.** Contact angle  $\phi$  on a hydrophilic surface

of the solid, counted towards the droplet surface is called the contact angle  $\theta$  [9, 10].

If a liquid drop completely or partially spreads over the sample surface and forms an acute angle  $\varphi < 90^\circ$  with it, as is shown in Fig. 3, then the liquid wets this surface. Only those liquids can moisten a solid surface that have lower the surface tension than a given solid at the boundary with air. Surfaces of solids wetted by water are called *hydrophilic*. Surfaces where water does not spread and forms an obtuse contact angle  $\varphi > 90^\circ$  are called *hydrophobic*.

### 3. Results and discussion

#### 3.1. X-ray phase analysis of PETG samples

Fig. 4 shows the results of analyzing the crystalline state of the samples under study with 5 different 3D printing patterns, 1\_Hilbert, 2\_Concentric, 3\_Archimedian, 4\_Rectilinear, 5\_Octogram, and the original filament (Filament) by X-ray methods in two intervals of Bragg angles: small angles  $2\theta = 1-10^\circ$  (upper Fig. 4 a) and large angles  $2\theta = 10-90^\circ$  (lower Fig. 4b).

The obtained results show that at small angles, all of the studied samples do not give

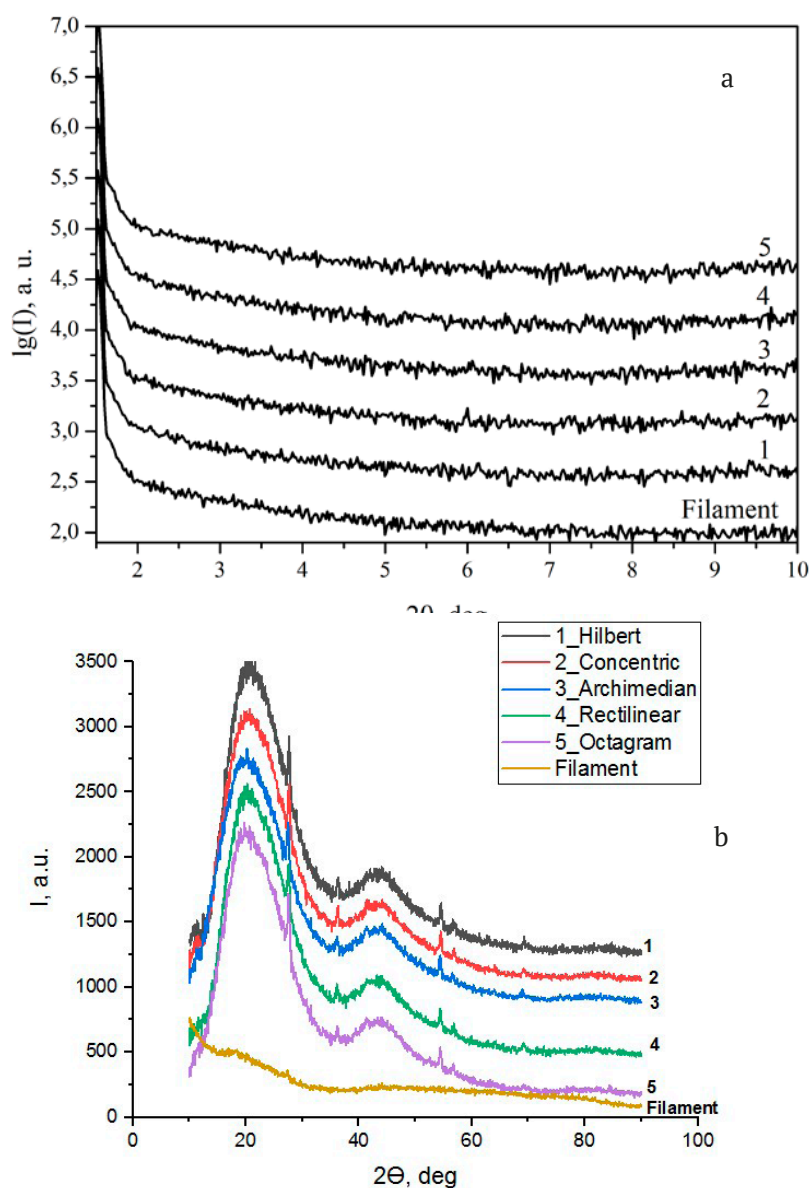


**Fig. 4.** Diffraction patterns of samples with model patterns 1\_Hilbert, 2\_Concentric, 3\_Archimedian, 4\_Rectilinear, 5\_Octogram and the original filament for 3D printing (Filament) in two intervals of Bragg angles: small angles  $2\theta = 1-10^\circ$  (upper Fig. 4a) and large angles  $2\theta = 10-90^\circ$  (lower Fig. 4b)



any reflections (Fig. 4a), while in the range of large angles, the diffraction patterns of all 5 printed samples with different patterns contain two wide reflections (halos) from the amorphous phase of PETG with the most intense reflection in the range of angles  $2\theta \approx 15\text{--}35^\circ$  and the second less intense in the range  $2\theta \approx 37\text{--}55^\circ$  (Fig. 4b). Against the background of these wide bands, all five printed samples show narrow diffraction lines from the crystalline phase of the coloring pigment of the PETG polymer [11], which is titanium dioxide  $\text{TiO}_2$  with a tetragonal rutile structure [11, 12].

At the same time, in the diffraction pattern of the original filament (6\_Filament, Fig. 4b), the intensity of the first halo with a maximum at  $2\theta \approx 20^\circ$  decreases by an order of magnitude, and the second halo is stretched two to three times in the  $2\theta$  scale, as compared to all printed samples. And against the background of the first halo of the original thread, only a trace is outlined from one of the most intense lines of the  $\text{TiO}_2$  (110) pigment. Such differences in the diffraction patterns of the printed samples from the diffraction pattern of the original thread are due to greater order in the orientation of the rigid polymer chains of amorphous PETG in the printed samples with different patterns, which occurs in the extruder under thermal and mechanical influences on the original thread-like sample during the 3D printing process. However, it should be noted that the characteristic amorphous structure of filamentary PETG samples from different manufacturers used for 3D printing may differ in the degree of ordering of polymer chains, which is reflected in the intensity of the first halo of the diffraction patterns of the initial filaments.

Nevertheless, in [11], when studying the effect of various 3D printing speeds on the microstructure, morphology and mechanical properties of the printed samples  $20 \times 20 \times 3$  mm in size, a PETG (filament) thread with a diameter of 1.75 mm, manufactured by FUEL INVEST, SE, Prague, Czech Republic, was used, and its diffraction pattern, in fact, did not differ from those ones of the printed samples with different printing speeds as well as our samples with different patterns. However, the differences observed in the diffraction pattern of the relative intensity of the first halo of our original filament

(Filament) in Fig. 4b from the original filament of work [11] may be due to the peculiarities of the technology of the manufacturer of filaments (Filaments) for 3D printing.

Table 1 shows the values of the Bragg angles  $2\theta$  and interplanar distances  $d$  of the  $\text{TiO}_2$  crystalline pigment in the printed PETG samples, related by Wolfe–Bragg formula:

$$2d \cdot \sin \theta = n \cdot \lambda,$$

where  $n$  – is the order of reflection,  $\lambda$  is the wavelength of X-ray radiation  $\text{CuK}\alpha$   $\lambda = 1.54 \text{ \AA}$ .

Analysis of the interplanar distances  $d_{hkl}$  of the crystalline phase of the  $\text{TiO}_2$  pigment shows that these values, measured in angstroms  $1 \text{ \AA} = 10^{-10} \text{ m}$ , are almost the same for all five samples (with an accuracy to the second decimal places) and are close to the values from the database [11]. This fact, together with the preservation of the relative intensities of the diffraction lines against the background of unchanged intense halos from the amorphous PETG phase of the printed samples, means that the initial filamentous PETG polymer experiences the same thermal and mechanical effects during layer-by-layer deposition by an extruder on a flat surface of any pattern out of the five studied samples.

### 3.2. IR spectra of PETG samples

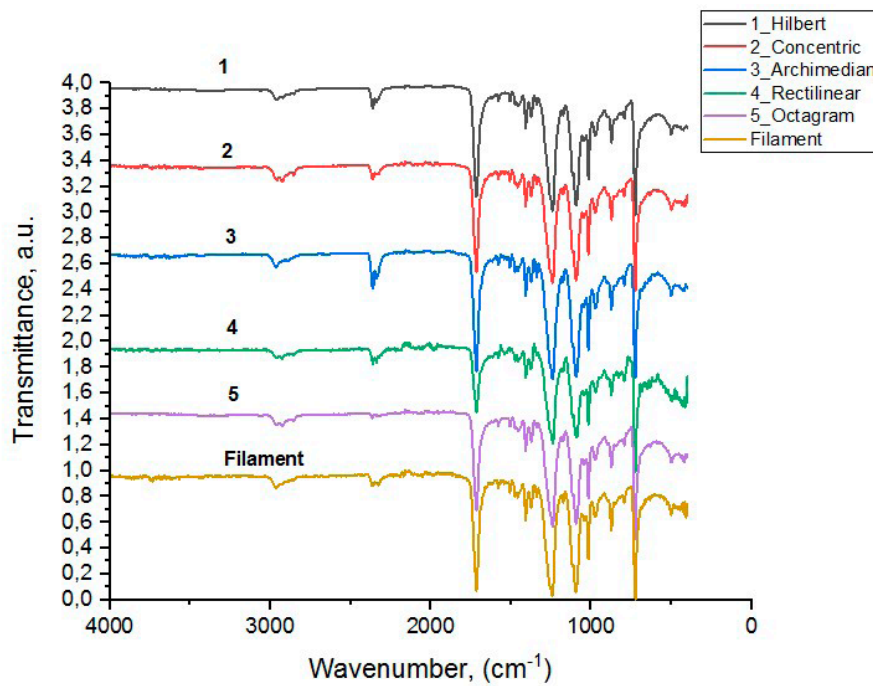
IR spectroscopy is a non-destructive optical method used to solve specific problems, including the determination of the fundamental characteristics of a molecule, the quantitative analysis of the known phases in a substance, the identification of chemical compounds and the elucidation of their structure. This optical method is based on the measurement of intensity of the infrared (IR) radiation absorbed or reflected by a certain material, which is associated with vibrational and rotational vibrations of molecular fragments and manifests itself in the distribution of intensity in absorption bands depending on the wavelength ( $\lambda$ ) or its reciprocal value, which known as the wavenumber ( $\nu$ ).

Fig. 5 shows the IR transmission spectra for the original filament (PETG filament) and five 3D printed samples with different PETG polymer patterns.

Table 2 shows the vibrational modes of the IR spectra for all six samples. In the last column of the table, for comparison, the vibrational modes

**Table 1.** Bragg angles  $2\theta$  and interplanar distances  $d$  (Å) of most intense lines of the  $\text{TiO}_2$  pigment tetragonal phase in printed PETG samples with different model patterns

Printed Sample PETG	$2\theta$ , (°)	$d_{hkl}$ (Å)	$d_{hkl}$ of tetragonal rutile structure $\text{TiO}_2$ [11]
1_Hilbert	27.70	3.222	3.247 (110)
	36.50	2.464	2.487 (101)
	54.65	1.681	1.687 (211)
	56.65	1.628	1.623 (220)
	69.40	1.356	1.359 (301)
2_Concentric	28.0	3.201	3.247 (110)
	36.15	2.489	2.487 (101)
	54.65	1.681	1.687 (211)
	56.85	1.621	1.623 (220)
	69.35	1.356	1.359 (301)
3_Archimedian	27.30	3.269	3.247 (110)
	36.0	2.497	2.487 (101)
	54.50	1.685	1.687 (211)
	56.80	1.621	1.623 (220)
	69.05	1.360	1.359 (301)
4_Rectilinear	27.45	3.256	3.247 (110)
	36.25	2.481	2.487 (101)
	54.55	1,685	1.687 (211)
	56.55	1.628	1.623 (220)
	69.25	1.358	1.359 (301)
5_Octilinear	27.65	3.229	3.247 (110)
	36.05	2.497	2.487 (101)
	54.65	1.681	1.687 (211)
	56.75	1.624	1.623 (220)
	69.55	1.353	1.359 (301)

**Fig. 5.** IR transmission spectra for the original sample of PETG thread and five samples with different model patterns of 3D printing from PETG polymer

**Table 2.** Vibration modes of the IR spectra of the original filament and PETG polymer samples with different 3D printing model patterns in comparison with the literature data for PET (PET) [15]

Identification of vibration modes	Vibration modes of samples PETG, cm <sup>-1</sup>						
	Original filament	1_Hilbert	2_Concentric	3_Archimedean	4_Rectilinear	5_Octagram	Modes of PET
Interaction of polar ester groups with benzene rings	723	723	723	725	723	723	712
Vibrations of neighboring aromatic protons in <i>para</i> -substituted aromatic rings	792	790 1978	791 1965	797 1965	791 1975	795 1987	795 1960
1,2,4,5-tetrasubstituted benzene rings	871 972	875 974	872 968	876 968	874 975	872 972	872 972
Methylene group and C-O ester bond vibrations	1043 1093	1043 1093	1043 1094	1047 1096	1045 1092	1043 1094	1050 1096
Terephthalate group (OCC <sub>6</sub> H <sub>4</sub> -HCOO)	– 1238	1112 1244	1114 1244	– 1234	1116 1238	1116 1240	1124 1240
Stretching vibrations of C-O in the C-O-H fragment of ethylene glycol and bending vibrations of this segment	1406 1460	1407 1454	1408 1458	1406 1458	1406 1458	1407 1454	1410 1453
Vibrations of the aromatic framework with bond stretching C=C	1504 1575	1506 1577	1506 1577	1535 1574	1502 1578	1502 1576	1504 1577
Stretching of the C=O carboxyl group	1716	1714	1713	1716	1717	1717	1730
Symmetrical stretching of the C-H bond	2918 2952	2922 2964 3068	– 2954 3051	2932 2955 –	2928 2966 3049	2922 2961 3060	2908 2969 3054

of the polyethylene terephthalate polymer PET (PET) from [13] are presented.

The results of IR spectroscopy show that the wave numbers and relative intensities of the vibration modes of all five printed samples with different patterns have almost the same values and coincide within the measurement accuracy with the corresponding values of the fundamental modes of the original PETG filament used in 3D printing of the samples and the literature data for PET polymer modes [12]. This means that the intrastructural chemical bonds of the PETG polymer are not subjected to mechanical and thermal influences during the 3D printing process. These effects impact only on the degree of ordering of polymer chains and they are manifested in a change in the relative intensity of the main diffraction maximum of the amorphous PETG polymer in the printed samples compared to the original thread, observed in Fig. 4b.

### 3.3. Wettability of the surface of printed samples with different model patterns

The wettability of a solid surface is a manifestation of intermolecular interaction at the contact boundary of three phases: solid, liquid and gas, which is expressed in the spreading of a liquid over the surface of a solid. Since the measurement of the contact angle of surface wetting is carried out only for the flat samples, this section presents the results of the study of wettability for only five printed samples. Fig. 6 shows the screen images of the setup for measuring the wetting angle of drops on the surface of five samples with different 3D printing patterns from PETG polymer.

Measurements of contact angles were carried out at five points of each sample, and in table 3 shows the average values of these angles.

A comparative analysis of the values of the contact angles of wetting shows that they all deviate only slightly from the angle  $\varphi \approx 50^\circ$ . And only one sample with pattern 1\_Hilbert shows an



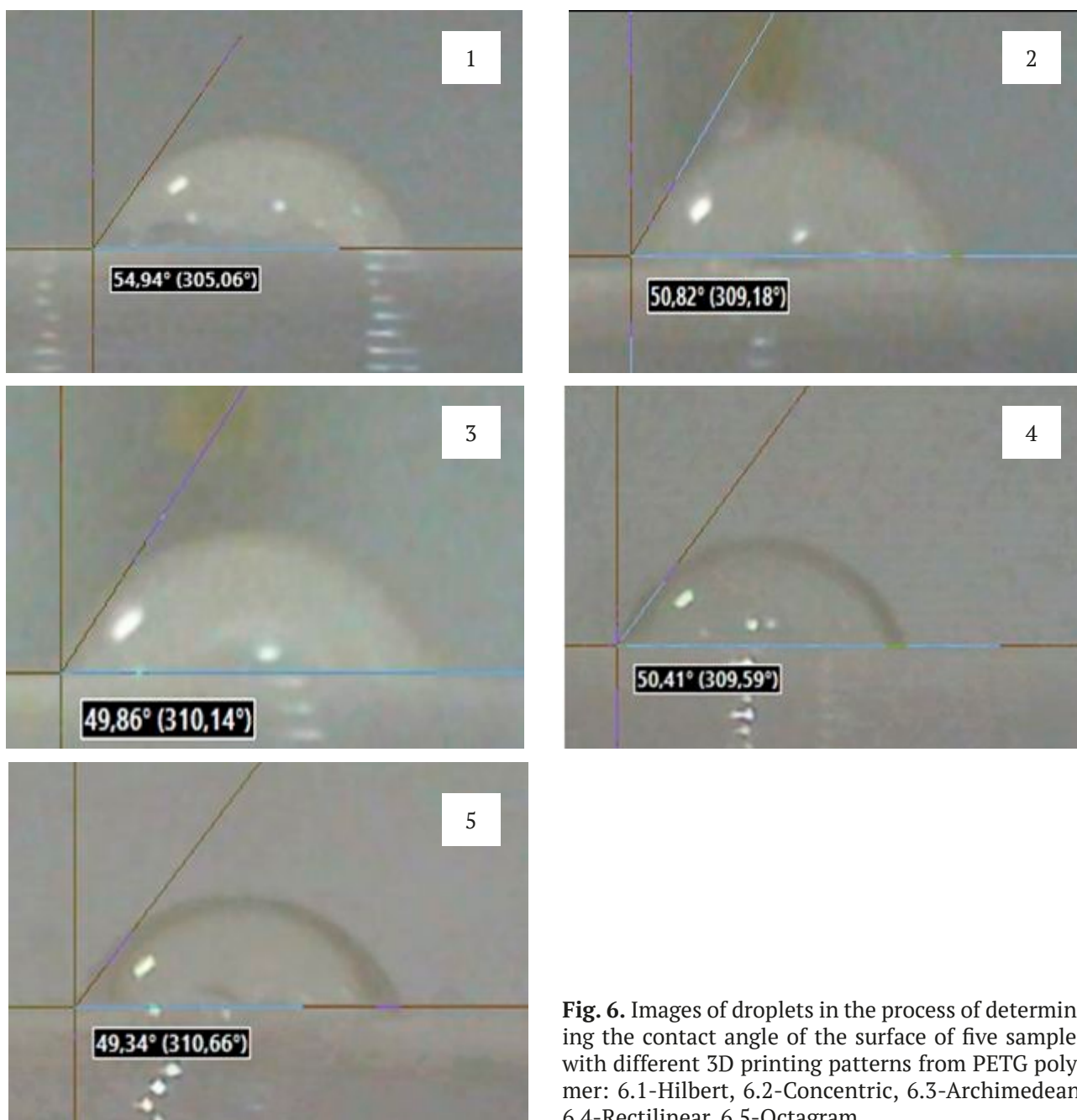


**Fig. 6.** Images of droplets in the process of determining the contact angle of the surface of five samples with different 3D printing patterns from PETG polymer: 6.1-Hilbert, 6.2-Concentric, 6.3-Archimedean, 6.4-Rectilinear, 6.5-Octagram

**Table 3.** Average contact angles of the surface of PETG polymer samples with different 3D printing patterns

Type of model pattern when 3D printing a sample	Average contact angle $\varphi$ , degree
1_Hilbert	52.84
2_Concentric	50.55
3_Archimedean	49.54
4_Rectilinear	50.10
5_Octagram	50.03

average contact angle  $\varphi = 52.84$ , which is slightly higher than the corresponding values for samples with other patterns by one or two degrees, i.e. by an amount within the accuracy of determining the contact angle.

However, the result of a large deviation of the average value of the contact angle  $\varphi \approx 50^\circ$  for all five samples with respect to the right angle of  $90^\circ$  shows that the surfaces of all printed samples with different patterns are hydrophilic, i.e. wettable.

And since the wettability of the surface of a solid body is a manifestation of intermolecular interactions at the interface of contact of the liquid with the surface of the solid body, it should be assumed that one of the mechanisms of such interaction may be the participation of polar ester groups of the PETG polymer in the formation of hydrogen bonds with water molecules on the surface of all five samples, leading to a significant decrease in contact angles relative to  $90^\circ$ .

#### 4. Conclusion

The results obtained in the study of the effect of 3D printing process by successively applying polymer layers employing FDM (Fused Deposition Modeling) method with the Hercules Original 3D printer at an extruder temperature of  $260^\circ\text{C}$  and a power of 500 W on the microstructural and hydrophilic properties of polyethylene terephthalate glycol (PETG) samples with different drawings, X-ray diffraction analysis, IR spectroscopy and measurement of the wetting angle showed that:

- differences between the diffraction patterns of printed samples and the diffraction pattern of the original thread are due to the greater ordering of the polymer chains of amorphous PETG in samples with different patterns, which occurs under thermal and mechanical effects on the original filamentous sample during 3D printing and manifests itself in an increase by an order of magnitude in the relative intensity of the main diffraction maximum of amorphous PETG polymer in printed samples;

- at the same time, the intrastuctural chemical bonds of the PETG polymer are not subjected to the effects of 3D printing process, and therefore the wave numbers and relative intensities of the vibration modes of all five printed samples with different patterns have almost the same values and coincide within the measurement accuracy with the corresponding values of the fundamental modes of the original thread PETG used in 3D printing of samples;

- contact angles for all printed samples show close values to the value of  $\theta \approx 50^\circ$ , which is much smaller than the right angle  $\theta = 90^\circ$ , show that the surfaces of all five printed PETG samples with different patterns are hydrophilic.

- one of the mechanisms of intermolecular interaction at the interface of a drop of water with the surface of printed samples may be the participation of polar ester groups of the PETG polymer in the formation of hydrogen bonds with water molecules on the surface of all five samples, leading to a significant decrease in contact angles relative to  $90^\circ$ .

Thus, according to the results of our study, PETG has asserted itself as a material suitable for 3D printing using a common printer model. At the same time, 3D printing causes statistically significant orientation of polymer chains in the amorphous PETG material, which is all the same for all five patterns, as a result of extrusion-induced molecular alignment, without destroying the intrastuctural chemical bonds of the polymer.

#### The declared contribution of the authors

All authors have made an equivalent contribution to the preparation of the publication

#### Conflict of interest

The authors state that they have no known financial conflicts, interests or personal relationships that could affect the work presented in this article.

#### References

1. Vidakis N., Petousis M., Velidakis E., Liebscher M., Mechtcherine V., Tzounis L. On the strain rate sensitivity of fused filament fabrication (FFF) processed PLA, ABS, PETG, PA6, and PP thermoplastic polymers. *Polymers*. 2022;12: 2924. <https://doi.org/10.3390/polym12122924>
2. Silva A. L., Salvador G. M. da S., Castro S. V. F., Carvalho N. M. F., Munoz R. A. A. 3D printer guide for the development and application of electrochemical cells and devices. *Frontiers in Chemistry*. 2021;9: 684256. <https://doi.org/10.3389/fchem.2021.684256>
3. Vidakis N., Petousis M., Tzounis L., ... Mountakis N. Sustainable additive manufacturing: mechanical response of polyethylene terephthalate glycol over multiple recycling processes. *Materials*. 2021;14: 1162. <https://doi.org/10.3390/ma14051162>
4. Gordeev E. G., Ananikov V. P. Widely accessible 3D printing technologies in chemistry, biochemistry and pharmaceuticals: applications, materials and prospects. *Russian Chemical Reviews*. 2020;89(12): 1507–1561. <https://doi.org/10.1070/rcr4980>

5. Bex G. J. P., Ingenhut B. L. J., Cate T., Sezen M., Ozkoc G. Sustainable approach to produce 3D-printed continuous carbon fiber composites: A comparison of virgin and recycled PETG. *Polymer Composites*. 2021;42: 4253–4264. <https://doi.org/10.1002/pc.26143>

6. Schneevogt H., Stelzner K., Yilmaz B., Abali B. E., Klunker A., Völlmecke C. Sustainability in additive manufacturing: exploring the mechanical potential of recycled PET filaments. *Composites and Advanced Materials*. 2021;30: 263498. <https://doi.org/10.1177/26349833211000063>

7. Latko-Durałek P., Dydek K., Boczkowska A. Thermal, rheological and mechanical properties of PETG/rPETG blends. *Journal of Polymers and the Environment*. 2019;27(11): 2600–2606. <https://doi.org/10.1007/s10924-019-01544-6>

8. Dolzyk G., Jung S. Tensile and fatigue analysis of 3D-printed polyethylene terephthalate glycol. *Journal of Failure Analysis and Prevention*. 2019;19: 511. <https://doi.org/10.1007/s11668-019-00631-z>

9. Hassan M. H., Omar A. M., Daskalakis E., ... B'artolo P. The potential of polyethylene terephthalate glycol as biomaterial for bone tissue engineering. *Polymers*. 2020;12: 3045. <https://doi.org/10.3390/polym12123045>

10. Sobolev D. I., Proyavin M. D., Parshin V. V., Belousov V. I., Ryabov A. V. Broadband, low-reflection microwave windows manufactured using 3D printing\*. In: *X All-Russian Scientific and Technical Conference "Microwave Electronics and Microelectronics". Collection of reports. Saint-Petersburg, 31 of May – 4 of June, 2021. Saint Petersburg*. St. Petersburg: St. Petersburg State Electrotechnical University "LETI" Publ.; 2021. p. 52. (In Russ.)

11. Kiselev M. G., Savich V. V., Pavich T. P. Determination of contact wetting angle on flat surfaces. *Vestnik BNTU*. 2006;1: 38. (In Russ., abstract in Eng.). Available at: <https://www.elibrary.ru/item.asp?id=21398120>

12. Elesina V. V. *Contact angle. Guidelines*. Altai State Technical University named after. I. I. Polzunov Publ.; 2019: 22. (In Russ.)

13. Loskot J., Jezbera D., Bušovský D., ... Zubko M. Influence of print speed on the microstructure, morphology, and mechanical properties of 3D-printed PETG products. *Polymer Testing*. 2023;123: 108055. <https://doi.org/10.1016/j.polymertesting.2023.108055>

14. ICDD Card: 04-003-0648 tetragonal TiO<sub>2</sub>

15. Pereira A. P. dos S., da Silva M. H. P., Júnior É. P. L., Paula A. dos S., Tommasini F. J. Processing and characterization of PET composites reinforced with geopolymer concrete waste. *Materials Research*. 2017;20(suppl 2): 411–420. <https://doi.org/10.1590/1980-5373-mr-2017-0734>

## Information about the authors

*Alexander S. Lenshin*, Dr. Sci. (Phys.–Math.), Leading Researcher, Department of Solid State Physics and Nanostructures, Voronezh State University (Voronezh, Russian Federation).

<https://orcid.org/0000-0002-1939-253X>  
lenshinas@mail.ru

*Vera E. Frolova*, Cand. Sci. (Phys.–Math.), Senior Lecturer, Department of Solid State Physics and Nanostructures, Voronezh State University (Voronezh, Russian Federation).

<https://orcid.org/0009-0000-2880-8958>  
ternovaya@phys.vsu.ru

*Sergey S. Ivkov*, Cand. Sci. (Phys.–Math.), Senior Electronics Engineer, Department of Solid State Physics and Nanostructures, Voronezh State University (Voronezh, Russian Federation).

<https://orcid.org/0000-0003-1658-5579>  
ivkov@phys.vsu.ru

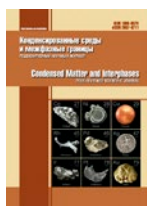
*Evelina P. Domashevskaya*, Dr. Sci. (Phys.–Math.), Full Professor, Department of Solid State Physics and Nanostructures, Voronezh State University (Voronezh, Russian Federation).

<https://orcid.org/0000-0002-6354-4799>  
fft@phys.vsu.ru

*Received 27.10.2023; approved after reviewing 18.11.2023; accepted for publication 25.12.2023; published online 25.03.2023.*

*Translated by Vera Frolova*





# Condensed Matter and Interphases

Kondensirovannyye Sredy i Mezhfaznye Granitsy  
<https://journals.vsu.ru/kcmf/>

## Original articles

Research article

<https://doi.org/10.17308/kcmf.2024.26/11811>

## An investigation of the electronic structure and optoelectronic properties of 4-((2-hydroxy-3-methoxybenzylidene)amino)-N-(thiazol-2-yl) benzene sulfonamide

D. M. Mamand<sup>1</sup>, D. M. Aziz<sup>2</sup>, H. M. Qadr<sup>1</sup>✉

<sup>1</sup>University of Raparin, College of Science, Department of Physics, Sulaymaniyah, Iraq

<sup>2</sup>University of Raparin, College of Science, Department of Chemistry, Sulaymaniyah, Iraq

### Abstract

Molecules of 4-((2-hydroxy-3-methoxybenzylidene)amino)-N-(thiazol-2-yl)benzene sulfonamide were investigated at varying concentrations in dimethyl sulfoxide (DMSO). Different temperatures were employed to assess bandgap energies, Tauc plots, refractive indices, optical and electrical properties, and dielectric constants. The refractive index was determined through a straightforward model based on energy gap data and subsequently compared to experimental values. For the examination of the materials' optical properties, reflection and reflection loss at plasma frequencies were considered as they play a crucial role. Density functional theory (DFT) with a 6-311G++ (d, p) basis set and Becke's three-parameter hybrid (B3LYP) level of theory were utilized through Gaussian software to conduct the studies. Chemical reactivity and selectivity parameters, including HOMO-LUMO, global hardness, softness, electronegativity, electrophilicity, nucleophilicity, chemical potential, bandgap energy, and electron affinity, were computed. Becke's three-parameter hybrid exchange-correlation functional (B3LYP) level was employed for optimizing the geometry of the title molecule.

**Keywords:** Optoelectronic, UV-visible spectroscopy, HOMO-LUMO, DFT

**For citation:** Mamand D. M., Aziz D. M., Qadr H. M. An investigation of the electronic structure and optoelectronic properties of 4-((2-hydroxy-3-methoxybenzylidene) amino)-N-(thiazol-2-yl) benzene sulfonamide. *Condensed Matter and Interphases*. 2024;26(1): 88–103. <https://doi.org/10.17308/kcmf.2024.26/11811>

**Для цитирования:** Маманд Д. М., Азиз Д. М., Квадр Х. М. Исследование электронной структуры и оптоэлектронных свойств 4-((2-гидрокси-3-метоксибензилиден)амино)-N-(тиазол-2-ил) бензолсульфонамида. *Конденсированные среды и межфазные границы*. 2024;26(1): 88–103. <https://doi.org/10.17308/kcmf.2024.26/11811>

✉ Hiwa M. Qadr, e-mail: [hiwa.physics@uor.edu.krd](mailto:hiwa.physics@uor.edu.krd)

© Mamand D. M., Aziz D. M., Qadr H. M., 2024



The content is available under Creative Commons Attribution 4.0 License.

## 1. Introduction

Numerous biodegradable materials, including those designed for electronic applications, hold potential for utilization in the fabrication of electronic devices. Through the application of optical absorption spectroscopy, the optical and electronic characteristics of these biomaterials have been investigated, providing insights into energy diagrams, energy band gaps, and optoelectronic properties associated with such materials [1–3]. The majority of biomaterials, including those with bandgap energies exceeding 2.5 eV such as gelatin, glycerol, and fibrinogen, have been previously documented in studies with values of 3, 3.54, and 3.02 eV, respectively [4–7]. Semiconductor materials typically exhibit bandgap energies falling within the range of 1–1.5 eV, exemplified by conventional semiconductors like gallium arsenide and silicon[8]. In contrast, wide-bandgap (WBG) semiconductors, characterized by bandgaps ranging from 2 to 4 eV, possess distinctive properties that enable devices to operate at higher voltages, frequencies, and temperatures compared to conventional semiconductors [9, 10]. For the investigation of optoelectronic properties, key parameters include bandgap energy, Tauc plot, refractive index, transmittance of light through the molecule, and dielectric properties [11, 12]. The refractive index, an optical property describing the relative speed of light through a material, is influenced by the material's crystalline structure and density, providing valuable physical and chemical characteristics for characterization[13, 14]. With diverse applications in fields such as the pharmaceutical industry, the refractive index plays a crucial role. This study focuses on the theoretical and experimental examination of the molecule 4-((2-hydroxy-3-methoxybenzylidene) amino)-N-(thiazole-2-yl)benzene sulfonamide in dimethyl sulfoxide (DMSO). The investigation aims to determine the applicability of this newly synthesized molecule by assessing physicochemical properties, including physical properties, solvation properties related to interactions with different media, and intrinsic chemical reactivity[15–18]. In recent years, the consideration of physical and chemical characteristics of drugs has gained prominence, as these properties significantly influence a

chemical compound's pharmacological and therapeutic effects. The action and responsivity of a drug can be correlated with its physical and chemical properties, encompassing neutralization, chelation, oxidation, and extracellular reactions [19, 20]. Given the advantages of photonics in various industries, such as optical communications, data storage, and image processing, there is growing interest in nonlinear optical reactions in diverse materials [21].

The primary objective of this study is to comprehensively examine the chemical, physical, and optoelectronic properties of the newly synthesized molecule, including a fully optimized geometrical structure (refer to Figs. 1 and 2) [22]. Quantitative calculations based on Density Functional Theory (DFT) were employed to determine the electronic structure and several quantitative chemical parameters.

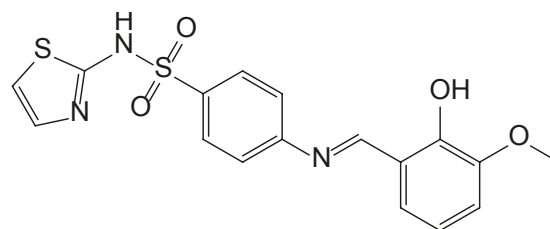


**Fig. 1.** Chemical structure of 4-((2-hydroxy-3-methoxybenzylidene) amino)-N-(thiazole-2-yl)benzene sulfonamide

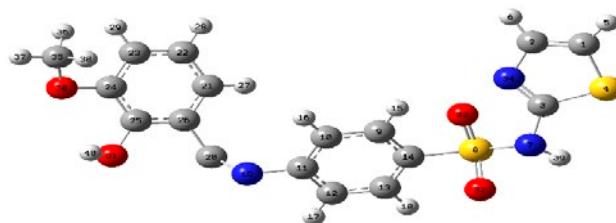


**Fig. 2.** Optimized structure

## 2. UV-visible spectroscopy

UV-visible spectroscopy stands out as a highly valuable and straightforward optical technique for probing the optical and electrical properties of nanomaterials. Numerous research endeavors have harnessed the power of UV-visible applications to elucidate the behavior of diverse nanomaterials, ranging from polymers and organic light-emitting materials to combinations of organic and inorganic semiconductors[23,

24]. The reflected spectra obtained through this technique offer insights into the fundamental electronic properties of the samples under investigation. The bandgap energy, a crucial parameter, plays a pivotal role in defining various optical properties such as refractive index, scattering angular frequency, electronegativity, and dielectric constant of materials. This parameter has emerged as a powerful tool for efficiently designing novel semiconductor devices, including 2D electron gas and LEDs [25]. Notably, the bandgap energy of materials has recently gained recognition not only in the context of advanced semiconductor technology but also in the construction of cutting-edge equipment. This recognition extends to its role as a technology platform facilitating the development of innovative devices like high-capacity batteries and ultra-efficient solar cells [25]. In scenarios involving embedded electric fields, the technique proves essential for ionizing holes from deep acceptor dopants. This ionization process is facilitated by the unbalanced polarization charge correlated with the gradient layer, thereby enabling the creation of electric fields. The material 4-((2-hydroxy-3-methoxybenzylidene)

amino)-N-(thiazol-2-yl)benzene sulfonamide, and materials derived from it, can be applied to semiconductor crystals capable of maintaining sufficient piezoelectric polarization and strong spontaneous polarization. These properties make them versatile candidates for a range of applications in the realm of nanoelectronics and advanced semiconductor devices.

The relationship between the absorbance of light at a specific frequency and the concentration of molecules is found to be directly proportional, as illustrated in Table 1. This association is further elucidated in Fig. 3, where an increase in the absorption of photon energy is observed in tandem with changes in concentration, akin to the effect of path length. The initial concentration of the solution is highest, resulting in a greater number of molecules for incident light to interact with as it traverses through the medium. Consequently, an elevated concentration leads to increased light absorption, signifying a higher number of molecules in the solution. This alignment with Beer-Lambert's law establishes a direct proportionality between absorbance and concentration, where an augmentation in the original concentration corresponds to an increase in absorption.

**Table 1.** Maximum absorption at different concentrations and temperatures 4-((2-hydroxy-3-methoxybenzylidene) amino)-N-(thiazole-2-yl) benzenesulfonamide in DMSO

Concentration (mg/l)	Temperature 303.15 K			Temperature 313.15 K		
	1.026	0.513	0.2565	1.026	0.513	0.2565
$\lambda_{\max}$ (nm)	362	331	328	362	353	325.32
Bandgap (eV)	3.425	3.746	3.78	3.425	3.512	3.811

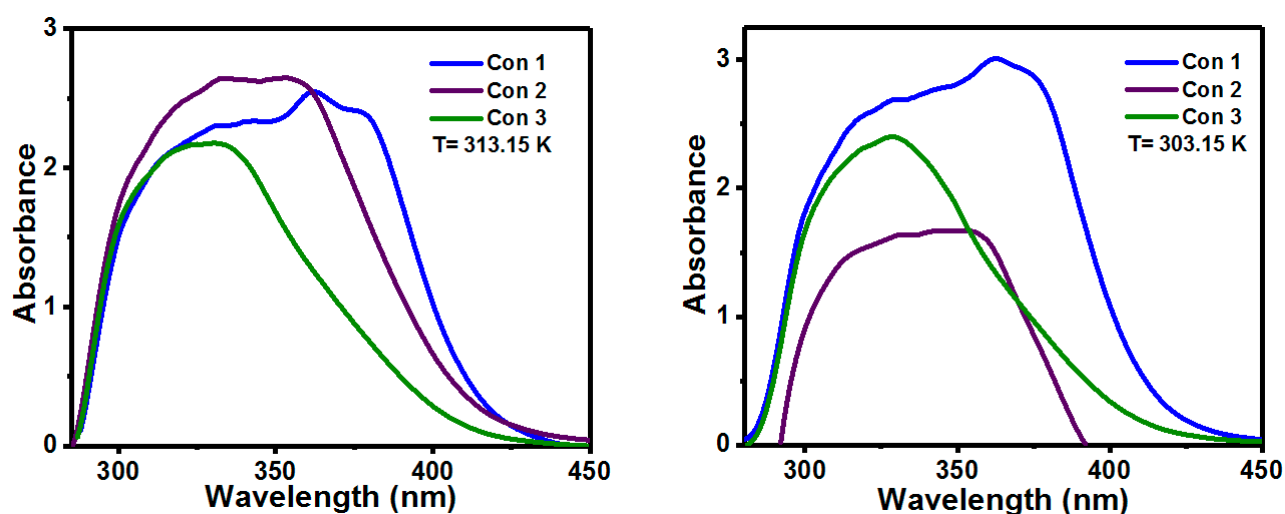


**Fig. 3.** UV-spectrum of 4-((2-hydroxy-3-methoxybenzylidene) amino)-N-(thiazol-2-yl) benzene sulfonamide in DMSO solvent at different temperatures



However, the second concentration exhibits a decrease in absorption. This deviation can be rationalized by considering the dilution of the solution, implying a reduction in the initial concentration. As the solution is diluted, the number of molecules available for light interaction decreases, resulting in a proportional decrease in absorption. This observation aligns with Beer-Lambert's law, emphasizing the direct relationship between absorbance and concentration. Therefore, in the present study, the reduction in absorption at the second concentration level can be attributed to the dilution of the solution, reflecting the anticipated proportional decrease in concentration.

The optical and electrical characteristics of semiconductor materials exhibit notable distinctions between wide bandgap energies and narrow bandgap energy configurations. The molecule 4-((2-hydroxy-3-methoxybenzylidene)amino)-N-(thiazol-2-yl)benzene sulfonamide possesses a wide bandgap exceeding 3 eV. Wide-bandgap semiconductors (WBGs) are characterized by a larger bandgap compared to conventional semiconductors, with the latter falling within the 1-1.5 eV range (e.g., germanium and silicon), while the former extends from 2 to 4 eV. Typically, WBGs exhibit electronic characteristics intermediate to insulators and conventional semiconductors. The distinct properties of WBG materials make them highly suitable for a broad spectrum of applications, allowing devices to operate at significantly elevated voltages, frequencies, and temperatures, approximately up to 300 °C. This capability surpasses the operational limits of conventional semiconductor materials like silicon and gallium arsenide. Applications utilizing WBG materials include a variety of devices and pigments such as radars, radiofrequency devices, lasers, and light-emitting diodes (LEDs), benefitting from their ability to function at higher power levels under normal conditions due to their enhanced thermal stability [26-28]. The electronic spectra of the 4-((2-hydroxy-3-methoxybenzylidene)amino)-N-(thiazol-2-yl)benzene sulfonamide compound reveal two discernible bands. The first band, located at  $\lambda_{\max} = 300-312$  nm, is attributed to the  $\pi \rightarrow \pi^*$  transition within the aromatic system of the phenyl group. The third

band, situated at  $\lambda_{\max} = 430-460$  nm, is associated with the C=N chromophore of these compounds, as indicated in Table 1. UV-visible spectra of this compound were investigated at different temperatures in dimethyl sulfoxide (DMSO), with Figure 3 depicting the UV spectra of compound at varying temperatures. At room temperature, the selected compound exhibits two absorptions in the range of 300–600 nm, specifically at 393 nm for the enol-imine form and at 453 nm for the keto-amine form. Upon cooling the solution to 15 °C, a color change from orange to yellow occurs, accompanied by the disappearance of the absorption band at 453 nm for the keto form in the UV-visible spectra. Upon reheating the solution, the absorption band for the keto form reappears. This behavior indicates the existence of an enol-keto equilibrium, and notably, the equilibrium is temperature-dependent.

This study aims to explore the optoelectronic properties of the 4-((2-hydroxy-3-methoxybenzylidene)amino)-N-(thiazol-2-yl)benzene sulfonamide molecule, garnering significant interest due to its noteworthy optical characteristics. The bandgap energy of this molecule is assessed through UV calculations, as depicted in Figures 2 and 3. The UV spectra reveal a singular peak across various concentrations and temperatures, as detailed in Table 1. The substantial bandgap within this range makes it particularly intriguing for applications in optoelectronic devices and transparent conductive oxide electrodes within solar cells. The utility of bandgap energy in this context is vital for extracting photo-generated carriers in solar cells. Transparent conducting oxide semiconductors, especially those with continuously graded bandgaps, have become a focal point of interest [29]. The ability to tune bandgap energy through continuous and independent manipulation of hole and electron properties adds versatility to its potential applications. The classification of optical bandgap is a prerequisite for device fabrication and holds significance in the optical characterization of these applications. Understanding and manipulating the bandgap energy of the 4-((2-hydroxy-3-methoxybenzylidene)amino)-N-(thiazol-2-yl)benzenesulfonamide molecule offer promising avenues for advancing optoelectronic

technologies, paving the way for innovative developments in solar cells and related devices.

### 3. Tauc-plot calculations

The absorption coefficient ( $\alpha$ ) with respect to photon energy ( $h\nu$ ) serves as a metric for characterizing the light absorption properties of semiconductor materials. The provided expression facilitates the computation of both the optical bandgap energy ( $E_g$ ) and the forbidden bandwidth associated with optical transitions in semiconductors. This formalism enables the determination of key parameters critical for understanding the semiconductor’s response to light absorption, offering insights into its optical behavior and facilitating the calculation of optical bandgap energy and forbidden bandwidth  $E_g$  [30]:

$$(\alpha h\nu) = A^* (h\nu - E_g)^m \tag{1}$$

Here,  $A^*$  denotes a constant, and  $m$  serves as the parameter associated with the characterization of band gaps based on the measurement type. For any transition to occur, the principles of crystal momentum conservation and energy conservation must be adhered to. In semiconductor physics, the bandgap of a semiconductor encompasses two distinct types: direct and indirect bandgaps. The maximal-energy state in the valence band and the minimal energy state in the conduction band within the Brillouin zone are distinctly characterized by specific crystal momentum [31].

The term “indirect bandgap” is applied when the crystal momentum of electrons and holes differs in both the conduction and valence bands. The determination of the type of bandgap energy for 4-((2-hydroxy-3-methoxybenzylidene)amino)-N-(thiazol-2-yl)benzene sulfonamide is achieved through a comparison between the UV-visible bandgap energy and the Tauc plot, revealing that it falls under the category of indirect bandgap. The value of  $m$  is contingent upon the type of semiconductor bandgap energy and encompasses four distinct values:  $3/2$  for forbidden transition,  $3$  for forbidden indirect transition,  $2$  for allowing indirect transition [32]:

$$(\alpha h\nu) = A^* (h\nu - E_g)^2 \tag{2}$$

Various methods can be employed to determine the bandgap energy, including Tauc plot, the first derivation of absorbance, and transmittance. For the 4-((2-hydroxy-3-methoxybenzylidene) amino)-N-(thiazol-2-yl)benzene sulfonamide molecule, the Tauc plot emerges as the most effective approach for calculating the bandgap energy ( $E_g$ ). The values of  $E_g$  obtained through the Tauc plot method exhibit high similarity with those derived from the UV-visible spectra. Specifically, the  $E_g$  values, according to the Tauc plot method, are found to be 3.03, 3.18, 3.23 eV at one set of conditions and 3.02, 3.15, 3.16 eV at another set of conditions, corresponding to temperatures of 30 and 40 °C, as illustrated in Fig. 4.

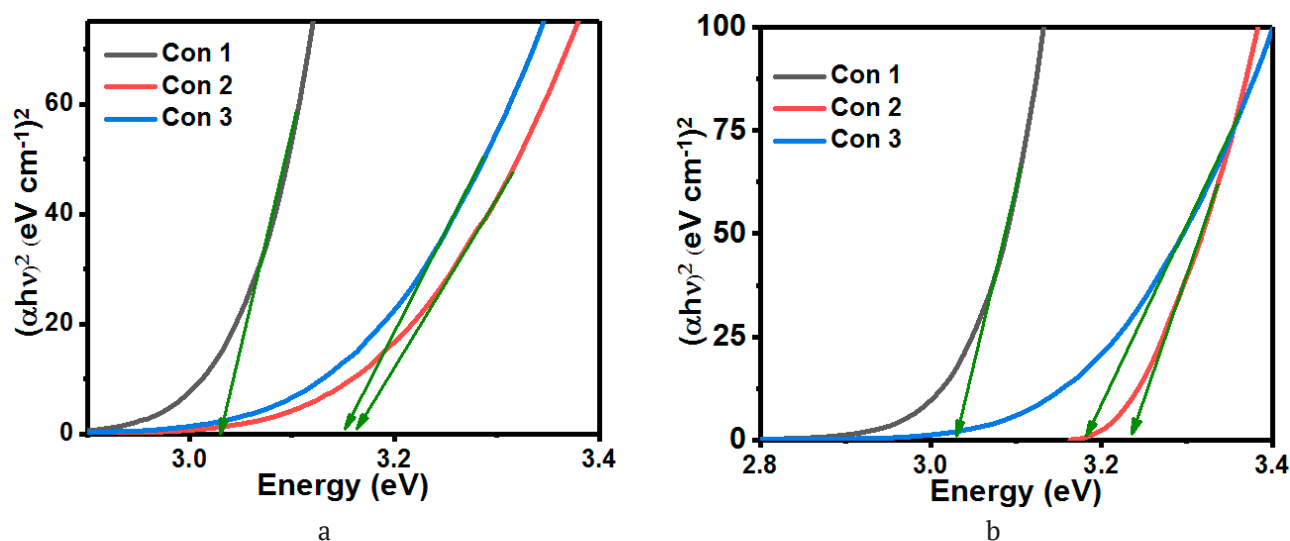


Fig. 4. Tauc-plot of 4-((2-hydroxy-3-methoxybenzylidene) amino)-N-(thiazol-2-yl) benzene sulfonamide in DMSO (A) at 303.15 K and (B) at 313.15 K

### 3.1. Refractive index

The refractive index of semiconductor materials holds considerable importance in determining various parameters, including electronegativity, bandgap energy, electrical and optical conductivity, and dielectric constant. The performance of devices is contingent on the refractive index, making it a crucial factor in optoelectronic applications and technologies. The refractive index, denoted by the symbol  $n$ , can be obtained from the following expression [33]:

$$n = \left\{ \left[ \frac{4R}{(R-1)^2} - k^2 \right]^{\frac{1}{2}} - \frac{R+1}{R-1} \right\}. \quad (3)$$

The characterization of semiconducting materials, fundamental to their optical and electrical properties, relies on two key parameters: energy gap and refractive index. The refractive index ( $n$ ) is a descriptor of transparency to incident photons, while the energy gap ( $E_g$ ) is determined by the threshold of photon absorption in a semiconductor. Various relationships exist between  $E_g$  and  $n$ , including those formulated by Moss, Ravindra, Hervé and Vandamme, as well as Reddy and Kumar, and Singh. The Moss and semi-empirical correlations, established as early as the 1950s, have been subjects of intensive study in subsequent years. These relationships play a crucial role in understanding and characterizing the optical and electrical properties of semiconducting materials [34–37].

Reddy relation:

$$n^4 (E_g - 0.365) = 154. \quad (4)$$

Moss relationship:

$$n^4 E_g = 95 \text{ eV}. \quad (5)$$

Ravindra relationship:

$$n = 4.084 - 0.62 E_g. \quad (6)$$

From the following equation of Tripathy, the relationship can calculate the refractive index:

$$n = n_0 \left[ 1 + \alpha e^{-\beta E_g} \right]. \quad (7)$$

Where,  $\alpha$ ,  $\beta$  and  $n_0$  are constants which are equal to 1.9017, 0.539 eV<sup>-1</sup> and 1.37 respectively.

Herve–Vandamme relationship:

$$n^2 = 1 + \left( \frac{A}{E_g + B} \right)^2. \quad (8)$$

Kumar and Singh relations:

$$n = K E_g^c. \quad (9)$$

Where,  $K$  and  $C$  are constants which are equal to 3.3668 and  $-0.32234$ .

The refractive index ( $n$ ) is a crucial parameter in the characterization of physical and chemical properties of materials, forming the basis for transparency measurements. Accurate knowledge of  $n$  is essential for designing optoelectronic devices due to its influence on electronic characteristics and the band structure of materials. In the case of the 4-((2-hydroxy-3-methoxybenzylidene)amino)-N-(thiazol-2-yl) benzene sulfonamide molecule, the refractive index is illustrated in Fig. 5. Experimental  $n$  values exhibit the lowest value compared to other relationships. Initially, the change in refractive index follows an approximately linear trend. Subsequently,  $n$  increases from 3.3 to 4.25 eV before decreasing to its initial position. At 6.19 eV,  $n$  is observed to be 0.18, with this value coinciding with the experimental and Ravindra relationship values. While each relationship has its unique characteristics, the Reddy relationship generally demonstrates the best compatibility with the refractive index. However, as the band gap exceeds 4 eV, the Moss relationship aligns more closely with experimental refractive index values. This relationship, for instance, at 6.2 eV, provides a closer match with experimental data in the middle to moderately high energy gap range. Nevertheless, it is noted that the Moss equation is inaccurate for materials with a band gap less than 0.365 eV [38]. The applicability of these relationships is contingent on the material type and bandgap energy. For instance, the Kumar & Singh relationship is more suitable for semiconductor binaries compared to other materials.

Moss's determination reveals that electron energy levels are scaled down by the effective dielectric constant, experienced by the electron within the material, based on photoconductivity [39]. The dielectric constant of materials is approximately proportional to the square of the

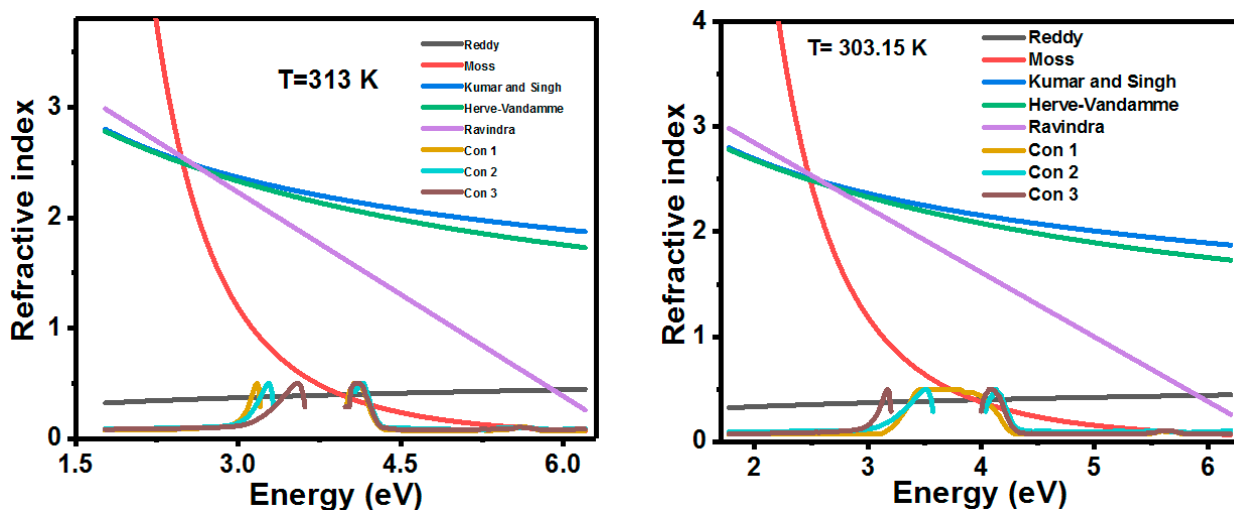


Fig. 5. Variation of refractive index of different relations with bandgap energy of 4-((2-hydroxy-3-methoxybenzylidene) amino)-N-(thiazol-2-yl) benzene sulfonamide molecule in DMSO solvent

refractive index. The Ravindra relation, used to calculate the refractive index for semiconductors, assumes a linear relationship in energy gap, postulating that the valence and conduction bands are more or less parallel to each other along symmetry directions[40]. This model posits a constant difference between UV resonance energy and the energy gap, based on oscillatory theory assumptions. In the context of the 4-((2-hydroxy-3-methoxybenzylidene)amino)-N-(thiazol-2-yl)benzene sulfonamide molecule in DMSO, the Kumar and Singh relationship yields a refractive index (*n*) value of 2.33. This model describes *n* as governed by an energy law behavior with respect to the energy gap, and the model parameters are fitted to experimental energy gaps and refractive index data. Moss’s calculation for *n* in DMSO results in the highest value in this study, reaching 4.856 as presented in Table 2. The refractive index is influenced by the wavelength of light and the concentration in the solution. The relationship between temperature and the refractive index of molecules is explained by the refractive index remaining unaffected by temperature changes

but varying due to alterations in density. With increasing temperature, materials typically expand, leading to a decrease in density. However, if the material undergoes compression, the density remains constant despite temperature changes. Notably, altering pressure does not induce changes in the refractive index [41–43].

Dispersion is a crucial parameter for comprehending the physical properties of materials, particularly how light bends at specific wavelengths. In Fig. 6, the Normal dispersion region of the 4-((2-hydroxy-3-methoxybenzylidene) amino)-N-(thiazol-2-yl)benzene sulfonamide molecule in DMSO is calculated by considering the relationship between the refractive index and angular frequency. The scattering area is a key property for designing optical pigments. As the angular frequency increases, the refractive index may fluctuate, leading to an expansion of the scattering area. Utilizing the refractive index and Normal dispersion area in the design of multi-element systems is highly valuable, enabling designers to precisely predict how light will behave throughout the entire optical path.

Table. 2. The average value of refractive indices of the 4-((2-hydroxy-3-methoxybenzylidene)amino)-N-(thiazol-2-yl) benzene sulfonamide molecule in DMSO for various relations and experimental

Moss	Reddy	Herve-Vandamme	Ravindra	Kumar and Singh	T = 303.15 K			T = 313.15 K		
					Concentration					
					1	2	3	1	2	3
4.856	0.3831	2.25505	1.62242	2.336455	0.0866	0.0706	0.0918	0.0738	0.0856	0.082



### 3.2. Reflectivity and reflection loss

The optical response of a material’s surface can be assessed through the reflectivity coefficient, which is defined as the ratio of reflected power to incident power. This coefficient holds significance in understanding the optical properties of materials. The reflectivity can be calculated in terms of the extinction coefficient and refractive index, and this relationship is expressed as follows [44, 45]:

$$R = \frac{(n - 1)^2 + k^2}{(n + 1)^2 + k^2} \tag{10}$$

Where  $k$  is represent the frequency-dependent extinction coefficient, for a weak absorber  $k$  can be considered too small and at the high frequency it vanishes. The following expression can calculate the reflectivity at a higher frequency:

$$R = \left( \frac{n - 1}{n + 1} \right)^2 \tag{11}$$

The relation between reflectivity and reflection coefficient can determine the reflection coefficient:

$$r = \sqrt{R} \tag{12}$$

The reflectivity exhibits its highest values at both the lowest and highest bandgap energies, as depicted in Figures 6 and 7. During the maximum absorption of light within the range of 3.2 to 3.9 eV for both temperature conditions, the reflectivity reaches its lowest values, indicating minimal reflection of light. At lower temperatures, the reflectivity is smaller compared to higher temperatures, which could be attributed to the expansion of the particle interiors within the

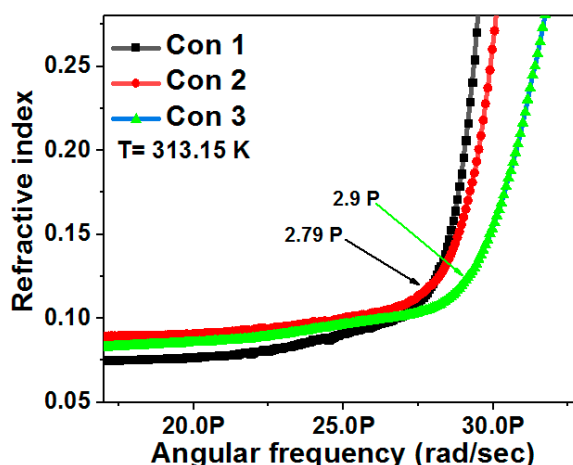
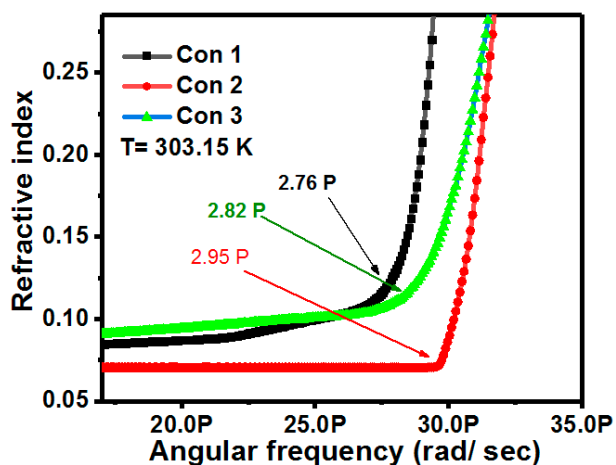


Fig. 6. Normal dispersion region of 4-((2-hydroxy-3-methoxybenzylidene) amino)-N-(thiazol-2-yl) benzene sulfonamide molecule in DMSO

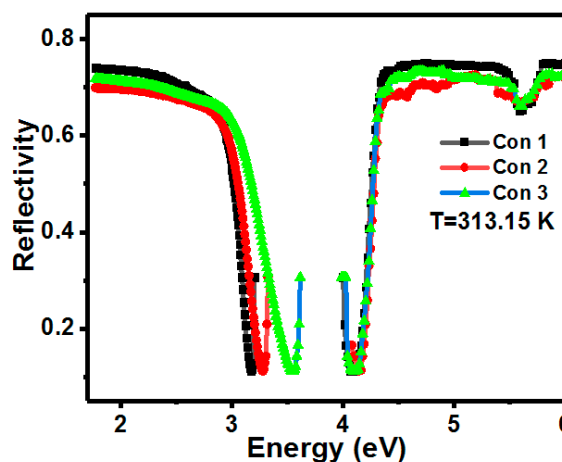
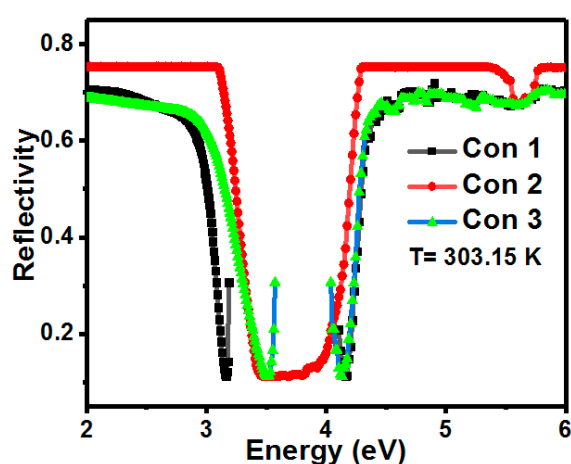


Fig. 7. Variation of reflectivity with bandgap energy of 4-((2-hydroxy-3-methoxybenzylidene) amino)-N-(thiazol-2-yl) benzene sulfonamide molecule in DMSO

molecule and the vibrational motion of atoms. As the aggregation proceeds, the medium becomes more turbid, leading to an increase in light absorption. By considering the ratio of the stability of these measurements to the constant aggregation rate  $k$ , the absorbance of photon energy is enhanced.

The optical behavior of semiconductor materials at very low frequencies exhibits characteristics akin to metals, while at high frequencies, they resemble insulators. The plasma frequency serves as a characteristic frequency at which the material transitions from a metallic to a dielectric response [46]. According to the Drude model, the plasma frequency is defined as frequency at which the real part of the dielectric function vanishes  $\epsilon_r(\omega_p) = 0$ .

Refractive index and absorption coefficient ( $k$ ) are the same at a low frequency while  $k$  and  $n$  are large. The following equation can describe the Normal reflectivity [47]:

$$R = \frac{(n-1)^2 + k^2}{(n+1)^2 + k^2} = \frac{n^2 + k^2 - 2n}{n^2 + k^2 + 2n} \quad (13)$$

$$= 1 - \frac{4n}{n^2 + k^2} \approx 1 - \frac{2}{n}.$$

A material with a large concentration at low frequency acts as a perfect reflector. The sharpness of the plasma structure, determined by the relaxation time at the plasma frequency, is indicative of a longer relaxation time when the plasma structure is sharper. The absorption property is crucial due to its relationship with electrical and optical properties through the conductivity tensor. A material that is a good electrical conductor exhibits high reflection, while transparent materials are generally expected to have reasonably poor electrical conductivity [48].

#### 4. Optical and electrical conductivity

The electrical and optical conductivity of semiconductor materials is very significant for the investigation of the variation of conductivity with bandgap energy. From the following expressions can calculate both of them [49]:

$$\sigma_{\text{opt}} = \frac{\alpha n c}{4\pi}, \quad (13)$$

$$\sigma_{\text{ele}} = \frac{2\lambda\sigma_{\text{opt}}}{\alpha}. \quad (14)$$

Here,  $\lambda$  is the wavelength of the incident light,  $c$  is the velocity of light and  $\alpha$  is the absorption coefficient.

Figs. 8 a and b show the photoconductivity variation at 303.15 and 313.15 K for three different concentrations in the range of 3.4 to 3.8 eV. The optical conductivity has the lowest value due to the lack of light absorption. At 3.2 and 3.9 eV, it has the highest value corresponding to the maximum absorption as mentioned in Fig. 3. From the explanation in Fig. 8c and d, when an increase in temperature leads to an increase in conductivity and a decrease in resistance. The electrons in the valence band get excited and jump into the conduction band from HOMO (highest occupied molecular orbital) to LUMO (lowest unoccupied molecular orbital) in the case of semiconductors as the temperature increases. Hence, resulting in the dwindling of resistance the conductance increases. The resistivity and conductivity increase, and the reciprocal of conductivity decreases.

#### 5. Dielectric constant

The dielectric constant of compounds plays a significant role in determining the conduction properties of the material. The electrical properties of a material are influenced by various factors, including different growth parameters such as deposition rate, substrate temperature, thickness, and film composition. The application of thin films for photovoltaic applications depends on the electrical properties of the materials, making it crucial for determining their suitability for specific applications. The dielectric constant can be calculated using the following expression [50]:

$$\epsilon^* = \epsilon' + j\epsilon'' \quad (16)$$

Where the two parameters  $\epsilon'$  and  $\epsilon''$  represent the real part dielectric constant and imaginary part (dielectric loss), respectively. The grain, charge storage capabilities of dielectric material, grain boundary, grain, insights into the structure of compounds and transport properties are related to the dielectric spectroscopy of materials that is very significant. The potential barrier generates at the grain boundaries, and

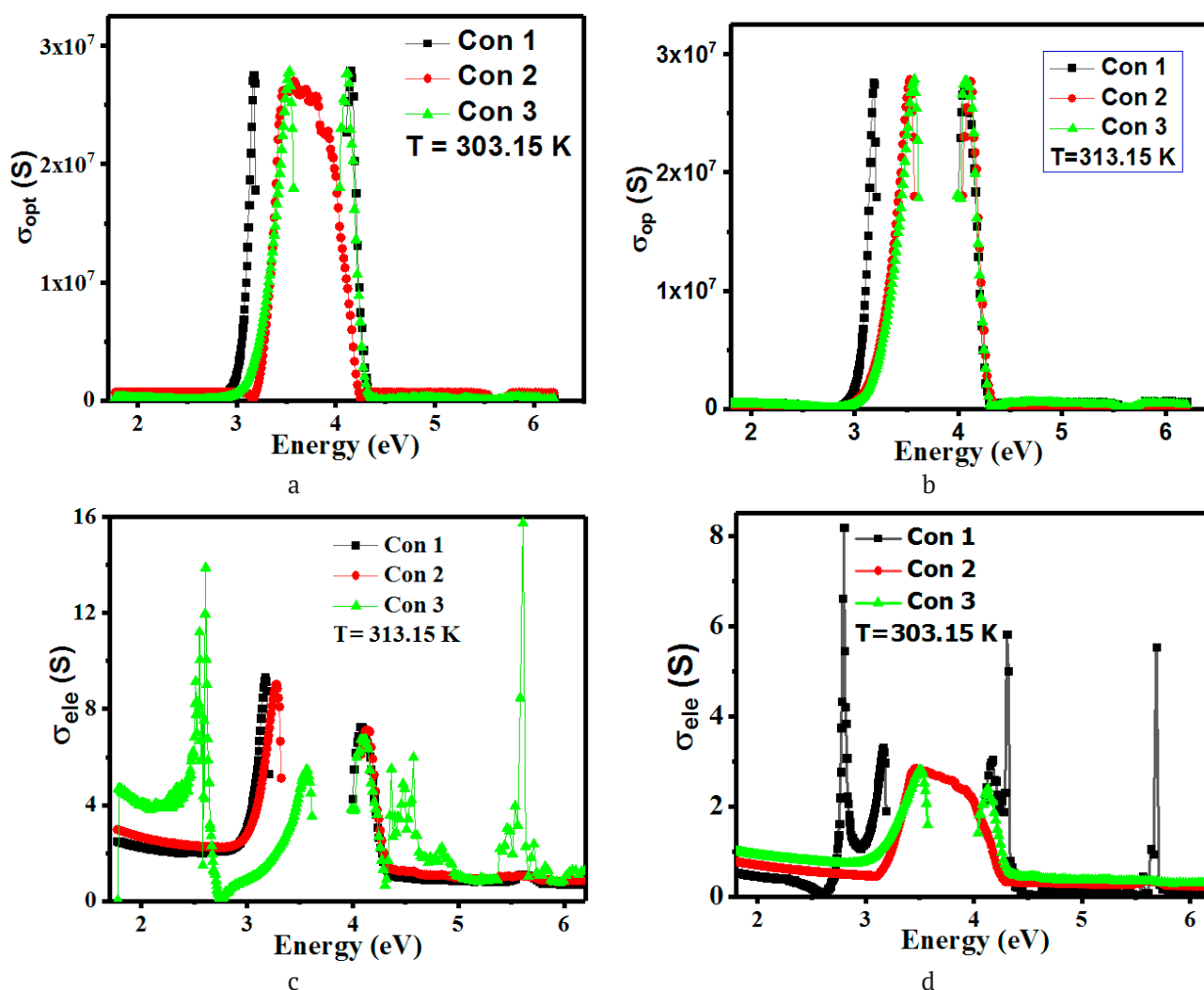


**Fig. 8.** Optical and electrical conductivity of 4-((2-hydroxy-3-methoxybenzylidene) amino)-N-(thiazol-2-yl) benzene sulfonamide molecule in DMSO

due to the presence of charge polarization, the dielectric constant increases with increased frequency [51].

At a specific frequency, the permittivity or dielectric constant represents the relationship between the electric field vector and the electric displacement vector. It's noteworthy that the dielectric constant can assume negative values at certain frequency bands, such as in plasmas at radio frequencies or metals at infrared frequencies. In Fig. 9, the real part of the dielectric constant is shown as negative, indicating negative permittivity, where the electric displacement vector and the electric field vector are in opposite directions. However, this negative value does not necessarily imply that the electrical energy stored in this medium is negative. The dielectric

constant of materials depends on the molecular structure. Whether the dielectric constant increases or decreases during a given phase change relies on the specific phases involved, and the dielectric constant can exhibit sudden changes at phase boundaries with variations in temperature, as illustrated in Fig. 9.

## 6. Electronic structure

Based on density functional theory at the B3LYP level of theory with 6-311G++ (*d*, *p*), quantum chemical calculations were carried out with the complete geometry optimizations of the chosen molecule [52]. The quantum chemical parameters from the HOMO and LUMO were performed. This study is to investigate the molecular properties regarding the reactivity and

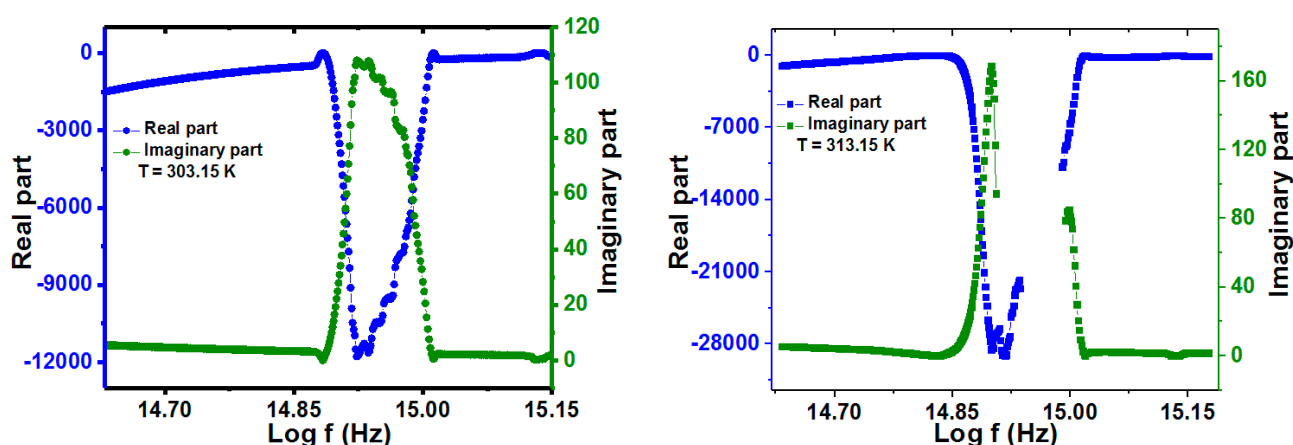


Fig. 9. Dielectric constant, real and imaginary part of 4-((2-hydroxy-3-methoxybenzylidene) amino)-N-(thiazol-2-yl) benzene sulfonamide molecule in DMSO at the second concentration associated with Table 1

selectivity of the compounds, they were estimated by Koopmans theory which related to HOMO ( $E_{\text{HOMO}}$ ) and LUMO ( $E_{\text{LUMO}}$ ) energy [53, 54].

Many quantitative chemical parameters such as ionization energy ( $I$ ) and electron affinity ( $A$ ) can be calculated. Ionization energy can be expressed in quantum computational chemistry and is the energy required to break an electron from a chemical species into a gas phase or isolated state. Based on Koopmans' theory, the ionization energies of chemical species are related to the HOMO energy which is the energy required to break an electron from HOMO. From the following equation can be calculated the ionization energy and is considered as the opposite sign of HOMO energy [55]:

$$I = -E_{\text{HOMO}}. \quad (17)$$

In the case of gas and isolated state, the change of electron energy absorption reaction of chemical species can be described by electron affinity. Electron affinity calculations are based on LUMO energy because in the basic type, the electron to be received will enter the lower-energy free orbital. Using Koopman's theorem, the electron affinity can be calculated for chemical species and is equal to the inverse sign of the LUMO energy:

$$A = -E_{\text{LUMO}}. \quad (18)$$

From the following equation, the bandgap energy of the particles can be calculated and is equal to the difference between  $E_{\text{LUMO}}$  and  $E_{\text{HOMO}}$ :

$$\Delta E = E_{\text{LUMO}} - E_{\text{HOMO}}. \quad (19)$$

The energy gaps are very different from each other in the intermolecular interaction such as the strong ionic interaction between molecules whose energy gap varies greatly. The energy gaps are very close to each other in the intermolecular interaction in strong covalent interaction. The hardness and softness property of molecules are useful parameters to describe chemical reactivity. Associate with corrosion inhibition efficiency, the soft molecule has a high inhibition efficiency than the hard molecule. Chemical hardness ( $\eta$ ) and softness ( $\sigma$ ) can be calculated using the following relation:

$$\eta = \frac{I - A}{2}, \quad (20)$$

$$\sigma = \frac{1}{\eta}. \quad (21)$$

Mulliken's electronegativity or absolute electronegativity is one of the essential factors that can calculate in quantum chemical computation, which is the arithmetic mean of ionization energy and electron affinity for species. The influential electron electrophiles or acceptors indicate the species with high electronegativity. The nucleophiles or donor electron represents low electronegativity. Mulliken electronegativity ( $\chi$ ) can be written as [56]:

$$\chi = \frac{I + A}{2}. \quad (22)$$

The calculated parameters for HOMO energy, LUMO energy, ionization energy ( $I$ ), electron affinity ( $A$ ), energy gap ( $\Delta E$ ), hardness ( $\eta$ ), softness



( $\sigma$ ), electronegativity ( $\chi$ ), chemical potential (CP), electrophilicity index ( $w$ ), Nucleophilicity (N), Back-donation energy ( $\Delta E_{B-d}$ ) and electron transferred ( $\Delta N$ ) are given in Table 3 for DMSO solvent. Fig. 10 shows HOMO and LUMO of DFT at 4-((2-hydroxy-3-methoxybenzylidene) amino)-N-(thiazol-2-yl) benzene sulfonamide molecule in DMSO and optimizing geometry performed at B3LYP level and the 6-311G ++ (d, p).

The theoretical and experimental values of bandgap energy agree well. The differences in  $E_g$  at different concentrations with temperature are slightly different from the theoretical. The electrophilicity index of this molecule has a high value and the molecule with a high electrophilicity index have more electron flux if they are involved in a transponder interaction and lower the energy more because of this electron flux

## 7. Electrostatic potential map

The charge distribution on the molecular surface is analyzed in three dimensions (X, Y, Z) through the molecule's electrical potential surface[57]. The Molecular Electrostatic Potential (MEP) allows for the visualization of variably charged regions on the molecule's surface, offering a valuable map to elucidate and discern chemical reactions and interactions with other molecules [58, 59]. This mapping is particularly useful in describing the characteristics of chemical bonds, commonly referred to as the "color code" section, as it vividly illustrates the charge distribution on the surface of Anthracene. Each color is distributed distinctively across the molecule's surface, and the geometry optimization was

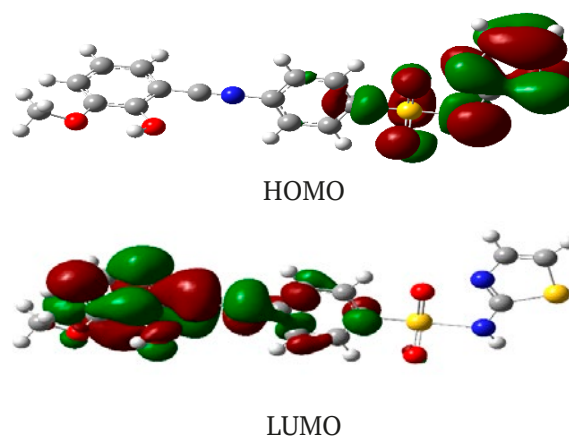


**Fig. 10.** HOMO and LUMO of DFT at 4-((2-hydroxy-3-methoxybenzylidene) amino)-N-(thiazol-2-yl) benzene sulfonamide molecule in DMSO and optimizing geometry performed at B3LYP level and the 6-311G ++ (d, p)

conducted at the B3LYP level with the 6-311G++ (d, p) basis set. In this color-coded representation, the red color signifies the presence of electrons, predominantly surrounding the sulfur bonds with O32 and O33 atoms, transitioning to yellow regions located between the carbon and hydrogen bonds. Hydrogen is distinctly depicted in green, denoting its lower electronegativity compared to red and yellow regions, as illustrated in Fig. 11. MEPs provide insights into the polarization range, with the molecule's electronegativity playing a significant role in determining the polarization of charges. The regions where colors do not intersect effectively help identify areas with high negative or positive charges. Notably,

**Table 3.** Quantum computational parameters based on DFT at 4-((2-hydroxy-3-methoxybenzylidene) amino)-N-(thiazol-2-yl) benzene sulfonamide molecule in DMSO and optimizing geometry performed at (B3LYP) level and the 6-311G ++ (d, p)

$E_{HOMO}$ (eV)	$E_{LUMO}$ (eV)	$\Delta E$ (eV)	$I$	$A$	$\eta$	$\sigma$	$\chi$	CP	$w$	N	$\Delta E_{B-d}$	$\Delta N$
-5.40	-2.54	2.86	5.40	2.54	1.43	0.69	3.97	-3.9	5.51	0.18	-0.358	1.05

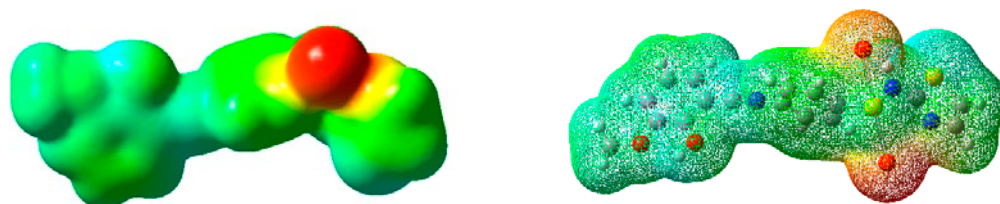


**Fig. 11.** Electrostatic potential map of 4-((2-hydroxy-3-methoxybenzylidene) amino)-N-(thiazol-2-yl) benzene sulfonamide molecule in DMSO based on DFT at 6-311G++ (d, p) basis set

negative potential sites are concentrated around the carbon resonant bonds of benzene rings. The molecular electrostatic potential map highlights a robust repulsion at positive potential sites on edge hydrogen atoms, while carbon bonds exhibit a compelling attraction.

## 8. Conclusion

The optical characteristics of the 4-((2-hydroxy-3-methoxybenzylidene)amino)-N-(thiazol-2-yl)benzene sulfonamide molecule in DMSO were systematically examined in this study. It was observed that the bandgap energy of the molecule could be manipulated by adjusting its concentration. Notably, the practical refractive index, determined in comparison to other relationships, exhibited its lowest value. The investigation also revealed that temperature exerts an influence on the spatial arrangement of atoms, forming the molecular structure. As temperature increases, the optical density of the sample medium decreases due to enhanced atomic vibration, leading to an expansion of interatomic distances. Consequently, the medium becomes less optically dense, resulting in a higher velocity of light and a lower refractive index, causing a slight alteration in the deflection angle at elevated temperatures. While the optical conductivity showed marginal differences, the electrical conductivity demonstrated higher values and variations at elevated temperatures. Additionally, based on Density Functional Theory (DFT) calculations, the molecule exhibited lower softness and higher global hardness in the DMSO solvent. The electrophilic and nucleophilic parameters, vital for describing electron-deficient (electrophilic) and electron-rich (nucleophile) species, indicated a high electrophilic value and a low nucleophilic value for this molecule.

## Author contributions

All authors made an equivalent contribution to the preparation of the publication.

## Conflict of interest

The authors declare no conflict of interest.

## References

1. Shafiee A., Ghadiri E., Kassis J., Williams D., Atala A. Energy band gap investigation of biomaterials:

A comprehensive material approach for biocompatibility of medical electronic devices. *Micromachines*. 2020;11(1): 105. <https://doi.org/10.3390/mi11010105>

2. Mamand D. M., Qadr H. M. Density functional theory and computational simulation of the molecular structure on corrosion of carbon steel in acidic media of some amino acids. *Russian Journal of Physical Chemistry A*. 2022;96: 2155–2165. <https://doi.org/10.1134/s0036024422100193>

3. Qadr H. M., Mamand D. Measuring energy loss of alpha particles in hydrogen gas. *El-Cezeri Fen ve Mühendislik Dergisi*. 2023;10: 433–438. <https://doi.org/10.31202/ecjse.1195041>

4. Vieira D. F., Avellaneda C. O., Pawlicka A. Conductivity study of a gelatin-based polymer electrolyte. *Electrochimica Acta*. 2007;53: 1404–1408. <https://doi.org/10.1016/j.electacta.2007.04.034>

5. Fujita S.-I., Kawamori H., Honda D., Yoshida H., Arai M. Photocatalytic hydrogen production from aqueous glycerol solution using NiO/TiO<sub>2</sub> catalysts: Effects of preparation and reaction conditions. *Applied Catalysis B: Environmental*. 2016;181: 818–824. <https://doi.org/10.1016/j.apcatb.2015.08.048>

6. Nan H., Ping Y., Xuan C., ... Tingfei, X. Blood compatibility of amorphous titanium oxide films synthesized by ion beam enhanced deposition. *Biomaterials*. 1998;19(7-9): 771–776. [https://doi.org/10.1016/s0142-9612\(98\)00212-9](https://doi.org/10.1016/s0142-9612(98)00212-9)

7. Qadr H. M. A Molecular dynamics study of temperature dependence of the primary state of cascade damage processes. *Russian Journal of Non-Ferrous Metals*. 2021;62: 561–567. <https://doi.org/10.3103/s1067821221050096>

8. Abram R. A., Childs G. N., Saunderson P. A. Band gap narrowing due to many-body effects in silicon and gallium arsenide. *Journal Of Physics C: Solid State Physics*. 1984;17: 6105. <https://doi.org/10.1088/0022-3719/17/34/012>

9. Hudgins J. L., Simin G. S., Santi E., Khan M. A. An assessment of wide bandgap semiconductors for power devices. *Ieee Transactions On Power Electronics*. 2003;18: 907–914. <https://doi.org/10.1109/tpel.2003.810840>

10. Rawal S. B., Bera S., Lee D., Jang D.-J., Lee W. I. Design of visible-light photocatalysts by coupling of narrow bandgap semiconductors and TiO<sub>2</sub>: Effect of their relative energy band positions on the photocatalytic efficiency. *Catalysis Science & Technology*. 2013;3: 1822–1830. <https://doi.org/10.1039/c3cy00004d>

11. Örek C., Arslan F., Gündüz B., Kaygili O., Bulut N. Comparison of experimental photonic and refractive index characteristics of the TBADN films with their theoretical counterparts. *Chemical Physics Letters*. 2018;696: 12–18. <https://doi.org/10.1016/j.cplett.2018.02.035>

12. Orek C., Gündüz B., Kaygili O., Bulut N. Electronic, optical, and spectroscopic analysis of TBADN organic semiconductor: Experiment and theory. *Chemical Physics Letters*. 2017;678: 130–138. <https://doi.org/10.1016/j.cplett.2017.04.050>
13. Mohan S., Kato E., Drennen Iii J. K., Anderson C. A. Refractive index measurement of pharmaceutical solids: A review of measurement methods and pharmaceutical applications. *Journal of Pharmaceutical Sciences*. 2019;108: 3478–3495. <https://doi.org/10.1016/j.xphs.2019.06.029>
14. Qadr H. M. Investigation of gamma ray buildup factor for some shielding absorber. *Cumhuriyet Science Journal*. 2022;43: 520–525. <https://doi.org/10.17776/cs.j.1098571>
15. Chaudhary A., Nagaich U., Gulati N., Sharma V. K., Khosa R. L., Partapur M. U. Enhancement of solubilization and bioavailability of poorly soluble drugs by physical and chemical modifications: A recent review. *Journal of Advanced Pharmacy Education and Research*. 2012;2: 32–67.
16. Al-Otaibi J. S., Mary Y. S., Thomas R., Kaya S. Detailed electronic structure, physico-chemical properties, excited state properties, virtual bioactivity screening and sers analysis of three guanine based antiviral drugs valacyclovir HCl hydrate, acyclovir and ganciclovir. *Polycyclic Aromatic Compounds*. 2022;42: 1260–1270. <https://doi.org/10.1080/10406638.2020.1773876>
17. Mamand D. M., Awla A. H., Anwer T. M. K., Qadr H. M. Quantum chemical study of heterocyclic organic compounds on the corrosion inhibition. *Chemica Techno Acta*. 2022;9: 20229203. <https://doi.org/10.15826/chimtech.2022.9.2.03>
18. Qadr H. M. Effect of ion irradiation on the mechanical properties of high and low copper. *Atom Indonesia*. 2020;46: 47–51. <https://doi.org/10.17146/aij.2020.923>
19. Zhang J., Tang H., Liu Z., Chen B. Effects of major parameters of nanoparticles on their physical and chemical properties and recent application of nanodrug delivery system in targeted chemotherapy. *International Journal of Nanomedicine*. 2017;12: 8483. <https://doi.org/10.2147/ijn.s148359>
20. Qadr H. M. A molecular dynamics calculation to cascade damage processes. *The Annals of “Dunarea de Jos” University of Galati. Fascicle IX, Metallurgy and Materials Science*. 2020;43: 13–16. <https://doi.org/10.35219/mms.2020.4.02>
21. Sechadri S., Rasheed M. P., Sangeetha R. Molecular structure, spectroscopic (FTIR, FT-Raman, <sup>13</sup>C and <sup>1</sup>H NMR, UV), polarizability and first-order hyperpolarizability, HOMO–LUMO analysis of 2,4-difluoroacetophenone. *Spectrochimica Acta Part A: Molecular and Biomolecular Spectroscopy*. 2015;7: 56–70. <https://doi.org/10.1016/j.saa.2014.09.069>
22. Aziz D. M., Azeez H. J. Synthesis of new  $\beta$ -lactam-N-(thiazol-2-yl)benzene sulfonamide hybrids: Their in vitro antimicrobial and in silico molecular docking studies. *Journal of Molecular Structure*. 2020;1222: 128904. <https://doi.org/10.1016/j.molstruc.2020.128904>
23. Brisdon A. K. *Inorganic spectroscopic methods*. New York: Oxford University Press; 1998. <https://doi.org/10.1093/hesc/9780198559498.001.0001>
24. Coskun D., Gunduz B., Coskun M. F. Synthesis, characterization and significant optoelectronic parameters of 1-(7-methoxy-1-benzofuran-2-yl) substituted chalcone derivatives. *Journal of Molecular Structure*. 2019;1178: 261–267. <https://doi.org/10.1016/j.molstruc.2018.10.043>
25. Choi W. S., Yoon J.-G. Optical characterization of band gap graded ZnMgO films. *Solid State Communications*. 2012;152: 345–348. <https://doi.org/10.1016/j.ssc.2011.12.019>
26. Tsukazaki A., Akasaka S., Nakahara K., ... Kawasaki M. Observation of the fractional quantum Hall effect in an oxide. *Nature Materials*. 2010;9: 889–893. <https://doi.org/10.1038/nmat2874>
27. Garimella S. V., Persoons T., Weibel J. A., Gektin V. Electronics thermal management in information and communications technologies: Challenges and future directions. *IEEE Transactions on Components, Packaging and Manufacturing Technology*. 2016;7: 1191–1205. <https://doi.org/10.1109/tcpmt.2016.2603600>
28. Trew R. J. Wide bandgap semiconductor transistors for microwave power amplifiers. *IEEE Microwave Magazine*. 2000;1: 46–54. <https://doi.org/10.1109/6668.823827>
29. Neudeck P. G., Okojie R. S., Chen L.-Y. High-temperature electronics - a role for wide bandgap semiconductors? *Proceedings of The Ieee*. 2002;90: 1065–1076. <https://doi.org/10.1109/jproc.2002.1021571>
30. Mamand D. M., Anwer T. M. K., Qadr H. M. Theoretical investigation on corrosion inhibition effect of oxadiazole: Dft calculations. *Oxidation Communications*. 2022;45: 600–267.
31. Mamand D. M., Qadr H. M. Corrosion inhibition efficiency of quinoxalines based on electronic structure and quantum computational analysis. *Revue Roumaine de Chimie*. 2023;68: 435–446.
32. Cassabois G., Valvin P., Gil B. Hexagonal boron nitride is an indirect bandgap semiconductor. *Nature Photonics*. 2016;10: 262–266. <https://doi.org/10.1038/nphoton.2015.277>
33. Mamand D. M., Anwer T. M., Qadr H. M., Mussa C. H. Investigation of spectroscopic and optoelectronic properties of phthalocyanine molecules. *Russian Journal of General Chemistry*. 2022;92: 1827–1838. <https://doi.org/10.1134/s1070363222090249>



34. Schütz A., Günthner M., Motz G., Greißl O., Glatzel U. Characterisation of novel precursor-derived ceramic coatings with glass filler particles on steel substrates. *Surface and Coatings Technology*. 2012;207: 319–327. <https://doi.org/10.1016/j.surfcoat.2012.07.013>
35. Tripathy S. K. Refractive indices of semiconductors from energy gaps. *Optical Materials*. 2015;46: 240–246. <https://doi.org/10.1016/j.optmat.2015.04.026>
36. Qadr H. M., Mamand D. M. A Computational study of substituent effect 1, 3, 4-thiadiazole on corrosion inhibition. *Azerbaijan Chemical Journal*. 2023; 19–29. <https://doi.org/10.32737/0005-2531-2023-2-19-29>
37. Mamad D. M., Omer P. K., Rasul H. H., Qadr H. M. A Theoretical study of structure and corrosion inhibition of some heterocyclic imidazoles: DFT investigation. *Surface Engineering and Applied Electrochemistry*. 2023;59: 489–501. <https://doi.org/10.3103/s1068375523040099>
38. Mamad D. M., Qadr H. M. Quantum computations and density functional theory on corrosion inhibition efficiency of BIA, HBT, MBI and PIZ compounds. *Himia, Fizika ta Tehnologija Poverhni*. 2023;14: 159–172. <https://doi.org/10.15407/hftp14.02.159>
39. Herve P., Vandamme L. K. J. General relation between refractive index and energy gap in semiconductors. *Infrared Physics & Technology*. 1994;35: 609–615. [https://doi.org/10.1016/1350-4495\(94\)90026-4](https://doi.org/10.1016/1350-4495(94)90026-4)
40. Reddy R. R., Ahammed Y. N. A study on the Moss relation. *Infrared Physics & Technology*. 1995;36: 825–830. [https://doi.org/10.1016/1350-4495\(95\)00008-m](https://doi.org/10.1016/1350-4495(95)00008-m)
41. Ravindra N. M., Ganapathy P., Choi J. Energy gap–refractive index relations in semiconductors – An overview. *Infrared Physics & Technology*. 2007;50: 21–29. <https://doi.org/10.1016/j.infrared.2006.04.001>
42. Aly K. M., Esmail E. Refractive index of salt water: effect of temperature. *Optical Materials*. 1993;2: 195–199. [https://doi.org/10.1016/0925-3467\(93\)90013-q](https://doi.org/10.1016/0925-3467(93)90013-q)
43. Mamand D. M., Qadr H. M. Corrosion inhibition efficiency and quantum chemical studies of some organic compounds: theoretical evaluation. *Corrosion Reviews*. 2023;41: 427–441. <https://doi.org/10.1515/corrrev-2022-0085>
44. Wesely M. L. The combined effect of temperature and humidity fluctuations on refractive index. *Journal of Applied Meteorology*. 1976; 43–49. [https://doi.org/10.1175/1520-0450\(1976\)015<0043:tceota>2.0.co;2](https://doi.org/10.1175/1520-0450(1976)015<0043:tceota>2.0.co;2)
45. Mamand D. M., Azeez Y. H., Qadr H. M. Monte Carlo and DFT calculations on the corrosion inhibition efficiency of some benzimide molecules. *Mongolian Journal Of Chemistry*. 2023;24: 1–10. <https://doi.org/10.5564/mjc.v24i50.2435>
46. Tripathy S. K., Pattanaik A. Optical and electronic properties of some semiconductors from energy gaps. *Optical Materials*. 2016;53: 123–133. <https://doi.org/10.1016/j.optmat.2016.01.012>
47. Dresselhaus M. S. *Solid State Physics part II Optical properties of solids*. Lecture Notes. Massachusetts Institute of Technology, Cambridge, Ma; 2001;17: 15–16.
48. Patterson J. D., Bailey B. C., Patterson J. D., Bailey B. C. Optical properties of solids. In: *Solid-State Physics*. Springer, Cham.; 2018. 649–704. [https://doi.org/10.1007/978-3-319-75322-5\\_10](https://doi.org/10.1007/978-3-319-75322-5_10)
49. Dalven R. *Introduction to applied solid state physics: Topics in the applications of semiconductors, superconductors, ferromagnetism, and the nonlinear optical properties of solids*. Springer Science & Business Media; 2012.
50. Dong H. M., Zhang J., Peeters F. M., Xu W. Optical conductance and transmission in bilayer graphene. *Journal of Applied Physics*. 2009;106: 043103. <https://doi.org/10.1063/1.3200959>
51. Yücedağ I., Altındal Ş., Tataroğlu A. On the profile of frequency dependent series resistance and dielectric constant in MIS structure. *Microelectronic Engineering*. 2007;84: 180–186. <https://doi.org/10.1016/j.mee.2006.10.071>
52. Dege N., Gökce H., Doğan O. E., ... Sert Y. Quantum computational, spectroscopic investigations on N-(2-((2-chloro-4,5-dicyanophenyl)amino)ethyl)-4-methylbenzenesulfonamide by DFT/TD-DFT with different solvents, molecular docking and drug-likeness researches. *Colloids And Surfaces A: Physicochemical and Engineering Aspects*. 2022;638: 128311. <https://doi.org/10.1016/j.colsurfa.2022.128311>
53. Mamand D. M., Qadr H. M. Comprehensive spectroscopic and optoelectronic properties of BBL organic semiconductor. *Protection of Metals and Physical Chemistry of Surfaces*. 2021;57: 943–53. <https://doi.org/10.1134/s207020512105018x>
54. Mamand D. M., Qadr H. M. Optoelectronic properties of benzimidazobenzophenanthroline thin film. *Russian Microelectronics*. 2023;52: 325–336. <https://doi.org/10.1134/s1063739723700531>
55. Qadr H. M., Mamand D. M. Molecular structure and density functional theory investigation corrosion inhibitors of some oxadiazoles. *Journal of Bio- and Tribo-Corrosion*. 2021;7: 140. <https://doi.org/10.1007/s40735-021-00566-9>
56. Putz M. V., Russo N., Sicilia E. About the Mulliken electronegativity in DFT. *Theoretical Chemistry Accounts*. 2005;114: 38–45. <https://doi.org/10.1007/s00214-005-0641-4>
57. Medimagh M., Mleh C. B., Issaoui N., ... Bousiakoug L. G.. DFT and molecular docking study of



the effect of a green solvent (water and DMSO) on the structure, MEP, and FMOs of the 1-ethylpiperazine-1,4-dium bis(hydrogenoxalate) compound. *Compound. Journal Of Molecular Liquids*. 2023;369: 120851. <https://doi.org/10.1016/j.molliq.2022.120851>

58. Ramalingam S., Babu P. D. S., Periandy S., Fereyduni E. Vibrational investigation, molecular orbital studies and molecular electrostatic potential map analysis on 3-chlorobenzoic acid using hybrid computational calculations. *Spectrochimica Acta Part A: Molecular and Biomolecular Spectroscopy*. 2011;84: 210–220. <https://doi.org/10.1016/j.saa.2011.09.030>

59. Mamand D. M., Rasul H. H., Omer P. K., Qadr H. M. Theoretical and experimental investigation on ADT organic semiconductor in different solvents. *Condensed Matter And Interphases*. 2022;24(2): 227–42. <https://doi.org/10.17308/kcmf.2022.24/9263>

### Information about the authors

*Dyari Mustafa Mamand*, MSc in Atomic and Molecular Physics, Department of Physics, University of Raparin (Sulaymaniyah, Iraq).

<https://orcid.org/0000-0002-1215-7094>

[dyari.mustafa@uor.edu.krd](mailto:dyari.mustafa@uor.edu.krd)

*Dara Muhammed Aziz*, PhD in Organic Chemistry, Department of Chemistry, University of Raparin (Sulaymaniyah, Iraq).

<https://orcid.org/0000-0003-3362-6301>

[darachem@uor.edu.krd](mailto:darachem@uor.edu.krd)

*Hiwa Mohammad Qadr*, MSc in Physics, Lecture of the Department of Physics, University of Raparin (Sulaymaniyah, Iraq).

<https://orcid.org/0000-0001-5585-3260>

[hiwa.physics@uor.edu.krd](mailto:hiwa.physics@uor.edu.krd)

*Received 24.02.2023; approved after reviewing 24.06.2023; accepted for publication 16.09.2023; published online 25.03.2024.*



## Original articles

Research article

<https://doi.org/10.17308/kcmf.2024.26/11812>

## Electrophysical properties of composite materials based on graphene oxide and polyaniline

T. N. Myasoedova, O. V. Nedoedkova, G. E. Yalovega 

*Southern Federal University*

*105/42 Bolshaya Sadovaya str., Rostov-on-Don 344006, Russian Federation*

### Abstract

The Hall method was used to study the electrical characteristics of composite materials based on polyaniline (PANI), graphene oxide (GO), and manganese. A comparison of these characteristics of GO-PANI and GO-PANI-Mn composite systems with GO and PANI monomaterials was carried out.

It was demonstrated that the electrical conductivity of composites was significantly higher than that of monomaterials and was determined by the charge carrier mobility.


Based on UV-visible and IR spectroscopy data, it was shown that the optical band gap ( $E_g$ ) of the GO-PANI composite increased with the addition of metal, but decreased compared to PANI; the shift of characteristic vibrations to lower frequencies indicated a covalent interaction of the GO-PANI composite with manganese cations.

**Keywords:** Composite materials, Polyaniline, Graphene oxide, Specific conductivity, Band gap

**Funding:** The study was supported by the Russian Science Foundation grant No. 23-22-00459 at the Southern Federal University.

**For citation:** Myasoedova T. N., Nedoedkova O. V., Yalovega G. E. Electrophysical properties of composite materials based on graphene oxide and polyaniline. *Condensed Matter and Interphases*. 2024;26(1): 104–110. <https://doi.org/10.17308/kcmf.2024.26/11812>

**Для цитирования:** Мясоедова Т. Н., Недоедкова О. В., Яловега Г. Э. Электрофизические свойства композитных материалов на основе оксида графена и полианилина. *Конденсированные среды и межфазные границы*. 2024;26(1): 104–110. <https://doi.org/10.17308/kcmf.2024.26/11812>

 Galina E. Yalovega, e-mail: [yalovega@sfedu.ru](mailto:yalovega@sfedu.ru)

© Myasoedova T. N., Nedoedkova O. V., Yalovega G. E., 2024



The content is available under Creative Commons Attribution 4.0 License.

## 1. Introduction

The combination of the advantages of various materials for the formation of electroactive composites is a technological breakthrough in the creation of advanced materials for the improvement of the performance of electronic devices and super capacitors. This is confirmed by a number of publications that have shown that nanocomposites based on polymers, nanostructured carbon and transition metal oxides can have high electronic conductivity [1–5]. At the same time, a sharp increase in charge transfer in hybrid structures was observed depending on the type of chemical bond between the components of the composites. In the process of diagnosing the properties of such nanocomposites, the significance of the influence of interfacial interactions and chemical bonds on their conductive properties becomes obvious.

As a conducting polymer, PANI is characterized electrical conductivity, which can be controlled by synthesis conditions [6]. The inclusion of components such as transition metals or their oxides into the PANI structure is often used to improve the selectivity and sensitivity of chemical interactions [7]. However the influence of the dopant on the characteristics of PANI is not clear. Doping PANI with divalent ions of copper, zinc, nickel, cobalt, and cadmium leads to an increase in the electrical conductivity of the composites compared to pure polyaniline, associated with the ordering of polymer chains as a result of interaction with metal ions [7, 8]. At the same time, modification of polyaniline with ZnO nanorods leads to a decrease in the electrical conductivity of the composite compared to pure PANI [9]. Modification of PANI with MnO<sub>2</sub> oxide showed that this material has high intrinsic electrical conductivity and good kinetic reversibility as a result of the interaction between MnO<sub>2</sub> and PANI [10]. It is assumed that the introduction of inorganic dopants into the conductive polymer matrix of polyaniline is the most promising way to create nanocomposites, where delocalized  $\pi$ -electrons can interact with inorganic nanoparticles, leading to an improvement in its conductive properties [11].

Graphene can form numerous nanocomposites with other elements or functional groups. The high conductivity of graphene and its oxide is

ensured by low resistance to ion diffusion, which leads to an increase in power and energy density [12, 13]. However, the processing of graphene materials is difficult due to agglomeration and repacking of graphene sheets as a result of interplanar  $\pi$ - $\pi$  interactions and van der Waals forces, which can significantly limit the diffusion of electrolyte ions between graphene layers [14]. A solution to the problem is to separate graphene by suitable spacers such as carbon-based materials, metals or metal oxides and other pseudo-capacitive materials such as conductive polymers [15]. Graphene-PANI nanocomposites are promising electrode materials due to the fact that graphene and nanostructures obtained from it have a significant effect on improving the properties of conducting polymers, such as electrical properties and structural stability [16]. The distribution of graphene in PANI matrix allows avoiding graphene aggregation, increasing the number of pathways for charge transfer and improving the charge carrier mobility. Functional groups of graphene oxide provide high interaction with polyaniline due to hydrogen and electrostatic interactions.

In this study, the electrical characteristics and structure of synthesized composite systems with the GO-PANI and GO-PANI-Mn compositions, in comparison with monomaterials were studied.

## 2. Materials and methods

Graphene oxide was prepared using a modified Hummers method [17]. So, 10 g of graphite was mixed with 10 g of sodium nitrate and 450 ml of concentrated H<sub>2</sub>SO<sub>4</sub> for 30 minutes at 0 °C. Then 60 g KMnO<sub>4</sub> was added, maintaining a temperature of 15–20 °C. The solution was stirred for 2 h at 40 °C. After addition of 800 ml of deionized water, the solution was stirred for 30 min, raising the temperature to 85–90 °C. Then 2000 ml of water and 60 ml of 30% H<sub>2</sub>O<sub>2</sub> were added. The resulting mixture was washed with a 30% HCl solution to remove sulphates from the graphite oxide solution. PANI powder was synthesized using an acid-free technique described previously [18]. To obtain the GO-PANI composite, at the first stage, GO was functionalized with an amino groups by a simple solvothermal method [19] by the following procedure. 100 mg of GO was dispersed in 35 ml of ethylene glycol, then the dispersed mixture was

stirred at ambient temperature for 30 min and placed in an autoclave. The autoclave was placed in a preheated convection oven at 180 °C for 6 h. The autoclave was then cooled to ambient temperature, the suspension was washed with deionized water and dried at 70 °C for 6 h. GO-PANI composites were prepared by mixing GO-NH<sub>2</sub> powder with aniline/ammonium persulfate solution. The aniline/GO ratio was 2:1. In the case of the GO-PANI-Mn composite, manganese sulphate was added to the specified solution in a way that the proportion of Mn in the sample was 3 wt. %.

IR absorption spectra were recorded using Fourier spectrophotometer (FSM-1202) in transmission mode in the wave number range 350–4250 cm<sup>-1</sup> with a step of 2 cm<sup>-1</sup>.

Absorption spectra in the UV and visible region were recorded using dual-beam spectrophotometer (Unico 2804, USA) in the wavelength range from 190 to 1100 nm. Optical band gap ( $E_g$ ) of the test samples were determined using the Tauc method:

$$(\alpha hv)^{1/n} = f(hv),$$

where  $\alpha$  – absorption coefficient,  $h$  – Planck's constant,  $\nu$  – photon frequency,  $n = 1/2$ .  $E_g$  was determined by extrapolating the tangent to the linear part of the spectrum to the intersection with the axis ( $h\nu$ ).

The specific conductivity, concentration and charge carrier mobility of the synthesized materials were measured using the four-probe Hall method on an HMS-3000 instrument. The powder samples were pressed under a pressure of 30 atm in the form of square tablets measuring 7×7 mm and 1 mm thick. The measurements were carried out at room temperature.

### 3. Results and discussion

As a result of Hall measurements, it was established (Table. 1), that the electrical conductivity of monomaterials is significantly

lower than that of composites. Thus, the specific conductivity of graphene oxide and polyaniline was  $1.12 \cdot 10^{-4}$  and  $1.1 \cdot 10^{-7}$  Ohm<sup>-1</sup>·cm<sup>-1</sup> respectively. For composites a significant increase in specific conductivity up to 1.16 (GO-PANI) Ohm<sup>-1</sup>·cm<sup>-1</sup> and 0.78 Ohm<sup>-1</sup>·cm<sup>-1</sup> (GO-PANI-Mn) compared to monomaterials (GO, PANI) was observed. This anomalous increase in specific conductivity may be due to  $\pi$ - $\pi$  stacking (interplanar interactions) between the polymer base and graphene oxide plates, Fig. 1 [20]. On the surface and in the pores of graphene oxide there are OH groups that promote the formation of hydrogen bonds between graphene oxide and nitrogen in the

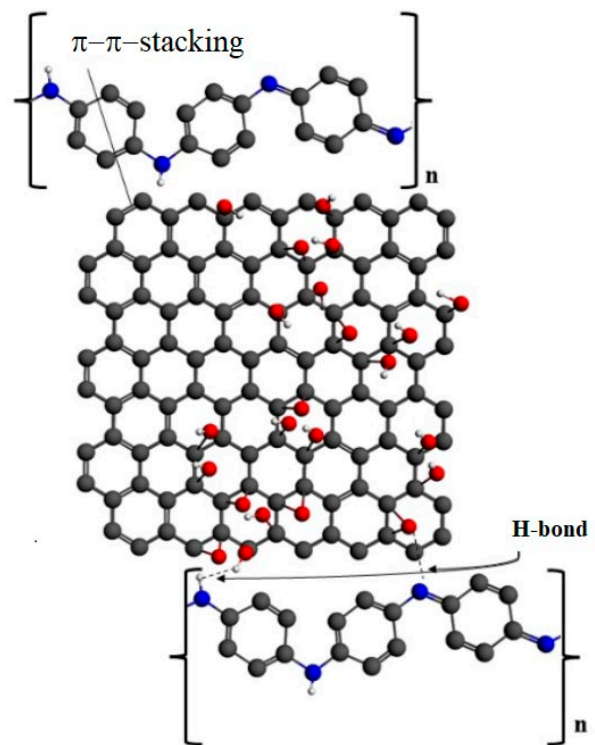


**Fig. 1.** Schematic representation of the interaction of graphene oxide with polyaniline (blue – nitrogen, red – oxygen, black – carbon, white – hydrogen). The figure is based on the figure from [19]

**Table 1.** Comparative electrophysical characteristics of GO, PANI, GO-PANI, GO-PANI-Mn, obtained by measurements with the four-probe Hall method

Characteristics	GO	PANI	GO-PANI	GO-PANI-Mn
Charge carrier density $N$ , cm <sup>-3</sup>	$2.74 \cdot 10^{12}$	$6.04 \cdot 10^{10}$	$5.8 \cdot 10^{18}$	$1.3 \cdot 10^{19}$
Charge carrier mobility $\mu$ , cm <sup>2</sup> /V·s	$2.5 \cdot 10^2$	$1.15 \cdot 10$	1.2	$3.6 \cdot 10^{-1}$
Specific resistance $R$ , Om·cm	$8.87 \cdot 10^5$	$8.9 \cdot 10^6$	$8.5 \cdot 10^{-1}$	1.27
Specific conductivity $C$ , Om <sup>-1</sup> ·cm <sup>-1</sup>	$1.12 \cdot 10^{-4}$	$1.1 \cdot 10^{-7}$	1.16	0.78
Tupes of conductivity	<i>p</i> -type	<i>p</i> -type	<i>n</i> -type	<i>p</i> -type



benzenoid and quinoid fragments of the polymer chain. The presence of a stretched hydrogen bond between polyaniline and graphene oxide affects the stretch of the  $\pi$ -conjugated bond in the polymer. In addition, polymerization on the surface and in the pores of graphene oxide sheets limits the twisting of the polymer chain, which plays an important role in increasing electrical conductivity [21]. When comparing the electrical parameters of composite materials, it was found that the introduction of manganese reduces the specific conductivity from 1.16 to 0.78  $\text{Ohm}^{-1}\cdot\text{cm}^{-1}$ , despite the fact that the concentration of charge carriers in the GO-PANI-Mn sample is higher than that of GO-PANI. Based on these results, it can be concluded, that the conductivity of composite materials is determined by the charge carrier mobility, which is noticeably lower for manganese-containing materials ( $3.6\cdot 10^{-1} \text{ cm}^2/\text{V}\cdot\text{s}$ ) compared to the GO-PANI sample ( $1.2 \text{ cm}^2/\text{V}\cdot\text{s}$ ).

In UV-visible spectra PANI, GO-PANI and GO-PANI-Mn three absorption bands were observed, characteristic of the transition  $\pi \rightarrow \pi^*$  (peak A, A\*), and shoulder B, characteristic of the transition  $n \rightarrow \pi^*$  (Fig. 2, inset). The peak A was due to the  $\pi$ - $\pi^*$  electronic transition in benzene rings and is characteristic of all forms of PANI. The A\* peak was due to the polaron/bipolaron transition [22]. The long-wavelength feature of B is associated with the excitation of an electron from the highest occupied molecular orbital of benzene rings to the lowest unoccupied molecular orbital of quinoid rings [23], i.e., an excitonic transition from the benzenoid fragment to the quinoid fragment [24]. Peaks A, A\* reflect intrachain interactions, and shoulder B indicates both intrachain and interchain interactions. The estimation of the band gap of GO, PANI, GO-PANI and GO-PANI-Mn are shown in Figure 2. Band gap values  $E_g$  were 2.7 eV for GO, 3.8 eV for PANI, 3.5 eV for GO-PANI, and 3.6 eV for GO-PANI-Mn. It can be noted that the addition of GO to the polymer sample led to a decrease in the band gap (GO-PANI). This is consistent with earlier results [25], where it was shown that the band gap in GO-PANI systems decreased with increased proportion of graphene in the composite. Optical absorption in conjugated polymers can be caused by the transition of charge carriers through the forbidden energy gap. Decrease in

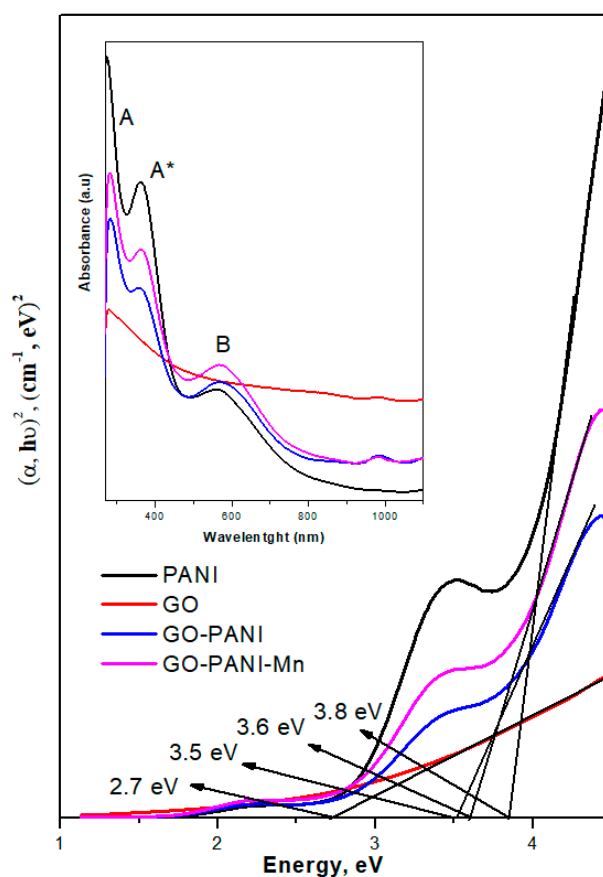


Fig. 2. UV-visible spectra (inset) and optical band gap ( $E_g$ ) of GO, PANI, GO-PANI and GO-PANI-Mn

$E_g$  was due to the appearance of new excitation energy levels due to charge transfer from GO to PANI. The addition of manganese increased the band gap of the GO-PANI-Mn sample, probably due to ordering of the structure. This led to a decrease in the number of localized states in the band gap, contributing to its increase. As a consequence, a decrease in specific conductivity with a simultaneous decrease in the charge carrier mobility was observed.

The IR-spectra of PANI were characterized by the presence of absorption bands corresponding to the C=N and C=C vibrations of the benzenoid and quinoid rings located at 1582 and 1505  $\text{cm}^{-1}$ . Peaks at 1297 and 1306  $\text{cm}^{-1}$  were associated with C=N vibrations of secondary aromatic amines [26] and also the presence of stretching vibrations in the O-H group, approximately from 3650 to 3050  $\text{cm}^{-1}$ . When graphene oxide was functionalized with an amine, bands that overlap with the O-H group at 3433, 1726, and 1619  $\text{cm}^{-1}$  appeared. Absorption bands between 3285 and 3527  $\text{cm}^{-1}$  were due to

the stretching of N-H bonds in amine groups, and the band at  $1580\text{ cm}^{-1}$  were determined by the stretching of N-H bonds in the same plane. During the formation of a composite GO-PANI three bands appeared at  $1481$ ,  $1293\text{ cm}^{-1}$ , and in the range  $\sim 1235\text{--}1022\text{ cm}^{-1}$ , which correspond to the C=C vibration of the benzene ring, the C-N vibration of the benzene ring, and the C-N stretching vibration of aromatic amines (Fig. 3) [18, 27]. When manganese was added to the GO-PANI composite, a shift of the bands (Fig. 3) corresponding to the characteristic vibrations of C=C, C-N, N=C, and C-H in GO-PANI-Mn to lower frequencies was observed in comparison with GO-PANI, which indicates the interaction of GO-PANI with metal cations.

#### 4. Conclusions

A comparison of the electrical characteristics of composite systems of GO-PANI and GO-PANI-Mn composition with GO and PANI monomaterials showed that the electrical conductivity of monomaterials is significantly lower than that of composites. During the formation of composites, an anomalous increase in electrical conductivity was observed, which may be due to interfacial interactions between the polymer base and graphene oxide plates, effective for improving the conductive properties of materials. It has

been shown that the conductivity of composite materials is determined by the charge carrier mobility. Optical band gap ( $E_g$ ) of GO-PANI composite increased with the addition of metal, but decreased compared to PANI. The decrease in  $E_g$  was due to the appearance of new excitation energy levels due to charge transfer from GO to PANI. The addition of manganese increased the band gap of the GO-PANI-Mn sample, probably due to ordering the structure. This led to a decrease in the number of localized states in the band gap, contributing to its increase. The shift of the characteristic vibration bands of C=C, C-N, N=C, and C-H in GO-PANI-Mn to lower frequencies indicates the covalent interaction of the GO-PANI composite with manganese cations.

#### Author contributions

Nedodkova O. V. – IR and UV measurements, analysis of results, design of text and drawings. Myasoedova T. N. – development of synthesis technology and synthesis of samples, measurements by the Hall method, writing of the article. Yalovega G. E. – concept of the article, scientific supervision of research, text writing.

#### Conflict of interests

The authors declare that they have no known competing financial interests or personal

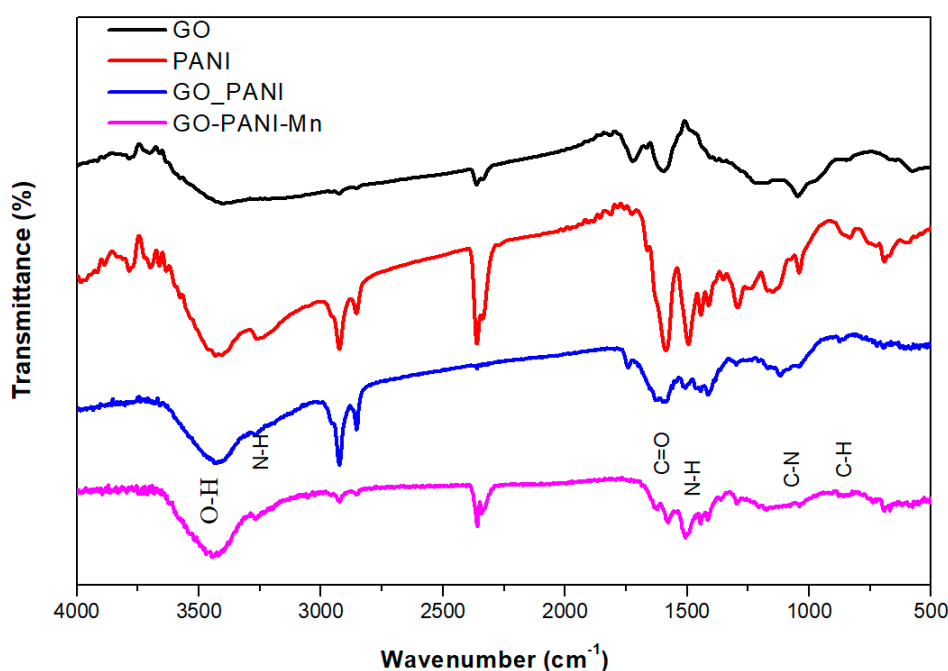


Fig. 3. IR-spectra of GO, PANI, GO-PANI and GO-PANI-Mn

relationships that could have influenced the work reported in this paper.

## References

1. Baskakov S. A., Shulga Yu. M., Baskakova Yu. V., Zolotarev A. D., Kuznetsov I. E., Efimov O. N., Gusev A. L. New composite materials for supercapacitor electrodes based on reduced oxide graphene and polyaniline. *International scientific journal for Alternative Energy and Ecology*. 2012;12(116): 66–76.
2. Yang D. Application of nanocomposites for supercapacitors: Characteristics and properties. *Nanocomposites – New Trends and Developments*. 2012. <https://doi.org/10.5772/50409>
3. Salvatierra R. V., Zitzer G., Savu S.-A., ... Rocco M. L. M. Carbon nanotube/polyaniline nanocomposites: Electronic structure, doping level and morphology investigations. *Synthetic Metals*. 2015;203: 16–21 <https://doi.org/10.1016/j.synthmet.2015.01.034>
4. Singh G., Kumar Y., Husain S. Fabrication of symmetric polyaniline/nano-titanium dioxide/activated carbon supercapacitor device in different electrolytic mediums: Role of high surface area of carbon and facile interactions with nano-titanium dioxide for high-performance supercapacitor. *Energy Technology*. 2023;11(1): 2200931. <https://doi.org/10.1002/ente.202200931>
5. Savić M., Janošević Ležaić A., Gavrilov N., ... Ćirić-Marjanović G. Carbonization of MOF-5/polyaniline composites to N, O-doped carbon/ZnO/ZnS and N, O-doped carbon/ZnO composites with high specific capacitance, specific surface area and electrical conductivity. *Materials*. 2023;16(3): 1018. <https://doi.org/10.3390/ma16031018>
6. Lv P., Tang X., Zheng R., Ma X., Yu K., Wei W. Graphene/polyaniline aerogel with superelasticity and high capacitance as highly compression-tolerant supercapacitor electrode. *Nanoscale Research Letters*. 2017;12(1): 1–11. <https://doi.org/10.1186/s11671-017-2395-z>
7. Wang S., Tan Z., Li Y., Sun L., Zhang T. Synthesis, characterization and thermal analysis of polyaniline/ZrO<sub>2</sub> composites. *Thermochimica Acta*. 2006;441(2): 191–194. <https://doi.org/10.1016/j.tca.2005.05.020>
8. Sawarkar M., Pande S. A., Agrawal P. S. Synthesis and characterization of polyaniline doped metal oxide nanocomposites. *International Research Journal of Engineering and Technology*. 2015;2(9): 2427–2432. <https://www.irjet.net/archives/V2/i9/IRJET-V2I9295.pdf>
9. Mostafaei A., Zolriasatein A. Synthesis and characterization of conducting polyaniline nanocomposites containing ZnO nanorods. *Progress in Natural Science: Materials International*. 2012;22(4): 273–280. <https://doi.org/10.1016/j.pnsc.2012.07.002>
10. Chen L., Sun L., Luan F., ... Liu, X. X. Synthesis and pseudocapacitive studies of composite films of polyaniline and manganese oxide nanoparticles. *Journal of Power Sources*. 2010;195(11):3742–3747. <https://doi.org/10.1016/j.jpowsour.2009.12.036>
11. Lei X., Su Z. Conducting polyaniline coated nano silica by in situ chemical oxidative grafting polymerization. *Polymer Advanced Technology*. 2007;18(6): 472–476 <https://doi.org/10.1002/pat.905>
12. Gorshkov N. V., Yakovleva E. V., Krasnov V. V., ... Yakovlev A. V. Electrode for a supercapacitor based on electrochemically synthesized multilayer graphene oxide. *Russian Journal of Applied Chemistry*, 2021;94(3): 388–396. <https://doi.org/10.1134/s1070427221030149>
13. Shao Y., El-Kady M. F., Wang L. J., ... Kaner R. B. Graphene-based materials for flexible supercapacitors. *Chemical Society Reviews*. 2015;44: 3639–3665. <https://doi.org/10.1039/c4cs00316k>
14. Cai Y., Ke Q., Zhang G., Feng Y. P., Vivek B. S., Zhang Y. W. Giant phononic anisotropy and unusual anharmonicity of phosphorene: interlayer coupling and strain engineering. *Advanced Functional Materials*. 2015;25: 2230e6. <https://doi.org/10.1002/adfm.201404294>
15. Wang G. K., Sun X., Lu F. Y., ... Lian J. Flexible pillared graphene-paper electrodes for high-performance electrochemical supercapacitors. *Small*. 2012;8: 452e9. <https://doi.org/10.1002/sml.201101719>
16. Moussa M., El-kady M. F., Zhao Z. Recent progress and performance evaluation for polyaniline/graphene nanocomposites as supercapacitor electrodes. *Nanotechnology* 2016;27(44): 42001–42021. <https://doi.org/10.1088/0957-4484/27/44/442001>
17. Kumar R., Jahan K., Nagarale R. K., Sharma A., Long N. Lasting electro-osmotic pump with polyaniline-wrapped aminated graphene electrodes. *ACS Applied Materials and Interfaces*. 2015;7(1): 593–601. <https://doi.org/10.1021/am506766e>
18. Shmatko V. A., Myasoedova T. N., Mikhailova T. A., Yalovega G. E. Features of the Electronic structure and chemical bonds of polyaniline-based composites obtained by acid-free synthesis. *Condensed Matter and Interphases*, 2019;21(4): 569–578. <https://doi.org/10.17308/kcmf.2019.21/2367>
19. Myasoedova T. N., Nedoedkova O. V., Kalusulingam R., Mikheykin A. S., Konstantinov A. S., Yalovega G. E. Morphology, molecular and electronic structure of a composite material based on graphene oxide and polyaniline. *Physics of the Solid State*. 2023;65(12). <https://doi.org/10.61011/FTT.2023.12.56723.4935k>
20. Konwer S., Guha A. K., Dolui S. K. Graphene oxide-filled conducting polyaniline composites as methanol-sensing materials. *Journal of Materials*

*Science*. 2013;48: 1729–1739. <https://doi.org/10.1007/s10853-012-6931-z>

21. Konwer S. Graphene oxide-polyaniline nanocomposites for high performance supercapacitor and their optical, electrical and electrochemical properties. *Journal of Materials Science: Materials in Electronics*, 2016;27(4): 4139–4146. <https://doi.org/10.1007/s10854-016-4273-3>

22. Mallick K., Witcomb M. J., Dinsmore A., Scurrall M. S. Polymerization of aniline by cupric sulfate: A facile synthetic route for producing polyaniline. *Journal of Polymer Research*. 2006;13: 397–401. <https://doi.org/10.1007/s10965-006-9057-7>

23. Hu F., Li W., Zhang J., Meng W. Effect of graphene oxide as a dopant on the electrochemical performance of graphene oxide/polyaniline composite. *Journal of Materials Science and Technology*. 2014;30(4): 321–327. <https://doi.org/10.1016/j.jmst.2013.10.009>

24. Lu X., Yu Y., Chen L., Mao H., Zhang W., Wei Y. Preparation and characterization of polyaniline microwires containing CdS nanoparticles. *Chemical Communications*. 2004;13: 1522–1523. <https://doi.org/10.1039/B403105A>

25. Harish C., Sai Sreeharsha V., Santhosh C., ... Nirmala Grace A. Synthesis of polyaniline/graphene nanocomposites and its optical, electrical and electrochemical properties advanced science. *Advanced Science, Engineering and Medicine*. 2013; 5(2): 140–148. <https://doi.org/10.1166/ asem.2013.1237>

26. Myasoedova T. N., Moiseeva T. A., Kremennaya M. A., Tirkeshov A., Yalovega G. E.

Structure and electrochemical properties of PANI/ZrO<sub>x</sub> and PANI/SiO<sub>x</sub> composites. *Journal of Electronic Materials*. 2020;49(8): 4707–4713. <https://doi.org/10.1007/s11664-020-08170-2>

27. Lai L., Chen L., Zhan D., ... Lin J. One-step synthesis of NH<sub>2</sub>-graphene from in situ graphene-oxide reduction and its improved electrochemical properties. *Carbon*. 2011;49: 3250–3257. <https://doi.org/10.1016/j.carbon.2011.03.051>

### Information about the authors

*Tatyana N. Myasoedova*, Cand. Sci. (Tech.), Associate Professor, Leading Researcher, Institute of Nanotechnologies, Electronics and Instrument Engineering, Southern Federal University (Taganrog, Russian Federation).

<https://orcid.org/0000-0002-2891-7780>  
tnmyasoedova@sfedu.ru

*Olga V. Nedoedkova*, 2nd year graduate student, Teaching Assistant at the Department of Physics of Nanosystems and Spectroscopy, Faculty of Physics, Southern Federal University (Rostov-on-Don, Russian Federation).

<https://orcid.org/0000-0003-1274-8449>  
olga.nedoedkova@mail.ru

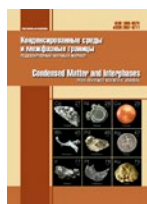
*Galina E. Yalovega*, Dr. Sci. (Phys.–Math.), Head of the Department of Physics of Nanosystems and Spectroscopy, Faculty of Physics, Southern Federal University (Rostov-on-Don, Russian Federation).

<https://orcid.org/0000-0002-0157-6955>  
yalovega@sfedu.ru

Received 18.11.2023, approved after reviewing 29.11.2023; accepted for publication 01.12.2023; published online 25.03.2024.

Translated by Valentina Mittova





## Original articles

Research article

<https://doi.org/10.17308/kcmf.2024.26/11814>**Spontaneous photomagnetolectric effect in ferromagnetic GaMnAs epitaxial layers**P. B. Parchinskiy<sup>1</sup>✉, A. S. Gazizulina<sup>1</sup>, R. A. Nusretov<sup>2</sup><sup>1</sup>National University of Uzbekistan,  
4 th University str., Tashkent 100174, Uzbekistan,<sup>2</sup>Uzbek-Japanese Youth Innovation Center,  
2-B University str., Tashkent 100095, Uzbekistan**Abstract**

Spontaneous photomagnetolectric effect in ferromagnetic GaMnAs epitaxial layers has been investigated. The goal of this work is to study the temperature dependence of the spontaneous PME effect, determined along [110] and [1 $\bar{1}$ 0] crystal axes. GaMnAs layers with Mn concentration of 2.9 atomic percent studied in this paper were grown by low-temperature molecular beam epitaxy on semi-insulating GaAs (001) substrate. It was shown that below Curie temperature in the illuminated GaMnAs epilayers a transverse voltage (photo-EMF) was observed. This photo-EMF is associated with the photomagnetolectric effect resulting from the separation the photogenerated carriers by the intrinsic magnetic field of the semiconductor matrix in ferromagnetic state. The temperature dependence of intrinsic photomagnetolectric effect in GaMnAs epilayer was determined along [110] and [1 $\bar{1}$ 0] crystallographic axes. It was found that the photo-EMF measured along [110] crystal axis exhibits a maximum at temperatures of 35–40 K, while the photo-EMF measured along [1 $\bar{1}$ 0] axis increases monotonically with temperature decay. It was shown that the non-monotonous temperature dependence of the photomagnetolectric effect along [110] axis can arise due to the reorientation of the easy axis of the sample with decreasing temperature.

**Keywords:** GaMnAs, Photomagnetolectric effect, Molecular beam epitaxy, Ferromagnetic ordering, Curie temperature, Photoconductivity

**Funding:** the study was financially supported by the Agency of Innovative Development under the Ministry of Higher Education, Science and Innovation of the Republic of Uzbekistan, project No. FZ-2020092435.

**For citation:** Parchinskiy P. B., Gazizulina A. S., Nusretov R. A. Spontaneous photomagnetolectric effect in ferromagnetic GaMnAs epitaxial layers. *Condensed Matter and Interphases*. 2024;26(1): 000-000. <https://doi.org/10.17308/kcmf.2024.26/11814>

**Для цитирования:** Парчинский П. Б., Газизулина А. С., Нусретов Р. А. Спонтанный фотомагнитноэлектрический эффект в эпитаксиальных слоях ферромагнитного GaMnAs. *Конденсированные среды и межфазные границы*. 2024;26(1): 111–116. <https://doi.org/10.17308/kcmf.2024.26/11814>

✉ Pavel B. Parchinskiy, e-mail: [p.parchinskiy@nuu.uz](mailto:p.parchinskiy@nuu.uz)  
© Parchinskiy P. B., Gazizulina A. S., Nusretov R. A., 2024



The content is available under Creative Commons Attribution 4.0 License.

## 1. Introduction

Nowadays, semiconductor GaMnAs solid solutions obtained by means of low-temperature molecular beam epitaxy (LT-MBE) are of great interest for scientists specializing in semiconductor materials. This is explained by the fact that low-temperature epitaxial growth (250–300 °C) allows obtaining GaMnAs solid solutions with a concentration of Mn which is several times higher than its solubility limit in the semiconductor matrix of gallium arsenide [1–2]. The presence of a large number of Mn magnetic ions enables ferromagnetic ordering in GaMnAs epitaxial layers. As a result, these materials combine semiconductor and magnetic properties, which is impossible for materials obtained by traditional methods [3–5].

It is known that spontaneous magnetization occurring in ferromagnetic materials at temperatures below the Curie temperature ( $T_C$ ) enables the origin of spontaneous galvanomagnetic effects in such materials, which are observed without an external magnetic field [6–8]. For GaMnAs, the most well-studied are the Hall and Nernst effects, known as the anomalous (spontaneous) Hall effect and the anomalous Nernst effect [9–11]. We should also note that the epitaxial layers of GaMnAs grown on GaAs substrates by means of LT-MBE can also demonstrate the spontaneous photomagnetolectric (PME) effect that manifests itself as the transverse voltage (photo-EMF) occurring when the materials are illuminated and the external magnetic field is zero [12]. Indeed, in epitaxial GaMnAs grown on GaAs substrates, the easy axis of magnetization and therefore the spontaneous magnetization vector  $\mathbf{M}_0$  are in the plane of the film [13, 14]. Then, when illuminating the surface of the epitaxial layer, the flow of photogenerated charge carriers from the surface to the depth of the epitaxial layer will be perpendicular to vector  $\mathbf{M}_0$ , which accounts for the formation of transverse photo-EMF. However, up to now, the photomagnetolectric effects of GaMnAs have not been thoroughly studied. Therefore, the purpose of our study was to investigate a spontaneous PME effect in the epitaxial layers of GaMnAs in the state of ferromagnetic order and determine the

dependence of the effect on temperature and crystallographic orientation.

## 2. Experimental

The epitaxial layers of GaMnAs investigated in our study were obtained via LT-MBE on a semi-insulating GaAs (001) substrate. Prior to the growth of the GaMnAs layers, a 200 nm GaAs buffer layer was grown at a temperature  $T_s = 580–600$  °C to heal the surface defects. Then the temperature of the substrate was lowered to 250 °C in order to grow GaMnAs layers. The thickness of the resulting GaMnAs epitaxial layers was 300 nm. The method of obtaining epitaxial layers used in our study is generally similar to the one presented in [15]. The quality of the obtained layers was controlled by means of X-ray diffraction analysis and (during the growth process) reflection high-energy electron diffraction. Both methods demonstrated that the obtained epitaxial films were homogeneous and did not contain any additional crystalline phases. The concentration of Mn in GaMnAs was measured by means of energy dispersive X-ray spectroscopy (EDX) using a JEOL JSM IT 200 electron microscope and was 2.9 at. %. To study the magneto-transport properties and the PME effect, a pattern was formed on the surface of the samples by the photolithography method. The pattern presented two mutually perpendicular Hall bars with side contacts. These bars were oriented along the  $[110]$  and  $[1\bar{1}0]$  crystal axes. The contacts on the GaMnAs surface were created using an indium solder applied to the surface of the epitaxial layer at a temperature of 220–230 °C.

## 3. Results and discussion

The Curie temperature ( $T_C$ ) of the studied epitaxial layer was determined based on the temperature dependence of its resistance ( $R$ ). As it was shown in [16] the temperature dependences  $R(T)$  in GaMnAs demonstrated a specific feature in the form of an inflection point near the paramagnetic-ferromagnetic phase transition. This feature is accounted for by the change in the dominating mechanism of charge carrier scattering. The position of the inflection point can be used to determine  $T_C$  with high accuracy. Fig. 1 demonstrates the temperature dependences

of the resistance  $R(T)$  and its first derivative  $dR(T)/dT$  for the studied GaMnAs layer. The dependence of  $R(T)$  was measured in the dark with no external magnetic field. For the convenience of presentation,  $R(T)$  was normalized to the value of  $R(300)$ , where  $R(300)$  is the resistance of the sample at room temperature.  $dR(T)/dT$  values were determined by means of numerical differentiation of  $R(T)$ .

The temperature dependence  $dR(T)/dT$  shown in fig. 1b demonstrates a pronounced minimum corresponding to the inflection point on the dependence  $R(T)$ . The position of the minimum can be used to determine the  $T_c$  of the studied epitaxial layer in the range of 80–85 K. We should note that at temperatures higher than  $T_c$  the resistance of the sample monotonously increases following a decrease in temperature. This indicates the semiconductor nature of the electrical conductivity of the studied GaMnAs epitaxial layers.

To study the PME effect, the investigated samples were illuminated with a white LED. The illumination intensity was controlled by the current value  $I_L$  in the LED. When illuminated, the samples demonstrated lower resistance, which indicates the presence of photoconductivity effects in GaMnAs. Fig. 2 presents the temperature dependence of the photoconductivity of the studied samples determined at  $I_L = 1–3$  mA. The photoconductivity of the samples was characterized by  $\Delta R$  determined as  $\Delta R = (R_1 - R_0)/R_0$ , where  $R_0$  is the dark resistance of the sample and  $R_1$  is the resistance of the sample illuminated with a LED. The dependences show that the photoconductivity of the studied samples is observed at temperatures below 100 K and  $\Delta R$  monotonously increasing with a decrease in temperature. This kind of behavior of the temperature dependence of photoconductivity appears to be quite predictable, taking into account the fact that the semiconductor nature of electrical conductivity results in a monotonous decay in the concentration of charge carriers with decreasing temperature. Obviously, if the number of photogenerated charge carriers in the semiconductor matrix does not depend on the temperature (or depends only insignificantly), the difference between the light and dark resistance of the sample and hence  $\Delta R$  will increase with

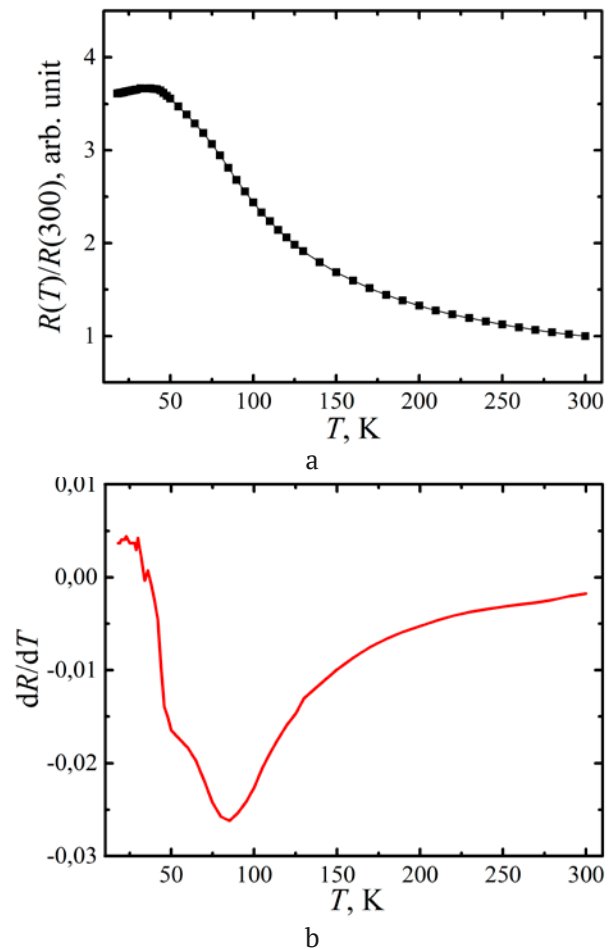


**Fig. 1.** *a* – temperature dependence of the resistance of the GaMnAs epitaxial layer normalized to the value of resistance measured at 300 K ( $R(300)$ ); *b* – temperature dependence of  $dR/dT$  of the GaMnAs epitaxial layer

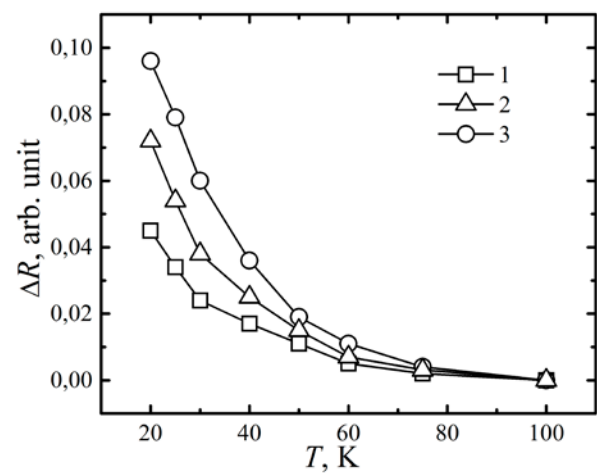


**Fig. 2.** Temperature dependence of the photoconductivity of GaMnAs measured at various values of the LED current: 1 –  $I_L = 1$  mA; 2 –  $I_L = 2$  mA; 3 –  $I_L = 3$  mA

a decrease in temperature. At the same time, at temperatures above 100 K, the concentration of photogenerated charge carriers is negligibly small as compared to the thermodynamically equilibrium concentration of charge carriers in GaMnAs. Therefore, there is practically no photoconductivity effect at such temperatures.

Fig. 3 shows dependences of the photo-EMF –  $U_1$  in the studied epitaxial layer on the temperature measured along the [110] and [1 $\bar{1}$ 0] crystal axes at  $I_L = 2$  and 3 mA. The dependences demonstrate that  $U_1$  increases with greater illumination of the sample. We believe that the fact that photo-EMF in the studied samples is only observed starting with temperatures lower than  $T_C$  indicates that this photo-EMF is accounted for by the PME effect, which occurs because the flow of photogenerated charge carriers is divided by the intrinsic magnetic field of the semiconductor matrix in the state of ferromagnetic ordering. It should be noted that  $U_1$ , measured along the [1 $\bar{1}$ 0] crystal axes monotonously increases with lower temperatures, while the temperature dependence of  $U_1$ , measured along the [110] crystal axis demonstrates a local maximum at 34–36 K.

The difference in the temperature dependences of  $U_1$  measured along different crystal axes can be explained taking into account the fact that the PME effect depends on both the absolute value of vector  $\mathbf{M}_0$  and its orientation with regard to the direction of measurements. It is obvious that at a

set magnetization value of the sample,  $U_1$  varies from maximum values (when the measurements are performed perpendicular to vector  $\mathbf{M}_0$ ) to zero (when the measurements are performed along the direction of vector  $\mathbf{M}_0$ ). Without an external magnetic field, the magnetization vector is oriented towards the easy axis of magnetization of the sample. In GaMnAs, the degree of ferromagnetic ordering and therefore the absolute value of vector  $\mathbf{M}_0$  monotonously increase with a decrease in the temperature. At the same time, the existing experimental data demonstrates that the orientation of the easy axis of magnetization in the epitaxial layers of GaMnAs in the state of ferromagnetic ordering is not constant. It depends on the dominant type of magnetocrystalline anisotropy and temperature [17,18]. When the concentration of photogenerated charge carriers does not depend on temperature, the temperature dependence of  $U_1$  is determined by the temperature dependence of the absolute value of vector  $\mathbf{M}_0$  and the temperature dependence of its orientation with regard to the [110] and [1 $\bar{1}$ 0] crystal axes. In this regard, the non-monotonic behavior of the temperature dependence of  $U_1$  along the [110] axis can be explained by a decrease in the angle between vector  $\mathbf{M}_0$  and the crystal axis at a temperature of 35–40 K. At the same time, the angle between the magnetization vector of the sample and the [1 $\bar{1}$ 0] crystal axis, on the contrary, increases, as evidenced by the increase in the rate of change in  $U_1$  observed for this axis in the same temperature range. Particularly, this can be the case, when the easy axis of magnetization in the epitaxial layer is reoriented from  $\langle 110 \rangle$  to  $\langle 100 \rangle$  direction with decreasing of temperature, as observed for GaMnAs in [17–19].

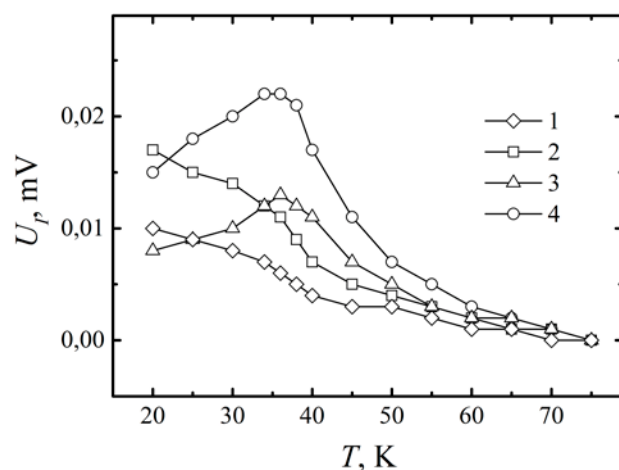


**Fig. 3.** Temperature dependence of the photo-EMF measured along [1 $\bar{1}$ 0] (curves 1 and 2) and [110] (curves 3 and 4) crystal axes at  $I_L = 2$  mA (curves 1 and 3) and  $I_L = 3$  mA (curves 2 and 4)

#### 4. Conclusions

Our study demonstrated that at temperatures below  $T_C$  illuminated GaMnAs epitaxial layers demonstrate transverse photo-EMF, which can be explained by a spontaneous PME effect in the semiconductor matrix in the state of ferromagnetic ordering. This effect is associated with the interaction of photogenerated charge carriers with the intrinsic magnetic field of the semiconductor matrix. For the first time we studied the temperature dependence of the



spontaneous PME effect for the [110] and [1 $\bar{1}$ 0] crystal axes. The study demonstrated that the temperature dependences of the PME effects measured along the [110] and [1 $\bar{1}$ 0] axes of GaMnAs epitaxial layer are significantly different. We believe that the observed difference can be explained by the fact that the value of the spontaneous PME effect is determined by both the absolute magnetization value of the sample and the orientation of the magnetization vector  $M_0$  with regard to the crystal axes along which the PME effect was measured. In this case, the non-monotonic behavior of the photo-EMF measured along the [110] axis can be explained by the reorientation of the easy axis of magnetization in the epitaxial layer from  $\langle 110 \rangle$  to  $\langle 100 \rangle$  directions, which is observed with decrease of temperature and a corresponding decrease in the angle between the spontaneous magnetization vector and the [110] crystal axis.

### Author contributions

Parchinskiy P. B. – scientific leadership, research concept, final conclusions, conducting research, text writing, and editing. Gazizulina A. S. – conducting research, processing the results, text writing, editing, and preparing the article for publication. Nusretov R. A. – conducting research and processing the results and their interpretation.

### Conflict of interests

The authors declare that they have no known competing financial interests or personal relationships that could have influenced the work reported in this paper.

### References

- Ohno H. Making nonmagnetic semiconductors ferromagnetic. *Science*. 1998;281(5379): 951–956. <https://doi.org/10.1126/science.281.5379.951>
- Pross A., Bending S., Edmonds K., Champion R. P., Foxon C. T., Gallaher B. Magnetic domain imaging of ferromagnetic GaMnAs films. *Journal of Applied Physics*. 2004;95(11): 7399–7401. <https://doi.org/10.1063/1.1669113>
- Ivanov V. A., Aminov T. G., Novotortsev V. M., Kalinnikov V. T. Spintronics and spintronics materials. *Russian Chemical Bulletin, International Edition*. 2004;53(11): 2357–2405. <https://doi.org/10.1007/s11172-005-0135-5>
- Men'shov V. K., Tugushev V. V., Caprara S., Chulkov E. V. Proximity-induced spin ordering at the interface between a ferromagnetic metal and a magnetic semiconductor. *Physical Review B*. 2010;81(23): 235212. <https://doi.org/10.1103/PhysRevB.81.235212>
- Dimitriev G. S., Krainov I. V., Sapega V. F., Averkiev N. S., Debus J., Lähderanta E. Energy structure of an individual Mn acceptor in GaAs:Mn. *Physics of the Solid State*. 2018;60: 1568–1577. <https://doi.org/10.1134/S106378341808005X>
- Onoda S., Sugimoto N., Nagaosa N. Quantum transport theory of anomalous electric, thermoelectric, and thermal Hall effects in ferromagnets. *Physical Review B*. 2008;77(16): 165103. <https://doi.org/10.1103/PhysRevB.77.165103>
- Nagaosa N., Sinova J., Onoda S., MacDonald A. H., Ong N. P. Anomalous Hall effect. *Reviews of Modern Physics*. 2010;82(2): 1539–1592. <https://doi.org/10.1103/RevModPhys.82.1539>
- Hirohata A., Yamada K., Nakatani Y., Prejbeanu I.-L., Dieny B., Pirro P., Hillebrands B. Review on spintronics: Principles and device applications. *Journal of Magnetism and Magnetic Materials*. 2020;509: 166711. <https://doi.org/10.1016/j.jmmm.2020.166711>
- Pu Y., Chiba D., Matsukura F., Ohno H., Shi J. Mott relation for Anomalous Hall and Nernst effects in Ga<sub>1-x</sub>Mn<sub>x</sub>As ferromagnetic semiconductors. *Physical Review Letters*. 2008;101(11): 117208. <https://doi.org/10.1103/PhysRevLett.101.117208>
- Chiba D., Nishitani Y., Matsukura F., Ohno H. Properties of Ga<sub>1-x</sub>Mn<sub>x</sub>As with high Mn composition (x>0.1). *Applied Physics Letters*. 2007;90(12): 122503. <https://doi.org/10.1063/1.2715095>
- Chiba D., Werpachowska A., Endo M., Nishitani Y., Matsukura F., Dietl T., Ohno H. Anomalous Hall Effect in Field-Effect Structures of (Ga,Mn)As. *Physical Review Letters*. 2010;104(10): 106601. <https://doi.org/10.1103/PhysRevLett.104.106601>
- Bonch-Bruyevich V. L., Kalashnikov S. G. *Physics of semiconductors\**. Moscow: Nauka Publ.; 1990. 688 p. (in Russ.)
- Brunner K., Gould C., Schmidt G., Molenkamp L. W. Structure, ferromagnetism and magnetotransport of epitaxial (Ga,Mn)As/GaAs structures. *Physica Status Solidi (a)*. 2006;203(14): 3565–3573. <https://doi.org/10.1002/pssa.200622382>
- Sadowski J., Domagała J. Z., ... Ilver L. Structural properties of MBE grown GaMnAs layers. *Thin Solid Films*. 2000;367(1-2): 165–167. [https://doi.org/10.1016/S0040-6090\(00\)00681-7](https://doi.org/10.1016/S0040-6090(00)00681-7)
- Yoon I. T., Kang T. W., Kim D. J. Analysis of magnetic field dependent mobility in ferromagnetic Ga<sub>1-x</sub>Mn<sub>x</sub>As layers. *Solid State Communications*.

2006;137(3): 171–176. <https://doi.org/10.1016/j.ssc.2005.10.004>

16. Kojima E., H eroux J. B., ... Kuwata-Gonokami M. Experimental investigation of polaron effects in  $\text{Ga}_{1-x}\text{Mn}_x\text{As}$  by time-resolved and continuous-wave midinfrared spectroscopy. *Physical Review. B.* 2007;76(19): 195323. <https://doi.org/10.1103/PhysRevB.76.195323>

17. Wang K. Y., Edmonds K. W., Campion R. P., Zhao L. X., Foxon C. T., Gallagher B. L. Anisotropic magnetoresistance and magnetic anisotropy in high-quality (Ga,Mn)As films. *Physical Review. B.* 2005;72(8): 085201. <https://doi.org/10.1103/PhysRevB.72.085201>

18. Hamaya K., Taniyama T., Kitamoto Y., Moriya R., Munekata H., Magnetotransport study of temperature dependent magnetic anisotropy in a (Ga,Mn)As epilayer. *Journal of Applied Physics.* 2003;94(12): 7657–7661. <https://doi.org/10.1063/1.1629134>

19. Lee S., Lee S., Bac S.-K., Choi S., Liu X., Dobrowolska M., Furdyna J. K. Spin-orbit-induced effective magnetic field in GaMnAs ferromagnetic semiconductor. *IEEE Transactions on Magnetics.* 2019;55(2): 2400206. <https://doi.org/10.1109/TMAG.2018.2862867>

\* *Translated by author of the article.*

## Information about the authors

*Pavel B. Parchinskiy*, PhD (Phys.-Math.), Associate Professor at the Department of Physics of semiconductors and polymers, National University of Uzbekistan (Tashkent, Uzbekistan).

<https://orcid.org/0009-0008-3812-9383>  
p.parchinskiy@nuu.uz

*Alisa S. Gazizulina*, Junior Research Fellow at the Department of Physics of Semiconductors and Polymers, National University of Uzbekistan (Tashkent, Uzbekistan).

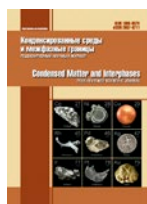
<https://orcid.org/0009-0003-8598-2479>  
alice.galashina@gmail.com

*Rafael A. Nusretov*, PhD (Phys.-Math.), Research Fellow at the Uzbek-Japanese Youth Innovation Center (Tashkent, Uzbekistan).

<https://orcid.org/0000-0002-4007-2039>  
rnusretov@yandex.ru

*Received 28.04.2023; approved after reviewing 18.05.2023; accepted for publication 15.06.2023; published online 25.03.2024.*

*Translated by Yulia Dymant*



## Original articles

Research article

<https://doi.org/10.17308/kcmf.2024.26/11815>

## Electrochemical activity of electroless Ni-P coatings in the hydrogen evolution reaction

I. V. Petukhov✉, V. I. Kichigin

Perm State University,  
15 ul. Bukireva, Perm 614990, Russian Federation

### Abstract

The purpose of this study was investigation of the electrochemical activity of Ni-P coatings, differing in phosphorus content and structure, in the hydrogen evolution reaction (HER) and the identification of the reasons for their high activity in the reaction being studied.

The coatings were deposited from an electroless nickel plating solution, the phosphorus content in the coatings (from 4.8 to 8.0 wt. %) varied by changing the pH of the solution. It was found that during cathodic polarization in 0.5 M H<sub>2</sub>SO<sub>4</sub> additional surface activation occurs as a result of dissolution of the surface layer of the coating, removal of phosphorus from the surface layer, and development of the electrode surface. Of all the coatings studied coatings containing 4.8% phosphorus were most susceptible to cathodic activation. Coatings with a phosphorus content of 8.0% were least susceptible to cathodic activation.

The similar electrochemical activity of the studied coatings (taking into account the roughness factor) in HER indicates that, as a result of cathodic polarization, the composition of the thin surface layer on which the cathodic reaction occurs is approximately the same, regardless of the initial phosphorus content.

**Keywords:** Electroless Ni-P coating, Electrochemical activity, Hydrogen evolution reaction, Roughness factor, Electrode capacitance

**Acknowledgements:** The study was supported by the Perm Scientific and Educational Centre “RATIONAL SUBSOIL USE”, 2023.

**For citation:** Petukhov I. V, Kichigin V. I. Electrochemical activity of electroless Ni-P coatings in the hydrogen evolution reaction. *Condensed Matter and Interphases*. 2024;26(1): 117–126. <https://doi.org/10.17308/kcmf.2024.26/11815>

**Для цитирования:** Петухов И. В., Кичигин В. И. «Электрохимическая активность Ni-P покрытий, полученных методом химического осаждения, в реакции выделения водорода. *Конденсированные среды и межфазные границы*. 2024;26(1): 117–126. <https://doi.org/10.17308/kcmf.2024.26/11815>

✉ Igor V. Petukhov, e-mail: [petukhov-309@yandex.ru](mailto:petukhov-309@yandex.ru)

© Petukhov I. V, Kichigin V. I., 2024



## 1. Introduction

The electrochemical activity of Ni-P alloys in the hydrogen evolution reaction (HER) has been studied for quite a long time [1–13]. This is mainly associated with the fact that these alloys have high electrochemical activity in this reaction. At the same time, the reasons for this activity have not yet been clearly established.

A number of studies [3] suggest that high catalytic activity is due to the amorphous structure of coatings; the transition of the amorphous structure of the coatings to a crystalline structure causes a decrease in catalytic activity. In other studies, the high catalytic activity of Ni-P coatings with a crystalline structure is explained by the developed surface of the coatings [2, 4].

A correlation between the catalytic activity of Ni-P alloys and their ability to absorb a sufficiently large amount of hydrogen was discovered [5]. Absorbed hydrogen changes the electronic structure of the alloys, which affects their catalytic activity in HER.

It was stated [6] that Ni-P alloys obtained by electrodeposition are more active in HER compared to alloys obtained by electroless deposition. The catalytic activity of Ni-P alloys is associated with the presence of internal stresses, since the activity of compact coatings was significantly higher than the activity of pressed porous electrodes made from the same compact coatings (there were no stresses in the porous electrodes). The activity of electrodeposited alloys obtained at temperatures above 338 K with fairly low internal stresses was also low. Tafel slopes for coatings obtained at low temperatures were in the range of 0.065–0.100 V, whereas electrodes obtained at temperatures above 338 K had slopes in the range of 0.19–0.27 V.

In [7], the electrocatalytic activity of electroless Ni-P coatings with different phosphorus contents (4–13.8 at. %) in HER in alkaline solutions was investigated. Two Tafel sections were identified on the polarization curves: the first section had a slope of more than 0.15 V, the second section had a slope of more than 0.3 V. The formation of the  $\text{NiH}_x$  hydride phase was detected using X-ray diffraction analysis at 1 hour of cathodic polarization of coatings. At the same time, the catalytic activity of freshly deposited coatings was somewhat lower than the activity

of polycrystalline nickel. The activity slightly increased after annealing of the coatings at a temperature of 400 °C, as well as after preliminary repeated cycling over a wide potential range. In [8], a higher activity of electroless Ni-P coatings with a lower phosphorus content was observed.

In [9, 10], HER was studied on Ni-P alloys of various compositions obtained by electrodeposition. It has been established that coatings obtained in galvanostatic mode had higher activity compared to coatings obtained in potentiostatic mode. Depending on the composition of the alloys, the nature of the activity was different: alloys containing no more than 6.5 wt. % phosphorus exhibited real activity, while alloys enriched with phosphorus ( $\leq 12.6\%$ ) increased the reaction rate due to surface development. At the same time, the HER mechanism does not depend on the phosphorus content in the coatings, but changes with increasing overvoltage.

Due to the search for effective cathode materials for HER, interest in studying the activity of Ni-P alloys continues unabated [11–14]. Ni-P coatings with chemical composition corresponding to nickel phosphide  $\text{Ni}_2\text{P}$ , which is considered to have high activity in HER were studied [12, 13]. The activity of the resulting amorphous coatings was compared with the activity of the same coatings, but annealed in vacuum at a temperature of 400 °C. It was found that amorphous coatings, compared to crystalline ones, have higher activity in alkaline solutions due to their inherent catalytic activity and greater hydrophilicity. In acidic media, amorphous coatings were less stable and inferior to crystalline (annealed) coatings.

To further increase the activity of Ni-P alloys, which in chemical composition correspond to various nickel phosphides, they were deposited on substrates with a developed surface (nickel foam, carbon fibers, carbon nanotubes). A review of methods for obtaining and properties of such coatings is provided in [12]. The catalytic activity of nickel phosphides is associated with their special electronic structure.

Thus, a review of even some studies shows that the activity of Ni-P alloys in HER depends on a large number of factors. This is partly due to the fact that the studied alloys were produced by



various methods (electrodeposition, electroless deposition, etc.); the alloys differ in composition, structure, methods of additional processing, and size of particles from which the electrode materials were formed. Nevertheless, systematization of information about the electrochemical activity of Ni-P alloys and its relationship with the structure, composition, as well as with changes in the surface of the alloys that can occur during the hydrogen evolution reaction is an urgent task. In this study, the electrochemical activity of Ni-P coatings with different composition and structure, obtained by electroless deposition was studied in 0.5 M H<sub>2</sub>SO<sub>4</sub> solution.

## 2. Experimental

For the deposition of Ni-P coatings, a solution of the following composition, g/l, was used: NiCl<sub>2</sub>·6H<sub>2</sub>O – 25; NaH<sub>2</sub>PO<sub>2</sub>·H<sub>2</sub>O – 20; CH<sub>3</sub>COONa·3H<sub>2</sub>O – 15; NH<sub>2</sub>CH<sub>2</sub>COOH – 20. Thiourea (1 mg/l) was used as a stabilizer. Solutions with different pH – 5.8, 5.3, 5.0 were used; pH was adjusted by adding a 25% ammonia solution.

The coatings were deposited on rectangular samples of nickel foil HO (99.96%) with a thickness of 80 μm. Preliminary preparation of the substrate surface consisted of degreasing with lime paste, washing with distilled water, and pickling in nitric acid (1:1) for 30–90 s. Bath loading was 1.0–1.5 dm<sup>2</sup>/l. Deposition was carried out under thermostatic conditions at 358 ± 1 K. The phosphorus content in the coatings was determined by energy-dispersive (micro-X-ray) analysis. The thickness of the coatings was calculated using the formula:

$$h = \Delta m / S\rho,$$

where  $\Delta m$  – weight gain, g;  $S$  – sample area, cm<sup>2</sup>;  $\rho$  – density, g/cm<sup>3</sup>. The density of Ni-P deposits was taken equal to 8.0 g/cm<sup>3</sup>.

The surface structure of the coatings, their composition, as well as changes in the surface composition after cathodic polarization were studied using a Hitachi S3400N scanning electron microscope with an attachment for energy-dispersive analysis.

The microhardness of the coatings was determined by the Vickers method (load – 50 g) using DM-8 Affri digital automatic microhardness tester.

X-ray diffraction analysis of coatings was carried out on cobalt K<sub>α</sub> radiation using a Bruker Advanced ECO X-ray diffractometer.

Electrochemical studies of coatings were carried out in a standard YASE-2 electrochemical cell in 0.5 M H<sub>2</sub>SO<sub>4</sub> at a temperature of 298 ± 1 K. The reference electrode was a chloridesilver electrode, the auxiliary electrode was a platinum electrode. Cathode curves were obtained using the potentiodynamic method; the potential sweep rate was 2·10<sup>-4</sup> V/s. After establishing a stationary potential (free corrosion potential), the samples were cathodically polarized for 5 min with a current of at least 260 A/m<sup>2</sup> (shift to the cathode region by 0.2–0.25 V), after which a potential sweep was set with its shift to the anode region. All electrochemical studies were carried out in an argon atmosphere, for which argon was first passed through the solution for 1 h before measurements. The thickness of the studied coatings was not less than 15 μm.

All potentials in the study were recalculated in the scale of a standard hydrogen electrode.

HER on Ni-P coatings was studied by polarization measurements and impedance spectroscopy using a Solartron-1280 device. The measurements included two types of experiments.

The first type included the following stages of measurements. After exposure for 30 min at open-circuit potential, the following procedures were carried out on the studied electrode:

- 1) cathodic polarization at a potential of –0.3 V for 5 min;
- 2) exposure at open-circuit potential for 30 min;
- 3) registration of cyclic voltammograms in the potential range from –0.12 to –0.24 V with a sweep rate of 2·10<sup>-4</sup> V/s (5 cycles);
- 4) exposure at an initial potential of –0.12 V for 20 min;
- 5) registration of the impedance spectrum at a given potential;
- 6) exposure at the next potential (shift to the cathode region by 0.01 V);
- 7) registration of the impedance spectrum at the next potential.

Impedance spectra were measured in the potential range from –0.12 to –0.24 V in the frequency range from 10 kHz to 0.01 Hz with an alternating signal amplitude of 0.01 V.

The second type included the following measurement stages:

- 1) cathodic polarization at a potential of  $-0.3$  V for 5 min;
- 2) exposure at open-circuit potential for 30 min;
- 3) exposure at a potential of  $-0.14$  or  $-0.15$  V for 20 min;
- 4) registration of the impedance spectrum at a given potential;
- 5) cathodic polarization at a potential of  $-0.3$  V for 5 min;
- 6) exposure at a potential of  $-0.14$  or  $-0.15$  V for 20 min;
- 7) registration of the impedance spectrum at the same potential.

Thus, at potentials of  $-0.14$  (or  $-0.15$  V), five cycles of measuring the impedance of the Ni-P electrode were carried out in order to establish the effect of cathodic polarization on the electrochemical behavior of Ni-P coatings in HER.

The analysis of solutions for nickel and phosphorus content in  $0.5$  M  $H_2SO_4$  solution after cathodic polarization of Ni-P coatings was carried out by inductively coupled plasma atomic emission spectroscopy using a Thermo iCAP 6500 Duo device, measurements were carried out in axial mode, the supplied power was  $1150$  W.

### 3. Results and discussion

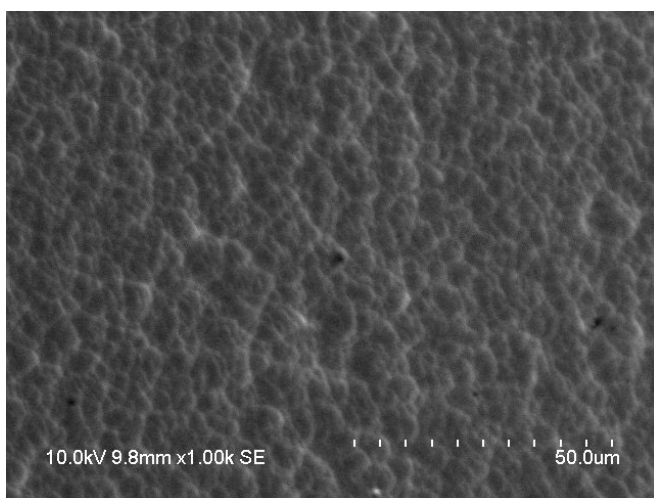
Changing the pH of the solution in the studied range slightly changed the deposition rate of

Ni-P coatings (Table 1). This was due to the fact that the used electroless nickel plating solution has a fairly high buffer capacity. Decrease of the pH of the solution increased the phosphorus content in coatings (Table 1). They had a typical spheroid structure (Fig. 1). Coatings deposited from this solution were characterized by high internal stresses, which caused a cracking of the coatings (Fig. 1b).

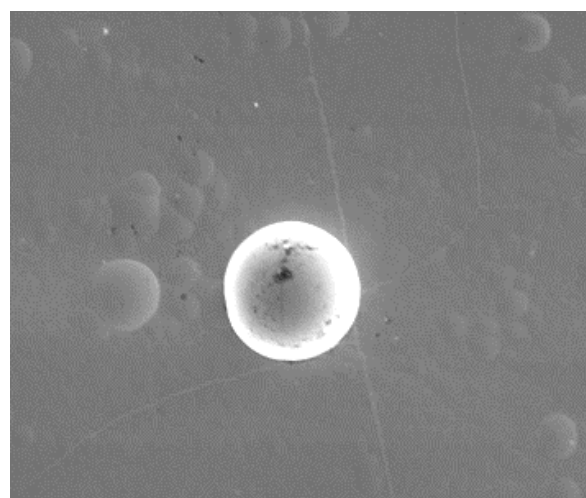
The absence of obvious crystalline faceting of the coatings in micrographs cannot unambiguously indicate the amorphous structure of the coatings; a diffraction pattern of a Ni-P coating with a phosphorus content of  $4.8$  wt. % is shown in Fig. 2. The most intense lines in the diffraction pattern were lines with indices (111) and (222). This was due to the presence of an axial texture in the coatings with the  $\langle 111 \rangle$  direction. Near to the intense line (111) there was a shoulder that corresponds to a fairly wide line with indices (200). The presence of several

**Table 1.** Parameters of Ni-P coatings obtained from electroless nickel plating solutions with different pH values

Parameters of coatings	pH of electroless nickel plating solution		
	5.0	5.3	5.8
Deposition rate, $\mu\text{m}/\text{h}$	$15.3 \pm 1.3$	$15.8 \pm 1.9$	$16.8 \pm 0.6$
Content of P, wt. %	$8.0 \pm 0.2$	$6.9 \pm 0.1$	$4.8 \pm 0.1$
Hardness, GPa	$447 \pm 16$	$454 \pm 34$	$532 \pm 37$



a



b

**Fig. 1.** Microphotographs of the surface of Ni-P coatings obtained from a solution with pH 5.0 (a) and 5.3 (b), 358 K. Magnification: a –  $\times 1000$ , b –  $\times 500$

diffraction maxima indicates the crystalline structure of these coatings.

Increasing the phosphorus content in coatings to 6.9 wt. % (Fig. 2) led to a weakening of the (220) and (311) lines. Due to the broadening of the (111) line, instead of a shoulder at the possible location of the (200) line, an asymmetric broadening of the (111) peak was observed, which may be associated with an increase in the dispersion of the crystalline phase and an increase in the proportion of the amorphous phase in the coatings.

At the maximum phosphorus content in the coating, instead of the (111) line, a wide “halo” was observed (Fig. 2). This indicated a significant proportion of the amorphous phase present in the coatings. The intensity of diffraction lines noticeably decreased. It should be noted that, along with the blurred line (222), rather sharp lines (220), and (311) were recorded. Their presence was probably due to the fact that the thickness of the studied coating was only 24  $\mu\text{m}$ . An estimate showed that a Ni-P coating layer of this thickness will absorb only ~75% of the incident X-ray radiation. Radiation transmitted through the coating layer can be reflected from the nickel substrate and produce weak reflections in the diffraction pattern. Coatings with lower phosphorus content (4.8 and 6.9% P) had thicknesses of more than 32  $\mu\text{m}$ , therefore there were no diffraction lines from the substrate.

One of the reasons for the high electrochemical activity of Ni-P coatings in HER in acidic sulphate solutions may be an increase in the electrode surface directly during cathodic polarization. This was indicated by the results of the following performed experiments.

Under cathodic polarization in 0.5 M  $\text{H}_2\text{SO}_4$  solution the loss of coating mass was determined and a sulfuric acid solution was analyzed to determine the content of nickel and phosphorus. The presence of the latter in the solution

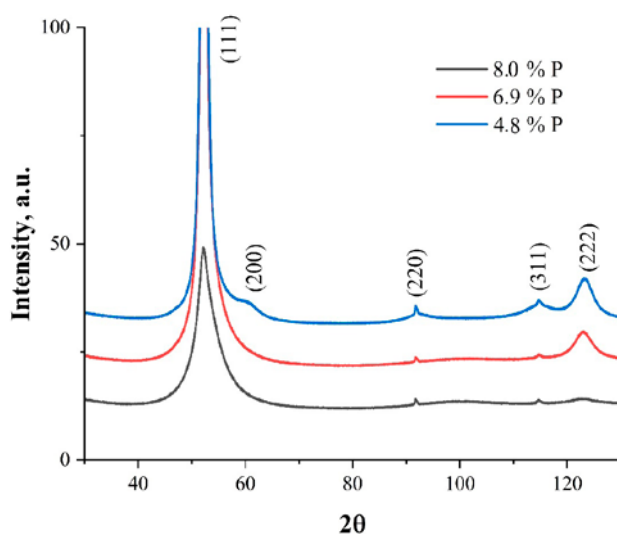


Fig. 2. Diffraction patterns of Ni-P coatings

indicates the dissolution of the coating during cathodic polarization. The dissolution of the coating may be due to the fact that part of the phosphorus was reduced during cathodic polarization and converted into phosphine. The nickel remaining in the thin surface layer was likely to be highly active and can be dissolved in a sulfuric acid solution. Modification of the chemical composition of a thin surface layer will be accompanied by an increase in the true surface of the electrode. The duration of cathodic polarization was 2 h. The results obtained are presented in Table 2.

With increasing phosphorus content, the process of dissolution of Ni-P coatings during cathodic polarization becomes more difficult. It should be noted that in the analyzed sample of sulfuric acid solution the phosphorus content was noticeably lower compared to its content in the coatings (Table 2). Under the condition of uniform dissolution, the ratio of phosphorus and nickel content in the analyzed solution would be equal to its content in the coatings. The lower content of phosphorus in the solution indicates that some

**Table 2.** Changes in the weight of Ni-P coatings and solution composition during cathodic polarization in a 0.5 M  $\text{H}_2\text{SO}_4$  solution ( $i \sim 300 \text{ A/m}^2$ , 2 h)

Phosphorus content in coatings, wt. %	Dissolution rate of coatings, $\text{g}/(\text{m}^2 \text{ h})$	Phosphorus content in solution referred to dissolved part of coating, wt. %
4.8±0.1	0.66±0.15	0.7±0.3
6.9±0.1	0.41±0.11	4.0±1.4
8.0±0.2	0.16±0.05	4.5±1.2



of it could pass into the gas phase in the form of phosphine. This process, as follows from Table 2, was most typical for coatings with a phosphorus content of 4.8 wt. %.

During cathodic polarization, intensive hydrogenation of the coatings occurred, which further increased the internal stresses that arose earlier in the deposition process and caused significant cracking of the coatings (Fig. 3).

During cathodic polarization, the state of the surface of the studied coatings changed. In order to obtain more reproducible results, before impedance measurements, the cycling of Ni-P electrode in the potential range from -0.12 V to -0.3 V with a low sweep rate –  $2 \cdot 10^{-4}$  V/s was performed (Fig. 4). After 5 potential sweep cycles,

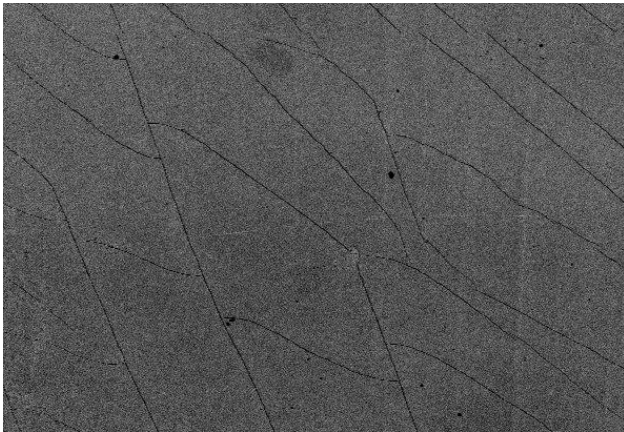


**Fig. 3.** Microphotograph of the surface of Ni-P coatings after cathodic polarization,  $\times 1000$

the cathode current increased more than twice. The increase in current was associated with the surface roughening of the Ni-P electrode during cycling.

The impedance hodographs of the Ni-P electrode were semicircles with a displaced center relative to the abscissa axis (Fig. 4b). With increase in cathodic polarization, the radius of the semicircle decreased. A detailed discussion of the results of impedance spectroscopy will be the subject of the next publication.

Since the real surface area of Ni-P coatings differs markedly from the geometric one and can change during measurements, it is important to have a method for assessing the real surface area for comparison of the activity of the studied coatings, taking into account the roughness factor.

For assessment of the true surface of the electrode, the imaginary part of the impedance  $Z''$  was recorded and the electrode capacitance was calculated using the equation:

$$C = -\frac{1}{(\omega Z'')},$$

where  $\omega$  is the angular frequency equal to  $\omega = 2\pi f$ . For these calculations, the frequency  $f = 1$  kHz was chosen. When choosing the frequency, the following was taken into account.

On the one hand, the frequency at which the electrode capacitance was determined must be

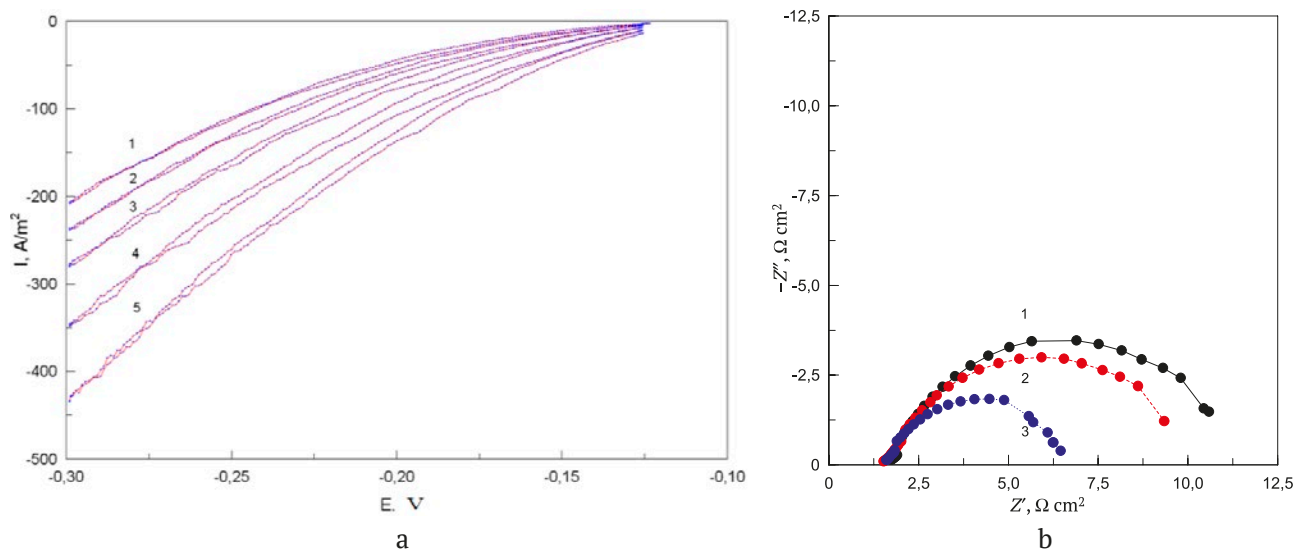


**Fig. 4.** a – Cyclic voltammograms of Ni-P coating (4.8 wt.% P) in 0.5 M  $H_2SO_4$  solution. Sweep rate of  $2 \cdot 10^{-4}$  V/s. b – Impedance hodographs of Ni-P electrode in 0.5 M  $H_2SO_4$  solution at potentials, V: 1: -0.12; 2: -0.13; 3: -0.15. Phosphorus content 4.8 wt.%



sufficiently low in order the alternating current penetrates into the depressions on the rough surface [15] and, thus, the entire electrode surface contributes to the measured capacitance. The frequency range in which roughness-related double-layer capacitance dispersion can be observed was approximately 1–100 kHz for moderately rough surfaces (protrusion heights up to 10  $\mu\text{m}$ ) with good electrical conductivity of the electrolyte [16, 17]. The frequency should not be too high also for the reason that capacitance dispersion at high frequencies can be associated not only with the properties of the electrode surface, but also with the measuring equipment [18, 19]. On the other hand, the selected frequency should not be too low; otherwise, a frequency-dependent term due to the Faradaic process will be added to the double layer capacitance. The relatively high capacitance values for the studied coatings (see below) contributed to the fact that the region of significant capacitance dispersion associated with the Faradaic reaction shifts towards lower frequencies. A frequency of 1 kHz can be considered suitable for determining the electrode capacitance for the calculation of the roughness factor of the surface of the electrodes.

After finding the capacity values, we calculated  $f_r$  (roughness factor) by dividing the capacitance  $C$  by the double-layer capacitance per real surface area ( $2 \cdot 10^{-5} \text{ F/cm}^2$ ) [2].

The calculated values of the capacitance of the Ni-P electrode at various potentials and the values of the roughness factor are shown in Table 3. Values  $C$  and  $f_r$  slightly change in the potential range shown in the Table 3.

During cathodic polarization, the surface roughening of Ni-P electrodes can occur. For further confirmation, the following experiments were carried out: the studied electrode was subjected to cathodic polarization at a potential of  $-0.3 \text{ V}$  for 5 min, then maintained at a potential of  $-0.14 \text{ V}$  (or  $-0.15 \text{ V}$ , in the case of coatings with a phosphorus content of 6.9 and 8.0%) for 20 min, after impedance measurements were carried out. In each subsequent cycle, the cathode currents increased and the impedance decreased, which could be due to an increase in the electrode surface area.

Impedance measurements (phosphorus content in coatings was 4.8%) were carried out at a potential of  $-0.14 \text{ V}$ , since according to the Table 3, a further increase in polarization did not

**Table 3.** Capacitance and roughness factor of Ni-P electrodes depending on the electrode potential at different phosphorus contents in the coating

$E, \text{ V}$	4.8 % P		6.9 % P		8.0 % P	
	$C, \text{ mF/cm}^2$	$f_r$	$C, \text{ mF/cm}^2$	$f_r$	$C, \text{ mF/cm}^2$	$f_r$
$-0.12$	1.26	63	–	–	0.229	12
$-0.13$	1.6	80	0,54	27	0.261	13
$-0.14$	1.58	79	0,58	29	0.285	14
$-0.15$	1.54	77	0,65	32	0.293	15
$-0.16$	1.68	84	0,66	33	0.316	16
$-0.17$	–	–	0,62	31	0.303	15
$-0.20$	–	–	0,59	30	0.303	15

**Table 4.** Changes in capacitance, roughness factor of Ni-P electrodes and current density at  $E = -0.14 \text{ V}$  (phosphorus content 4.8%) or  $E = -0.15 \text{ V}$  (phosphorus content 6.9 and 8.0%) during cycling of the potential

Cycle number	4.8 % P				6.9 % P				8.0 % P			
	$C, \text{ mF/cm}^2$	$f_r$	$i, \text{ A/m}^2$	$i/f_r, \text{ A/m}^2$	$C, \text{ mF/cm}^2$	$f_r$	$i, \text{ A/m}^2$	$i/f_r, \text{ A/m}^2$	$C, \text{ mF/cm}^2$	$f_r$	$i, \text{ A/m}^2$	$i/f_r, \text{ A/m}^2$
1	0.715	36	24.8	0.69	0.376	19	6.2	0.33	0.140	7.0	5.4	0.77
2	0.896	45	34.2	0.76	0.439	22	8.2	0.37	0.143	7.2	5.9	0.81
3	1.05	52	44.8	0.85	0.542	27	11.3	0.42	0.148	7.4	6.2	0.84
4	1.27	64	53.6	0.84	0.620	31	14.0	0.45	0.160	8.0	6.8	0.85
5	1.33	66	58.9	0.89	0.708	35	17.0	0.48	0.174	8.7	7.1	0.81

lead to a significant increase in the roughness factor. The roughness factor values based on the electrode capacitance calculated at a frequency of 1 kHz are shown in Table 4.

As can be seen from Table 4, in the process of cathodic polarization the real surface area increased from cycle to cycle, which was accompanied by an almost twofold increase in the roughness factor. This led to an increase in the cathode current recorded in each cycle at a potential of  $-0.14$  V. If the cathode current density is divided by the value  $f_r$ , then the normalized current density is obtained. Taking into account the roughness factor, the cathode current increased slightly from cycle to cycle. An increase in the normalized current density indicates that during cathodic polarization not only the surface roughness increased, but also the state of the surface changed: the chemical composition, structure of the surface layer and, consequently, the catalytic activity.

For the performance of measurements on Ni-P coatings with 6.9 and 8.0% P based on the data shown in the Table 3, a potential of  $-0.15$  V was chosen. At this potential, the roughness factor increased from cycle to cycle (Table 4). The normalized current density also increased slightly with cathodic polarization.

Coatings with a phosphorus content of 6.9 wt. % in the process of cathodic polarization increased their activity in the HER, but the effects described above were manifested to a lesser extent. The roughness factor of these coatings was noticeably lower than that of coatings with a phosphorus content of 4.8%. It weakly changed

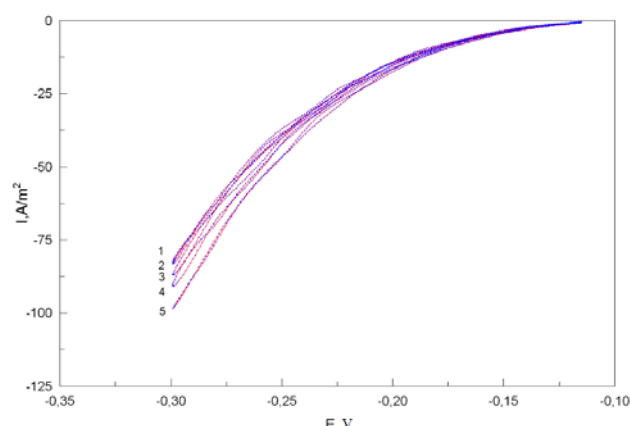


**Fig. 5.** Cyclic voltammograms of Ni-P coating (8.0 wt. % P) in  $0.5$  M  $H_2SO_4$  solution. Sweep rate of  $2 \cdot 10^{-4}$  V/s

in the indicated potential range (Table 3). This further supports the conclusion that coatings with a phosphorus content of 6.9% were less susceptible to cathodic activation.

Increase in phosphorus content to 8.0 wt. % significantly affected the cathodic behavior of Ni-P coatings. The registration of five successive potential sweep cycles caused a slight increase in the cathodic current density (Fig. 5). This indicates that Ni-P coatings with a given phosphorus content were least susceptible to cathodic activation.

The roughness factors of coatings with a phosphorus content of 8.0% were several times lower than the roughness factors of coatings with a lower phosphorus content and slightly changed with potential (Table 3). Preliminary cathodic polarization at  $E = -0.3$  V did not lead to a significant increase in the cathodic current density from cycle to cycle, i.e., the cathodic activation of Ni-P coatings in this case was insignificant. The roughness factor of the surface of Ni-P coatings varied slightly from cycle to cycle of measurements. Changes in the normalized cathode current density from cycle to cycle did not exceed 10% (Table 4).

Based on cathode currents, recorded at various potentials before each impedance measurement (holding for 20 min), stationary polarization curves were obtained. Since quite high values of cathode currents were achieved, a correction was made for the ohmic drop when constructing the cathode curves. Solution resistance  $R_s$  between the working electrode and Luggin capillary tip in  $0.5$  M  $H_2SO_4$  solution was obtained based on impedance measurements. Polarization curves constructed taking into account the correction are presented in Fig. 6a. From the obtained polarization curves, the coefficients of the Tafel equation were calculated (Table 5).

**Table 5.** Coefficients of the Tafel equation calculated based on stationary polarization curves taking into account correction for ohmic drop

Phosphorus content in coatings, wt. %	Coefficients in Tafel equation			
	$a, B$	$a^*, B$	$b, B$	$b^*, B$
4.8	0.25	0.39	0.058	0.058
6.9	0.29	0.38	0.060	0.060
8.0	0.32	0.37	0.063	0.063

$a^*$ ,  $b^*$  are the coefficients in the Tafel equation with regard to the roughness factor

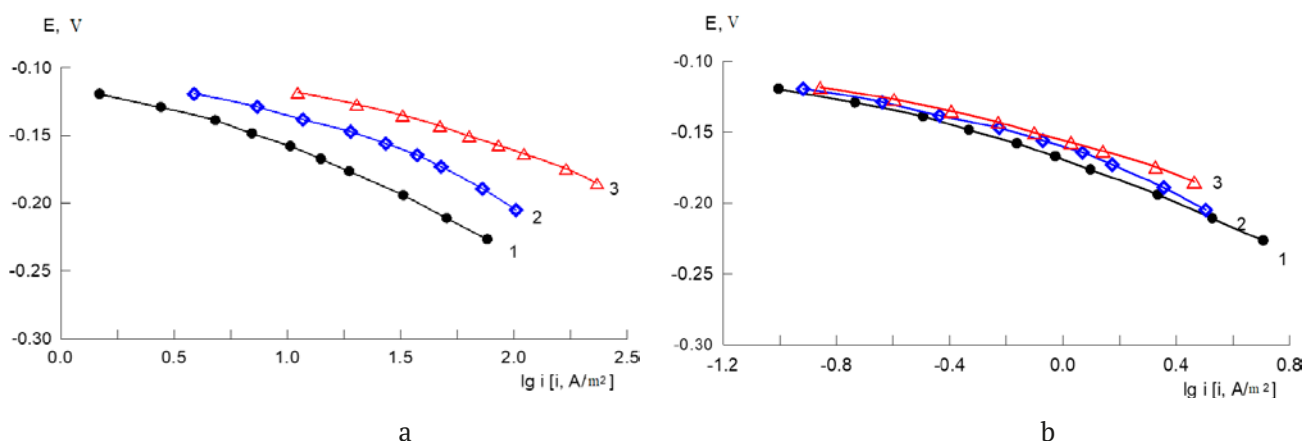


**Fig. 6.** Polarization curves of Ni-P coatings, plotted taking into account corrections for ohmic losses: a – based on the geometric surface area; b – based on the real surface area. Phosphorus content in coatings, wt.%: 1: 8.0; 2: 6.9; 3: 4.8

Since coatings obtained at different pH values of the electroless nickel plating solution after cathodic polarization were characterized by different roughness factor, their activities were compared taking into account this factor (Fig. 6b). The resulting curves differ slightly by Tafel slopes, but were located close to each other. At the same potentials, the normalized cathode currents for coatings with maximum and minimum phosphorus contents differ by not more than 20%, while without taking into account the roughness factor, the cathode currents differed by more than an order of magnitude (Fig. 6a). When taking into account the roughness factor for all studied phosphorus contents in coatings, close values of the coefficient  $a$  of Tafel equation were obtained (Table 5). At the same time, a decrease in phosphorus content in coatings led to a slight decrease in the coefficient  $b$ . Some difference in the polarization curves, which persisted even after dividing the current by  $f_r$  (Fig. 6b), was probably due to the fact that during cathodic activation of the electrodes, the increase in current was somewhat faster than the increase in the roughness factor, and this effect was more pronounced for coatings with 4.8 and 6.9% phosphorus (Table 3).

#### 4. Conclusions

The high activity of Ni-P coatings in HER is due to the fact that during cathodic polarization, additional activation of the surface occurs as a result of the dissolution of the surface layer of the coating, the removal of phosphorus from

its surface layer and the development of the electrode surface. Out of the studied coatings, coatings containing 4.8% phosphorus were most prone to cathodic activation. Coatings with a phosphorus content of 8.0% were least prone to cathodic activation. The similar electrochemical activity of the studied coatings (taking into account the roughness factor) in HER indicates that, as a result of cathodic polarization, the composition of the thin surface layer on which the cathodic reaction occurs is approximately the same, regardless of the initial phosphorus content. The high activity of Ni-P coatings is also evidenced by the low coefficients of the Tafel equation.

#### Contribution of the authors

The authors contributed equally to this article.

#### Conflict of interests

The authors declare that they have no known competing financial interests or personal relationships that could have influenced the work reported in this paper.

#### References

- Podesta J. J., Piatti R. C. V., Arvia A. J., Ekdunge P., Jüttner K., Kreysa G. The behaviour of Ni-Co-P base amorphous alloys for water electrolysis in strongly alkaline solutions prepared through electroless deposition. *International Journal of Hydrogen Energy*. 1992;17: 9–22. [https://doi.org/10.1016/0360-3199\(92\)90216-J](https://doi.org/10.1016/0360-3199(92)90216-J)
- Shervedani R. K., Lasia A. Studies of the hydrogen evolution reaction on Ni-P electrodes.

- Journal of The Electrochemical Society*. 1997;144(2): 511–518. <https://doi.org/10.1149/1.1837441>
3. Burchardt T., Hansen V., Valand T. Microstructure and catalytic activity towards the hydrogen evolution reaction of electrodeposited NiP<sub>x</sub> alloys. *Electrochimica Acta*. 2001;46(18): 2761–2766. [https://doi.org/10.1016/S0013-4686\(01\)00456-X](https://doi.org/10.1016/S0013-4686(01)00456-X)
4. Krolkowski A., Wiecko A. Impedance studies of hydrogen evolution on Ni-P alloys. *Electrochimica Acta*. 2002;47(13-14): 2065–2069. [https://doi.org/10.1016/S0013-4686\(02\)00074-9](https://doi.org/10.1016/S0013-4686(02)00074-9)
5. Paseka I. Sorption of hydrogen and kinetics of hydrogen evolution on amorphous Ni-P and Ni-S<sub>x</sub> electrodes. *Electrochimica Acta*. 1993;38(16): 2449. [https://doi.org/10.1016/0013-4686\(93\)85115-F](https://doi.org/10.1016/0013-4686(93)85115-F)
6. Paseka I. Hydrogen evolution reaction on Ni-P. The internal stress and the activities of electrodes. *Electrochimica Acta*. 2008;53(13): 4537–4543. <https://doi.org/10.1016/j.electacta.2008.01.045>
7. Abrantes L. M., Fundo A. M. The electrocatalytic behaviour of electroless Ni-P plating. *Journal of Electroanalytical Chemistry*. 2007;600: 63–79. <https://doi.org/10.1016/j.jelechem.2006.03.023>
8. Petukhov I. V., Medvedeva N. A., Subakova I. R., Kichigin V. I. Corrosion electrochemical behavior of Ni-P coatings in deaerated acidic sulfate solutions. *Protection of Metals and Physical Chemistry of Surfaces*. 2014;50(7): 876–883. <https://doi.org/10.1134/S2070205114070144>
9. Dolgikh O. V., Kravtsova Yu. G., Sotskaya N. V. The effect of composition of electrodeposited Ni-P alloys on the hydrogen evolution. *Russian Journal of Electrochemistry*. 2010;46(8): 918–924. <https://doi.org/10.1134/S1023193510080094>
10. Sotskaya N. V., Dolgikh O. V., Sapronova L. V., Kravtsova Yu. G. Kinetics of cathodic evolution of hydrogen on Ni-P systems electrodeposited alloys. *Protection of Metals and Physical Chemistry of Surfaces*. 2015;51 (3): 360–365. <https://doi.org/10.1134/S2070205115030247>
11. Zhao X., Chen X., Wang Y., Song P., Zhang Y. High-efficiency Ni-P catalysts in amorphous and crystalline states for the hydrogen evolution reaction. *Sustainable Energy & Fuels*. 2020;4: 4733–4742. <https://doi.org/10.1039/d0se00201a>
12. Hu C., Lv C., Liu S., ...Watanabe A. Nickel phosphide electrocatalysts for hydrogen evolution reaction. *Catalysts*. 2020;10(188): 1–32. <https://doi.org/10.3390/catal10020188>
13. Huo L., Jin C., Jiang K., Bao Q., Hu Z., Chu J. Applications of nickel-based electrocatalysts for hydrogen evolution reaction. *Advanced Energy and Sustainability Research*. 2022;3: 2100189. <https://doi.org/10.1002/aesr.202100189>
14. Jo W., Jeong D., Jeong J., ... Jung H. Electrocatalytic properties of pulse-reverse electrodeposited nickel phosphide for hydrogen evolution reaction. *Frontiers in Chemistry*. 2021;9: 781838. <https://doi.org/10.3389/fchem.2021.781838>
15. Alexander C. L., Tribollet B., Orazem M. E. Contribution of surface distributions to constant-phase-element (CPE) behavior: 1. Influence of roughness. *Electrochimica Acta*. 2015;173: 416–424. <https://doi.org/10.1016/j.electacta.2015.05.010>
16. Pajkossy T. Impedance of rough capacitive electrodes. *Journal of Electroanalytical Chemistry*. 1994;364: 111–125. [https://doi.org/10.1016/0022-0728\(93\)02949-I](https://doi.org/10.1016/0022-0728(93)02949-I)
17. Gunning J. The exact impedance of the de Levie grooved electrode. *Journal of Electroanalytical Chemistry*. 1995;392: 1–11. [https://doi.org/10.1016/0022-0728\(95\)03951-C](https://doi.org/10.1016/0022-0728(95)03951-C)
18. Jović V. D., Jović B. M. EIS and differential capacitance measurements onto single crystal faces in different solutions. Part I: Ag(111) in 0.01 M NaCl. *Journal of Electroanalytical Chemistry*. 2003;541: 1–11. [https://doi.org/10.1016/S0022-0728\(02\)01309-8](https://doi.org/10.1016/S0022-0728(02)01309-8)
19. Schalenbach M., Durmus Y. E., Tempel H., Kungl H., Eichel R.-A. Double layer capacitances analysed with impedance spectroscopy and cyclic voltammetry: validity and limits of the constant phase element parameterization. *Physical Chemistry Chemical Physics*. 2021;23: 21097–21105. <https://doi.org/10.1039/D1CP03381F>

### Information about the authors

Igor V. Petukhov, Cand. Sci. (Chem.), Associate Professor at the Department of Physical Chemistry, Perm State University, (Perm, Russian Federation).

<https://orcid.org/0000-0002-3110-668x>  
petukhov-309@yandex.ru

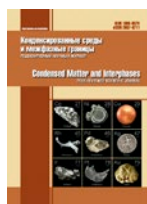
Vladimir I. Kichigin, Cand. Sci. (Chem.), Research Fellow, Research Fellow at the Department of Physical Chemistry, Perm State University (Perm, Russian Federation).

<https://orcid.org/0000-0002-4668-0756>  
kichigin@psu.ru

Received 21.03.2023; approved after reviewing 28.06.2023; accepted for publication 15.09.2023; published online 25.03.2024.

Translated by Valentina Mittova





# Condensed Matter and Interphases

Kondensirovannye Sredy i Mezhfaznye Granitsy  
<https://journals.vsu.ru/kcmf/>

## Original articles

Research article

<https://doi.org/10.17308/kcmf.2024.26/11816>

## Study of the thermal conductivity of natural carbonates

P. A. Popov<sup>1</sup>, A. A. Zentsova<sup>1</sup>, V. V. Voronov<sup>2</sup>, I. A. Novikov<sup>2</sup>, E. V. Chernova<sup>2</sup>, P. P. Fedorov<sup>2</sup>✉

<sup>1</sup>Bryansk State Academician I. G. Petrovski University,  
14, Bezhitskaya str., Bryansk 241036, Russian Federation

<sup>2</sup>Prokhorov General Physics Institute of the Russian Academy of Sciences,  
38, Vavilova str., Moscow 119991, Russian Federation

### Abstract

The thermal conductivity of natural monoliths of calcite, dolomite marble, and limestone from various deposits was measured using the absolute stationary method of longitudinal heat flow in the temperature range of 50–300 K and the dynamic method in the range of 323–573 K. A majority of calcite marbles were inferior in thermal conductivity to dolomite marbles. At room temperature, the thermal conductivity coefficients of all studied samples were lower  $k = 5 \text{ W/(m K)}$ .

The obtained data were compared with the literature data. The diversity of experimental data from different authors on the thermal conductivity of carbonates is associated with qualitative differences in the samples studied.

**Keywords:** Minerals, Marble, Calcite, Dolomite, Limestone, Siderite, Thermal conductivity, Phonon-defect scattering, Temperature dependence

**Funding:** The study was carried out using the scientific equipment of the Centre for Collective Use of Bryansk State University and the Centre for Collective Use of the Prokhorov General Physics Institute of the Russian Academy of Sciences.

**Acknowledgements:** The authors are grateful to V. A. Maslov and Yu. V. Yashunsky for providing samples No. 6 and No. 7, respectively.

**For citation:** Popov P. A., Zentsova A. A., Voronov V. V., Novikov I. A., Chernova E. V., Fedorov P. P. Study of the thermal conductivity of natural carbonates. *Condensed Matter and Interphases*. 2024;26(1): 127–134. <https://doi.org/10.17308/kcmf.2024.26/11816>

**Для цитирования:** Попов П. А., Зенцова А. А., Воронов В. В., Новиков И. А., Чернова Е. В., Федоров П. П. Исследование теплопроводности природных карбонатов. *Конденсированные среды и межфазные границы*. 2024;26(1): 127–134. <https://doi.org/10.17308/kcmf.2024.26/11816>

✉ Pavel P. Fedorov, e-mail: [ppfedorov@yandex.ru](mailto:ppfedorov@yandex.ru)

Popov P. A., Zentsova A. A., Voronov V. V., Novikov I. A., Chernova E. V., Fedorov P. P., 2024



## 1. Introduction

Calcium carbonate  $\text{CaCO}_3$  and calcium magnesium carbonate  $\text{CaMg}(\text{CO}_3)_2$  (dolomite) are the basis of many limestone rocks. Calcium carbonate is mainly represented by crystal structures such as calcite (sp. gr. *R3c*) and aragonite (sp. gr. *Pmcn*), less common is water-soluble vaterite (sp. gr. *P63/mmc*). Among natural carbonates, magnesite  $\text{MgCO}_3$  and siderite  $\text{FeCO}_3$ , isostructural to calcite, are also common. Marble is a limestone recrystallized at elevated temperature and pressure (metamorphosed), consisting mainly of calcite. The basis of dolomite marble is calcium-magnesium carbonate (sp. gr. *R3*).

The area of application of marble is extremely wide. Their use as a construction, finishing and facing material for bathrooms, swimming pools, fireplaces, etc. requires the presence of a certain heat flow and a corresponding temperature difference. The value of the latter is associated with such a thermophysical characteristic of the material as the thermal conductivity coefficient. Knowledge of the thermal conductivity values of rocks is necessary for the production of geophysical models. Thermal conductivity, related to the propagation rate of sound waves, for polycrystalline materials depends on the porosity and structure of grain boundaries and, thus, allows evaluating the mechanical characteristics of rocks.

The objective complexity of heat transfer processes does not allow to provide a sufficiently accurate a priori assessment of this characteristic, therefore experimental methods of determination is a priority. Studies [1–16] are devoted to the study of the thermal conductivity of natural carbonates. Theoretical calculations were provided in [17]. However, the publications we found provide the values of the thermal conductivity coefficient at room temperature or consider the behavior of the thermal conductivity of both rocks and crystalline calcite and dolomite at elevated temperatures. However, the low-temperature region is of practical and scientific interest, for example, for geophysical calculations in the Arctic. At the same time, experimental data of different authors on the thermal conductivity of marbles and other limestone rocks vary significantly, probably, mainly due to the qualitative diversity of the studied samples.

The purpose of this study was experimental investigation of the thermal conductivity coefficients of natural carbonate samples in a wide temperature range, from sub nitrogen to elevated. This study continues our measurements of the thermal conductivity of natural minerals and rocks [18–21].

## 2. Experimental

Natural samples listed in Table 1 and shown in Fig. 1 were used as research objects. Four metamorphosed samples (marbles № 1–4) and four sedimentary rock samples (№ 5–8) were examined.

X-ray phase analysis (XPA) was carried out using Bruker D8 Advance diffractometer ( $\text{CuK}\alpha$ -radiation). The TOPAS software package was used to calculate the lattice parameters. The microstructure of the samples was assessed by optical microscopy using a microscope  $\mu\text{Vizor}$  103 and scanning electron microscopy (SEM) on an EVO 10 microscope (Zeiss, Germany) with  $\text{LaB}_6$  cathode. Semi-quantitative chemical microanalysis (SEM-EDS) was performed using a Smart EDX spectrometer (METEK-Zeiss, USA & Germany).

Samples for thermal conductivity measurements were cut from homogeneous areas of the monoliths. For the temperature range of 50–300 K, samples in the form of parallelepipeds with the dimensions indicated in the Table 2 were used. For studies at elevated temperatures, samples were prepared in the form of tablets with a diameter of 15 mm and a thickness of 5 mm. It should be remembered that the indicated dimensions assume averaging of measurement results over a fairly large volume of samples. This distinguishes our method from the method used, for example by Merriman et al. [14] when studying samples with dimensions of ~1 mm.

Thermal conductivity coefficient in the temperature range 50–300 K was measured using the absolute stationary method of longitudinal heat flow. The experimental equipment and measurement technique are described in [23]. To ensure a flat heat front, a resistive heater that sets the measured temperature difference along the sample was glued to its end surface. The measurement error for the thermal conductivity coefficient value was not higher than  $\pm 5\%$ .



**Fig. 1.** Photographs of the studied samples: a – No. 1; b – No. 2 (marble); c – No. 3; d – No. 4; e – No. 5; f – No. 6; g – No. 7; h – No. 8



**Table 1.** Characteristics of the studied samples

No.	Name, location	Phase and chemical composition	Lattice parameters		Average grain size, microns
			$a$ , Å	$c$ , Å	
1	Dolomite marble, Ulan-Ude	Dolomite, $\text{CaMg}(\text{CO}_3)_2$	4.8142±0.0001	16.033±0.004	250
2	Marble, Slyudyanka, Dynamitny quarry	Magnesian calcite $\text{Ca}_{0.934}\text{Mg}_{0.07}\text{CO}_3$ + dolomite, $\text{CaMg}(\text{CO}_3)_2$	4.963±0.001	16.95±0.01	1000
			4.808±0.001	16.02±0.05	
3	Marble, Palanga	Calcite, $\text{Ca}_{0.96}\text{Mg}_{0.04}\text{CO}_3$	4.984±0.001	17.03±0.01	30
4	Marble, Greece, Kassandra Peninsula	Calcite, $\text{Ca}_{0.96}\text{Mg}_{0.04}\text{CO}_3$	4.990±0.001	17.01±0.01	20
5	Limestone, Ruza	Calcite	4.984±0.001	17.03±0.01	
6	Dense limestone, Tarusa (“Tarus marble”)	Calcite, $\text{Ca}_{0.96}\text{Mg}_{0.04}\text{CO}_3$	4.985±0.001	17.04±0.01	40
7	Dolomite, Vazuza River	Dolomite $\text{CaMg}(\text{CO}_3)_2$ + quartz $\text{SiO}_2$	4.814±0.002	16.06±0.01	40
8	Siderite, Ruza [22]	Siderite, $\text{FeCO}_3$	4.705±0.003	15.45±0.01	5–10

**Table 2.** Geometric dimensions of samples in the form of parallelepipeds  $\text{mm}^3$  and thermal conductivity coefficient values ( $W/(m \times K)$ ) of the studied samples at different temperatures

$T$ , K	No 1	No 2	No 3	No 4	No 5	No 6	No 7	No 8
50	15.2	10.5	9.4	8.23	8.67	4.76	2.30	1.17
100	9.37	7.83	6.72	5.84	5.38	4.42	3.33	1.47
150	7.06	6.14	5.15	4.61	4.15	3.88	3.49	1.67
200	5.89	5.14	4.22	3.91	3.48	3.40	3.39	1.80
250	5.21	4.52	3.62	3.51	3.07	3.04	3.25	1.87
300	4.72	4.06	3.24	3.22	2.76	2.79	3.08	1.90
350	4.3	3.7	3.0	3.0	2.5	2.6	–	1.9
400	4.0	3.4	2.7	2.8	2.4	2.4	–	2.0
450	3.7	3.2	2.6	2.6	2.3	2.2	–	2.0
500	3.5	3.1	2.5	2.4	2.2	2.1	–	2.0
550	3.3	3.0	2.4	2.3	2.1	2.1	–	2.0
573	3.3	2.9	2.4	2.3	2.1	2.1	–	2.0
Geometric dimensions of samples cut for measurements, $\text{mm}^3$								
	10.1× 9.4× 25	12.4× 10.7× 25	10.7× 9.6× 19	9.6× 8.1× 23	12.2× 13.7× 25	11.1× 8.7× 23	9.7× 9.7× 20	11.5× 12.5× 25

To study thermal conductivity coefficient in the range of 323–573 K, an ITλ-400 thermal conductivity meter was used with a measurement error within  $\pm 10\%$ .

### 3. Results and discussion

The studied samples were single-phase, with the exception of sample No. 2 (two-phase mixture of magnesian calcite with dolomite) and sample No. 7 (dolomite with a significant content of non-isomorphic impurities: about 3% quartz, traces of calcium phosphate). Using the phase

diagram of the  $\text{CaCO}_3$ - $\text{MgCO}_3$  system [24] as a geothermometer, it can be stated that in two-phase sample No. 2 the magnesium content in the  $\text{Ca}_{1-x}\text{Mg}_x\text{CO}_3$  solid solution corresponded to a metamorphization temperature of about 600° C.

Extrapolation of the limiting solubility curve of magnesium in the  $\text{Ca}_{1-x}\text{Mg}_x\text{CO}_3$  solid solution, obtained by Golschmit and Hurd [24], up to room temperature provided the value  $x \leq 10^{-4}$ . Increased magnesium content in single-phase calcite samples (Table 1), several orders of magnitude higher than the equilibrium solubility of magnesium in a



solid solution in the  $\text{CaCO}_3\text{-MgCO}_3$  system at low temperatures probably indicates the biogenic origin of these limestones [25].

Graphs of the temperature dependence of thermal conductivity coefficient  $k(T)$  of studied samples are shown in Fig. 2. In numerical form, the measurement results  $k(T)$  are shown in Table 2.

It can be seen that the obtained data varied widely, especially in the low temperature region. The dependence of thermal conductivity coefficient on temperature varied from monotonically decreasing, characteristic of single-crystal samples, to increasing, characteristic of highly disordered materials.

At room and higher temperatures, the thermal conductivity coefficient of all studied samples was below  $5 \text{ W}/(\text{m}\cdot\text{K})$ , which conditionally allows these materials to be classified as thermal insulators. The low hardness of the compounds (less than 4 according to Mohs), the characteristic cleavage of single crystals and the relatively low melting and decomposition temperatures indicate the weakness of interionic bonds, which negatively affects the efficiency of the heat transfer process.

The  $k(T)$  points of dolomite sample No. 1 (curve 1) are located above all in Fig. 2. Over the entire temperature range studied, they were satisfactory (correlation coefficient  $R = 0.9978$ ) approximated by a power function  $k(T) = 190.8 \cdot T^{-n}$ , where the exponent  $n = 0.651$  is not much lower than the corresponding values, close to  $n = 1$ , for many dielectric single crystals with a perfect structure [26–28]. When the temperature was decreased to minimal  $T = 50 \text{ K}$ , the increase in growth rate  $k(T)$  with a transition to an exponential dependence characteristic for crystals [29], or, conversely, a decrease in growth rates  $k(T)$  with reaching the maximum were not observed. Probably, this maximum  $k(T)$  characteristic of crystalline materials occurs at significantly lower temperatures. For samples of marble No. 4 and limestone No. 5, a similar approximating function has the form  $k(T) = 67.08T^{-0.533}$  ( $R = 0.9986$ ) and  $k(T) = 97.333 \cdot T^{-0.623}$  ( $R = 0.9967$ ) respectively. The coverage of such a wide temperature range by one function can probably be explained by the dominance of phonon scattering processes at grain boundaries.

The  $k(T)$  graphs of marbles No. 2, No. 3, and, to a greater extent, limestone No. 6 (curves 2,

3 and 6 accordingly) demonstrate a decrease in growth rates when the temperature was decreased to  $T = 50 \text{ K}$ . For a low absolute value of thermal conductivity, this is a common circumstance for materials with partial structural disorder.

Quartz inclusions (sample no. 7, curve 7) into the dolomite matrix led to a sharp drop in thermal conductivity coefficient with a blurred maximum  $k(T)$  with  $k \rightarrow 0$  at  $T \rightarrow 0$ . The obvious reason for this is significant phonon-defect scattering.

The thermal conductivity of siderite demonstrated (curve 8) maximum disorder of the structure with the average phonon mean free path probably reaching the minimum possible value comparable to interstitial distances. The small sizes of crystal grains suggest the manifestation of intense phonon scattering due to the frequent intersection of grain boundaries by the heat flow. It should be noted that for the sample studied [22], the broadening of lines in the X-ray diffraction pattern indicates the size of the coherent scattering regions  $D = 26 \text{ nm}$ .

The comparison of the data obtained for dolomite (No. 1) and calcite (No. 4) marble samples with literature data based on the results of measuring the thermal conductivity of related materials is shown in Fig. 3.

It can be seen that the thermal conductivity coefficient of dolomite determined in our study

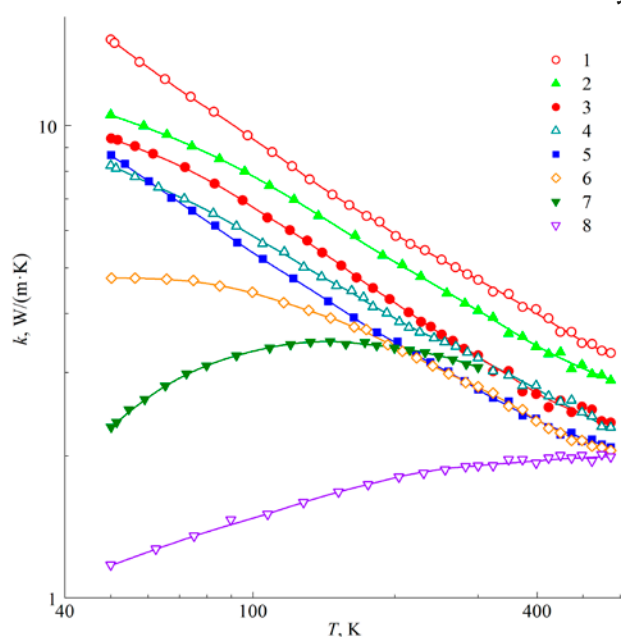


**Fig. 2.** Temperature dependences of thermal conductivity coefficients of samples: No. 1 (1); No. 2 (2); No. 3 (3); No. 4 (4); No. 5 (5); No. 6 (6); No. 7 (7); No. 8 (8)

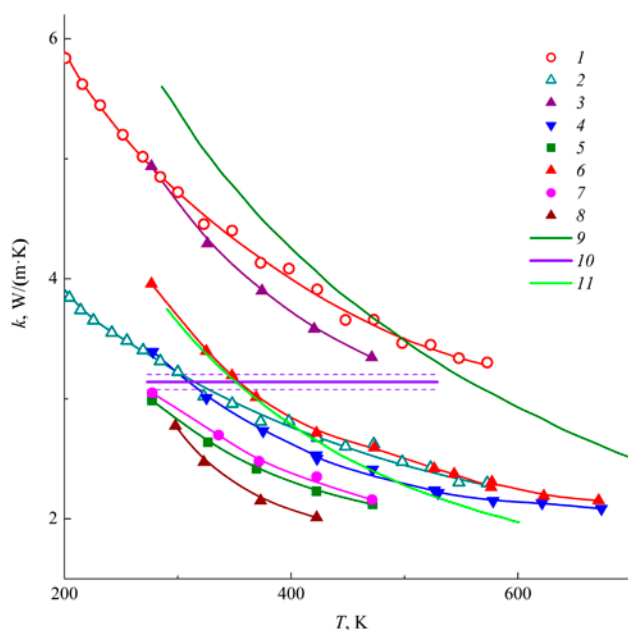


**Fig. 3.** Temperature dependences of thermal conductivity coefficients: sample No. 1 (1); sample No. 4 (2); dolomite [1] (3); calcite single crystal perpendicular to the c axis [1] (4); marble perpendicular to the layer [1] (5); single crystal of calcite along the c axis [1] (6); marble parallel to the layer [1] (7); marble [13] (8); dolomite, averaging for four samples [14] (9); dolomite [13] (10); calcite [14] (11)

is close to that obtained by Merriman et al. [14] (curve 9), which presented the result of averaging  $k(T)$  for four mineral samples with an average grain size of 0.369 mm, skeletal density of 2.83 g/cm<sup>3</sup> and porosity less than 1% and containing small quantities of iron (FeO = 0.18–0.42 wt. %) and manganese (MnO = 0.1 wt. %). Moreover, the total content of CaO + MgO in this mineral is 98.94–99.23 wt. % compared to ideal dolomite, and trace impurities (<0.1 wt. %) include oxides of Al, Na and Ti [14]. We should note the steepness of the dependence  $k(T)$ , when describing it by a power function  $k \sim T^{-n}$  the value of the exponent in the high temperature region exceeds  $n = 1$ . Such a strong dependence is not typical for materials in a stable crystalline state [29, 30]. In terms of the absolute value of thermal conductivity coefficient, the  $k(T)$  data of Birch and Clark [1] for dolomite (curve 3) with a density of 2.826 g/cm<sup>3</sup> and average grain size of 0.01 mm also not significantly differ from our data. At the same time, the different degrees of steepness of graphs 1 and 3 should be noted.

It was also recorded [13] that there was virtually no dependence of thermal conductivity

coefficient on the temperature (horizontal line 10 in Fig. 3) of dolomite with a density of 2.70 g/cm<sup>3</sup> and open porosity of 1–2%. Emirov et al. explained this feature by the presence of an amorphous component in the structure of the material.

Marbles studied by Birch and Clark [1] (curves 5 and 7) and Garcia [11] (curve 8), were significantly inferior by thermal conductivity to the marble sample No. 4 which we studied (curve 2). It is important to note that the obtained  $k(T)$  graph for sample No. 4 at elevated temperatures occupies an intermediate position between the curves 4 and 6 for single-crystalline calcite according to [1].

Thus, in general, it can be stated that the thermal conductivity coefficient of crystalline dolomite is higher than that of calcite. The structures of these two minerals are similar to each other; dolomite differs by the substitution of half of the calcium cations with magnesium cations, which formed ordered layers located perpendicular to the c axis (Fig. 4). Usually, the substitution of some cations with the formation of a solid solution with isovalent isomorphism leads to a decrease in thermal conductivity. This fact has been documented in numerous examples for compounds with a fluorite structure [31]. However, the calcite-dolomite pair falls out of this pattern. The increased thermal conductivity of dolomite may be associated with a sharper increase in mechanical characteristics in relation to the increase in density during the transition from calcite to dolomite.

#### 4. Conclusions

Thus, experimental data on the thermal conductivity of dolomite, calcite marbles and limestones in a wide temperature range - from sub nitrogen to elevated temperatures were obtained. In most cases, the thermal conductivity decreased in the specified range of materials. The revealed wide variations in the nature of the temperature dependence of thermal conductivity were associated with significant differences in the degree of disorder of the studied objects.

#### Contribution of the authors

The authors contributed equally to this article.

#### Conflict of interests

The authors declare that they have no known competing financial interests or personal

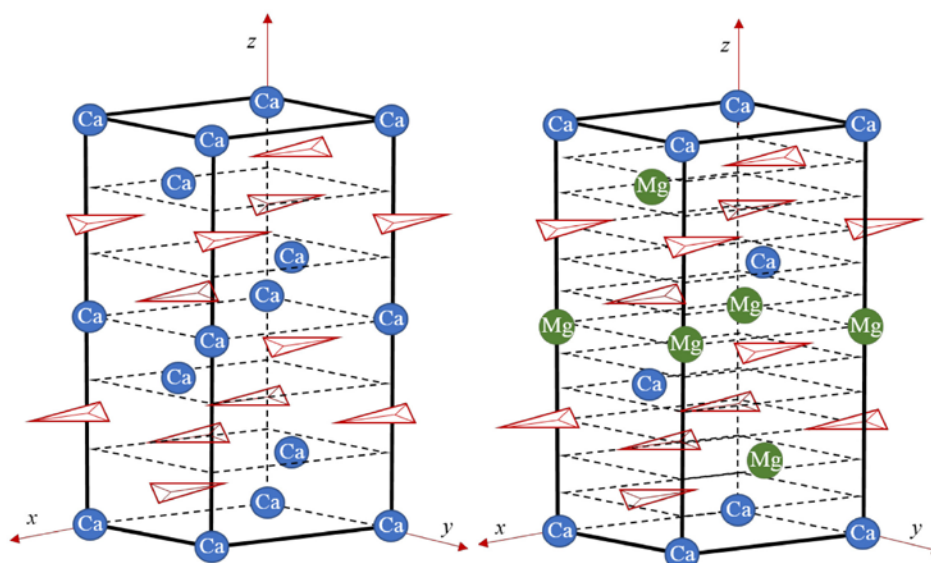


Fig. 4. Crystal structure of calcite (a) and dolomite (b): Red triangles indicate  $\text{CO}_3$  groups [17]

relationships that could have influenced the work reported in this paper.

## References

- Birch F., Clark H. The thermal conductivity of rocks and its dependence upon temperature and composition. *American Journal of Science*. 1940;238(8): 529–558. <https://doi.org/10.2475/ajs.238.8.529>
- Clark H. The effects of simple compression and wetting on the thermal conductivity of rocks. *American Geophysical Union Transactions*. 1941;22: 543–544. <https://doi.org/10.1029/TR022i002p00543>
- Zierfuss H., Vliet van der G. Measurement of heat conductivity of sedimentary rocks. *American Association of Petroleum Geologists Bulletin*. 1956;40: 2475–2488. <https://doi.org/10.1306/5CEAE5A4-16BB-11D7-8645000102C1865D>
- Zierfuss H. Heat conductivity of some carbonate rocks and clayey sandstones. *American Association of Petroleum Geologists Bulletin*. 1969;53: 251–260. <https://doi.org/10.1306/5D25C607-16C1-11D7-8645000102C1865D>
- Meincke W., Hurtig E., and Weiner J. Temperaturerteilung, Wärmeleitfähigkeit und Warmefluss in Thüringer Becken. *Geophysik und Geologic*. 1967;(11): 40–71.
- Ki-iti Horai. Thermal conductivity of rock-forming minerals. *Journal of Geophysical Research*. 1971;76(5): 1278–1308. <https://doi.org/10.1029/jb076i005p01278>
- Beck A. E., Anglin F. M., Sass, J. H. Analysis of heat flow data-in situ thermal conductivity measurements. *Canadian Journal of Earth Sciences*. 1971;8: 1–19. <https://doi.org/10.1139/e71-001>
- Thomas J., Jr. Frost R. R., Harvey R. D. Thermal conductivity of carbonate rocks. *Engineering Geology*. 1973;7(4): 3–12. [https://doi.org/10.1016/0013-7952\(73\)90003-3](https://doi.org/10.1016/0013-7952(73)90003-3)
- Robertson E. C. Thermal properties of rocks. *Open-File Report*. 1988; 88–441. Reston, Virginia. <https://doi.org/10.3133/ofr88441>
- Shin K., Kinoshita N., Okuno T. Mechanical, thermal properties and permeability of rocks under high temperature. *Journals Free Access*. 1988;29(3): 242–253. <https://doi.org/10.5110/jjseg.29.242>
- García E., de Pablos A., Bengoechea M. A., Guaita L., Osendi M. I., Miranzo P. Thermal conductivity studies on ceramic floor tiles. *Ceramics International*. 2011;37(1): 369–375. <https://doi.org/10.1016/j.ceramint.2010.09.023>
- Clauer C., Huenges E. Thermal Conductivity of Rocks and Minerals. In: *Rock Physics and Phase Relations: a Handbook of Physical Constants*. Ed. Ahrens T. J. 1995;3: 105–126 (print). *American Geophysical Union*, 2013 (on line). <https://doi.org/10.1029/rf003p0105>
- Emirov S. N., Ibragimov A. I., Ramazanov E. N. Thermal properties of sedimentary rocks in the conditions of their natural occurrence. *Scientific and methodological electronic journal concept*. 2013;13: 1096–1100. (In Russ., abstract in Eng.). Available at: <https://e-koncept.ru/2013/53222.htm>
- Merriman J. D., Hofmeister A. M., Roy D. J., Whittington A. G. Temperature-dependent thermal transport properties of carbonate minerals and rocks. *Geosphere*. 2018;14(4): 1961–1987. <https://doi.org/10.1130/GES01581.1>
- Semenov V. P., Zheleznyak M. N., Kirillin A. R., Zhizhin V. I. Thermal conductivity of sedimentary



rocks in the Leno-Viluy oil-and-gas bearing province. *Earth's Cryosphere*. 2018;22(5): 30–38. (In Russ., abstract in Eng.). [https://doi.org/10.21782/KZ1560-7496-2018-5\(30-38\)](https://doi.org/10.21782/KZ1560-7496-2018-5(30-38))

16. Lindawati L., Yuliza N. F., Irwansyah I. Thermal Conductivity of Some Marble Stones Available in South Aceh District. *IOP Conf. Series: Materials Science and Engineering*. 2020;854: 012064. <https://doi.org/10.1088/1757-899x/854/1/012064>

17. Momenzadeh L., Moghtaderi B., Liu X., Sloan S. W., Belova I. V., Murch G. E. The thermal conductivity of magnesite. Dolomite and calcite as determined by molecular dynamics simulation. *Diffusion Foundations*. 2018;19: 18–34. <https://doi.org/10.4028/www.scientific.net/DF.19.18>

18. Popov P. A., Dukel'skii K. V., Mironov I. A., Smirnov A. N., Smolyanskii P. L., Fedorov P. P., Osiko V. V., Basiev T. T. Thermal conductivity of CaF<sub>2</sub> optical ceramic. *Doklady Physics*. 2007; 52(1): 7–9. <https://doi.org/10.1134/s1028335807010028>

19. Popov P. A., Fedorov P. P., Kuznetsov S. V. Thermal conductivity of FeS<sub>2</sub> pyrite crystals in the temperature range 50–300 K. *Crystallography Reports*. 2013; 58(2): 319–321. <https://doi.org/10.1134/s1063774513020223>

20. Fedorov P. P., Maslov V. A., Voronov V. V., Chernova E. V., Yarotskaya E. G., Gaynutdinov R. V., Popov P. A. Flintstone as nanocomposite material. *Nanosystems: Physics, Chemistry, Mathematics*. 2018;9(5): 603–608. <https://doi.org/10.17586/2220-8054-2018-9-5-603-608>

21. Popov P. A., Kuznetsov S. V., Krugovykh A. A., Mitroshenkov N. V., Balabanov, S. S., Fedorov P. P. Study of the thermal conductivity of PbS, CuFeS<sub>2</sub>, ZnS. *Condensed Matter and Interphases*. 2020;22(1): 97–105. <https://doi.org/10.17308/kcmf.2020.22/2533>

22. Fedorov P. P., Novikov I. A., Voronov V. V., Bad'yanova L. V., Kuznetsov S. V., Chernova E. V. Transformation of siderite in the zone of hypergenesis. *Nanosystems: Physics, Chemistry, Mathematics*. 2022;13(5): 539–545. <https://doi.org/10.17586/2220-8054-2022-13-5-539-545>

23. Popov P. A., Sidorov A. A., Kul'chenkov E. A., Anishchenko A. M., Avetissov I. Ch., Sorokin N. I., Fedorov P. P. Thermal conductivity and expansion of PbF<sub>2</sub> single crystal. *Ionics*. 2017;23(1): 233–239. <https://doi.org/10.1007/s11581-016-1802-2>

24. Goldsmith J. R., Heard H. C. Subsolidus phase relations in the system CaCO<sub>3</sub>–MgCO<sub>3</sub>. *Journal of Geology*. 1961;69(1): 45–74. <https://doi.org/10.1086/626715>

25. Vinn O. Calcite in skeletons of annelids. In: *Calcite: formation, properties and applications*. NOVA Science Publ.; 2012. p. 245.

26. Oskotsky V. S., Smirnov I. A. *Defects in crystals and thermal conductivity*. Moscow: Nauka Publ.; 1972. 159 p. (In Russ.)

27. Ziman J. M. *Electrons and phonons. The theory of transport phenomena in solids*. Clarendon Press; 1960. 554 p.

28. *Thermal conductivity of solids: Handbook*. Ed.: A. S. Okhotina. Moscow: Energoatomizdat Publ.; 1984. 320 p.

29. Klemens P. G. The thermal conductivity of dielectric solids at low temperatures (Theoretical). *Proceedings of the Royal Society of London. Series A. Mathematical and Physical Sciences*. 1951;208(1092): 108–133. <https://doi.org/10.1098/rspa.1951.0147>

30. Berman R. *Thermal conduction in Solids* Oxford: Clarendon; 1976. 193 p.

31. Popov P. A., Fedorov P. P. *Thermal conductivity of fluoride optical materials*. Bryansk: Group of companies “Desyatochka” Publ.; 2012. 210 p. (In Russ.)

### Information about the authors

*Pavel A. Popov*, Dr. Sci. (Phys.–Math.), Professor, Bryansk State Academician I. G. Petrovski University (Bryansk, Russian Federation).

<https://orcid.org/0000-0001-7555-1390>  
tfbgubry@mail.ru

*Alena A. Zentsova*, student, Bryansk State Academician I. G. Petrovski University (Bryansk, Russian Federation).

<https://orcid.org/0000-0002-9793-7099>  
alenazen01@mail.ru

*Ivan A. Novikov*, Researcher, Prokhorov General Physics Institute of the Russian Academy of Sciences (Moscow, Russian Federation).

<https://orcid.org/0000-0003-4898-4662>  
i.novikov@niigb.ru

*Valery V. Voronov*, Cand. Sci. (Phys.–Math.), Leading Researcher, Prokhorov General Physics Institute of the Russian Academy of Sciences (Moscow, Russian Federation).

<https://orcid.org/0000-0001-5029-8560>  
voronov@lst.gpi.ru

*Elena V. Chernova*, Junior Researcher, Prokhorov General Physics Institute of the Russian Academy of Sciences (Moscow, Russian Federation).

<https://orcid.org/0000-0001-7401-5019>  
e-chernova@yandex.ru

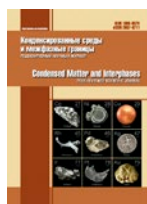
*Pavel P. Fedorov*, Dr. Sci. (Chem.), Full Professor, Chief Researcher, Prokhorov General Physics Institute of the Russian Academy of Sciences (Moscow, Russian Federation).

<https://orcid.org/0000-0002-2918-3926>  
ppfedorov@yandex.ru

Received 15.06.2023; approved after reviewing 10.07.2023; accepted for publication 15.09.2023; published online 25.03.2024.

Translated by Valentina Mittova





## Original articles

Research article

<https://doi.org/10.17308/kcmf.2024.26/11817>

## Electrochemical impedance of porous tantalum solids: modeling of frequency response

A. V. Syugaev✉, V. E. Porsev

<sup>1</sup>Udmurt Federal Research Centre of the Ural Branch of the Russian Academy of Sciences  
34 Tatyana Baramzina str., Izhevsk 426067, Russian Federation

### Abstract

The paper proposes a new approach to the analysis of electrochemical impedance spectra of porous tantalum bodies, which involves modeling the frequency response via an equivalent circuit that takes into account the pore hierarchy. It was shown that the proposed circuit describes well the experimental data and allows characterization of the porous structure, including the contribution of different types of pores to the total capacitance of the porous body, characteristic relaxation times, and activation frequencies for different type pores. Two types of samples were analyzed: a porous tantalum body obtained by sintering Ta powder and a porous tantalum body covered with a Ta<sub>2</sub>O<sub>5</sub> dielectric layer. Modeling showed a significant redistribution of contributions from pores of different types into the total capacitance after the formation of Ta<sub>2</sub>O<sub>5</sub> due to the preferential isolation of the smallest pores and/or those difficult to access. The results of modeling of the frequency response of the analyzed samples agree well with the scanning electron microscopy data. The proposed approach has the potential to be advantageous for the technology of tantalum capacitors.

**Keywords:** Electrochemical impedance, Porous structure, Modeling

**Funding:** The studies were carried out using the equipment of the Center for Shared Use “Center for Physical and Physico-Chemical Methods of Analysis, Study of the Properties and Characteristics of Surfaces, Nanostructures, Materials, and Products” of the Udmurt Federal Research Centre of the Ural Branch of the Russian Academy of Sciences within the framework of the state assignment of the Ministry of Science and Higher Education of the Russian Federation (state registration No. FUUE-2024-0011).

**Acknowledgements:** The authors are grateful to A. I. Chukavin (Udmurt Federal Research Centre of the Ural Branch of the Russian Academy of Sciences) for scanning electron microscopy studies and O. B. Baryshev (AO *Elekond*) for providing samples of porous tantalum bodies.

**For citation:** Syugaev A. V., Porsev V. E. Electrochemical impedance of porous tantalum solids: modeling of frequency response. *Condensed Matter and Interphases*. 2024;26(1): 135–145. <https://doi.org/10.17308/kcmf.2024.26/11817>

**Для цитирования:** Сюгаев А. В., Порсев В. Е. Электрохимический импеданс и моделирование частотного отклика пористых танталовых тел. *Конденсированные среды и межфазные границы*. 2024;26(1): 135–145. <https://doi.org/10.17308/kcmf.2024.26/11817>

✉ Alexander V. Syugaev, e-mail: [syual@udman.ru](mailto:syual@udman.ru), [syual@mail.ru](mailto:syual@mail.ru)

© Syugaev A. V., Porsev V. E., 2024



The content is available under Creative Commons Attribution 4.0 License.

## 1. Introduction

Tantalum capacitors belong to electrolytic capacitors and are widely used in practice. In such capacitors, a porous pellet of sintered tantalum powder covered with a thin insulating layer of amorphous tantalum oxide,  $Ta_2O_5$ , serves as an anode. The electrolyte can be either liquid or solid, and being made of  $MnO_2$  or conductive polymer (poly(3,4-ethylenedioxythiophene) polystyrene sulfonate). Since the capacitance arises at the interfaces, greater surface area of the porous body and its accessibility to the electrolyte improves capacitance characteristics of tantalum capacitors. To further develop the production technology of tantalum capacitors, new approaches to the characterization of the porous body structure are needed.

Electrochemical impedance spectroscopy is an effective technique for studying the electrochemical behavior of porous materials in various electrochemical systems and devices [1]. The frequency response of three-dimensional porous electrodes differs significantly from the response of flat electrodes, which allows an analysis of geometric factors of the porous structure [1–7]. An alternative approach to the study of porous structures is BET analysis which is based on the measurement of adsorption isotherms of gas molecules. However, the penetration of gases and fluids into a porous body is different, especially in the cases of small pores and/or high fluid viscosity. Viscous fluids (concentrated solutions of manganese nitrate hydrates, solutions of poly(3,4-ethylenedioxythiophene) polystyrene sulfonate) are widely used to form solid electrolyte layer in the porous body of tantalum capacitors. As a consequence, the BET analysis may give overestimated results of the surface area available for the fluid. That is why the electrochemical impedance technique is still preferable for porous tantalum bodies, since it allows studying the interaction of the porous structure with the fluid used as an electrolyte.

This work focuses on modeling the frequency response of porous tantalum bodies via an equivalent circuit that takes into account the hierarchy of pores and the features of ion transport in them. Using the modeling results the contributions from different type pores to the total capacitance and AC frequencies for their activation

were determined. Samples of porous bodies were analyzed both before and after the formation of a  $Ta_2O_5$  dielectric layer on their surface.

## 2. Experimental: samples, techniques and data processing

Porous tantalum samples were prepared as rectangular parallelepipeds  $4.45 \times 3.10 \times 1.46$  mm in size (anodes for tantalum capacitors) with a welded tantalum current collector. Samples were obtained from tantalum powder TaK-80 (detailed information on its morphology and chemical composition can be found in [8]), which was sintered at  $1,330$  °C in a vacuum furnace. The density of the samples after sintering was  $5.0$  g/cm<sup>3</sup>, which was much smaller than that of tantalum ( $16.65$  g/cm<sup>3</sup>) and indicated their high porosity. Hereinafter, this sample will be referred to as *Ta*. Both as-sintered samples and samples with a grown  $Ta_2O_5$  dielectric layer ( $\sim 100$  nm) formed by electrochemical oxidation in an aqueous solution of  $H_3PO_4$  were analyzed. Hereinafter, the later is referred to as *Ta/Ta<sub>2</sub>O<sub>5</sub>*. The morphology of samples was studied with a Thermo Fisher Scientific Quattro S scanning electron microscope.

Electrochemical impedance was measured on a P-45X potentiostat with a built-in impedance measurement module (Electrochemical Instruments, Chernogolovka). The electrolyte was an aqueous solution of sodium sulphate with a concentration of 1 mol/l, deaerated with high-purity argon. To provide high-quality penetration of the electrolyte into the entire pore space, the samples were kept in the electrolyte for 16 hours. Measurements were taken in a glass cell with separated spaces for the working, auxiliary (Pt), and reference electrodes (Ag/AgCl). The distance between the sample and the Luggin capillary was 1 mm. The current collectors were insulated with paraffin.

Electrochemical impedance spectra were measured at potentials 100 mV higher than the open-circuit potentials ( $E_{o.c.} = -215$  mV for *Ta*; 635 mV for *Ta/Ta<sub>2</sub>O<sub>5</sub>* rel. Ag/AgCl electrode) to exclude the reduction reactions at the interface. Comparison of the porous structure relaxation of samples significantly different in structure is best done by analyzing the spectra measured at  $\sim E_{o.c.}$  It was difficult to apply the same potential for both samples, since a significant potential

shift from  $E_{o.c}$  led to intensive side processes, which strongly affected the impedance spectra. For example, sample *Ta* at 600 mV relative to Ag/AgCl started to strongly oxidize. For sample *Ta/Ta<sub>2</sub>O<sub>5</sub>*, polarization at negative potentials caused transformations in the surface oxide layer.

Before measuring the spectra, the samples were kept for 45 min at a given potential to provide a steady state of the system. When measuring the spectra, the potential changed with the amplitude of  $\pm 5$  mV and the frequency was ranged from 50 kHz to 10 mHz. Experimental data modeling was performed using the ZView software.

Capacitance characteristics of the samples are determined as follows [9, 10]. The impedance ( $Z$ ) and capacitance ( $C$ ) of the capacitor are related by the equation:

$$Z(\omega) = \frac{1}{j\omega C(\omega)}, \quad (1)$$

where  $\omega$  is the angular frequency and  $j$  is the imaginary unit.

The impedance can also be expressed in a complex form:

$$Z(\omega) = Z'(\omega) + jZ''(\omega), \quad (2)$$

where  $Z'$  and  $Z''$  are the real and imaginary parts of impedance, respectively.

It follows from equations (1) and (2), that

$$C(\omega) = \frac{1}{\omega(jZ'(\omega) - Z''(\omega))} = \frac{-(Z''(\omega) + jZ'(\omega))}{\omega|Z(\omega)|^2}. \quad (3)$$

Capacitance can also be described by the following equation:

$$C(\omega) = C'(\omega) + jC''(\omega), \quad (4)$$

where  $C'$  and  $C''$  are the real and imaginary parts of the capacitance, respectively.

From (3) and (4) it follows that

$$C'(\omega) = \frac{-Z''(\omega)}{\omega|Z(\omega)|^2}, \quad (5)$$

$$C''(\omega) = \frac{-Z'(\omega)}{\omega|Z(\omega)|^2}, \quad (6)$$

The real part of the capacitance ( $C'$ ) is close to the real capacitance of samples, which is observed, for example, in direct-current capacitance measurements (voltammograms, galvanostatic charge-discharge). The imaginary

part ( $C''$ ) corresponds to the energy dissipation under irreversible processes [9].

All dependences are given relative to the frequency  $f$  (Hz) related to the angular frequency as follows:

$$\omega = 2\pi f. \quad (7)$$

When calculating the impedance modulus ( $|Z|$ ) and the phase angle ( $\varphi$ ), the following equations are used:

$$|Z(f)| = \sqrt{(Z'(f))^2 + (Z''(f))^2}, \quad (8)$$

$$\varphi(f) = \arctg \frac{Z''(f)}{Z'(f)}. \quad (9)$$

The modified phase angle corrected for the resistance  $Z'$  at  $f \rightarrow \infty$  is also calculated by formula [11]:

$$\varphi(f)_m = \arctg \frac{Z''(f)}{Z'(f) - Z'(f \rightarrow \infty)}. \quad (10)$$

The value of  $Z'$  at  $f \rightarrow \infty$  is determined from the  $Z'(Z'')$  relationships by extrapolating a linear section with a slope of  $\sim 45^\circ$  to the  $Z'$  axis. The use of the modified phase angle allows one to avoid a distortion of the phase angle in the high-frequency range associated with increased electrical resistance of the samples and the electrolyte, and provides better description of the  $\varphi(f)$  dependence in terms of the porous structure response.

### 3. Results and discussion

#### 3.1. Electrochemical impedance and capacitance of porous tantalum bodies

Fig. 1 shows electron microscopic images of the sample cleavage surfaces. The porous structure of the samples is clearly visible. In sample *Ta*, pores with a size of 1–3  $\mu\text{m}$  (a-c) of almost spherical shape and pores of irregular shape in the range of 0.1–1  $\mu\text{m}$  (on average  $\sim 0.3$   $\mu\text{m}$ ) are observed. Many finer pores with a size of less than 0.1  $\mu\text{m}$  are also observed (b-d). The porous structure of the *Ta/Ta<sub>2</sub>O<sub>5</sub>* sample is markedly different (e-g), which is due to a dielectric layer. The oxide layer is visible as a grey-coloured shell  $\sim 100$  nm thick along the edges of the particles in elastically scattered electrons (h). Large pores in *Ta/Ta<sub>2</sub>O<sub>5</sub>* are 0.7–2  $\mu\text{m}$  in size (e, f). There are also small pores (0.2  $\mu\text{m}$ ) and even smaller ones (f and g).



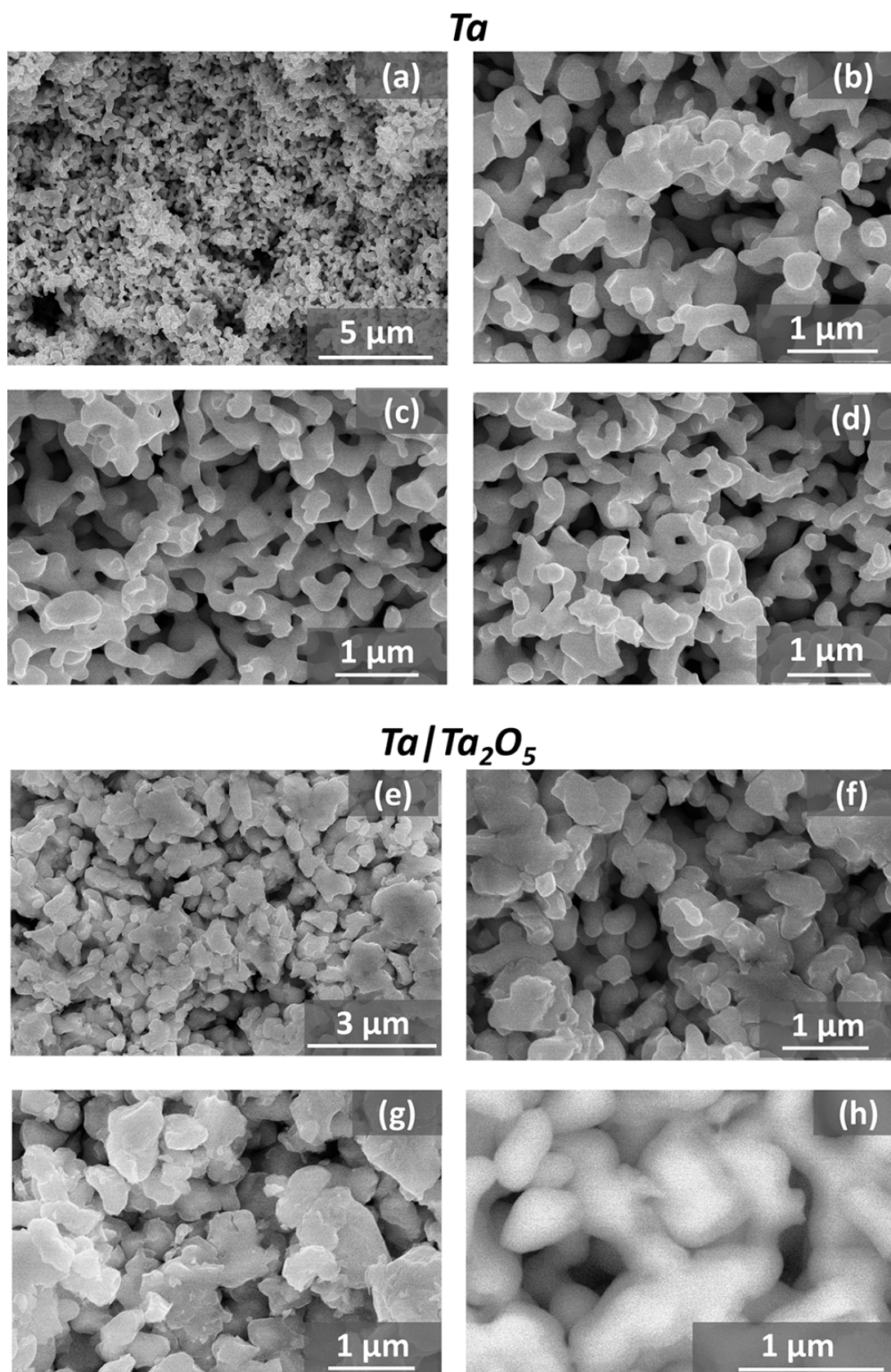


**Fig. 1.** Electron microscopic images of *Ta* (a-d) and *Ta/Ta<sub>2</sub>O<sub>5</sub>* (e-h) cleavages in secondary (a-g) and in back-scattered electrons (h)



The dependences  $Z'(Z'')$ ,  $|Z|(f)$ , and  $\varphi(f)$  are shown in Fig. 2. For porous electrodes, the impedance phase angle is equal to half the phase shift angle for a smooth electrode with the same nature of interphase processes at  $f \rightarrow \infty$  [1]. In the case of perfectly polarizable walls of a porous material, this should lead to the appearance at high frequencies of a characteristic section with a slope angle of  $\sim 45^\circ$ , which becomes a vertical line. A similar shape of the impedance hodographs is observed for the studied porous tantalum bodies (see Fig. 2a, b).

The phase shift (Fig. 2c) for  $Ta$  and  $Ta/Ta_2O_5$  at the high frequencies is in the range of  $-5^\circ$  to  $-15^\circ$ . Such value of  $\varphi$  is due to the phase shift distortion associated with the increased ESR (*Equivalent Series Resistance*) of the samples, which corresponds to  $Z'$  at  $f \rightarrow \infty$  due to the electronic resistance of the contacts, the current collector, the material of the porous body,

including the internal resistance of the particles and the resistance between the particles, as well as the ionic resistance of the electrolyte. The correction of the phase shift by the value of  $Z'(f \rightarrow \infty)$  according to equation (10) gives the values of  $\sim -45^\circ$  at high frequencies (see the insert of Fig. 2c), which is most characteristic of porous electrodes [1–5].

The value of  $Z'(f \rightarrow \infty)$  is significantly greater for  $Ta/Ta_2O_5$  ( $6.7 \Omega$ ) as compared to the  $Ta$  sample ( $1.5 \Omega$ ). Since the same cell and electrolyte are used for the samples, the increase in  $Z'(f \rightarrow \infty)$  corresponds to the increase in the electrical resistance of the porous body caused by the formation of the  $Ta_2O_5$  dielectric layer. The  $Ta/Ta_2O_5$  sample has significantly greater impedance over the entire AC frequency range (Fig. 2d).

At low frequencies, on  $Z'(Z'')$  dependences, a line inclined relative to the  $Z'$  axis ( $\varphi \sim -85^\circ$ ) is observed instead of a vertical line ( $\varphi = -90^\circ$ )

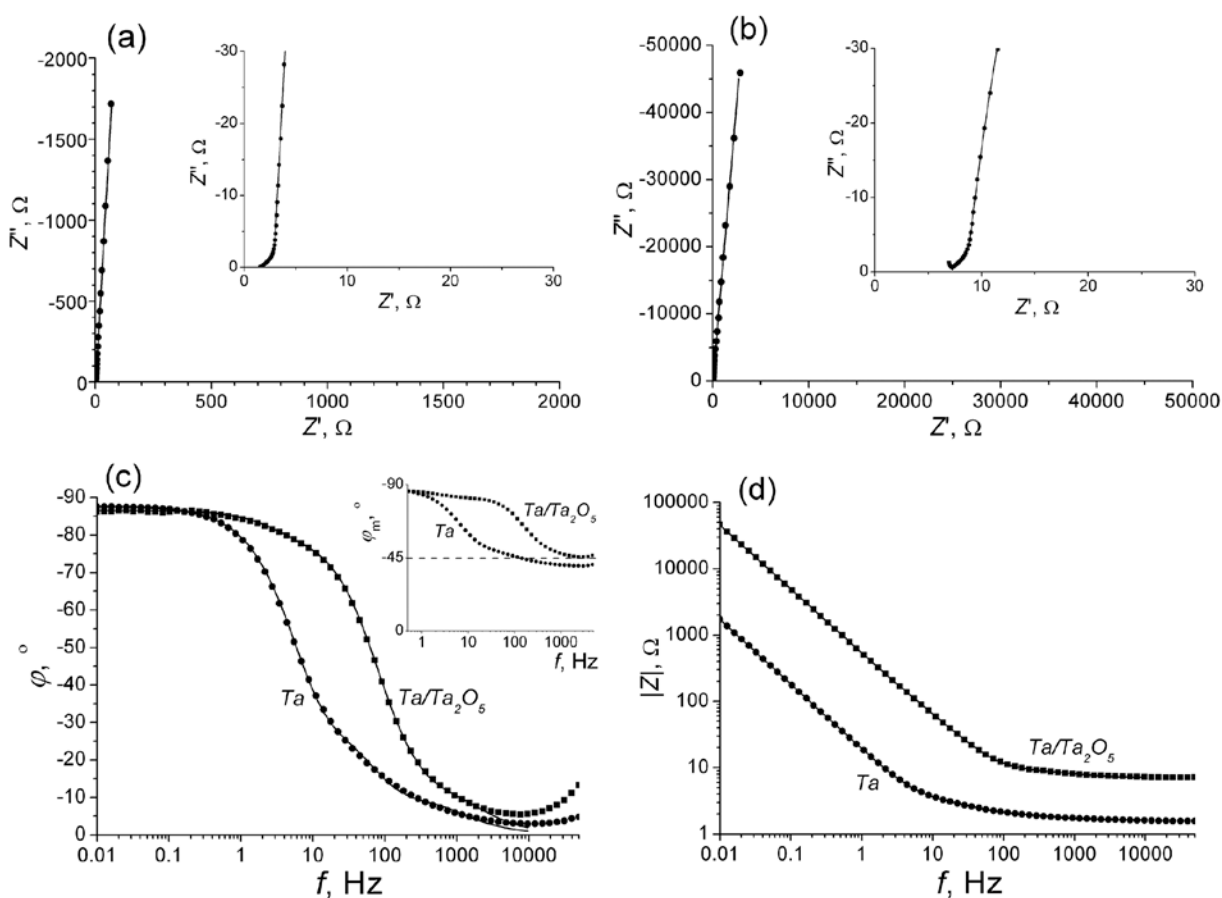


**Fig. 2.** Nyquist plots for  $Ta$  (a) and  $Ta/Ta_2O_5$  (b) samples;  $\varphi(f)$  (c) and  $|Z|(f)$  (d) dependences. The lines show the results of fitting using an equivalent circuit (see Section 3.2 for details). Inserts on (a) and (b) are the fragments of the Nyquist plots in the high-frequency region, an insert on (c) is the dependence of the phase shift vs. frequency, corrected according to equation (10)

characteristic of an ideal capacitor, which indicates non-ideal behavior modeled using the CPE element (*Constant Phase Element*). For an ideal capacitor, the impedance is:

$$Z_c = \frac{1}{j\omega C}, \quad (11)$$

For the CPE element, it is:

$$Z_{CPE} = \frac{1}{(j\omega)^\beta Q}, \quad (12)$$

where  $\beta$  is the ideality factor, usually located in the range of  $0.9 < \beta < 1$  and  $Q$  is an imperfect capacitance ( $F \cdot s^{\beta-1}$ ) [1]. Non-ideal behavior in the case of flat samples is usually due to the surface roughness [1, 12]. In the case of porous bodies, it can also be associated with the frequency response of the porous structure, depending on geometric factors and the pore size distribution [2, 3].

Higher frequency leads to deeper penetration of the AC signal into the pore and the gradual “activation” of the deeper walls of the pores [4, 13]. In an alternative approach which takes into account the pore size distribution, it is assumed that at the same frequency of alternating current, the depth of penetration into small pores is less than into large pores [2, 3]. At low enough frequencies, the entire surface of pores, including the smallest ones, contributes to interfacial impedance. Under these conditions, the impedance of the porous electrode becomes equal to the impedance of a flat electrode with a surface area equal to the total surface of the porous body.

Figure 3 shows the capacitance characteristics calculated from equations (5) and (6). The real part of the capacitance ( $C'$ ) is the closest to the real capacitance of the samples, which is observed,

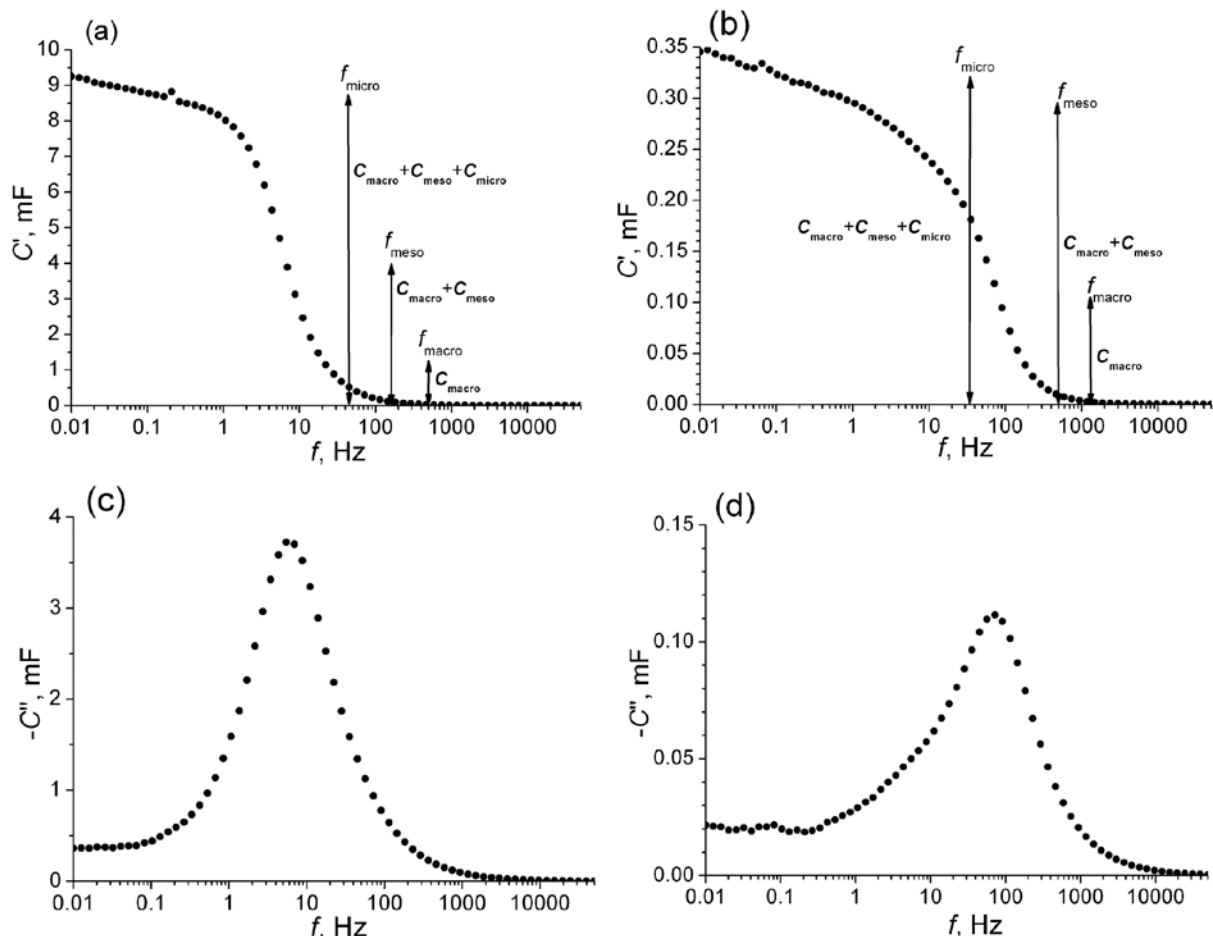


**Fig. 3.** Dependences of the real and imaginary part of the capacitance for  $Ta$  (a, c) and  $Ta/Ta_2O_5$  (b, d) on the AC frequency. The arrows in figures 3a and 3b additionally mark the activation frequencies of different types of pores and the capacitance per pores of different types, calculated from the modeling results using an equivalent circuit (see Section 3.2 for details)

for example, in direct current measurements (potentiodynamic voltammograms; galvanostatic charge-discharge) [9]. For the sample covered with a  $Ta_2O_5$  layer,  $C'$  decreases significantly ( $\sim 27$  times at  $f = 0.01$  Hz), which is associated with the appearance of a dielectric layer and a decrease in the surface area available for the electrolyte. Despite the different capacitance values, the  $C'(f)$  relationship is similar for both samples, although the activation frequencies of  $C'$  were different.

The imaginary part  $C''$  corresponds to the energy dissipation during irreversible processes [9]. For example, it could be heat losses associated with the rotation and movement of water molecules under the influence of alternating current, similar to heating in a microwave oven. It could also be losses associated with the redistribution of charges in the porous matrix [7].  $C''(f)$  dependences of the analyzed samples (Fig. 3c, d) are characterized by an extremum corresponding to the relaxation time of the entire system and the transition from the predominantly resistive to capacitive behavior of the samples [14]. The extremum on  $C''(f)$  dependences is observed at a frequency at which  $\varphi = -45^\circ$  (Fig. 2c).

### 3.2. Modeling the frequency response of porous tantalum bodies

In the case of porous tantalum bodies, when constructing an equivalent electrical circuit, it is necessary to take into account various elements that contribute to the overall resistance of the system: the resistance of the material itself, both between individual tantalum particles and within individual particles; the contact resistance between the current collector and the porous body; the resistance of the surface oxide; the ionic resistance of the electrolyte, consisting of the “external” surface resistance at the interphase boundaries, as well as the “internal” resistance of the electrolyte inside the pores of various sizes. The contribution of the charge transfer resistance in the case of Faradaic processes is also possible. The selection of a suitable transmission line modeling the frequency response of the porous structure is of key importance. At the moment, there are a number of approaches to modeling the frequency response of porous bodies, for example described in [2–6, 13, 15, 16]. The main approaches to the analysis of the electrochemical

impedance of porous electrodes were considered in one of the latest reviews [17].

One of the recent papers [7] proposed an interesting approach to modeling the behavior of porous carbon materials which took into account the pore hierarchy. The authors of that study compared the modeling results with BET analysis and mercury porosimetry data. It was assumed that electrolyte ions first penetrate into the larger pores (macropores), then into medium-sized pores (mesopores), and finally reach the smaller pores (micropores). This is schematically illustrated in Fig. 4a. The figure also demonstrates the difference in alternating current frequencies corresponding to the activation of pores of different types. This should lead to a deviation of the frequency response of the porous structure from the behavior of the ideal capacitor and should be taken into account when constructing an equivalent circuit. In the equivalent circuit proposed in [7] (Fig. 4b), the inductance element ( $L$ ) modeled electrical contacts; the  $ESR$  referred mainly to the resistance of the electrolyte and the material itself. Then,  $R_{CT}$  is the charge transfer resistance with the constant phase element ( $CPE_{CT}$ ) connected in parallel to take into account possible Faradaic processes at the interphase boundaries. Also, there is a short transmission line modeling the frequency response of the hierarchical porous structure. The focus is on determining the relaxation times ( $RCPE$ ) for each pore type modeling the migration of ions through a hierarchical porous structure and related to their sizes. The sizes of macropores ( $> 50$  nm), mesopores (2–50 nm), and micropores ( $< 2$  nm) in [7] match those used in the standard classification of pore sizes. This circuit is successfully used to describe the electrochemical impedance of a series of carbon samples with different porosities obtained by cellulose pyrolysis. This approach also appears to be informative when analyzing the frequency response of porous samples of laser-induced graphene [18].

In this paper, an equivalent circuit is used, similar to that proposed in [7]. However, it has been modified. Charge transfer elements have been eliminated from the circuit. Since tantalum is an inert corrosion-resistant metal, the contribution of Faradaic processes to interfacial impedance and capacitance can be neglected under

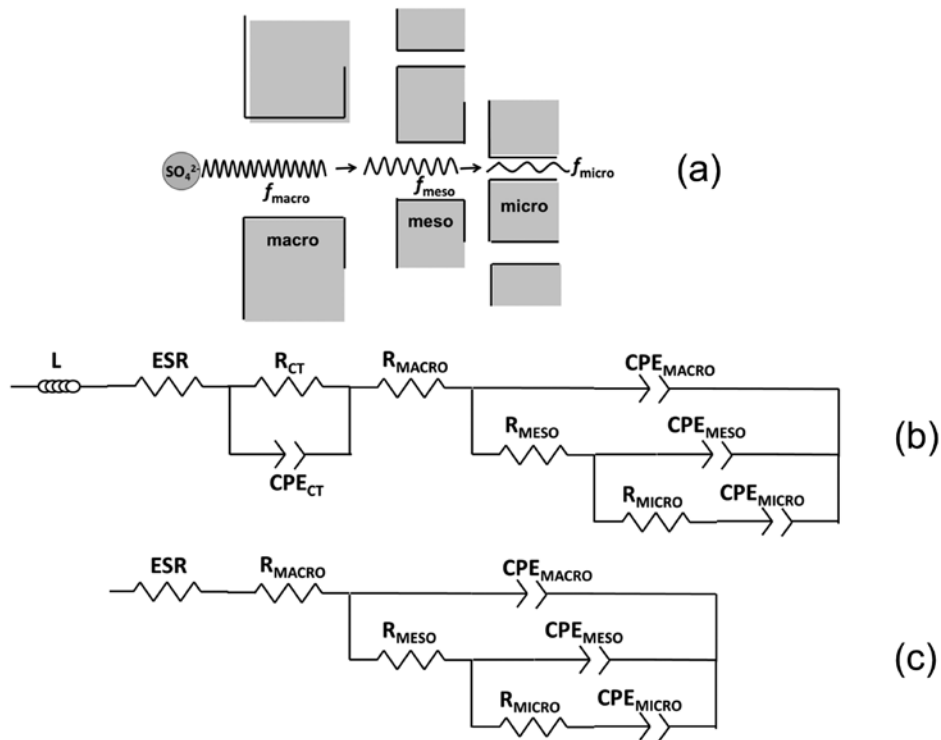


**Fig. 4.** Diagram demonstrating electrolyte transport in a porous structure, where ions move from macropores to mesopores, after which they enter micropores (a); equivalent circuit, modeling the frequency response of a hierarchical porous structure from [7] (b); modified equivalent circuit used to model the frequency response of porous tantalum bodies (c)

experimental conditions. The  $L$  element has also been eliminated, since in our case no inductance is observed in the high-frequency region, but it may be needed when measuring under other conditions, for example, with another electrolyte or in the AC frequency range. The modified circuit is shown in Fig. 4c. In the proposed circuit, the used designations of pores (macro-, meso-, and micro-) are just conventional names not related to the generally accepted classification of pores by size but only indicate their position in the hierarchy (Fig. 4a) and in the equivalent circuit (Fig. 4c). Relaxation times ( $\tau$ ) for each pore type were calculated as follows [7]:

$$\tau_{\text{macro}} = CPE_{\text{macro}} (ESR + R_{\text{macro}}), \quad (13)$$

$$\tau_{\text{meso}} = CPE_{\text{meso}} (ESR + R_{\text{macro}} + R_{\text{meso}}), \quad (14)$$

$$\tau_{\text{micro}} = CPE_{\text{micro}} (ESR + R_{\text{macro}} + R_{\text{meso}} + R_{\text{micro}}), \quad (15)$$

where  $CPE$  is non-ideal capacitance.

Fitting the electrochemical impedance spectra using a modified equivalent circuit (in the range of 0.01–10000 Hz) demonstrates good results:  $\chi^2 = 0.00070071$  for  $Ta$  and  $\chi^2 = 0.00080137$  for

$Ta/Ta_2O_5$ . The fitting results are shown with solid lines in Fig. 2, with the main parameters given in Table 1 for the elements. Table 1 shows the total resistance for  $ESR$  and  $R_{\text{macro}}$  since it is not possible to separate their contributions in series circuits. For the  $Ta/Ta_2O_5$  porous body, all resistive elements in the circuit exhibit greater resistance as compared to  $Ta$ , which was associated with

**Table 1.** The main parameters of the equivalent circuit elements determined by fitting the experimental results

Element	$Ta$	$Ta/Ta_2O_5$
$ESR + R_{\text{macro}}, \Omega$	1.621	7.212
$Q(CPE_{\text{macro}}), \text{mF} \cdot \text{s}^{\beta-1}$	1.233	0.105
$\beta_{\text{macro}}$	0.93	0.96
$R_{\text{meso}}, \Omega$	0.603	3.515
$Q(CPE_{\text{meso}}), \text{mF} \cdot \text{s}^{\beta-1}$	2.745	0.186
$\beta_{\text{meso}}$	0.99	0.96
$R_{\text{micro}}, \Omega$	2.604	1074
$Q(CPE_{\text{micro}}), \text{mF} \cdot \text{s}^{\beta-1}$	4.719	0.027
$\beta_{\text{micro}}$	0.98	1.01



a dielectric layer and an increase in electrolyte resistance with decreasing pore sizes [15]. While  $(ESR+R_{\text{macro}})$  and  $R_{\text{meso}}$  increased 4–6 times,  $R_{\text{micro}}$  increases ~400 times, i.e. the most significant changes are due to pores of smaller size difficult to access.

The obtained modeling results provide additional data on the behavior of the porous structure, not available in [7]. Since factor  $\beta$  for *CPE* elements varies from 0.93 to 1.01 which means low deviation from the ideal capacitance for pores of any type, the non-ideal *CPE* capacitance ( $Q$ ) may be considered as the ideal capacitance ( $C$ ) for each type of pores. This is supported by the fact that the sum of capacitances ( $\Sigma C$ ) for all types of pores determined from the model agreed well with the values of  $C$  (at a minimum frequency of  $f = 0.01$  Hz) obtained in the experiment. For the *Ta* sample,  $\Sigma C = 8.70$  mF,  $C(0.01) = 9.26$  mF, the difference was only 6%. For *Ta/Ta<sub>2</sub>O<sub>5</sub>*,  $\Sigma C = 0.318$  mF,  $C(0.01) = 0.345$  mF, the difference was 8%.

In this paper, we also determined frequencies of the activation onset (activation frequencies) of each pore type based on the calculated relaxation time, which corresponded to the transition from predominantly resistive to capacitive behavior. The activation frequency was determined as follows:

$$f_{\text{pore}} = \frac{1}{\tau_{\text{pore}}} \quad (16)$$

Table 2 shows the fractions of the capacitance attributable to each type of pores, as well as the relaxation times and activation frequencies of different type pores, determined from equations (13)–(16). For clarity, the activation frequencies and the fraction of the capacitance for different types of pores obtained by modeling of the frequency response are shown by the arrows on the  $C$ - $f$  dependences (Fig. 3a and b).

Relatively low relaxation times indicate that the majority of pores according to the standard classification are macropores ( $> 50$  nm). For example, the relaxation time for macropores in [7] is on the order of ten milliseconds. As mentioned above, the used classification of pores is based on their position in the hierarchy (Fig. 4a). The hierarchy of the porous structure is clearly observed in electron microscopic images (Fig. 1).

For the *Ta* sample, the “macropores” contributing 14% of the capacitance are most likely pores 1–3  $\mu\text{m}$  in size (Fig. 1a-c). “Mesopores” making 32% of the capacitance are 0.1–1  $\mu\text{m}$  in size, with the average size of ~0.3  $\mu\text{m}$  (Fig. 1b-c). More than half of the capacitance arises from “micropores” with a size of  $\leq 0.1$   $\mu\text{m}$  (Fig. 1b-c). The ratio of capacitance fractions from “macropores” and “mesopores” is approximately 1 to 2, being comparable for *Ta* and *Ta/Ta<sub>2</sub>O<sub>5</sub>*. The dimensions of “macropores” (0.7–2) and “mesopores” ( $\leq 0.2$   $\mu\text{m}$ ) for *Ta/Ta<sub>2</sub>O<sub>5</sub>* are smaller (Fig. 1d-f) than for *Ta*, which is associated with the appearance of a 100 nm thick oxide layer in them. There is a sharp decrease in the contribution from the “micropores” from 54 to 9% on going from the *Ta* sample to the *Ta/Ta<sub>2</sub>O<sub>5</sub>* sample. This is due to the fact that “micropores” are blocked by the oxide layer, since the dimensions of “micropores” in *Ta* are comparable to the thickness of the dielectric layer in *Ta/Ta<sub>2</sub>O<sub>5</sub>*. However, they are not blocked completely. It is difficult to observe “micropores” in electron microscopic images for *Ta/Ta<sub>2</sub>O<sub>5</sub>* because of their small size and low amount.

Relaxation times can be used to compare pore sizes in samples with similar pore shapes, interphase boundaries, and processes. Provided that all other conditions are equal, the smaller the pore size, the longer the relaxation time and the lower its activation frequency [2, 3, 7]. Due to the difference in the thickness of oxide layers in *Ta* and *Ta/Ta<sub>2</sub>O<sub>5</sub>*, it is impossible to compare the pore sizes in these samples based

**Table 2.** Capacitance fractions, characteristic relaxation times, and activation frequencies for pores of different type calculated from the parameters of the circuit modeling the frequency response of a porous body

	«Macropores»			«Mesopores»			«Micropores»		
	$N, \%$	$\tau_{\text{macro}}, \text{ms}$	$f_{\text{macro}}, \text{Hz}$	$N, \%$	$\tau_{\text{meso}}, \text{ms}$	$f_{\text{meso}}, \text{Hz}$	$N, \%$	$\tau_{\text{micro}}, \text{ms}$	$f_{\text{micro}}, \text{Hz}$
<i>Ta</i>	14	2.00	500	32	6.10	164	54	22.8	44
<i>Ta/Ta<sub>2</sub>O<sub>5</sub></i>	33	0.76	1316	58	2.00	500	9	29.3	34

on the calculated relaxation times. The oxide layer of large thickness leads to a decrease in the relaxation times of “macro-” and “mesopores” in the case of  $Ta/Ta_2O_5$  as compared to  $Ta$  despite the reduction in their sizes. On the other hand, a longer “micropore” relaxation time for  $Ta/Ta_2O_5$  as compared to  $Ta$  may indicate a particularly significant decrease in their size in  $Ta/Ta_2O_5$ .

#### 4. Conclusions

It has been shown that using an equivalent circuit that takes into account the hierarchy of pores in the porous body allows one to describe the electrochemical impedance of porous tantalum bodies. It can also provide valuable information about the features of the porous structure and its interaction with the liquid phase. The results obtained by modeling the frequency response of real samples agree well with the data obtained by scanning electron microscopy. The proposed approach to modeling the impedance spectra makes it possible to estimate the accessibility of the porous structure for the electrolyte and to determine the fraction of the surface related to each type of pores. These data can be useful for determining the characteristics of a porous structure depending on the modes of preparing and treatment of a porous body in the tantalum capacitors technology. It is also possible to model the interaction of the porous structure of tantalum bodies with fluids used to prepare solid electrolytes of tantalum capacitors (concentrated solutions of manganese nitrate, solutions of poly(3,4-ethylenedioxythiophene) polystyrene sulfonate).

#### Author contributions

A. V. Sugaev: research concept, methodology development, conducting research, text writing, final conclusions. V. E. Porsev: conducting research, writing and editing the text.

#### Conflict of interests

The authors declare that they have no known competing financial interests or personal relationships that could have influenced the work reported in this paper.

#### References

1. Kichigin V. I., Sherstobitova I. N., Shein A. B. *Impedance of electrochemical and corrosion systems:*

*textbook\**. Perm State University Publ.; 2009. 238 p. (In Russ.)

2. Song H.-K., Jung Y.-H., Lee K.-H., Dao L. H. Electrochemical impedance spectroscopy of porous electrodes: the effect of pore size distribution. *Electrochimica Acta*. 1999;44(20): 3513–3519. [https://doi.org/10.1016/S0013-4686\(99\)00121-8](https://doi.org/10.1016/S0013-4686(99)00121-8)

3. Song H.-K., Hwang H.-Y., Lee K.-H., Dao L. H. The effect of pore size distribution on the frequency dispersion of porous electrodes. *Electrochimica Acta*. 2000;45(14): 2241–2257. [https://doi.org/10.1016/S0013-4686\(99\)00436-3](https://doi.org/10.1016/S0013-4686(99)00436-3)

4. Keiser H., Beccu K. D., Gutjahr M. A. Abschätzung der Porenstruktur poröser Elektroden aus Impedanzmessungen. *Electrochimica Acta*. 1976;21(8): 539–543. [https://doi.org/10.1016/0013-4686\(76\)85147-X](https://doi.org/10.1016/0013-4686(76)85147-X)

5. Candy J.-P., Fouilloux P., Keddami M., Takenouti H. The characterization of porous electrodes by impedance measurements. *Electrochimica Acta*. 1981;26(8): 1029–1034. [https://doi.org/10.1016/0013-4686\(81\)85072-4](https://doi.org/10.1016/0013-4686(81)85072-4)

6. Raistrick I. D. Impedance studies of porous electrodes. *Electrochimica Acta*. 1990;35(10): 1579–1586. [https://doi.org/10.1016/0013-4686\(90\)80013-E](https://doi.org/10.1016/0013-4686(90)80013-E)

7. Abouelamaiem D. I., He G., Neville T. P., ... Brett D. J. L. Correlating electrochemical impedance with hierarchical structure for porous carbon-based supercapacitors using a truncated transmission line model. *Electrochimica Acta*. 2018;284: 597–608. <https://doi.org/10.1016/j.electacta.2018.07.190>

8. Treshchev S. Yu., Starostin S. P., Mikhailiva S. S., ... Lebedev S. P. Comparative analysis of the composition and structure of condenser tantalum powder. *Chemical Physics and Mesoscopy*. 2014;16(4): 609–615. (In Russ., abstract in Eng.). Available at: <https://www.elibrary.ru/item.asp?id=22662614>

9. Taberna P. L., Simon P., Fauvarque J. F. Electrochemical characteristics and impedance spectroscopy studies of carbon-carbon supercapacitors. *Journal of The Electrochemical Society*. 2003;150(3): A292–A300. <https://doi.org/10.1149/1.1543948>

10. Itagaki M., Suzuki S., Shitanda I., Watanabe K. Electrochemical impedance and complex capacitance to interpret electrochemical capacitor. *Electrochemistry*. 2007;75(8): 649–655. <https://doi.org/10.5796/electrochemistry.75.649>

11. Orazem M. E., Pébère N., Tribollet B. Enhanced graphical representation of electrochemical impedance data. *Journal of The Electrochemical Society*. 2006;153(4): B129–B136. <https://doi.org/10.1149/1.2168377>

12. Pajkossy T. Impedance spectroscopy at interfaces of metals and aqueous solutions – Surface roughness, CPE and related issues. *Solid State Ionics*. 2005;176(25–28): 1997–2003. <https://doi.org/10.1016/j.ssi.2004.06.023>

13. Macdonald D. D., Urquidi-Macdonald M., Bhakta S. D., Pound B. G. The electrochemical impedance of porous nickel electrodes in alkaline media: II. Nonuniform transmission line analysis. *Journal of The Electrochemical Society*. 1991;138: 1359–1363. <https://doi.org/10.1149/1.2085786>

14. Lima-Tenório M. K., Ferreira C. S., Rebelo Q. H. F., ... Aparecido Pocrifka L. Pseudocapacitance properties of  $\text{Co}_3\text{O}_4$  nanoparticles synthesized using a modified sol-gel method. *Materials Research*. 2018;21(2): e20170521. <https://doi.org/10.1590/1980-5373-mr-2017-0521>

15. Nquyen P. H., Paasch G. Transfer matrix method for the electrochemical impedance of inhomogeneous porous electrodes and membranes. *Journal of Electroanalytical Chemistry*. 1999;460(1-2): 63–79. [https://doi.org/10.1016/S0022-0728\(98\)00343-X](https://doi.org/10.1016/S0022-0728(98)00343-X)

16. Conway B. E. *Electrochemical supercapacitors: scientific fundamentals and technological applications*. Springer Science & Business Media; 2013. 607 p.

17. Huang J., Gao Y., Luo J., ... Zhang J. Editors' choice—review—impedance response of porous electrodes: theoretical framework, physical models and applications.. *Journal of The Electrochemical Society*. 2020;167: 166503. <https://doi.org/10.1149/1945-7111/abc655>

18. Syugaev A. V., Zonov R. G., Mikheev K. G., Maratkanova A. N., Mikheev G. M. Electrochemical impedance of laser-induced graphene: Frequency response of porous structure. *Journal of Physics and Chemistry of Solids*. 2023;188: 111533. <https://doi.org/10.1016/j.jpics.2023.111533>

### Information about the authors

Alexander V. Syugaev, Cand. Sci. (Chem.), Research Fellow at the Laboratory of Ultrafine Systems, Department of Physics and Chemistry of Nanomaterials of Physical-Technical Institute, Udmurt Federal Research Center (Izhevsk, Russian Federation).

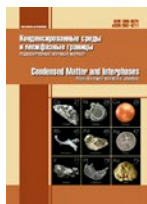
<https://orcid.org/0000-0002-2190-395X>  
syual@udman.ru

Vitaly E. Porsev, Cand. Sci. (Phys.-math), Leading Research Fellow at the Laboratory of Mechanical Activation of Organic Systems, Department of Physics and Chemistry of Nanomaterials of Physical-Technical Institute, Udmurt Federal Research Center (Izhevsk, Russian Federation).

<https://orcid.org/0000-0003-1949-7371>  
porsev@udman.ru

Received 21.03.2023; approved after reviewing 19.04.2023; accepted for publication 15.06.2023; published online 25.03.2024.

Translated by Irina Charychanskaya



# Condensed Matter and Interphases

Kondensirovannye Sredy i Mezhfaznye Granitsy  
<https://journals.vsu.ru/kcmf/>

## Original articles

Research article

<https://doi.org/10.17308/kcmf.2024.26/11818>

## Composition and structure of tungsten antimony acid

P. V. Timushkov<sup>1</sup>✉, V. A. Burmistrov<sup>1</sup>, M. N. Ulyanov<sup>1</sup>, V. N. Semenov<sup>2</sup>

<sup>1</sup>Chelyabinsk State University,  
70b ul. Molodogvardeytshev, Chelyabinsk 45402, Russian Federation

<sup>2</sup>Voronezh State University,  
1 Universitetskaya pl., Voronezh 394018, Russian Federation

### Abstract

Tungsten antimony acids (TAA) with the composition  $H_{(2)}Sb_{(2)}W_xO_6 \cdot nH_2O$  ( $0 < x \leq 1.45$ ;  $0 < n \leq 2.0$ ) have been synthesized by hydrolysis of antimony trichloride pre-oxidized with nitric acid in the presence of varying amounts of  $Na_2WO_4$ . To obtain TAA protonated forms, the samples were kept in a 96% solution of sulphuric acid, the precipitate was washed until reaction became neutral and dried in air. The amount of tungsten, antimony, and silver ions in TAA was determined using energy dispersive analysis. Changes in structural parameters upon doping of AA with tungsten ions were studied using a Bruker D8 ADVANCE X-ray diffractometer ( $CuK_{\alpha 1}$ -radiation). The number of oxonium ions in TAA was determined by the substitution of these ions by silver ions in equivalent amounts ( $Ag^+$ -TAA forms).

All obtained TAA samples and  $Ag^+$  TAA forms had a pyrochlore-type structure, space group symmetry  $Fd\bar{3}m$ . Refinement of the arrangement of atoms in the structure using the Rietveld method showed that tungsten ions replace antimony ions and are statistically located in 16c, oxygen anions in 48f, and oxonium ions and water molecules in 16d and 8b positions, respectively.

When tungsten ions were introduced into samples, the structural parameters of the resulting phases changed. There was a decrease in the unit cell parameter and the distance between antimony ions and oxygen anions, while an increase in the distance between oxonium ions and oxygen anions located in 48f positions was observed. This allowed the removal of a proton from oxonium molecules and its transport via a system of hydrogen bonds formed by water molecules.

**Keywords:** Solid electrolytes of antimony oxide, Tungsten oxides, Antimony acid, Pyrochlore type structure

**For citation:** Timushkov P. V., Burmistrov V. A., Ulyanov M. N., Semenov V. N. Composition and structure of tungsten antimony acid. *Condensed Matter and Interphases*. 2024;26(1): 146–152. <https://doi.org/10.17308/kcmf.2024.26/11818>

**Для цитирования:** Тимушков П. В., Бурмистров В. А., Ульянов М. Н., Семенов В. Н. Состав и структура вольфрамсурьмяной кислоты. *Конденсированные среды и межфазные границы*. 2024;26(1): 146–152. <https://doi.org/10.17308/kcmf.2024.26/11818>

✉ Pyotr V. Timushkov, e-mail: [p.timushkov@mail.ru](mailto:p.timushkov@mail.ru)

© Timushkov P. V., Burmistrov V. A., Ulyanov M. N., Semenov V. N., 2024



The content is available under Creative Commons Attribution 4.0 License.



## 1. Introduction

Materials with high proton conductivity can be used for the production of electrochemical current sources [1–2]. One of these compounds is antimony acid (AA), which has a pyrochlore-type structure (space group symmetry  $Fd\bar{3}m$ ) [3]. The peculiarity of AA is the structure formed from jointed antimony–oxygen octahedra with a negative charge. The compensation of negative charge requires the presence of positively charged particles, such as oxonium, silver, potassium, sodium ions, etc. [4]. In this case, water molecules are located in some positions located in hexagonal cavities and can form oxonium ions or diaquahydrogen ions with protons [4]. The amount of proton conductivity of AA depends on the number of water and oxonium molecules [5].

Studies [6–9] demonstrated that the substitution of antimony ions Sb(V) with W(VI) in complex antimony oxides creates defects in the oxygen sublattice and promotes an increase in ionic conductivity. Probably, the creation of additional vacancies, which can be filled with water molecules, should lead to a restructuring of the proton hydrate sublattice of AA, as a consequence, to an increase in proton conductivity. The formation of vacant positions is possible by introducing W(VI) ions with a similar ionic radius [5] but having a different valence from Sb(V) ions into the structure of AA. However, data on the synthesis and study of the structure of complex antimony oxides doped with tungsten, sodium, and potassium ions are limited and refer to samples synthesized by the solid-phase method [5–10]. Protonated forms obtained by substitution of monovalent ions in these compounds with oxonium ions [11] are not fully hydrated compounds.

Therefore, the goal of the study was to develop a method for the synthesis of tungsten antimony acid (TAA) with different contents of W(VI) ions, determination of the concentration range of stability of the resulting phases and their structural parameters.

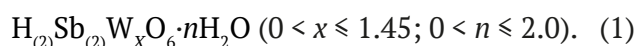
## 2. Experimental

The synthesis of TAA samples was carried out by hydrolysis of pre-oxidized  $SbCl_3$  with nitric acid in the presence of  $Na_2WO_4$ . The resulting precipitate was boiled for 6 hours, kept in the

mother solution for seven days, washed with distilled water and dried. The W/Sb ratio in the resulting phases was varied by changing the amount of  $Na_2WO_4$  in the original solutions.

To obtain the protonated form, the samples were kept in a 96% solution of sulphuric acid at room temperature for a long time, the precipitate was washed until neutral and dried in air.

The resulting TAA samples were a white powder and had a composition that can be described by the chemical formula:



The number of protons (oxonium) in the structure of the obtained TAA phases was determined using an ion exchange. For this, the sample was placed in a concentrated  $AgNO_3$  solution and kept for 24 hours, after which it was washed from excess of silver and nitric acid until there was no reaction to  $Ag^+$  ions. The amount of silver, antimony and tungsten ions in the structure was determined by energy-dispersive X-ray fluorescence spectroscopy using an EDXRF spectrometer (AR QUANT'X from Thermo Fisher Scientific) according to standard methods.

The phase composition was monitored using Bruker D8 ADVANCE diffractometer ( $CuK_{\alpha 1}$ -radiation) in the range of diffraction angles  $2\theta$  from 10 to 70° with a step of 0.01°. The structure of the resulting compounds was refined by the Rietveld approach using the PowderCell software package. For generation of the linear shape of the diffraction maxima, pseudo-Voigt function was used. For calculation of the distance between the 16d, 16c, and 48f positions, the formulas provided in [12] was used.

## 3. Results and discussion

The X-ray diffraction patterns of the AA and TAA samples have the same set of diffraction maxima, the totality of which is satisfactorily described by the extinction laws for crystals with cubic structure of the pyrochlore type of space group symmetry  $Fd\bar{3}m$  [13]. As the amount of tungsten ions in the TAA increases, no significant redistribution of the relative intensities of reflections with even and odd indices was observed. In this case, the reflections shift toward larger angles (Fig. 1). This may indicate the

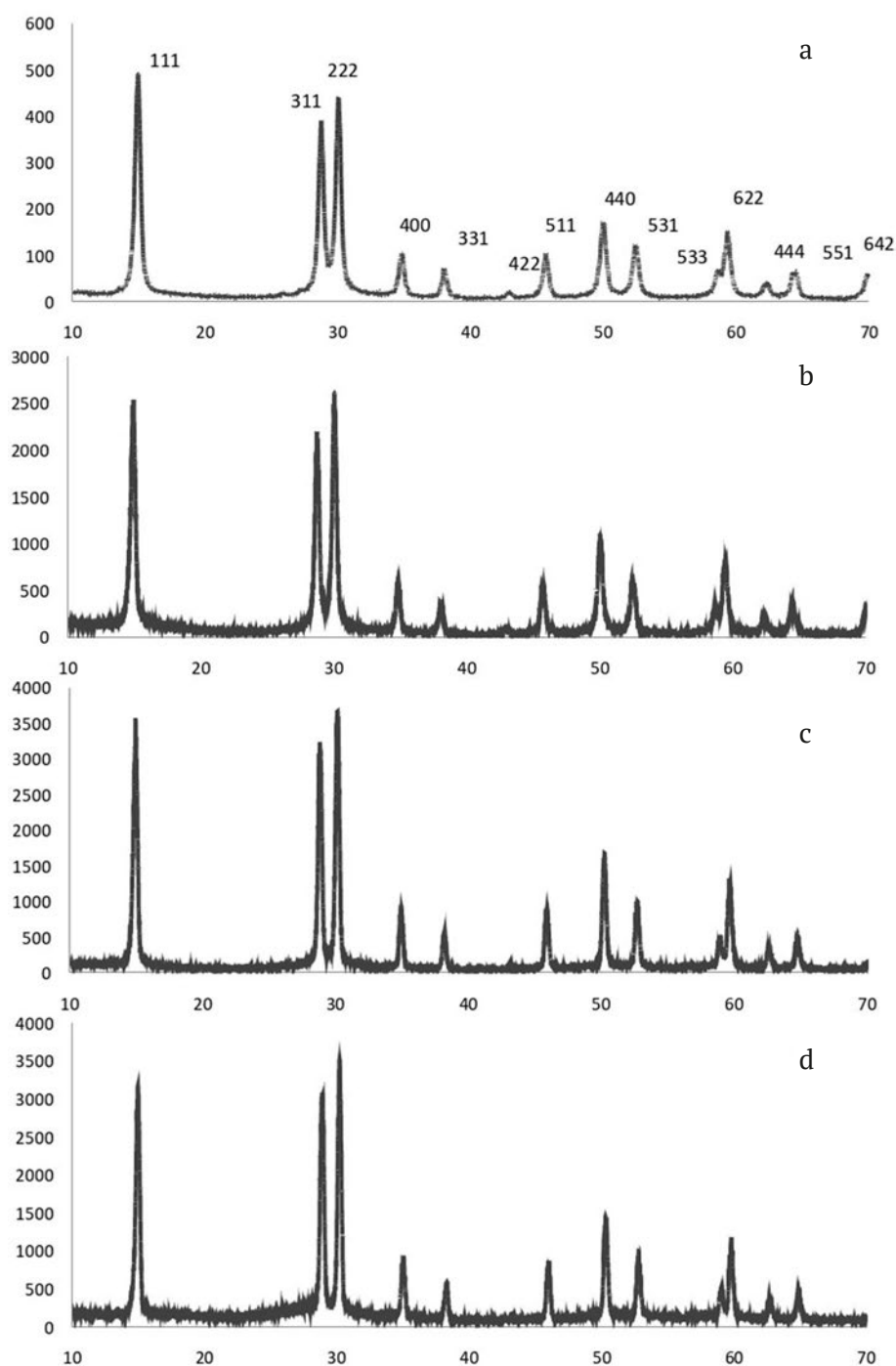


**Fig. 1.** X-ray diffraction patterns of AA and TAA samples obtained by coprecipitation in solutions containing antimony and tungsten ions in different ratios: AA(a), W/Sb = 1/15(b), W/Sb = 3/5(c), W/Sb = 5/3(d)

substitution of some antimony ions with tungsten ions and a change in structural parameters.

Elemental analysis of TAA showed that with an increase in the concentration of tungsten ions in the initial solutions, they increase with a simultaneous decrease in the number of antimony ions in the solid phase. In this

case, the dependence of the change in W/Sb ratios according to X-ray spectral analysis data coincides with those calculated using formula (1) (Fig. 2). Taking into account X-ray analysis, this allows us to confirm the substitution of Sb(V) ions with W(VI) in the same crystallographic positions and consider the resulting TAA samples

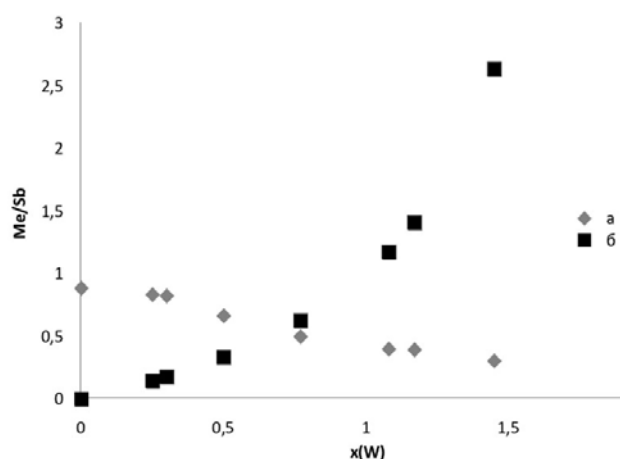


**Fig. 2.** Change in the ratio of Ag/(Sb + W) (a) and W/Sb (b) ions when doping AA with tungsten ions according to data of X-ray fluorescent spectroscopy and calculated (solid lines) according to formula (1) for TAA and Ag-forms of TAA with an average degree of proton substitution by silver ions equal to 0.93

as substitutional solid solutions. Under the assumption that the number of oxygen anions in the octahedra does not change, and the number of protons should correspond to the electrical neutrality of the compounds, chemical formulas have been proposed that describe the compositions of the resulting TAA phases (Table 1).

For experimental clarification of the number of protons in TAA, additional studies on samples in which hydrogen ions in solutions of silver nitrate were substituted by silver ions (Ag forms of TAA) were carried out.

As follows from the X-ray analysis data, during ion exchange the set of diffraction maxima

does not change, but a decrease in the relative intensities of reflections with even and odd indices was observed (Fig. 3). This indicates the substitution of protons (oxonium) with silver ions in TAA [11] without changing the symmetry of the crystal lattice. The number of silver ions in TAA samples decreases with an increase in the number of substituted antimony ions for tungsten ions (Fig. 2), which indicates a decrease in the number of protons in TAA samples with the introduction of tungsten ions.

The data obtained on the composition of the samples allow to propose a model for the arrangement of ions along a regular system of points in a pyrochlore-type structure. The main framework of the structure is formed by antimony-oxygen and tungsten-oxygen octahedra, connected by vertices. In this case, antimony and tungsten ions are located in the centre of the octahedra (16c positions), and oxygen anions are located at their vertices (48f positions). Oxonium ions and water molecules are statistically located in the 16d and 8b positions.

A full-profile analysis of the TAA showed good agreement between the proposed model of ion distribution over positions of a pyrochlore-type structure and experimental data (Table 2). At the same time, with an increase in the number of tungsten ions in the TAA samples, the unit cell parameter decreased from 10.337 Å to 10.254 Å for TAA with composition  $H_{0.55}Sb_{0.55}W_{1.45}O_6 \cdot nH_2O$  (Table 2). At the same time, a decrease in the distance between 16c(Sb,W) – 48f(O) positions was observed, as well as an increase in the distance between 16d( $H_3O^+$ ) – 48f(O) positions

**Table 1.** The number of Sb(V) and W(VI) ions in TAA samples and silver ions in Ag-forms of TAA obtained by X-ray fluorescence spectroscopy

No	H-form of TAA			Ag-form of TAA	Gross formula of TAA
	Sb, at.%	W, at.%	W/Sb	Ag/Sb	
1	100	0	0	0.886	$H_2Sb_2O_6 \cdot nH_2O$
2	87.5	12.5	0.142	0.954	$H_{1.75}Sb_{1.75}W_{0.25}O_6 \cdot nH_2O$
3	85.0	15.0	0.176	0.970	$H_{1.70}Sb_{1.70}W_{0.30}O_6 \cdot nH_2O$
4	75.0	25.0	0.333	0.887	$H_{1.50}Sb_{1.50}W_{0.50}O_6 \cdot nH_2O$
5	61.5	38.5	0.626	0.813	$H_{1.25}Sb_{1.25}W_{0.77}O_6 \cdot nH_2O$
6	46.0	54.0	1.173	0.869	$H_{0.92}Sb_{0.92}W_{1.08}O_6 \cdot nH_2O$
7	41.5	58.5	1.409	0.951	$H_{0.85}Sb_{0.85}W_{1.17}O_6 \cdot nH_2O$
8	27.5	72.5	2.636	1.092	$H_{0.55}Sb_{0.55}W_{1.45}O_6 \cdot nH_2O$

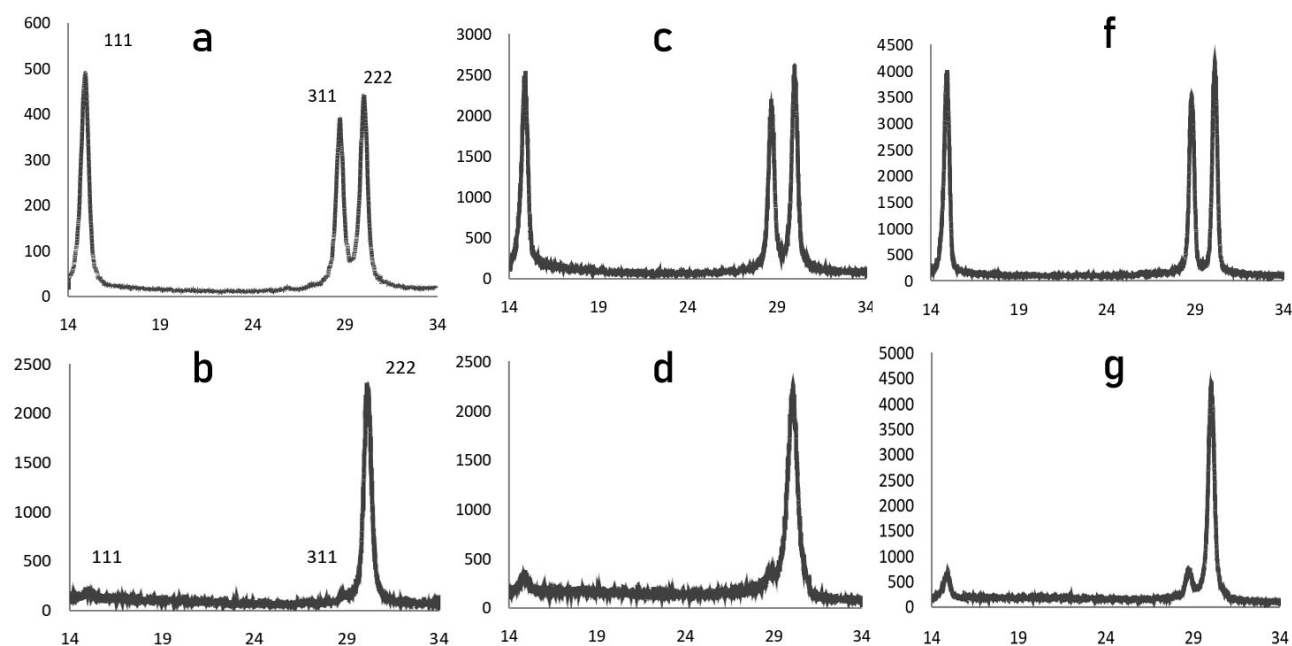


**Fig. 3.** X-ray diffraction patterns of AA, TAA, and Ag-form of samples of AA and TAA with compositions  $H_2Sb_2O_6 \cdot nH_2O$  (a);  $Ag_2Sb_2O_6 \cdot nH_2O$  (b);  $H_{1.70}Sb_{1.70}W_{0.30}O_6 \cdot nH_2O$  (c);  $Ag_{1.70}Sb_{1.70}W_{0.30}O_6 \cdot nH_2O$  (d);  $H_{0.85}Sb_{0.85}W_{1.17}O_6 \cdot nH_2O$  (e);  $Ag_{0.85}Sb_{0.85}W_{1.17}O_6 \cdot nH_2O$  (f)

**Table 2.** Arrangement of atoms according to crystallographic positions of the structure of air-dry AA and TAA samples with composition  $H_{(2)}Sb_{(2)}W_xO_6 \cdot nH_2O$  (where  $0 < x \leq 1.45$ ;  $0 < n \leq 2.0$ ) according to full-profile X-ray analysis. Parameter values  $a$  of unit cell,  $x$  coordinate (O) and correlation factor Rwp

No	TAA composition	16d	16c		48f	8b	$a, \text{\AA}$	Rwp	$x(O)$
		$H^+/H_3O^+$	$Sb^{5+}$	$W^{6+}$	$O^{2-}$	$H_2O$			
1	$H_2Sb_2O_6 \cdot nH_2O$	16	16	0	48	8	10.34	11	0.32
2	$H_{1.75}Sb_{1.75}W_{0.25}O_6 \cdot nH_2O$	14	14	2	48	8	10.32	11.03	0.327
3	$H_{1.70}Sb_{1.70}W_{0.30}O_6 \cdot nH_2O$	13.6	13.6	2.4	48	8	10.31	9.84	0.329
4	$H_{1.50}Sb_{1.50}W_{0.50}O_6 \cdot nH_2O$	12	12	4	48	8	10.31	9.28	0.330
5	$H_{1.25}Sb_{1.25}W_{0.77}O_6 \cdot nH_2O$	9.84	9.84	6.16	48	8	10.29	8.44	0.330
6	$H_{0.92}Sb_{0.92}W_{1.08}O_6 \cdot nH_2O$	7.36	7.36	8.64	48	8	10.28	9.74	0.330
7	$H_{0.85}Sb_{0.85}W_{1.17}O_6 \cdot nH_2O$	6.64	6.64	9.36	48	8	10.27	9.72	0.330
8	$H_{0.55}Sb_{0.55}W_{1.45}O_6 \cdot nH_2O$	4.4	4.4	11.6	48	8	10.25	10.45	0.330

(Fig. 4.). An increase in the parameter  $x$  of oxygen atoms was recorded (Table. 2).

This may be due to the fact that tungsten ions have a higher electronegativity than antimony ions and change the electron density near oxygen anions, which led to distortion of antimony-oxygen octahedra, a decrease in interionic distances and the unit cell parameter. An increase in the distances between oxonium and oxygen anions makes the removal of proton from oxonium molecules and its transport via the system of hydrogen bonds formed by water molecules more probable.

#### 4. Conclusions

The conditions for the synthesis of TAA samples with the composition  $H_{(2-x)}Sb_{(2-x)}W_xO_6 \cdot nH_2O$  ( $0 < x \leq 1.45$ ;  $0 < n \leq 2.0$ ) were established for a wide range of concentrations and it was shown that the TAA phases have a pyrochlore-type structure, with antimony and tungsten ions statistically located in 16c, oxygen anions located in 48f, and oxonium ions and water molecules located in 16d and 8b positions, respectively.

The substitution of some antimony ions with tungsten ions in AA led to a decrease in the unit cell parameter and a change in interionic



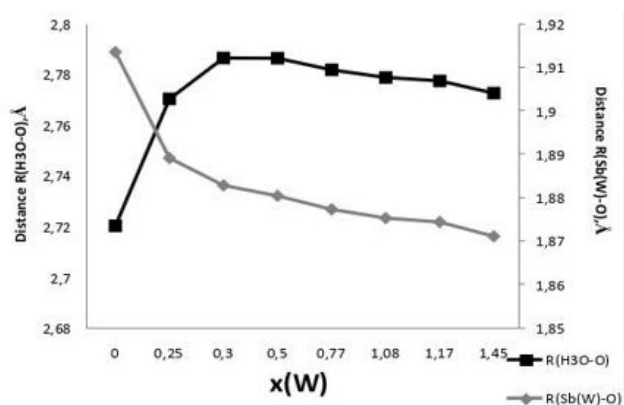


**Fig. 4.** The distance between the 16d, 16c, and 48f positions from the ratio of substitution with tungsten calculated using formula 2.  $R(H_3O-O)$  – distance between the 16d and 48f positions,  $R(Sb(W)-O)$  – distance between the 16c and 48f positions

distances, which was caused by a change in the interaction energy in tungsten-oxygen octahedra and a decrease in the number of protons in the structure.

### Contribution of the authors

The authors contributed equally to this article.

### Conflict of interests

The authors declare that they have no known competing financial interests or personal relationships that could have influenced the work reported in this paper.

### References

1. Kurzina E. A., Stenina I. A., Dalvi A., Yaroslavtsev A. B. Synthesis and ionic conductivity of lithium titanium phosphate-based solid electrolytes. *Inorganic Materials*, 2021;57(10): 1035–1042. <https://doi.org/10.1134/S0020168521100071>
2. Bedin V. Y., Kazachiner O. V., Asabina E. A., ... Yaroslavtsev A. B. Phase formation and ionic conductivity of  $Na_{1+2x}Zn_xZr_{2-x}(PO_4)_3$  phosphates. *Inorganic Materials*. 2022;58(1): 64–70 <https://doi.org/10.1134/S0020168522010046>
3. Polynova T. N., Poray-Koshits M. A. Stereochemistry of pentavalent antimony compounds\*. *Journal of Structural Chemistry*. 1966;7(4): 642–655. (In Russ.). Available at: <https://jsc.niic.nsc.ru/article/59076/>

4. Stroganov E. V., Smirnov Yu. N., Saltykova V. A., Markin V. N. The structure of pyrochlore based in the consideration of elementary structural motifs\*. *Pushkin Leningrad State University Journal*. 1979;4(1), 46–48. (In Russ.)

5. Kovalenko L. Y., Burmistrov V. A., Zakharevich D. A., Kalganov D. A. On the mechanism of proton conductivity of polyantimonic acid. *Chelyabinsk Physical and Mathematical Journal*. 2021;6(1): 95–110. <https://doi.org/10.47475/2500-0101-2021-16108>

6. Burmistrov V. A., Zakharevich D. A. Ion-conducting defect pyrochlore phases in the  $K_2O-Sb_2O_3-WO_3$  system. *Inorganic Materials*. 2003;39: 68–71. <https://doi.org/10.1023/A:1021895304326>

7. Lupitskaya Yu. A., Burmistrov V. A. Phases with a pyrochlore-type structure formed in the system  $(yx)K_2CO_3-xNa_2CO_3-ySb_2O_3-2(2-y)WO_3$  ( $0 \leq x \leq y$ ,  $1.0 \leq y \leq 1.375$ ) when heated\*. *Bulletin of Chelyabinsk State University*. 2009;(25): 50–54. (In Russ.). Available at: <https://elibrary.ru/item.asp?id=12786139>

8. Lupitskaya Yu. A., Burmistrov V. A., Kalganov D. A. Structure and ionic conductivity of solid solutions in the system  $K_2CO_3-AgNO_3-Sb_2O_3-MeO_3$  ( $Me = W, Mo$ ). \* *Journal of Surface Investigation: X-Ray, Synchrotron and Neutron Techniques*. 2015;(6): 83–83. (In Russ.). Available at: <https://doi.org/10.7868/S0207352815060141>

9. Knyazev A. V., Tananaev I. G., Kuznetsova N. Y., Smirnova N. N., Letyanina I. A., Ladenkov I. V. Crystal structure and thermodynamic properties of potassium antimony tungsten oxide. *Thermochimica Acta*. 2010;499(1-2): 155–159. <https://doi.org/10.1016/j.tca.2009.12.002>

10. Mezhenina O. A., Burmistrov V. A., Biryukova A. A. Structure and ion-exchange properties of crystalline tungstoantimonic acid. *Inorganic Materials*. 2015;51: 167–171. <https://doi.org/10.1134/S0020168515010136>

11. Riviere M., Fourquet J. L., Grins J., Nygren M. The cubic pyrochlores  $H_{2x}Sb_{2x}W_{2-2x}O_6 \cdot nH_2O$ ; structural, thermal and electrical properties. *Materials Research Bulletin*. 1988;23(7): 965–975. [https://doi.org/10.1016/0025-5408\(88\)90051-7](https://doi.org/10.1016/0025-5408(88)90051-7)

12. Mikhailova L. I., Semenov N. E., Fedorov N. F. *Calculation of the parameters of elementary cells of cubic pyrochlore\**. Leningrad Institute of Technology Publ.; 1979. 25 p. (In Russ.)

13. Groult D., Michel C., Raveau B. Sur de nouveaux pyrochlores  $ASbWO_6$  ( $A = H_3O, NH_4$ ) et  $AgSbWO_6 \cdot H_2O$ . *Journal of Inorganic and Nuclear Chemistry*. 197;35(9): 3095–3101. [https://doi.org/10.1016/0022-1902\(73\)80007-7](https://doi.org/10.1016/0022-1902(73)80007-7)

\* Translated by author of the article

**Information about authors**

*Pyotr V. Timushkov*, Assistant at the Department of Solid State Chemistry and Nanoprocesses, Chelyabinsk State University (Chelyabinsk, Russian Federation).

<https://orcid.org/0009-0005-2226-3076>

[p.timushkov@mail.ru](mailto:p.timushkov@mail.ru)

*Vladimir A. Burmistrov*, Dr. Sci. (Phys.-Math.), Full Professor, Department of Solid State Chemistry and Nanoprocesses, Chelyabinsk State University (Chelyabinsk, Russian Federation).

<https://orcid.org/0000-0002-7862-6017>

[burmistrov@csu.ru](mailto:burmistrov@csu.ru)

*Maxim N. Ulyanov*, Cand. Sci. (Phys.-Math.), Assistant Professor at the Department of General and Theoretical Physics Chelyabinsk State University (Chelyabinsk, Russian Federation).

<https://orcid.org/0000-0003-0066-9559>

[max-39@yandex.ru](mailto:max-39@yandex.ru)

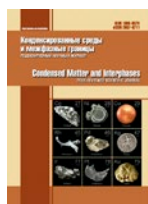
*Victor N. Semenov*, Dr. Sci. (Chem.), Full Professor, Head of the Department of General and Inorganic Chemistry, Voronezh State University (Voronezh, Russian Federation).

<https://orcid.org/0000-0002-4247-5667>

[office@chem.vsu.ru](mailto:office@chem.vsu.ru)

*Received 28.04.2023; approved after reviewing 19.05.2023; accepted for publication 15.06.2023; published online 25.03.2024.*

*Translated by Valentina Mittova*



# Condensed Matter and Interphases

Kondensirovannye Sredy i Mezhfaznye Granitsy  
<https://journals.vsu.ru/kcmf/>

## Original articles

Research article

<https://doi.org/10.17308/kcmf.2024.26/11897>

## Electronic structure and composition of tin oxide thin epitaxial and magnetron layers according to synchrotron XANES studies

O. A. Chuvenkova<sup>1</sup>, N. I. Boikov<sup>1</sup>, S. V. Ryabtsev<sup>1</sup>, E. V. Parinova<sup>1</sup>, R. G. Chumakov<sup>2</sup>,  
A. M. Lebedev<sup>2</sup>, D. Smirnov<sup>3</sup>, A. Makarova<sup>4</sup>, S. S. Titova<sup>1</sup>, K. A. Fateev<sup>1</sup>, S. Yu. Turishchev<sup>1</sup>✉

<sup>1</sup>Voronezh State University,  
1 Universitetskaya pl., Voronezh 394018, Russian Federation

<sup>2</sup>National Research Center “Kurchatov Institute”,  
1 Akademika Kurchatova pl., Moscow 123182, Russian Federation

<sup>3</sup>Dresden University of Technology,  
18 Zellescher Weg, Dresden 01069, Germany

<sup>4</sup>Free University of Berlin,  
22 Arnimallee, Berlin 14195, Germany

### Abstract

The materials of the tin-oxygen system and thin-film structures based on them are modern and actual for the creation of a wide range of electronic devices, for example, resistive gas sensors of high sensitivity and short response time with low energy consumption and high manufacturability. An important direction in the study of such materials and structures is the control of properties with variations in technological formation regimes. Information on the composition, local atomic and electronic structure of thin layers of the tin-oxygen system with varying approaches to their production is in demand.

The work is devoted to the study of the electronic structure of thin layers of tin oxides obtained by modern methods of molecular beam epitaxy and magnetron sputtering. A study of the local partial density of electronic states in the conduction band by X-ray absorption near edge structure spectroscopy of tin and oxygen has been carried out. The data were obtained using high-intensity synchrotron radiation, which allows varying the monochromatized radiation quantum energy without loss in intensity, that is necessary to obtain high-resolution X-ray spectral data.

It is shown that the composition, local atomic surrounding, electronic spectrum and their features depend on the technology of formation and storage conditions of the studied structures. Synchrotron X-ray spectroscopy data show the presence of intermediate oxides of the tin-oxygen system in the studied materials after prolonged storage in laboratory conditions. The data obtained indicate the possibility of controlled variation in the composition, local atomic surrounding and electronic spectrum of thin-film structures of tin oxides of small thickness. The results of the work can be used in the formation and subsequent modification of thin and ultrathin layers of tin oxides by magnetron sputtering and molecular beam epitaxy, as well as in their further application as active layers of microelectronics devices.

**Keywords:** Tin and its oxides, Electronic structure, Density of states, Local atomic surrounding, Composition, Epitaxial nanolayers, Magnetron nanolayers, X-ray absorption near edge structure, Synchrotron investigations

**Funding:** The study was supported by Russian Science Foundation (Project 23-22-00465).

**For citation:** Chuvenkova O. A., Boikov N. I., Ryabtsev S. V., Parinova E. V., Chumakov R. G., Lebedev A. M., Smirnov D., Makarova A., Titova S. S., Fateev K. A., Turishchev S. Yu. Electronic structure and composition of tin oxide thin epitaxial and magnetron layers according to synchrotron XANES studies. *Condensed Matter and Interphases*. 2024;26(1): 153–160. <https://doi.org/10.17308/kcmf.2024.26/11897>

**Для цитирования:** Чувенкова О. А., Бойков Н. И., Рябцев С. В., Паринова Е. В., Чумаков Р. Г., Лебедев А. М., Смирнов Д., Макарова А., Титова С. С., Фатеев К. А., Турищев С. Ю. Электронное строение и состав тонких эпитаксиальных и магнетронных слоев оксида олова по данным синхротронных XANES исследований. *Конденсированные среды и межфазные границы*. 2024;26(1): 153–160. <https://doi.org/10.17308/kcmf.2024.26/11897>

✉ Sergey Yu. Turishchev, e-mail: [tsu@phys.vsu.ru](mailto:tsu@phys.vsu.ru)

© Chuvenkova O. A., Boikov N. I., Ryabtsev S. V., Parinova E. V., Chumakov R. G., Lebedev A. M., Smirnov D., Makarova A., Titova S. S., Fateev K. A., Turishchev S. Yu., 2024



The content is available under Creative Commons Attribution 4.0 License.

## 1. Introduction

Thin layers of SnO<sub>2</sub> tin oxide are widely used in various fields of technology, including microelectronics, such as resistive gas sensors, transparent electrodes, catalysts, etc. [1-4]. The methods of producing tin dioxide largely determine its properties. In addition, the properties are influenced by the size and morphology of the obtained materials, in the case of layers, this is primarily the thickness, macro- and microstructure. Thus, due to the significant influence of the surface, the properties of nanometer range structures differ greatly from large ones in size, and can be used to create devices with significantly improved characteristics. These characteristics primarily include response speed, miniaturization, power consumption, and others. The creation of heterostructures based on tin and silicon oxide is also promising for use in such fields of technology as thermoelectrics [5]. One of the effective and high-precision methods of forming heterostructures consisting of ultrathin ordered layers is the method of molecular beam epitaxy [6–8]. This method is characterized by a high degree of perfection of the grown layers, including nanometer thickness, their structural and phase boundaries and the ability to control the composition, structure and functional properties of the structures being formed. This method makes it possible to obtain very thin layers of tin on the surface of prepared substrates, for example, silicon. The magnetron sputtering method makes it possible to obtain high-quality tin layers in a wide range of thicknesses for use in various fields of technology. The advantage of the method is the simplicity and flexibility of controlling the modes of structure formation [9-11]. The most noticeable disadvantage is the difficulty of obtaining structurally highly organized continuous layers of small thickness comparable to epitaxial ones. It is known that the properties of small-dimensional objects are largely determined by the contribution of the surface. Thin layers of the tin-oxygen system are no exception. High-precision experimental methods with increased sensitivity to the composition, the specifics of the local atomic surrounding, the electronic spectrum, and the structure of the surface layers of the object under study are especially in demand. One of

these methods is the X-ray absorption near edge structure (XANES) spectroscopy using high-intensity synchrotron radiation. The possibility of changing the quantum energy of synchrotron radiation without changes in its extremely high intensity is a prerequisite for obtaining high-resolution XANES spectra. In the ultra-soft X-ray region of the synchrotron radiation spectrum, XANES spectroscopy is highly sensitive to the local surrounding of a given sort of studied material or structure surface atoms, and therefore is particularly relevant for the analysis of nanostructures of various compositions, including those based on silicon [12–16] and tin [17–21]. This paper presents the results of studies using the XANES synchrotron method of the composition, atomic and electronic structure of thin tin layers formed by molecular beam epitaxy and magnetron sputtering on crystalline silicon substrates.

## 2. Experimental

The studied samples of “Epitaxy Sn/Si” were obtained by molecular beam epitaxy on a Si (001) substrate with a 50 nm thick Si buffer layer [5]. During the formation of the samples, the purified and dried substrates were transported to an ultrahigh vacuum film growth chamber, where the thermal oxide was desorbed at a temperature of 840 °C. Then, 5 monolayers of tin atoms (~1.6 nm) were grown (deposited) from an effusion cell onto a 50 nm thick silicon buffer layer. Before conducting synchrotron experiments, the samples were stored in the laboratory for several weeks. The method of high-resolution transmission electron microscopy showed the continuity and uniformity of the formed tin layer.

A series of “Magnetron Sn/Si” samples was obtained by magnetron sputtering on a direct current of a tin target with a purity of 99.999% in argon plasma on Si (100) substrates. The argon pressure in the working chamber was 10<sup>-3</sup> Torr, the discharge current was 60 mA, the voltage was 360 V. The film thickness was determined by the sputtering time at constant operating modes of the formation unit and amounted to 30 nm. Morphology control performed by scanning electron microscopy showed the formation of a continuous uniform granular layer. The size of the single granule did not exceed the thickness



of the layer. Before conducting synchrotron experiments, the samples were stored in the laboratory for several weeks.

Studies of the samples electronic structure were carried out using the non-destructive XANES method, which allows obtaining information about the local surrounding of absorbing tin and oxygen atoms specificity and the effects of ordering in the structural grid of these atoms of the analyzed surface layer [22]. The XANES method allows obtaining direct experimental information on the distribution of the local partial density of free electronic states in the conduction band of the studied surface layer [14–17, 20]. The high-intensity radiation of the ultra-soft X-ray range of BESSY-II synchrotron, the Russian-German beamline (Helmholtz-Zentrum-Berlin, Berlin, Germany) [23] and KISI-Kurchatov synchrotron, the NANOPES beamline (NRC “Kurchatov Institute”, Moscow, Russia) [24] were used. The photon flux was  $10^9$ – $10^{11}$  photons/s, the storage ring current was 50–300 mA. The depth of the analyzed surface layer [25, 26] and the energy resolution for the Sn  $M_{4,5}$  and O K edges were  $\sim 10$  nm and 0.1 eV, respectively. The total electron yield (TEY) detection mode was used when registering the compensation (drain) current of the sample. The vacuum in the experimental chambers was  $\sim 10^{-10}$  Torr. The angle of incidence of synchrotron radiation was  $90^\circ$  to the surface plane.

### 3. Results and discussion

Fig. 1 shows the XANES Sn  $M_{4,5}$  spectra of reference materials and studied samples of epitaxial (Epitaxy Sn/Si) and magnetron (Magnetron Sn/Si) tin layers. The reference materials include sintered compressed powder of polycrystalline tetragonal tin dioxide – SnO<sub>2</sub>(T), metal foil refreshed in situ in ultrahigh vacuum of the spectrometer without natural oxide – Sn foil refresh, metal foil of tin – Sn foil, for which the XANES Sn  $M_{4,5}$  spectra were recorded experimentally, under the same conditions as the studied samples and previously known ones [17, 19]. We also present data obtained from ab-initio calculations [20] of XANES Sn  $M_{4,5}$  spectra for compounds unstable in laboratory conditions such as orthorhombic tin dioxide SnO<sub>2</sub>(O) and tin single oxide SnO.

XANES Sn  $M_{4,5}$  (3d) absorption spectra represent the distribution of p states in the conduction band, which, according to dipole selection rules, reflect transitions from core 3d states to free *p*- and *f*-states in the conduction band. The distribution of the main spectral features and their relative intensities, given in a single range for the convenience of comparing the spectra in Fig. 1, show that the spectra of the used references are sufficiently different from each other and from the formed nanolayers in terms of their fine structure. A detailed discussion of the reference spectra fine structure is presented in [19–20]. In the spectrum of the studied magnetron layer of the Magnetron Sn/Si sample, a sufficiently pronounced structure of the absorption edges M5 and M4 is observed, the most intense features of which are located at energies  $\sim 487.1$  eV and  $\sim 495.5$  eV, B-C and G in

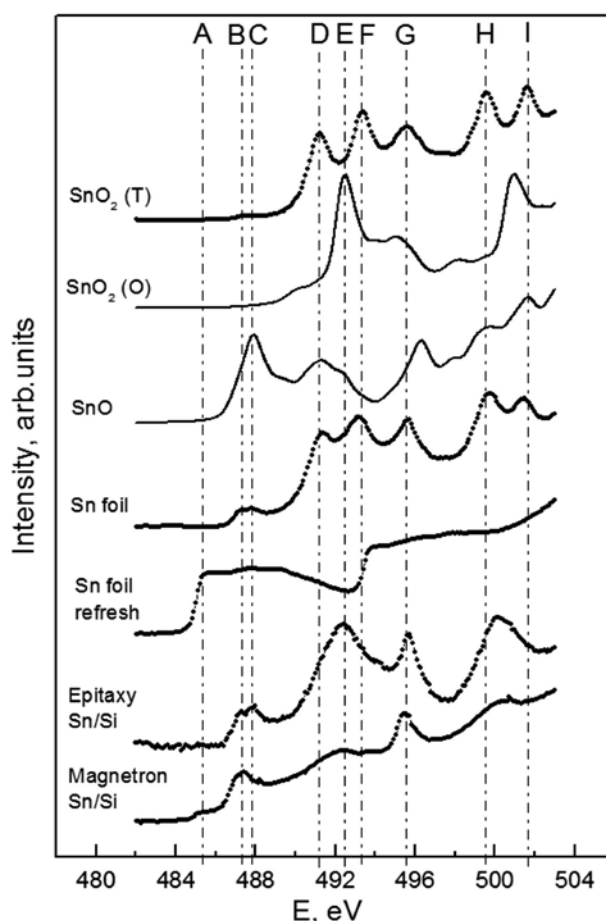


**Fig. 1.** XANES Sn  $M_{4,5}$  of references (SnO<sub>2</sub>(T), SnO<sub>2</sub>(O), SnO, Sn foil, Sn foil refresh) and studied samples of epitaxial (Epitaxy Sn/Si) and magnetron (Magnetron Sn/Si) tin layers

Fig. 1, respectively. Thus, spin-doublet splitting of these edges is observed  $\sim 8.4$  eV. These features correspond in their energy position to tin single oxide SnO with a fine structure of the XANES spectrum at energies of  $\sim 487.9$  eV,  $\sim 491.3$  eV. At the same time, a less intense structure is also observed at energies 485.1 eV (A) and 493.5 eV (F), with the same spin-doublet splitting, corresponding to metallic tin without natural oxide (reference spectrum of the Sn foil refresh sample). Another “set” of high-energy features at energies of  $\sim 492.3$  eV and  $\sim 500.7$  eV corresponds to orthorhombic tin dioxide. Thus, in the sample obtained by magnetron sputtering, single oxide and orthorhombic tin dioxide were formed along with metallic tin in a surface layer of  $\sim 10$  nm, accessible to XANES sensing when registering Sn  $M_{4,5}$  absorption edges. Thus, the 30 nm tin layer obtained by magnetron sputtering of a tin target does not completely oxidize when exposed to air, even for a long time. However, the oxides formed in this layer are unstable under normal conditions. In addition, there is no phase of stable tetragonal tin dioxide with a characteristic fine structure of the M4 edge of DFG (Fig. 1) at energies 491.3 eV, 493.2 eV and 495.6 eV and the M5 edge of HI at energies  $\sim 499.5$  eV and  $\sim 501.6$  eV, respectively. Note that when considering the tin metal foil (Fig. 1), stored without any special conditions, the formation of stable tetragonal tin dioxide along with unstable phases of tetragonal tin single oxide and orthorhombic tin dioxide is observed on its surface, as evidenced by the “blurring” of the dip E between the features D and F at energies 491.3 eV and 493.2 eV. On the surface of the studied 30 nm tin layer obtained by magnetron sputtering, only the initial stage of tin oxidation is observed, passing through the formation of intermediate unstable phases of single oxide and orthorhombic tin dioxide. The absence of a stable phase of tetragonal tin dioxide, despite being in laboratory conditions for several weeks, indicates, perhaps, an insufficiently elapsed period of oxidation of the tin layer or the need for additional conditions for its production.

When considering the XANES Sn  $M_{4,5}$  absorption edge of the epitaxial tin film (Epitaxy Sn/Si), it can be seen that it also has a very pronounced fine structure. The most intense

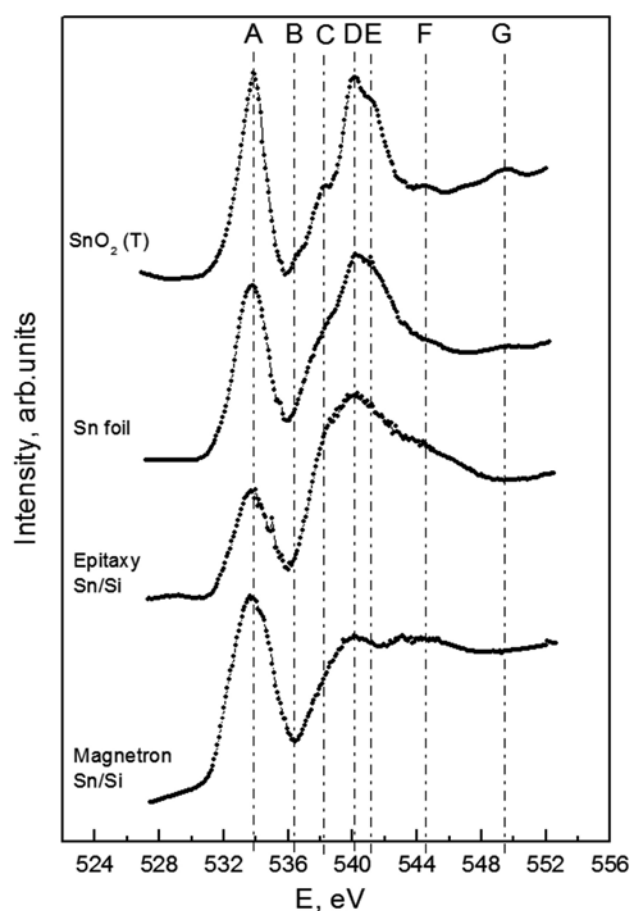
features were noted at energies of 492.3 eV (E) and 500.3 eV, which, in general, are located closest to the characteristic features of the fine structure of the orthorhombic tin dioxide SnO<sub>2</sub> (O) spectrum. We note the observed electronic states in the region of low-energy spectral features  $\sim 487.2$  eV and  $\sim 495.6$  eV, which also correspond to tin single oxide. It is worth noting that the distribution of electronic states in the energy range of  $\sim 487$ – $488$  eV, unlike tin layers obtained by magnetron sputtering, has a double, split structure of the sun at energies of  $\sim 487.2$  eV and 487.8 eV. We observe a similar peak splitting for the surface of the metal tin foil (Sn foil), which is probably due to the simultaneous presence of vacancies in the sublattice of oxygen and the phase of tin single oxide on the surface of this sample. The high intensity of the fine structure features of XANES Sn  $M_{4,5}$ , corresponding to orthorhombic tin dioxide, indicates the predominance of this phase compared with tin single oxide. Thus, in the sample of tin layers formed epitaxially, the same phases of the “intermediate” tin oxides SnO and SnO<sub>2</sub>(O) are observed as in the layers obtained by magnetron sputtering, except for metallic tin. The latter fact is related to the critically small thickness of the epitaxial tin nanolayer, all atoms of which are exposed to interaction with oxygen atoms. In particular, due to the silicon buffer layer presence under the epitaxial tin layer. This layer of crystalline Si, as a result of its noticeable electronegativity, attracts oxygen atoms diffusing through the thin tin layer at least to the tin-silicon interface. At the same time, the XANES Sn  $M_{4,5}$  spectrum also lacks fine structure features corresponding to the phase of stable tetragonal tin dioxide. Thus, it is possible to epitaxially obtain thin layers of intermediate phases of tin oxides. To obtain a stable phase of tin dioxide SnO<sub>2</sub>(T), the formation regimes should be changed or additional modifying conditions should be applied, for example, oxidative annealing.

Fig. 2 shows the O K XANES spectra of references (SnO<sub>2</sub>(T) and Sn foil) and studied samples of magnetron (Magnetron Sn/Si) and epitaxial (Epitaxy Sn/Si) tin layers. XANES O K (1s) absorption spectra represent transitions from the core 1s oxygen level to free  $p$  states in the conduction band. It can be seen that the

spectra of the presented reference samples, as in the case of the absorption spectra of XANES Sn M<sub>4,5</sub>, differ in their fine structure. Thus, tetragonal tin dioxide has a pronounced peak A at an energy of 533.9 eV, as well as features B (536.5 eV), C (538 eV), D (540 eV), E (541.2 eV), F (544.2 eV) and G (549.2 eV). The main peaks A at an energy of 533.85 eV and D at an energy of 540 eV are most pronounced in tin metal foil. The remaining features of the fine structure are smoothed out. The lack of data on the oxygen edge in orthorhombic tin dioxide and tin monoxide makes the interpretation of the oxygen edge of the studied samples insufficiently complete and is the subject of further research.

When considering the oxygen absorption edge in a sample of tin layers obtained by magnetron sputtering, A peak is observed at an energy of 533.9 eV, as well as D at an energy of 540 eV. In general, the edge structure is similar in its features and their energy position to the fine structure of the absorption spectrum of the Sn foil reference, where there are also no pronounced features of the B, C, E and G of the spectra of the tin dioxide reference. The difference observed only in the distribution of intensities between the two main peaks of the structure A and D and in the observation of an insignificant dip in intensity at an energy of 541.6 eV.

In the epitaxially obtained sample (Epitaxy Sn/Si), A peak is also observed at an energy of 533.9 eV and D at an energy of 540 eV. However, the intensity of the low-energy peak A is lower than that of peak D. Here, a wide feature in the D peak region probably indicates the oxidation of the crystalline silicon epitaxial buffer surface, which is located under the nanolayer of epitaxial tin. We noted above that the tin-silicon layer boundary is available for interaction with atmospheric oxygen. At the same time, this interface is in the range of the XANES O K spectrum probing depth. Moreover, the shape and position of feature D correlates well with the data on the fine structure of the XANES O K absorption edges of naturally oxidized silicon [for example see 14]. Thus, the signal from the oxidized silicon atoms of the Si-Sn interface is superimposed on the signal from the tin oxide of the epitaxial nanolayer, forming the spectrum shown in Fig. 2.



**Fig. 2.** XANES O K of references (SnO<sub>2</sub>(T), Sn foil) and studied samples of epitaxial (Epitaxy Sn/Si) and magnetron (Magnetron Sn/Si) tin layers

#### 4. Conclusions

There is a general agreement between the data on the analysis of synchrotron XANES spectra of tin (Sn M<sub>4,5</sub>) and oxygen (O K). On the surface of the studied Epitaxy Sn/Si and Magnetron Sn/Si samples there are oxides similar to natural ones found on the surface of tin foil, but different from tin dioxide tetragonal modification. The layers obtained by molecular beam epitaxy are completely oxidized with the predominance of intermediate phases of tin oxides. Tin layers obtained by magnetron sputtering contain the same phases of intermediate tin oxides SnO and SnO<sub>2</sub>(O) on the surface, however, the presence of non-oxidized metallic tin is noted. That is, tin layers undergo the same stages of oxide formation during oxidation from the surface, regardless of the method of obtaining these layers. At the same time, the result of interaction with atmospheric oxygen significantly depends on the thickness



of the formed nanolayer as an indicator of the amount of tin metal available for oxidation. Absence of obvious traces (fine structure of spectra) in the recorded synchrotron data of stable tetragonal tin dioxide indicates insufficient formation conditions for its formation. Thus, the considered approaches require additional effects or conditions to obtain nanolayers of stable tetragonal tin dioxide. The obtained data show the possibility of fine, through the modes of formation and composition, control of the local atomic structure and electronic spectrum of thin layers of tin oxides formed by molecular beam epitaxy or magnetron sputtering, which is important for use in modern structures, including microelectronic ones.

### Contribution of the authors

All authors made an equivalent contribution to the preparation of the publication.

### Conflict or interests

The authors declare that they have no known competing financial interests or personal relationships that could have appeared to influence the work reported in this paper.

### References

1. Chopra K. L., Major S., Pandya D. K. Transparent conductors – A status review. *Thin Solid Films*. 1983;102: 1–46. [https://doi.org/10.1016/0040-6090\(83\)90256-0](https://doi.org/10.1016/0040-6090(83)90256-0)
2. Lee S. U., Choi W. S., Hong B. Synthesis and characterization of SnO<sub>2</sub> : Sb film by DC magnetron sputtering method for applications to transparent electrodes. *Physica Scripta*. 2007;129: 312–315. <https://doi.org/10.1088/0031-8949/2007/T129/069>
3. Niranjana R. S., Hwang Y. K., Kim D.-K., Jhung S. H., Chang J.-S., Mulla I. S. Nanostructured tin oxide: Synthesis and gas-sensing properties. *Materials Chemistry and Physics*. 2005;92: 384–388. <https://doi.org/10.1016/j.matchemphys.2005.01.050>
4. Subramanian N. S., Santhi B., Sundareswaran S., Venkatakrishnan K. S. Studies on spray deposited SnO<sub>2</sub>, Pd:SnO<sub>2</sub> and F:SnO<sub>2</sub> thin films for gas sensor applications. *Synthesis and Reactivity in Inorganic, Metal-Organic, and Nano-Metal Chemistry*. 2006;36: 131–135. <https://doi.org/10.1080/15533170500478883>
5. Tonkikh A. A., Zakharov N. D., Eisenschmidt C., Leipner H. S., Werner P. Aperiodic SiSn/Si multilayers for thermoelectric applications. *Journal of Crystal Growth*. 2014;392: 49–51. <http://doi.org/10.1016/j.jcrysgro.2014.01.047>
6. Arthur J. R. Molecular beam epitaxy. *Surface Science*. 2002;500(1-3):189–217. [https://doi.org/10.1016/S0039-6028\(01\)01525-4](https://doi.org/10.1016/S0039-6028(01)01525-4)
7. Wang T., Prakash A., Warner E., Gladfelter W. L., Jalan B. Molecular beam epitaxy growth of SnO<sub>2</sub> using a tin chemical precursor. *Journal of Vacuum Science & Technology A*. 2015;33(2): 020606-1-4. <http://doi.org/10.1116/1.4913294>
8. Rosental A., Tarre A., Gerst A., ... Uustare T. Epitaxial single and double nanolayers of SnO<sub>2</sub> and TiO<sub>2</sub> for resistive gas sensors. *IEEE Sensors Journal*. 2013;13(5): 1648–1655. <https://doi.org/10.1109/JSEN.2013.2238227>
9. Gangwar A. K., Godiwal R., Jaiswal J., ... Singh P. Magnetron configurations dependent surface properties of SnO<sub>2</sub> thin films deposited by sputtering process. *Vacuum*. 2020;177: 109353-1-9. <https://doi.org/10.1016/j.vacuum.2020.109353>
10. Nguyen T. T., Dang H. P., Luc Q. H., Le T. Studying the influence of deposition temperature and nitrogen contents on the structural, optical, and electrical properties of N-doped SnO<sub>2</sub> films prepared by direct current magnetron sputtering. *Ceramics International*. 2019;45: 9147–9156. <https://doi.org/10.1016/j.ceramint.2019.01.255>
11. Domashevskaya E. P., Chuvenkova O. A., Ryabtsev S. V., ...Turishchev S. Yu. Electronic structure of undoped and doped SnO<sub>x</sub> nanolayers. *Thin Solid Films*. 2013;537(30): 137–144. <https://doi.org/10.1016/j.tsf.2013.03.051>
12. Brown F. C., Rustgi O. P. Extreme ultraviolet transmission of crystalline and amorphous silicon. *Physical Review Letters*. 1972;28: 497–500. <https://doi.org/10.1103/PhysRevLett.28.497>
13. Barranco A., Yubero F., Espinos J. P., Groening P., Gonzalez-Elipe A. R. Electronic state characterization of SiO<sub>x</sub> thin films prepared by evaporation. *Journal of Applied Physics*. 2005;97: 113714. <https://doi.org/10.1063/1.1927278>
14. Turishchev S. Yu., Parinova E. V., Pisliaruk A. K., ... Sivakov V. Surface deep profile synchrotron studies of mechanically modified top-down silicon nanowires array using ultrasoft X-ray absorption near edge structure spectroscopy. *Scientific Reports*. 2019;9(8066): 1–7. <https://doi.org/10.1038/s41598-019-44555-y>
15. Koyuda D. A., Titova S. S., Tsurikova U. A., ... Turishchev S. Yu. Composition and electronic structure of porous silicon nanoparticles after oxidation under air- or freeze-drying conditions. *Materials Letters*. 2022;312: 131608-1-3. <https://doi.org/10.1016/j.matlet.2021.131608>
16. Ming T., Turishchev S., Schleusener A., ... Sivakov V. Silicon suboxides as driving force for efficient light-enhanced hydrogen generation on silicon nanowires. *Small*. 2021;19: 2007650-1-6. <https://doi.org/10.1002/smll.202007650>



17. Kucheyev S., Baumann T. F., Sterne P. A., ... Willey T. M. Surface electronic states in three-dimensional SnO<sub>2</sub> nanostructures. *Physical Review B*. 2005;72(3): 035404-1-5. <https://doi.org/10.1103/PhysRevB.72.035404>

18. Sharma A., Varshney M., Shin H. J., Chae K. H., Won S. O. X-ray absorption spectroscopy investigations on electronic structure and luminescence properties of Eu:SnO<sub>2</sub>-SnO nanocomposites. *Current Applied Physics*. 2016;16: 1342–1348. <http://dx.doi.org/10.1016/j.cap.2016.08.005>

19. Chuvenkova O. A., Domashevskaya E. P., Ryabtsev S. V., ... Turishchev S. Yu. XANES and XPS investigations of surface defects in wire like SnO<sub>2</sub> crystals. *Physics of the Solid State*. 2015;57(1): 153–161. <https://doi.org/10.1134/s1063783415010072>

20. Manyakin M. D., Kurganskii S. I., Dubrovskii O. I., ... Turishchev S. Yu. Electronic and atomic structure studies of tin oxide layers using X-ray absorption near edge structure spectroscopy data modelling. *Materials Science in Semiconductor Processing*. 2019;99: 28–33. <https://doi.org/10.1016/j.mssp.2019.04.006>

21. Domashevskaya E. P., Yurakov Yu. A., Ryabtsev S. V., Chuvenkova O. A., Kashkarov V. M., Turishchev S. Yu. Synchrotron investigations of the initial stage of tin nanolayers oxidation. *Journal of Electron Spectroscopy and Related Phenomena*. 2007;156–158: 340–343. <https://doi.org/10.1016/j.elspec.2006.11.042>

22. Stohr J. *NEXAFS spectroscopy*. Berlin: Springer; 1996. 403 p.

23. Fedoseenko S. I., Iossifov I. E., Gorovikov S. A., ... Kaindl G. Development and present status of the Russian-German soft X-ray beamline at BESSY II. *Nuclear Instruments and Methods in Physics Research Section A: Accelerators, Spectrometers, Detectors and Associated Equipment*. 2001;470: 84–88. [https://doi.org/10.1016/S0168-9002\(01\)01032-4](https://doi.org/10.1016/S0168-9002(01)01032-4)

24. Lebedev A. M., Menshikov K. A., Nazin V. G., Stankevich V. G., Tsetlin M. B., Chumakov R. G. NanoPES photoelectron beamline of the Kurchatov Synchrotron Radiation Source. *Journal of Surface Investigation: X-ray, Synchrotron and Neutron Techniques*. 2021;15: 1039–1044. <https://doi.org/10.1134/S1027451021050335>

25. Kasrai M., Lennard W. N., Brunner R. W., Bancroft G. M., Bardwell J. A., Tan K. H. Sampling depth of total electron and fluorescence measurements in Si L- and K-edge absorption spectroscopy. *Applied Surface Science*. 1996;99: 303–312. [https://doi.org/10.1016/0169-4332\(96\)00454-0](https://doi.org/10.1016/0169-4332(96)00454-0)

26. Erbil A., Cargill III G. S., Frahm R., Boehme R. F. Total-electron-yield current measurements for near-surface extended x-ray-absorption fine structure. *Physical Review B*. 1988;37: 2450–2464. <https://doi.org/10.1103/PhysRevB.37.2450>

## Information about authors

*Olga A. Chuvenkova*, Cand. Sci. (Phys.-Math.), Senior Researcher, Joint Scientific and Educational Laboratory “Atomic and Electronic Structure of Functional Materials” of Voronezh State University and the National Research Center “Kurchatov Institute”, Voronezh State University (Voronezh, Russian Federation).

<https://orcid.org/0000-0001-5701-6909>  
chuvenkova@phys.vsu.ru

*Nikolai I. Boikov*, Engineer-Physicist, Joint Scientific and Educational Laboratory “Atomic and Electronic Structure of Functional Materials” of Voronezh State University and the National Research Center “Kurchatov Institute”, Voronezh State University (Voronezh, Russian Federation).

<https://orcid.org/0000-0002-0512-8666>  
boikov-hfmm@bk.ru

*Stanislav V. Ryabtsev*, Dr. Sci. (Phys.-Math.), Head of the Institute of Physics, Voronezh State University (Voronezh, Russian Federation).

<https://orcid.org/0000-0001-7635-8162>  
ryabtsev@phys.vsu.ru

*Elena V. Parinova*, Cand. Sci. (Phys.-Math.), Assistant Professor, General Physics Department, Voronezh State University (Voronezh, Russian Federation).

<https://orcid.org/0000-0003-2817-3547>  
parinova@phys.vsu.ru

*Ratibor G. Chumakov*, Cand. Sci. (Phys.-Math.), Senior Researcher of the National Research Center “Kurchatov Institute” (Moscow, Russian Federation).

<https://orcid.org/0000-0002-3737-5012>  
ratibor.chumakov@gmail.com

*Alexei M. Lebedev*, Cand. Sci. (Phys.-Math.), Senior Researcher of the National Research Center “Kurchatov Institute” (Moscow, Russian Federation).

<https://orcid.org/0000-0002-4436-6077>  
lebedev.alex.m@gmail.com

*Dmitry Smirnov*, Cand. Sci. (Phys.-Math.), Researcher, Institut für Festkörper- und Materialphysik, Technische Universität Dresden (Dresden, Germany).

anna.makarova@fu-berlin.de

*Anna Makarova*, Cand. Sci. (Phys.-Math.), Researcher, Institut für Chemie und Biochemie, Freie Universität Berlin (Berlin, Germany).

anna.makarova@fu-berlin.de

*Sofiia S. Titova*, Teacher of General Physics Department, Voronezh State University, (Voronezh, Russian Federation).

<https://orcid.org/0000-0001-6860-401X>  
titova@phys.vsu.ru

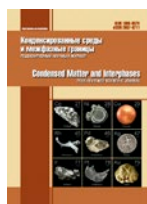
*Kirill A. Fateev*, Laboratory Assistant in Physics of General Physics Department, Voronezh State University, (Voronezh, Russian Federation).  
fateev@phys.vsu.ru

*Sergey Yu. Turishchev*, Dr. Sci. (Phys.-Math.), Associate Professor, Head of the General Physics Department, Voronezh State University (Voronezh, Russian Federation).

<https://orcid.org/0000-0003-3320-1979>  
tsu@phys.vsu.ru

*Received 01.09.2023; approved after reviewing 08.11.2023; accepted for publication 10.11.2023; published online 25.03.2024.*

*Translated by Sergey Turishchev*



# Condensed Matter and Interphases

Kondensirovannye Sredy i Mezhfaznye Granitsy  
<https://journals.vsu.ru/kcmf/>

## Original articles

Research article

<https://doi.org/10.17308/kcmf.2024.26/11819>

## Photoluminescent porous silicon nanowires as contrast agents for bioimaging

M. G. Shatskaia<sup>1</sup>, D. A. Nazarovskaia<sup>1</sup>, K. A. Gonchar<sup>1</sup>, Ya. V. Lomovskaya<sup>1,2</sup>, I. I. Tsiniiaikin<sup>1</sup>, O. A. Shalygina<sup>1</sup>, A. A. Kudryavtsev<sup>1,2,3</sup>, L. A. Osminkina<sup>1,3</sup>✉

<sup>1</sup>Lomonosov Moscow State University, Faculty of Physics,  
1 Leninskie Gory, Moscow 119991, Russian Federation

<sup>2</sup>Institute of Theoretical and Experimental Biophysics Russian Academy of Sciences,  
3 Institutskaya str., Pushchino 142290, Russian Federation

<sup>3</sup>Institute for Biological Instrumentation of the Russian Academy of Sciences,  
7 Institutskaya str., Pushchino 142290, Russian Federation

### Abstract

Porous silicon nanowires (pSi NWs) have attracted considerable interest due to their unique structural, optical properties and biocompatibility. The most common method for their top-down synthesis is metal-assisted chemical etching (MACE) of crystalline silicon (c-Si) wafers using silver nanoparticles as a catalyst. However, the replacement of silver with bioinert gold nanoparticles (Au NPs) markedly improves the efficiency of pSi NWs in biomedical applications. The present study demonstrates the fabrication of porous pSi NWs arrays using Au NPs as the catalyst in MACE of c-Si wafers with a resistivity of 1–5 mOhm-cm. Using scanning electron microscopy (SEM), the formation of arrays of porous nanowires with a diameter of 50 nm that consist of small silicon nanocrystals (nc-Si) and pores was observed. Raman spectroscopy analysis determined the size of nc-Si is about 4 nm. The pSi NWs exhibit effective photoluminescence (PL) with a peak in the red spectrum, which is attributed to the quantum confinement effect occurred in small 4 nm nc-Si. In addition, the pSi NWs exhibit low toxicity towards MCF-7 cancer cells, and their PL characteristics allow them to be used as contrast agents for bioimaging.

**Keywords:** Porous silicon nanowires, Photoluminescence, Raman spectroscopy, Contrast agents, Bioimaging

**Funding:** The study was supported by the Russian Science Foundation grant No. 22-72-10062, <https://rscf.ru/en/project/22-72-10062/> and the Theoretical Physics and Mathematics Advancement Foundation “BASIS” grant No. 23-2-2-18-1.

**Acknowledgements:** The equipment of the Educational and Methodological Centre for Lithography and Microscopy of Lomonosov Moscow State University was used in the study.

**For citation:** Shatskaia M. G., Nazarovskaia D. A., Gonchar K. A., Lomovskaya Ya. V., Tsiniiaikin I. I., Shalygina O. A., Kudryavtsev A. A., Osminkina L. A. Photoluminescent porous silicon nanowires as contrast agents for bioimaging. *Condensed Matter and Interphases*. 2024;26(1): 161–167. <https://doi.org/10.17308/kcmf.2024.26/11819>

**Для цитирования:** Шатская М. Г., Назаровская Д. А., Гончар К. А., Ломовская Я. В., Циньяйкин И. И., Шалыгина О. А., Кудрявцев А. А., Осминкина Л. А. Фотолюминесцентные пористые кремниевые нанонити как контрастные агенты для биовизуализации. *Конденсированные среды и межфазные границы*. 2024;26(1): 161–167. <https://doi.org/10.17308/kcmf.2024.26/11819>

✉ Liubov A. Osminkina, e-mail: [osminkina@physics.msu.ru](mailto:osminkina@physics.msu.ru)

© Shatskaia M. G., Nazarovskaia D. A., Gonchar K. A., Lomovskaya Ya. V., Tsiniiaikin I. I., Shalygina O. A., Kudryavtsev A. A., Osminkina L. A., 2024



The content is available under Creative Commons Attribution 4.0 License.

## 1. Introduction

Now, technologies for the design and use of nanomaterials in biomedicine are being intensively developed, and silicon nanowires and nanoparticles occupy a special place among them. It has been shown that silicon nanostructures can be used in a variety of fields: from drug delivery to tissue engineering [1]. This is possible due to such unique properties of nanostructured silicon as biocompatibility [2, 3], biodegradability [4, 5] and photoluminescence (PL) in the visible region of the spectrum [6,7]. PL is explained by the quantum confinement effect (QCE) in 2–6 nm silicon nanocrystals (nc-Si) [1, 4]. Due to the PL properties, porous silicon nanostructures have great potential in bioimaging [8–10]. In addition, the surface of porous silicon can be easily functionalized with silane groups, antibodies, polymers, etc., depending on the purpose [8, 11, 12].

There are several main methods for obtaining porous nanostructures on the surface of crystalline silicon substrates, and the most commonly used method is electrochemical (EC) etching [11, 13]. The result of EC etching of c-Si substrates is porous silicon (PSi) film, a spongy structure of nc-Si and pores. At the same time, by changing the parameters of the applied voltage, the level of c-Si doping and the concentration of electrolyte solutions used, macro-, meso-, and microporous films with pore sizes of 1–5 nm, 5–50 nm and 50–100 nm, respectively can be obtained [14]. The EC etching method is quite simple and easily scalable; however, mesoporous silicon films often used for biomedical purposes do not have sufficient PL properties for visualizing biological objects. The reason for this is that the nc-Si in them have too large size, far from the conditions for the occurrence of QCE. Therefore, to intensify the PL, PSi films or nanoparticles obtained from them are oxidized, thereby reducing the size of nc-Si, by incubating the samples in water, sodium tetraborate, or selecting drying conditions [8, 15, 16].

Metal-assisted chemical etching (MACE) of c-Si substrates is also the most commonly used method for producing silicon nanostructures [17]. Silver nanoparticles are usually used as a catalyst in MACE [18–20]. The result of MACE is arrays of silicon nanowires (SiNWs) with a diameter

of 20–100 nm on the c-Si surface. It has been shown that the porosity of SiNWs depends on the doping level of c-Si: the etching of low-doped substrates results in non-porous SiNWs, while the etching of highly doped substrates leads to the synthesis of porous SiNWs [18, 19, 21]. Porous SiNWs, immediately after their preparation, are characterized by mesoporous structure and effective stable PL, which undoubtedly facilitates the preparation of samples for potential use in the theranostics of diseases [22]. It should be noted, however, that there are no studies where PL of SiNWs synthesized by MACE with gold nanoparticles (Au NPs) would be investigated. It should be noted that the use of bioinert Au NPs can significantly improve the characteristics of SiNWs for their biomedical applications.

The purposes of the presented study were to obtain and investigate the morphology and PL properties of porous SiNWs synthesized using Au NPs as catalysts in MACE, and to show their use as contrast agents for the bioimaging of living cells.

## 2. Experimental

Porous SiNWs (pSi NWs) were synthesized by MACE of c-Si (100) substrates with a resistivity of 1–5 mOhm·cm. At the preliminary stage, c-Si was washed in acetone and isopropanol in an ultrasonic bath (Elmasonic US bath 37 KHz) for 5 min, then washed with deionized water (Millipore) and dried in air. To remove the oxide layer, the c-Si substrate was kept in 5 M HF for 2–5 min, then washed again with water and dried. Gold nanoparticles were reduced on the c-Si surface from an aqueous solution of 0.01 M AuCl<sub>3</sub>, mixed with 5 M HF in a ratio of 1:1, for 15 s. Silicon etching was performed in a solution of 5 M HF and 30% H<sub>2</sub>O<sub>2</sub> (10:1) for 60 min, the process was stopped by moving the wafers into water. Next, the samples were dried at room temperature in air. Removal of Au NPs was carried out by immersing the samples in aqua regia for 3 min.

To study the morphology of the obtained pSi NWs, a Carl Zeiss ULTRA 55 FE-SEM scanning electron microscope was used. To measure the PL or Raman spectra, the pSi NWs were mechanically separated from the c-Si substrate and placed on a metal substrate. Raman spectra were measured using a Confotec™ MR350 confocal microscope with laser excitation at 633 nm and low power of



1 mW to protect the samples from overheating. The PL spectra of the samples were measured upon excitation by a He-Cd laser at a wavelength of 325 nm (power of 10 mW, spot diameter of 1 mm). The PL signal was recorded using a grating monochromator (MS750, SOLAR TII) equipped with a CCD matrix.

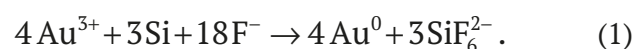
To study the cytotoxicity of pSi NWs, human ductal adenocarcinoma cell line MCF-7 was used. Cells were grown for 2 days in a culture flask with an area of 25 cm<sup>2</sup> in DMEM culture medium with the addition of 5% fetal bovine serum at 37 °C, 5% CO<sub>2</sub>. For the experiment, 0.1 ml of cell suspension with an initial cell concentration of 10<sup>5</sup>/ml was transferred into a 96-well plate. Then, pSi NWs with different concentrations were added to the wells, for which pSi NWs were mechanically separated from the c-Si substrates, the resulting powder was weighed and placed in a phosphate buffered saline solution. To determine the number of viable cells after a 24 h incubation with pSi NWs, the Alamar Blue test was performed: resazurin with a concentration of 0.03 mg/ml was added to the wells; living cells were able to oxidize it into luminescent resorufin. Luminescence intensity was recorded using an Infinite F200 plate spectrofluorimeter (Tecan).

For the biovisualization of cells with pSi NWs, a Leica confocal fluorescence microscope with a 63/NA 1.40 oil immersion objective and PL excitation with a 405 nm laser was used. pSi NWs with a concentration of 0.2 mg/ml were incubated with MCF-7 cells for 9 h before the start of the experiment. The cells were then stained by adding 3 mg/ml calcein-AM, Sigma for cytoplasmic

staining, and 5 mg/ml bisbenzimidazole H 33342 (Hoechst, Calbiochem) for nuclear staining.

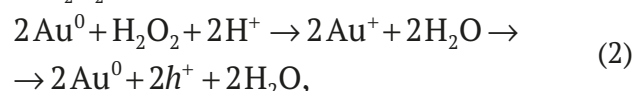
### 3. Results and discussion

Figure 1 shows a diagram of the production of pSi NWs using gold-assisted chemical etching (GACE) of highly doped c-Si wafers. At the first stage GACE, gold nanoparticles (Au NPs) were deposited from a solution of 0.01 M gold (III) chloride and 5 M HF, which dissociates in water into individual cations and anions and participates in the process of electrochemical reduction of Au<sup>3+</sup> ions into the metallic state on c-Si substrates [23]:

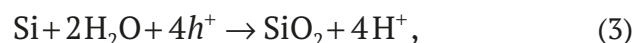


At the second stage of GACE, chemical etching of the c-Si substrate coated with Au NPs occurs in a solution of 5 M HF and 30% H<sub>2</sub>O<sub>2</sub> according to two parallel processes [18, 24].

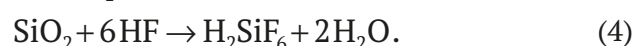
Au NPs (cathode site) catalyze the reduction of H<sub>2</sub>O<sub>2</sub>:



injected holes oxidize Si (anode site) to SiO<sub>2</sub>:



the SiO<sub>2</sub> layer is etched by hydrofluoric acid:



As a result of the presented redox reactions catalyzed by Au NPs, the c-Si surface is etched, and the remaining unetched areas have a nanowire-like morphology. Individual pSi NWs

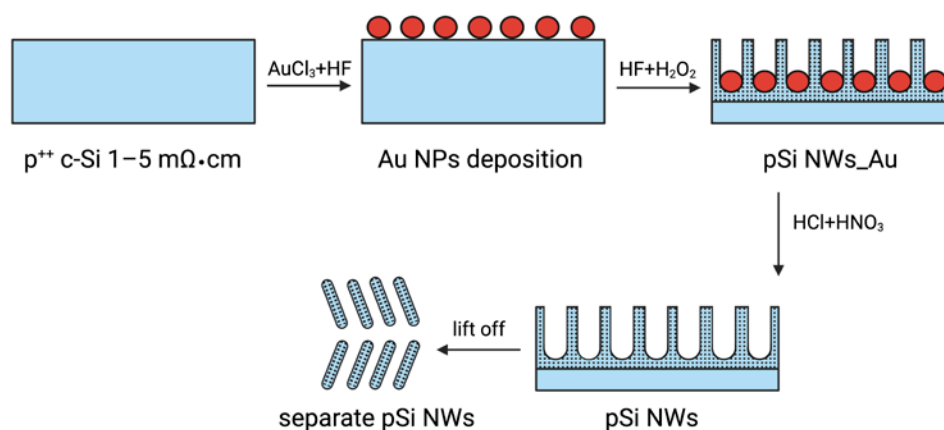


**Fig. 1.** Scheme for obtaining pSi NWs by gold-assisted chemical etching of highly doped c-Si wafers.

were obtained by mechanical separation from the c-Si substrate using tweezers.

The SEM micrograph of a cross-sectional view of porous pSi NWs on c-Si after 60 minutes of GACE is shown in Fig. 2a. pSi NWs appear as quasi-ordered arrays with a preferred orientation along the [100] crystallographic direction.

The pSi NWs layer thickness is 20  $\mu\text{m}$ . The tops of the pSi NWs stick together when they were dried due to capillary forces. The pore formation of pSi NWs was catalyzed by Au ions in the etching solution [18]. At the same time, the enlarged image (Fig. 2a) shows that the average diameter of the nanowires was 50 nm, and the pSi NWs consisted of small nanocrystals and pores. Micrographs of individual porous pSi NWs after their mechanical separation from the c-Si substrate are shown in Fig. 2b. The nanowires can break during the separation process; the average length of the obtained pSi NWs is 8  $\mu\text{m}$ .

The Raman spectrum (RS) of the obtained pSi NWs is shown in Fig. 3. Here, a scattering line characteristic of nanocrystalline silicon was observed with the position of the maximum shifted by  $\Delta\omega$  relative to  $520.5\text{ cm}^{-1}$ , corresponding to longitudinal vibrations of optical phonons in c-Si (shown by the dashed line). Such a low-frequency Raman shift occurs due to the quantum confinement of phonons arising in small-sized nc-Si contained in pSi NWs, their diameter ( $d_{RS}$ ) can be calculated using the formula [25, 4]:

$$d_{RS} = 0.543 \left( \frac{52.3}{\Delta\omega} \right)^{0.63}. \quad (5)$$

The nc-Si sizes calculated from formula (5) is 4.5 nm.

Using the MagicPlot package, deconvolution of the RS was obtained by Lorentian and Gaussian, responsible for the crystalline and amorphous phases in nc-Si, respectively. The percentage of crystalline silicon in porous SiNWs samples calculated in this way was 46.7%, and the percentage of amorphous silicon was 53.3%.

The PL spectrum of pSi NWs, represented by the wide band with a maximum at 755 nm is shown in Fig. 4. Such effective PL of pSi NWs was possible due to quantum confinement effects (QCE) arising in the nc-Si inside pSi NWs upon photoexcitation. QCE consists of secondary quantization of the energy of charge carriers of both electrons and holes in a quantum dot, nc-Si, which leads to an increase in the effective band gap [13]. This energy corresponds to the energy of emitted photons by photoluminescent nc-Si in such a way that the position of the maximum of the PL spectrum,  $E_{PL}$  related to the average size of nc-Si ( $d_{PL}$ ) in accordance with the empirical formula [7]:

$$E_{PL} = E_0 + \frac{3.73}{d_{PL}^{1.39}}, \quad (6)$$

Where  $E_0$  is the band gap in c-Si. From here an expression for the calculation of  $d_{PL}$  can be obtained:

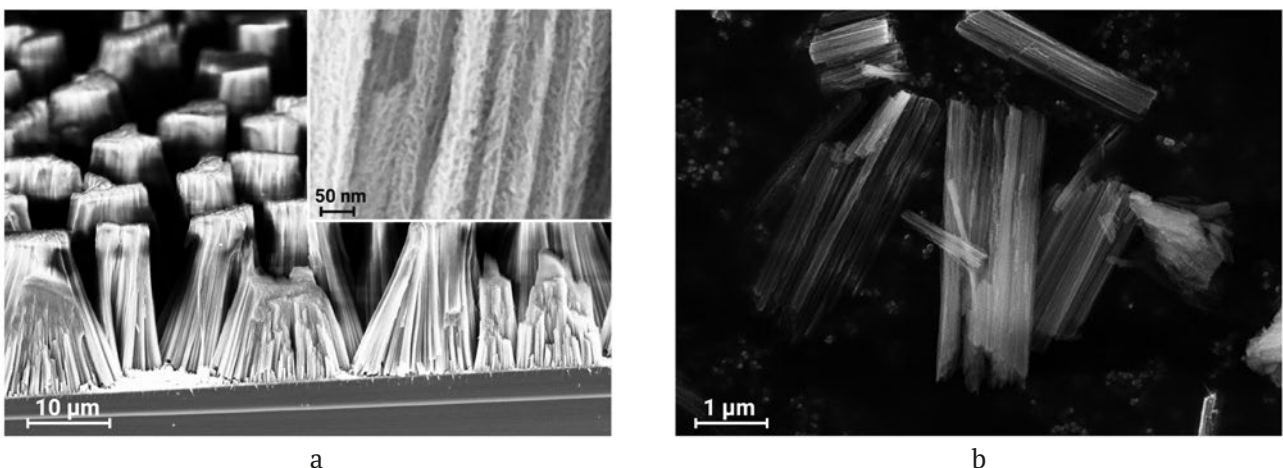


**Fig. 2.** SEM micrographs of pSi NWs, side view at an angle of  $38^\circ$  (a); and individual pSi NWs after their separation from the c-Si substrate (b). The inset in (a) shows an enlarged fragment of pSi NWs, demonstrating their porous structure

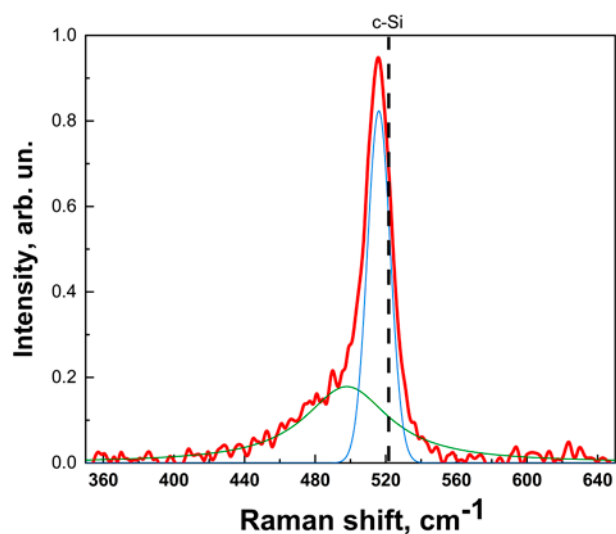


**Fig. 3.** Raman spectrum of pSi NWs. Thin lines represent the deconvolution of the spectrum. The dashed vertical line shows the position of the c-Si Raman maximum on  $520.5 \text{ cm}^{-1}$

$$d_{PL} = \left( \frac{3.73}{\Delta E_g} \right)^{0.72}, \quad (7)$$

where  $\Delta E_g = E_{PL} - E_0$ . The average size of nc-Si calculated using formula (7) is 4 nm, which is in good agreement with the Raman data.

The result of measuring the cytotoxicity of pSi NWs after 24 h incubation with MCF-7 cells is shown in Fig. 5. All points were taken in relation to the control group, to which pSi NWs was not added. It can be seen that over the entire range of concentrations studied, pSi NWs

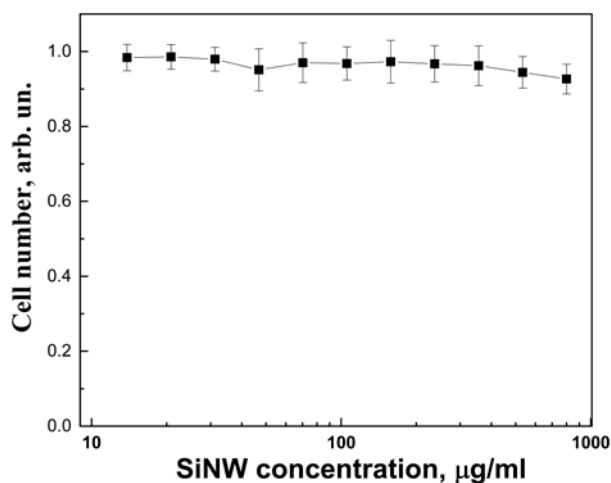


**Fig. 5.** Cytotoxicity of pSi NWs incubated for 24 h with MCF-7 cells. All points were taken in relation to the control group, to which pSi NWs was not added

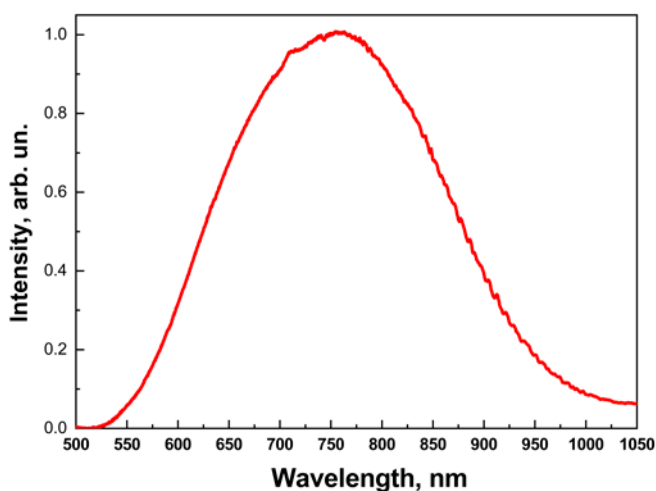


**Fig. 4.** PL spectrum of pSi NWs.

were characterized by extremely low toxicity, which is certainly a good result for their future applications in biomedicine.

Luminescent images of live MCF-7 cells after 9 h incubation with pSi NWs are shown in Fig. 6. Green, blue, and red colors correspond to the luminescence of the cell membrane, cell nucleus, and PL of pSi NWs, respectively. The merged image of cells with pSi NWs is shown in the lower right corner. In the presented micrograph, pSi NWs are visible as PL red thread-like structures located on the membrane and inside the cells. Thus, it has been shown that low-toxic PL pSi

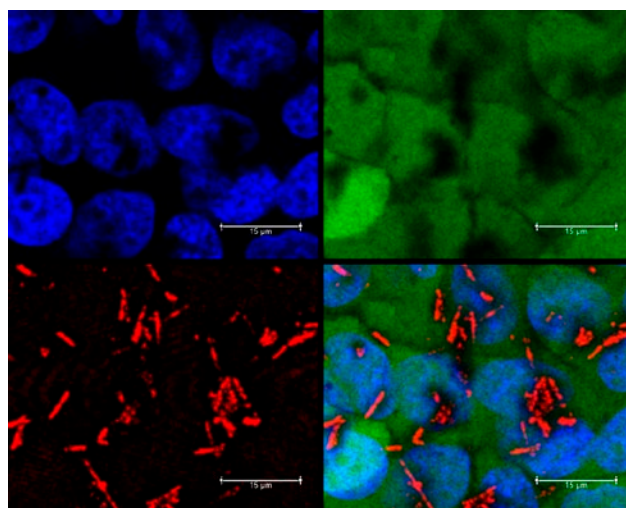


**Fig. 6.** Luminescence images of live MCF-7 cells after 9 h of incubation with pSi NWs. Green, blue, and red colors correspond to the luminescence of the cell membrane, cell nucleus, and PL of pSi NWs, respectively. The lower right corner shows a merged image of cells with pSi NWs.



NWs can be used as contrast agents for cell bioimaging.

#### 4. Conclusions

In this study, pSi NWs arrays were obtained by the GACE method, where Au NPs were used as a catalyst. The morphology of the samples was studied by scanning electron microscopy. It has been shown that GACE of c-Si wafers with a resistivity of 1–5 mOhm-cm produced arrays of porous nanowires with the diameter of 50 nm consisting of nc-Si and pores. The size of nc-Si was calculated based on the Raman spectra of pSi NWs and was about 4.5 nm. It was shown that, due to the quantum confinement effect, effective PL with a maximum in the red region of the spectrum can be excited in such pSi NWs. In this case, the size of nc-Si, calculated from the PL spectra of pSi NWs, was about 4 nm, which is in good agreement with the Raman data. It has been shown that pSi NWs were characterized by low toxicity towards MCF-7 cancer cells up to concentrations of 1 mg/ml, and the PL properties of pSi NWs allow their use as contrast agents for bioimaging. The presented data open up new possibilities for the use of low-toxic PL pSi NWs for theranostics of various diseases.

#### Contribution of the authors

The authors contributed equally to this article.

#### Conflict of interests

The authors declare that they have no known competing financial interests or personal relationships that could have influenced the work reported in this paper.

#### References

1. Canham L. (Ed.). *Handbook of porous silicon*. Berlin, Germany: Springer International Publishing; 2018. <https://doi.org/10.1007/978-3-319-71381-6>
2. Canham L. T. Nanoscale semiconducting silicon as a nutritional food additive. *Nanotechnology*. 2007;18: 185704. <https://dx.doi.org/10.1088/0957-4484/18/18/185704>
3. Low S. P., Voelcker N. H., Canham L. T., Williams K. A. The biocompatibility of porous silicon in tissues of the eye. *Biomaterials*. 2009;30: 2873–2880. <https://doi.org/10.1016/j.biomaterials.2009.02.008>
4. Gongalsky M. B., Tsurikova U. A., Gonchar K. A., Gvindgilliiia G. Z., Osminkina L. A. Quantum-confinement effect in silicon nanocrystals during their dissolution in model biological fluids. *Semiconductors*. 2021;55(1): 61–65. <https://doi.org/10.1134/s1063782621010097>
5. Maximchik P. V., Tamarov K., Sheval E. V., ... Osminkina L. A. Biodegradable porous silicon nanocontainers as an effective drug carrier for regulation of the tumor cell death pathways. *ACS Biomaterials Science & Engineering*. 2019;5(11): 6063–6071. <https://doi.org/10.1021/acsbomaterials.9b01292>
6. Delerue C., Allan G., Lannoo M. Theoretical aspects of the luminescence of porous silicon. *Physical Review B*. 1993;48: 11024. <https://doi.org/10.1103/PhysRevB.48.11024>
7. Ledoux G., Guillois O., Porterat D., ... Pillard V. Photoluminescence properties of silicon nanocrystals as a function of their size. *Physical Review B*. 2000;62: 15942. <https://doi.org/10.1103/PhysRevB.62.15942>
8. Park J. H., Gu L., von Maltzahn G., Ruoslahti E., Bhatia S. N., Sailor M. J. Biodegradable luminescent porous silicon nanoparticles for in vivo applications. *Nature Materials*. 2009;8: 331–336. <https://doi.org/10.1038/nmat2398>
9. Tolstik E., Gongalsky M. B., Dierks J., ... Lorenz K. Raman and fluorescence microspectroscopy applied for the monitoring of sunitinib-loaded porous silicon nanocontainers in cardiac cells. *Frontiers in Pharmacology*. 2022;13: 962763. <https://doi.org/10.3389/fphar.2022.962763>
10. Gu L., Hall D. J., Qin Z., ... Sailor M. J. In vivo time-gated fluorescence imaging with biodegradable luminescent porous silicon nanoparticles. *Nature Communications*. 2003;4: 2326. <https://doi.org/10.1038/ncomms3326>
11. Salonen J., Lehto V. P. Fabrication and chemical surface modification of mesoporous silicon for biomedical applications. *Chemical Engineering Journal*. 2008;137: 162–172. <https://doi.org/10.1016/j.cej.2007.09.001>
12. Gongalsky M. B., Kharin A. Y., Osminkina L. A., ... Chung B. H. Enhanced photoluminescence of porous silicon nanoparticles coated by bioresorbable polymers. *Nanoscale Research Letters*. 2012;7: 1–7. <https://doi.org/10.1186/1556-276X-7-446>
13. Canham L. T. Silicon quantum wire array fabrication by electrochemical and chemical dissolution of wafers. *Applied Physics Letters*. 1990;57: 1046–1048. <https://doi.org/10.1063/1.103561>
14. Lehmann V., Stengl R., Luigart A. On the morphology and the electrochemical formation mechanism of mesoporous silicon. *Materials Science and Engineering: B*. 2000;69: 11–22. [https://doi.org/10.1016/S0921-5107\(99\)00286-X](https://doi.org/10.1016/S0921-5107(99)00286-X)
15. Gongalsky M. B., Kargina J. V., Cruz J. F., ... Sailor M. J. Formation of Si/SiO<sub>2</sub> Luminescent quantum dots from mesoporous silicon by sodium tetraborate/



citric acid oxidation treatment. *Frontiers in Chemistry*. 2019;7: 165. <https://doi.org/10.3389/fchem.2019.00165>

16. Titova S. S., Osminkina L. A., Kakuliia ... Turishchev S. Y. X-ray photoelectron spectroscopy of hybrid 3T3 NIH cell structures with internalized porous silicon nanoparticles on substrates of various materials. *Condensed Matter and Interphases*. 2023;25(1): 132–138. <https://doi.org/10.17308/kcmf.2023.25/10983>

17. Peng K. Q., Hu J. J., Yan Y. J., ... Zhu J. Fabrication of single-crystalline silicon nanowires by scratching a silicon surface with catalytic metal particles. *Advanced Functional Materials*. 2006;16(3): 387–394. <https://doi.org/10.1002/adfm.200500392>

18. Chiappini C., Liu X., Fakhoury J. R., Ferrari M. Biodegradable porous silicon barcode nanowires with defined geometry. *Advanced Functional Materials*. 2010;20(14): 2231–2239. <https://doi.org/10.1002/adfm.201000360>

19. Turishchev S. Yu., Terekhov V. A., Nesterov D. N. ... Domashevskaya E. P. Electronic structure of silicon nanowires formed by MAWCE method. *Condensed Matter and Interphases*. . 2016;18(1): 130–141. Available at: <http://https://journals.vsu.ru/kcmf/article/view/117>

20. Gonchar K. A., Zubairova A. A., Schleusener A., Osminkina L. A., Sivakov V. Optical properties of silicon nanowires fabricated by environment-friendly chemistry. *Nanoscale Research Letters*. 2016;11: 1–5. <https://doi.org/10.1186/s11671-016-1568-5>

21. Tolstik E., Osminkina L. A., Akimov D., ... Popp J. Linear and non-linear optical imaging of cancer cells with silicon nanoparticles. *International Journal of Molecular Sciences*. 2016;17(9): 1536. <https://doi.org/10.3390/ijms17091536>

22. Osminkina L. A., Sivakov V. A., Mysov G. A., ... Timoshenko V. Yu. Nanoparticles prepared from porous silicon nanowires for bio-imaging and sonodynamic therapy. *Nanoscale Research Letters*. 2014; 9: 463. <https://doi.org/10.1186/1556-276X-9-463>

23. Osminkina L. A., Žukovskaja O., Agafilushkina S. N., ... Sivakov V. Gold nanoflowers grown in a porous Si/SiO<sub>2</sub> matrix: The fabrication process and plasmonic properties. *Applied Surface Science*. 2020;507: 144989. <https://doi.org/10.1016/j.apsusc.2019.144989>

24. Akan R., Parfeniukas K., Vogt C., Toprak M. S., Vogt, U. Reaction control of metal-assisted chemical etching for silicon-based zone plate nanostructures. *RSC Advances*. 2018;8(23): 12628–12634. <https://doi.org/10.1039/C8RA01627E>

25. Zi J., Zhang K., Xie X. Comparison of models for Raman spectra of Si nanocrystals. *Physical Review B*. 1997;55(15): 9263. <https://doi.org/10.1103/PhysRevB.55.9263>

## Information about authors

*Maria G. Shatskaia*, student, Faculty of Physics, Lomonosov Moscow State University (Moscow, Russian Federation).

[shatskaia.mg19@physics.msu.ru](mailto:shatskaia.mg19@physics.msu.ru)

*Daria A. Nazarovskaia*, graduate student, Faculty of Physics, Lomonosov Moscow State University (Moscow, Russian Federation).

<https://orcid.org/0000-0001-8151-9602>

[nazarovskaia.da22@physics.msu.ru](mailto:nazarovskaia.da22@physics.msu.ru)

*Kirill A., Gonchar*, Cand. Sci. (Phys.–Math.), Researcher, Faculty of Physics, Lomonosov Moscow State University (Moscow, Russian Federation).

<https://orcid.org/0000-0002-2301-2886>

[k.a.gonchar@gmail.com](mailto:k.a.gonchar@gmail.com)

*Yana V. Lomovskaya*, graduate student, Institute of Theoretical and Experimental Biophysics Russian Academy of Sciences (Pushchino, Russian Federation).

[yannalomovskaya@gmail.com](mailto:yannalomovskaya@gmail.com)

*Iliia I. Tsiniiaikin*, graduate student, Faculty of Physics Lomonosov Moscow State University (Moscow, Russian Federation).

<https://orcid.org/0000-0002-5820-8774>

[ii.tcinyaykin@physics.msu.ru](mailto:ii.tcinyaykin@physics.msu.ru)

*Olga A. Shalygina*, Cand. Sci. (Phys.–Math.), Associate Professor, Faculty of Physics, Lomonosov Moscow State University (Moscow, Russian Federation).

<https://orcid.org/0000-0002-0067-318X>

[shalygina@physics.msu.ru](mailto:shalygina@physics.msu.ru)

*Andrey A. Kudryavtsev*, Cand. Sci. (Phys.–Math.), Leading Researcher, Institute of Theoretical and Experimental Biophysics Russian Academy of Sciences, Institute for Biological Instrumentation of the Russian Academy of Sciences (Pushchino, Russian Federation).

[centavr42@mail.ru](mailto:centavr42@mail.ru)

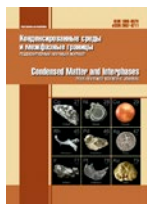
*Liubov A. Osminkina*, Cand. Sci. (Phys.–Math.), Leading Researcher, Faculty of Physics, Moscow Lomonosov Moscow State University (Moscow, Russian Federation), Institute for Biological Instrumentation of the Russian Academy of Sciences (Pushchino, Russian Federation).

<https://orcid.org/0000-0001-7485-0495>

[osminkina@physics.msu.ru](mailto:osminkina@physics.msu.ru)

Received 19.04.2023; approved after reviewing 28.04.2023; accepted for publication 10.05.2023; published online 25.03.2024.

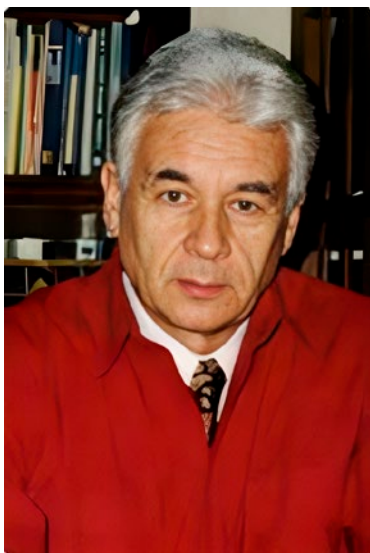
Translated by Valentina Mittova



## Condensed Matter and Interphases

Kondensirovannye Sredy i Mezhfaznye Granitsy  
<https://journals.vsu.ru/kcmf/>

### In memory of Professor V. A. Shaposhnik



This issue of the journal *Condensed Matter and Interphases* includes an article by Vladimir A. Shaposhnik, Professor at the Department of Analytical Chemistry of Voronezh State University, a remarkable scientist and lecturer, who passed away on 23 November 2023. It is difficult to believe! Vladimir Shaposhnik loved life, science, and his job and always treated his colleagues and students with a lot of respect. He was an extraordinary man of profound intellect and culture who was always seeking and finding.

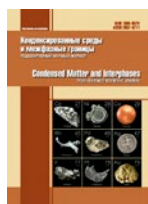
V. A. Shaposhnik published outstanding research papers (monographs, reviews, articles) not only in the field of electromembrane

processes, to which he devoted all his scientific life, but also in other fields of chemistry and chemical technology. His articles on the history of science and the history of outstanding scientific discoveries are widely cited all around the world. Vladimir Shaposhnik was dedicated to the issues of philosophy and methodology of science, he gave lectures in chemistry, the philosophy of chemistry, and the methodology of scientific knowledge to undergraduate and postgraduate students. He supervised PhD and DSc dissertations related to the development of various aspects of the method of electro dialysis. His students work not only at the Faculty of Chemistry of VSU, but also at other universities of our city, and in many other cities in Russia and beyond. Vladimir Shaposhnik repeatedly gave lectures as a guest lecturer at many Russian and international universities. He gave brilliant talks at international and Russian conferences.

Professor Shaposhnik was deeply respected by his colleagues and students, who were always impressed by his versatility, creativity, and remarkable breadth of knowledge. He was a great communicator and a master of rhetoric. Vladimir Shaposhnik was a fighter till his last days despite his age and other difficulties. He passed on his passion for science to the younger generations in the community of grateful students.

The memory of Vladimir Shaposhnik will live in the hearts of many generations of students and employees of the Faculty of Chemistry and in the hearts of all who knew him.





## Guide for Authors – 2024

Manuscripts should be submitted as single **Microsoft Word 2003** files.

**Preferred font** 12 pt Times New Roman (please, do not use any other fonts, except for Symbol), 1.5 spaced lines, 1.25 cm first-line indent. Decimal values (e.g. 0.1; 0.9; 2.3) should be written using a decimal point.

Review/Original article/Short communication  
<https://doi.org/10.17308/kcmf.2024.26/000>

### **Modelling of interdiffusion and phase formation in thin-film two-layer systems of polycrystalline oxides of titanium and cobalt**

*(All proper nouns should be capitalized; titles and subtitles should be left-aligned)*

**N. N. Afonin<sup>\*1</sup>, V.A. Logacheva<sup>2</sup>**

<sup>1</sup>Voronezh State Pedagogical University,  
86 ul. Lenina, Voronezh 394043, Russian Federation

*(Official name and address of the organisation)*

<sup>2</sup>Voronezh State University,  
1 Universitetskaya pl., Voronezh 394018, Russian Federation

#### **Abstract**

The abstract should be 200–250 words and include the following sections.

**Purpose:** States the problem considered in the article, its importance, and the purpose of the research.

**Experimental:** Provides information about the objects being studied and the methods used.

**Conclusions:** Provides a brief description of the principal results, major conclusions, and their scientific and practical relevance.

**Keywords:** Please, provide 5–10 keywords for the principal concepts, results, and terms used in the article.

**Funding:** This work was funded by RFBR according to the research project No. 18–29–24128.

**Acknowledgments:** The DTATGA, XRD and SEM studies were performed on the equipment of the Engineering Center of Saint Petersburg State Institute of Technology.

**For citation:** Afonin N. N., Logacheva V. A. Modelling of interdiffusion and phase formation in the thin-film two-layer system of polycrystalline oxides of titanium and cobalt. *Condensed Matter and Interphases*. 2023;25(1): 000–000. <https://doi.org/10.17308/kcmf.2023.25/0000>

<sup>\*</sup>Nikolay N. Afonin, [nafonin@vspu.ac](mailto:nafonin@vspu.ac)  
© Afonin N. N., Logacheva V. A., 2023

## Article structure

The main text of the manuscript should have the following structure.

### 1. Introduction

*The introduction* (1–2 pages) states the problem under consideration, its relevance, and the most important tasks that need to be resolved. Describe the scientific problems which have not yet been solved and which you sought to solve in your research. The introduction should contain a short critical review of previously published works in this field and their comparative analysis. It is recommended that the analysis is based on 20–30 studies (no more than 20% of references to the author's own works, at least 50% of the references should be to articles published within the previous 5 years). **The purpose** of the article is indicated by the problem statement.

The Vancouver reference style is used in the journal: bibliographic references in the text of the article are indicated by numbers in square brackets; in the references section, the references are numbered in the order they are mentioned in the text.

#### *Example of references in-text citations:*

Single crystals of difluorides of alkaline earth elements are widely used as photonics materials [1–3] as well as matrices for doping with rare-earth ions [4, 10].

References should primarily be made to original articles published in scientific journals indexed by global citation databases. References should indicate the names of all authors, the title of the article, the name of the journal, year of publication, volume (issue), number, pages, and DOI (Digital Object Identifier <https://search.crossref.org/>). If a DOI is lacking, a link to the online source of the article must be indicated. References to dissertation abstracts are acceptable if the texts are available online. It is vital that our readers can find any of the articles or other sources listed in the reference section as fast as possible. Links to unpublished literature sources or sources not available online are unacceptable.

### 2. Experimental

*The experimental section* (2–3 pages) provides the details of the experiment, the methods, and the equipment used. The object of the study and the stages of the experiment are described in detail and the choice of research methods is explained.

### 3. Results and discussion

*Results and discussion* (6–8 pages) should be brief, but detailed enough for the readers to assess the conclusions made. It should also explain the choice of the data being analysed. Measurement units on graphs and diagrams should be separated with a comma. **Formulae should be typed using Microsoft Office Equation 3 or Math Type** and aligned on the left side. Latin letters should be in italics. Do not use italics for Greek letters, numbers, chemical symbols, and similarity criteria.

All subheadings should be in italics.

#### *Example:*

1.1. X-ray diffraction analysis

*Example of figure captions in the text of the article:* Fig. 1, curve 1, Fig. 2b.

A complete list of figures should be provided at the end of the paper after the information about the authors.

**Figures and tables should not be included in the text of the article.** They should be placed on a separate page. Figures should also be **submitted as separate \*.tif, \*.jpg, \*.cdr, or \*.ai** files. **All figures should have a minimum resolution of 300 dpi.** Name each figure file with the name of the first author and the number of the figure.



#### 4. Conclusions

*Conclusions* (1 paragraph) should briefly state the main conclusions of the research. Do not repeat the text of the article. The obtained results are to be considered with respect to the purpose of the research. This section includes the conclusions, a summary of the results, and recommendations. It states the practical value of the research and outlines further research problems in the corresponding field.

#### Contribution of the authors

At the end of the Conclusions the authors should include notes that explain the actual contribution of each co-author to the work.

##### Example 1:

Nikolay N. Afonin – Scientific management, Research concept, Methodology development, Writing – original draft, Final conclusions.

Vera A. Logachova – Investigation, Writing – review & editing.

##### Example 2:

The authors contributed equally to this article.

#### Conflict of interests

The authors declare that they have no known competing financial interests or personal relationships that could have influenced the work reported in this paper.

#### References

*(The references are to be formatted according to the Vancouver Style. The reference list should only include articles published in peer-reviewed journals)*

#### Examples:

##### Articles in scientific journals

1. Bahadur A., Hussain W., Iqbal S., Ullah F., Shoaib M., Liu G., Feng K. A morphology controlled surface sulfurized CoMn<sub>2</sub>O<sub>4</sub> microspike electrocatalyst for water splitting with excellent OER rate for binder-free electrocatalytic oxygen evolution. *Journal of Materials Chemistry A*. 2021;20(9): 12255–12264. <https://doi.org/10.1039/D0TA09430G>

2. Alexandrov A. A., Mayakova M. N., Voronov V. V., Pominova D. V., Kuznetsov S. V., Baranchikov A. E., Ivanov V. K., Fedorov P. P. Synthesis upconversion luminophores based on calcium fluoride. *Condensed Matter and Interphases*. 2020;22(1): 3–10. <https://doi.org/10.17308/kcmf.2020.22/2524>

3. Kopeychenko E. I., Mittova I. Y., Perov N. S., Alekhina Y. A., Nguyen A. T., Mittova V. O., Pham V. Synthesis, composition and magnetic properties of cadmium-doped lanthanum ferrite nanopowders. *Inorganic Materials*. 2021;57(4): 367–371. <https://doi.org/10.1134/S0020168521040075>

##### Books: print

4. Nakamoto K. *Infrared and Raman spectra of inorganic and coordination compounds*. New York: John Wiley; 1986. 479 p.

5. Fedorov P. P., Osiko V. V. *Crystal growth of fluorides*. In: *Bulk Crystal Growth of Electronic, Optical and Optoelectronic Materials*. P. Capper (ed.). Wiley Series in Materials for Electronic and Optoelectronic Applications. John Wiley & Son. Ltd.; 2005. pp. 339–356. <https://doi.org/10.1002/9780470012086.ch11>

6. *Nanostructured oxide materials in modern micro-, nano- and optoelectronics*. V. A. Moshnikov, O. A. Aleksandrova (eds.). Saint Petersburg: Izd-vo SPbGETU “LETI” Publ., 2017. 266 p. (in Russ.)

##### Conference proceedings: individual papers

7. Afonin N. N., Logacheva V. A., Khoviv A. M. Synthesis and properties of functional nanocrystalline thin-film systems based on complex iron and titanium oxides. In: *Amorphous and microcrystalline semiconductors: Proc. 9th Int. Conf., 7–10 July 2014*. St. Petersburg: Polytechnic University Publ.; 2014. p. 356–357. (In Russ.)

**Website**

8. NIST Standard Reference Database 71. *NIST Electron Inelastic-Mean-Free-Path Database: Version 1.2*. Available at: [www.nist.gov/srd/nist-standard-reference-database-71](http://www.nist.gov/srd/nist-standard-reference-database-71)

**Patent**

9. Chekanov V. V., Kandaurova N. V., Rakhmanina Yu. A., Chekanov V. S. *Ultrasound indicator 2*. Patent RF, no. 2446384, 2012. Publ. 27.03.2012, bull. no. 9. (In Russ.)

**Information about the authors**

This section should include the full last and first name(s) of the author(s), their academic degree, academic title, affiliation, position, city, country, e-mail, and ORCID (register for an ORCID here <https://orcid.org/register>).

**Example:**

*Nikolay N. Afonin*, Dr. Sci. (Chem.), Research Fellow, Professor at the Department of Science and Technology Studies, Voronezh State Pedagogical University (Voronezh, Russian Federation).

<https://orcid.org/0000-0002-9163-744X>  
nafonin@vspu.ac.ru

*Vera A. Logachova*, Cand. Sci. (Chem.), Research Fellow at the Department of General and Inorganic Chemistry, Voronezh State University (Voronezh, Russian Federation).

<https://orcid.org/0000-0002-2296-8069>  
kcmf@main.vsu.ru

*Tien Dai Nguyen*, PhD in Advanced Materials Science and Engineering, Lecturer/ Research at Institute of Theoretical and Applied Research (ITAR), Duy Tan University (DTU), Hanoi, Vietnam.

<https://orcid.org/0000-0002-9420-210X>  
nguyentiendai@duytan.edu.vn

*Valery V. Voronov*, Cand. Sci. (Phys.-Math.), Head of the Laboratory, Prokhorov General Physics Institute of the Russian Academy of Science (Moscow, Russian Federation).

<https://orcid.org/0000-0001-5029-8560>  
voronov@lst.gpi.ru

*Received 04.03.2023; approved after reviewing 13.04.2023; accepted for publication 15.05.2023; published online 25.09.2023.*

A complete list of figures should be provided at the end of the paper after the information about the authors.

**Example:**

**Fig. 1.** Dependences of the parameters  $a$  and  $c$  of the tetragonal lattice of nanocrystalline PdO films on the oxidation temperature  $T_{ox}$ : 1 – single-phase PdO films, 2 – heterophase PdO + Pd films; 3 – data of the ASTM standard [22, 23]

**Table 1.** The values of relative electronegativity (ENE) of some chemical elements [30] and the proportion of the ionic component of the chemical bond in binary compounds of the AB composition formed by these elements

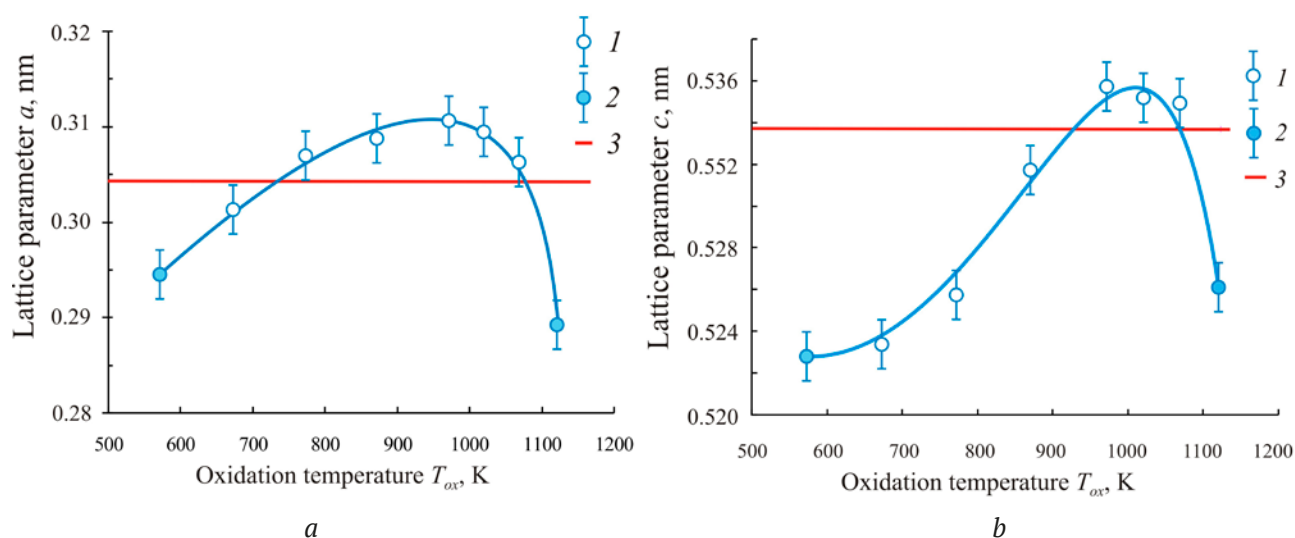


**Fig. 1.** Dependences of the parameters  $a$  and  $c$  of the tetragonal lattice of nanocrystalline PdO films on the oxidation temperature  $T_{ox}$ : 1 – single-phase PdO films; 2 – heterophase PdO + Pd films; 3 – data of the ASTM standard [22, 23]

**Table 1.** Values of the ionic radii of palladium  $Pd^{2+}$  and oxygen  $O^{2-}$  [30–32]

Ion	Coordination number CN	Coordination polyhedron	Values of ionic radii $R_{ion}$ , nm
$Pd^{2+}$	4	Square (rectangular)	0.078 [30]; 0.086 [31]; 0.078 [32]
$O^{2-}$	4	Tetragonal tetrahedron	0.132 [30]; 0.140 [31]; 0.124* [31]; 0.132 [32]

\*The values of ionic radius were obtained on the basis of quantum mechanical calculations.

## ACCOMPANYING DOCUMENTS

*(The following documents should be submitted as PDF files)*

1. Covering letter (with authorisation for open access publication)
2. License agreement (signed by all authors) <https://journals.vsu.ru/kcmf/Licensingcontract>
3. Manuscript.

## EDITING AND PROOFREADING

When the layout is ready it is sent back to the authors for proofreading. The article should be sent back to the publisher within a maximum of three days. The authors may only correct printing mistakes and introduce minor changes to the text or tables.